SPATIOTEMPORAL DYNAMICS OF T CELL ACTIVATION DURING LOCALISED HSV INFECTION

Jyh Liang Hor

Submitted in total fulfilment of the requirements of the degree of Doctor of Philosophy

May, 2016

Department of Microbiology and Immunology
The University of Melbourne
Australia

“Empty your mind, be formless, shapeless, like water.
Now you put water into a cup, it becomes the cup.
You put water into a bottle, it becomes the bottle.
And if you put it into a teapot… it *becomes* the teapot.

Now, water can flow, or creep, or drip, or crash!
Be water, my friend.”

- Bruce Lee

“Impatience asks for the impossible,
wants to reach the goal without the means of getting there.
The length of the journey has to be borne with,
for every moment is necessary.”

- G. W. F. Hegel

ABSTRACT

The induction of cell-mediated immune responses against localised infection requires complex orchestration involving multiple subsets of immune cells; from antigen acquisition by tissue-derived antigen-presenting cells (APC), to the priming of antigen-specific T lymphocytes in the secondary lymphoid tissues. The spatiotemporal coordination of T cell priming and the dynamic interplay between T cells and APC during localised viral infection, as well as how $CD4^+$ T cells deliver help are poorly understood. Using a mouse localised cutaneous herpes simplex virus type 1 (HSV-1) infection model, this thesis investigated the intricate relationship of both innate and adaptive immune cells in shaping the optimal generation of cell-mediated immunity against localised viral infection.

In light of recent studies demonstrating neutrophils involving in the crosstalk between innate and adaptive immunity, we examined the immunomodulatory roles of this innate immune cell during cutaneous HSV-1 infection. We identified an early transient wave of neutrophil infiltration to both the skin and draining lymph nodes (LN) triggered by dermal scarification. However, we found only minimal migration of neutrophils from skin to draining LN, and ablation of neutrophils did not affect T cell priming, or their migration to the infected skin, suggesting that neutrophils are dispensable for the generation of T cell responses against localised HSV-1 infection.

To understand the spatiotemporal dynamics of T cell priming, the activation kinetics and cellular dynamics of $CD4^+$ and $CD8^+$ T cells was characterised in the draining LN through the combined use of flow cytometry, immunofluorescence confocal microscopy and intravital two-photon microscopy. The work here revealed that $CD4^+$ and $CD8^+$ T cells are activated at distinct times, facilitated by distinct dendritic cell (DC) subsets. $CD4^+$ T cells were first activated at ~12 hr post-infection and preferentially clustered with migratory $CD11b^+$ DC, whereas $CD8^+$ T cells were activated at a later phase, ~36-48 hr post-infection and clustered with LN-resident $XCR1^+$ DC. These findings highlight the complex interactions involving multiple DC and T cell subsets, and importantly the pivotal

role of XCR1$^+$ DC not only as the primary APC subset that primes CD8$^+$ T cells, but also serving as the central platform for the delivery of CD4$^+$ T cell help.

Finally, we investigated the role of dedicator of cytokinesis 8 (DOCK8) proteins in the formation of CD8$^+$ tissue-resident memory T cells (T_{RM}) after skin HSV-1 infection. DOCK8-deficient CD8$^+$ T cells exhibited severely impeded survival and T_{RM} forming capacity, resulting in the loss of protection against subsequent HSV-1 challenge.

DECLARATION

The work presented in this thesis was conducted at the University of Melbourne, in the laboratories of Associate Professor Scott N Mueller and Professor William R Heath. The project was funded by the grants from the National Health and Medical Research Council and the Australian Research Council. Jyh Liang Hor was supported by Melbourne International Research Scholarship.

This is to certify that,

(i) the thesis comprises only my original work towards the PhD, except where indicated in the Preface,

(ii) due acknowledgment has been made in the text to all other material used,

(iii) the thesis is less than 100,000 words in length exclusive of figures, tables and references.

Jyh Liang Hor

PREFACE

My contribution to experiments in each of the Chapters was as follows:

Chapter 3: 100%

Chapter 4: 95%

Chapter 5: 100%

Chapter 6: 100%

I acknowledge the important contributions of others to experiments presented in this thesis:

Chapter 4: Paul Whitney

Download links for movies presented in this thesis are provided in **Appendix B**.

High-resolution movies can be obtained by downloading the .mov files.

ACKNOWLEDGEMENTS

I am deeply grateful to my supervisors Scott Mueller and Bill Heath, not only for providing an excellent opportunity for my training as a scientist but also for your mentorship, encouragement and inspiration. To Scott, I have learned so much from our countless hours of discussion over the years. Thanks for putting up with me through the ups and downs of this exciting journey. To Bill, thanks for being so intimidating to me, to which I could only respond by holding myself to a higher standard.

To Ali, thanks for teaching me literally everything, and for showing me how life and science could mix really well. Your dynamism, versatility and intellect have been sorely missed in the past few months. To Gayle and Claerwen, life in the lab would have been infinitely more difficult without the both of you ensuring the proper operation of the lab. I apologise for being a troublemaker sometimes! To Laura and Linda, thanks for the occasional advices (which I truly appreciate), and for being such an inspiration to me. I could only wish that I had learned more from you over the years. To Prof. Stock, your timeless advice will always stay with me, and it's been an honour to have a glimpse into your brilliant mind.

Special thanks to the rest of PIs from the Heath-Carbone Empire: Frank Carbone, Thomas Gebhardt and Sammy Bedoui for your invaluable insight, advice and critique over the years. Also to my PhD advisory committee Nicole La Gruta and Andrew Brooks for your support, encouragement and appraisal.

To all the animal house staff, and to all the RAs, my sincerest thanks for all the tedious and hard work in making the work in this thesis possible. It should go without saying that I have greatly benefited from a congenial atmosphere made possible by all the lab members, past and present. It's been a pleasure to work alongside with you over the years.

Everyone who has given up time to talk to me, or simply to discuss or critique ideas, you have my sincerest thanks!

To my peers and friends, thanks for injecting what I consider a treasurable amount of friendship to my (understandably) non-existent social life. I wish you all the best in your future endeavours.

To my fellow climbers, thanks for keeping me alive all this while, for it would have been literally impossible to complete this work were it not for your watchful eyes. I wish all of you to send your dream routes in no time.

Finally, I'd like to thank my family for encouraging me to forge my own path. None of this would be possible without your unconditional support, care and love.

LIST OF PUBLICATIONS

Macleod, B.L., Bedoui, S., **Hor, J.L.**, Mueller, S.N., Russell, T.A., Hollett, N.A., Heath, W.R., Tscharke, D.C., Brooks, A.G., and Gebhardt, T. (2014). Distinct APC subtypes drive spatially segregated CD4+ and CD8+ T-cell effector activity during skin infection with HSV-1. PLoS Pathog. *10*, e1004303.

Zhang, Q., Dove, C.G.†, **Hor, J.L.**†, Murdock, H.M., Strauss-Albee, D.M., Garcia, J.A., Mandl, J.N., Grodick, R.A., Jing, H., Chandler-Brown, D.B., Lenardo, T.E., Crawford, G., Matthews, H.F., Freeman, A.F., Cornall, R.J., Germain, R.N., Mueller, S.N., Su, H.C. (2014). DOCK8 regulates lymphocyte shape integrity for skin antiviral immunity. J. Exp. Med. *211*, 2549–2566.

Hor, J.L.*, Whitney, P.G.*, Zaid, A., Brooks, A.G., Heath, W.R., and Mueller, S.N. (2015). Spatiotemporally Distinct Interactions with Dendritic Cell Subsets Facilitates CD4+ and CD8+ T Cell Activation to Localized Viral Infection. Immunity *43*, 554–565.

* Co-first author
† Co-second author

ABBREVIATIONS

2P	two-photon
α-DG	α-dystroglycan
aLN	axillary LN
APC	antigen-presenting cell
BCG	Bacillus Calmette–Guérin
bLN	brachial LN
BP	band-pass
Ca	calcium
CCL	CC chemokine ligand
CCR	CC chemokine receptor
CD	Cluster of differentiation
CFU	colony-forming unit
cLN	cervical LN
CPE	cytopathic effect
CTL	cytotoxic T lymphocyte
CTV	CellTrace Violet
CXCL	CXC chemokine ligand
CXCR	CXC chemokine receptor
D	day
DAMP	danger-associated molecular patterns
DC	dendritic cell
dDC	dermal dendritic cell
dLN	draining LN
DNA	deoxyribonucleic acid
DNFB	dinitrofluorobenzene
DOCK8	Dedicator of cytokinesis 8
DRG	dorsal root ganglia
EGFP	enhanced green fluorescent protein
FDC	follicular dendritic cell
FRC	fibroblastic reticular cell
g	gram
G	gauge

GAG	glycosaminoglycan
gB	glycoprotein B
gBT-I	***gB***-specific, MHC class ***I***-restricted ***T***CR transgenic mice
gC	glycoprotein C
gD	glycoprotein D
gDT-II	***gD***-specific, MHC class ***II***-restricted ***T***CR transgenic mice
gE	glycoprotein E
gH	glycoprotein H
gL	glycoprotein L
HEV	high endothelial venule
hr	hour
HSV	herpes simplex virus
HSV-1	herpes simplex virus type 1
HSV-2	herpes simplex virus type 2
HVEM	herpesvirus entry mediator
ICP	Infected cell protein
i.d.	intradermal
IFN	interferon
IFR	interfollicular region
IgE	Immunoglobulin E
IgG	Immunoglobulin G
IL	interleukin
iLN	inguinal LN
IS	immunological synapse
ISG	IFN stimulated gene
kDa	kilodalton
LC	Langerhans cell
LCMV	lymphocytic choriomeningitis virus
LN	lymph node
LPS	lipopolysaccharide
LTαβ	lymphotoxin αβ
LTβR	lymphotoxin β receptor
LysM	Lysozyme M
M	molar

MFI	mean fluorescence intensity
µg	microgram
mg	milligram
MHC-I	Major Histocompatibility Complex Class I
MHC-II	Major Histocompatibility Complex Class II
min	minute
µL	microliter
mL	millilitre
µm	micrometre
mm	millimetre
µM	micromolar
mM	millimolar
MMV	murine cytomegalovirus
m.o.i.	multiplicity of infection
MVA	Modified Vaccinia Ankara
NDD	non-descanned detector
NET	neutrophil extracellular traps
ng	nanogram
NK	natural killer
NLO	non-linear optics
nm	nanometre
nM	nanomolar
OVA	ovalbumin
p.i.	post-infection
PAMP	pathogen-associated molecular patterns
PBS	phosphate buffered saline
pDC	plasmacytoid DC
pfu	plaque-forming unit
pLN	popliteal LN
pMHC	peptide-MHC complex
PRR	pathogen recognition receptor
RAG	recombination activating gene
ROI	reactive oxygen intermediates
RT-PCR	reverse transcription polymerase chain reaction

S1P	sphingosine-1-phosphate
$S1P_1$	sphingosine-1-phosphate receptor
s.c.	subcutaneous
SCID	Severe combined immunodeficiency
SCS	subcapsular sinus
SHG	second harmonic generation
SLO	secondary lymphoid organ
T_{CM}	central memory T cell
T_{EM}	effector memory T cell
T_{FH}	follicular helper T cell
T_{RM}	tissue-resident memory T cell
TCR	T cell receptor
TGFβ	Transforming growth factor beta
Th1	Type 1 T helper
TLR	Toll like receptor
TNF	tumour necrosis factor
TRAIL	TNF-related apoptosis-inducing ligand
TRITC	tetramethylrhodamine
UV	ultraviolet
VV	Vaccinia virus
WT	wildtype
XCL	XC chemokine ligand
XCR	XC chemokine receptor
YFP	yellow fluorescent protein

TABLE OF CONTENTS

CHAPTER ONE:
LITERATURE REVIEW

1.1 INTRODUCTION

The generation of an adaptive immune response against pathogen infection relies on the clonal expansion of rare antigen-specific lymphocytes from a pre-generated repertoire. The secondary lymphoid organs (SLO), including the spleen and the lymph nodes (LN), represent an evolutionary strategy to resolve the fundamental challenge of allowing a rare antigen-specific lymphocyte to encounter another equally rare antigen-bearing presenting cell in a timely fashion in order to promote effective pathogen clearance.

1.2 THE LYMPH NODE: REACTION CENTRE OF AN IMMUNE RESPONSE

Basic Architecture

Lymph nodes (LNs) are a set of highly organised tissues arranged in chains, forming the intricately linked network of the SLOs. Apart from serving as strategic checkpoints through which lymph collected from the periphery must pass, allowing immune surveillance and filtering of the entire body for foreign antigen, LNs also function as hubs where naïve lymphocytes from the circulation and APC from the periphery can conveniently interact.

The highly compartmentalised nature of the LN architecture suggests a sophisticated solution to the pressure exerted by constant pathogen threats, and studies dissecting these anatomically distinct regions have unravelled the functional properties of various specialised LN compartments that promote efficient immune surveillance (**Fig. 1.1**). Broadly, disparate B follicles occupy the superficial cortex and surround the deeper T cell zone located in the paracortex.

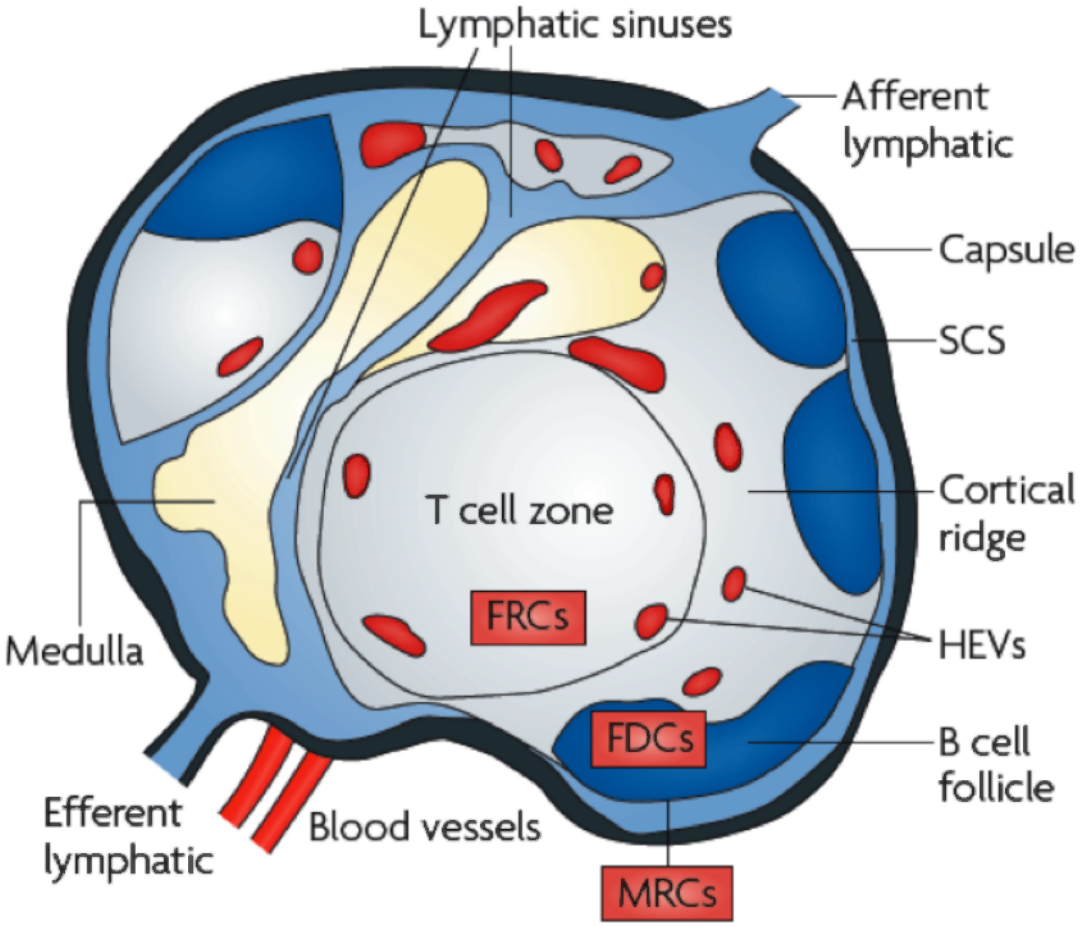

Figure 1.1 Anatomical compartments of a lymph node
Lymph nodes are highly compartmentalised organs and can be delineated into several distinct regions: B follicles, T cell zone and medulla. The transition between T cell zone and B follicles is termed the cortical ridge, where high endothelial venules (HEV) are abundant. Naïve lymphocytes in the circulation enter the LN through HEV. Lymph from the periphery enters the LN via afferent lymphatics, situated in the LN cortex, which opens into the subcapsular sinus (SCS) underneath the LN capsule and allows the lymph to percolate through the organ. DC from peripheral tissues enter LN with lymph and migrate to the T cell zone to facilitate encounter with T cells. Lymph is collected in the medulla and drains from the efferent lymphatics at the LN hilum. Stromal cells constitute the structural network of the LN: fibroblastic reticular cells (FRCs) in the paracortex, follicular dendritic cells (FDCs) in the B follicles, and marginal reticular cells (MDCs) that separate the SCS from FDCs. Figure adapted from Mueller and Germain, 2009.

Non-haematopoietic stromal cells, namely follicular dendritic cells (FDC) and fibroblastic reticular cells (FRC) populate the B follicles and T cell zone, respectively. Medullary cords form the medulla at the hilum of the LN (Mueller and Germain, 2009).

Lymph, carrying immune cells, soluble proteins and other macromolecules from the periphery or upstream nodes, enters the LN through afferent lymphatics at the cortex, which opens into a cavity underneath the LN capsule known as the subcapsular sinus (SCS). Separating the B follicles from the SCS is a layer of specialised $CD169^+$ macrophages that, together with $F4/80^+$ macrophages in the medulla, filter the incoming lymph and capture potential lymph-borne antigen (Norbury et al., 2002; Phan et al., 2009). Parts of the SCS branch off to form blind-ended cortical sinuses in the cortical ridges (also known as interfollicular regions – the transition between B follicles in the cortex and T cell zone in the paracortex) and eventually merge with the medullary sinuses at the medulla (Cyster and Schwab, 2012). Smaller conduits, abundant in collagenous fibre and ensheathed by FRC, also branch off from these sinuses, forming the stromal network in T cell zone as well as allowing low molecular weight proteins and macromolecules to be delivered to the deeper region of the node (Gretz et al., 1997; Gretz et al., 2000). Lymph percolates through the LN and is collected at the medulla, exits the node through efferent lymphatics and continues to drain into other LNs down the chain before emptying into the circulation through the thoracic duct.

Transient residence in LN by naïve lymphocytes – entry, retention and egress

Lymphocytes in the circulation enter the LN from specialised post-capillary venules known as high endothelial venules (HEV) that pass through the node at the cortical ridges between B follicles and T cell zone. Lymphocytes expressing L-selectin (CD62L) tether and roll along the HEV through interaction with L-selectin ligands (including GlyCAM-1 and MadCAM-1) expressed on endothelial cells (von Andrian and Mempel, 2003). Further interactions between the lymphocyte chemokine receptor CCR7 with CCL21, as well as the binding of

lymphocyte function-associated antigen 1 (LFA-1) with intracellular adhesion molecule 1 (ICAM-1) expressed on HEV endothelia trigger the arrest and the subsequent transmigration of lymphocytes through the capillary vessel into the LN parenchyma (Girard et al., 2012). From the cortical ridge, T cells expressing CCR7 are guided by chemokine cues (CCL19 and CCL21, abundantly expressed by FRC; Luther et al., 2000) toward the deep T cell zone whereas B cells expressing CXCR5 migrate into the B follicles by sensing CXCL13 produced by FDC (Ansel et al., 2000).

Within the T cell zone, T cells traverse through the LN by migrating along the stromal mesh formed by FRC in a "random walk" fashion (Bajenoff et al., 2006). This form of intranodal motility along FRC fibres is partially mediated by CCR7 (Worbs et al., 2007). Naïve T cells transiently interact with dendritic cells (DCs) (averaging 3-4 minutes per interaction; Mandl et al., 2012) that have been integrated into the stromal network (Lindquist et al., 2004). In the steady state, T cells usually reside in the LN for 12-18 hours and if no cognate interaction with DC is made, they exit through the sinuses and migrate to the downstream node via efferent lymphatics (Gowans and Knight, 1964; Tomura et al., 2008).

Lymphocyte transmigration into the lymphatic sinuses from the LN parenchyma is primarily mediated by sphingosine-1-phosphate receptor ($S1P_1$). Sensitive to its ligand S1P, lymphocytes internalise $S1P_1$ in the circulation and lymphatics due to the higher S1P concentration in the blood plasma and lymph. In contrast, lower concentration of S1P within the LN environment allows lymphocytes to re-express $S1P_1$, and is essential for their entry into the lymphatic sinuses from the LN parenchyma.

The balance between $S1P_1$ and CCR7 expression is thought to influence the decision by lymphocytes to exit LN (Cyster and Schwab, 2012). Whereas CCR7 promotes retention, increased expression of $S1P_1$ as T cells dwell within the LN eventually allows the signals from the latter to overcome and facilitate T cell transmigration into the sinuses. During inflammation, CD69 interacts with $S1P_1$ and inhibits its capacity to signal by causing internalisation and degradation in

the cytosol (Shiow et al., 2006; Bankovich et al., 2010). This promotes T cell retention during inflammation and improves the chances of T cell-DC encounter. However, after T cell activation and division for 3-4 cycles, $S1P_1$ expression is regained (the mechanism remains undefined, and is thought to be due to dilution of negative regulators as cells divide) while at the same time CCR7 is downregulated (Pham et al., 2008). This shift in balance allows $S1P_1$ signalling to prevail and promote lymphocyte egress and homing to inflamed tissues.

Cortical sinuses (the blind-ended sinuses located within the cortical ridges), rather than the medullary sinuses, have recently been identified as the principal sites of T cell exit during steady state (Grigorova et al., 2009). Once in the cortical sinuses, T cells continue to migrate and are then "caught" in the flow as they enter the larger branch and are carried to the medullary sinuses and eventually exit the node through efferent lymphatics. However, because of the proximity of cortical sinuses to the HEV, and because T cells have been observed to transmigrate into cortical sinuses relatively quickly upon exit from HEV, it has been suggested that T cells often re-enter the LN parenchyma from cortical sinuses at multiple occasions to account for the significantly longer dwell time within an individual LN (Grigorova et al., 2010).

Therefore, the LN provides an ideal environment in which the potential encounter between rare antigen-specific T cells and antigen-bearing presenting cells can be substantially improved through distinct anatomical organisation, highly specialised structural arrangements, as well as the regulation of chemokine and various biochemical pathways.

1.3 DYNAMICS OF PRIMARY IMMUNE RESPONSES

Optimal induction of cell-mediated immunity critically relies upon three key components: a) antigen presentation (acquisition of antigen by APC and its presentation to rare antigen-specific lymphocytes); b) delivery of co-stimulatory and 'help' signals to enhance and amplify the response; and c) differentiation factors present within the lymphoid tissue microenvironment that promote and sustain the acquisition and execution of effector and memory-forming capabilities of activated lymphocytes.

All three aspects require highly coordinated cellular level interactions involving integration of signals derived from a diverse array of immune cells – from the rapid encounter between antigen-specific lymphocytes and antigen-presenting cells, to the cooperative effort between helper $CD4^+$ and cytotoxic $CD8^+$ T cells in mediating pathogen clearance – and thus highlighting the importance of the dynamic events that lead to the successful generation of a primary immune response.

In this thesis, we wished to investigate the spatial and temporal dynamics of T cell activation during localised viral infection, as well as understanding how initiation of cell-mediated immunity is orchestrated by key immune cells in the lymphoid tissues (Chapters 4 & 5). As such, in the following sections, emphasis will be given to the current understanding of the spatiotemporal dynamics of immune cell interactions during lymphocyte priming, differentiation and memory-formation. Some of these studies were made possible by the advent of intravital imaging technology that allows visualisation of immune events *in vivo*. This technique is prominently utilised in this thesis, and thus will be briefly introduced in the next section.

1.3.1 A BRIEF OVERVIEW OF INTRAVITAL TWO-PHOTON MICROSCOPY

While flow cytometry has permitted examination of a wide array of cellular markers, it nevertheless falls short of providing spatial information on the cells of interest with respect to the microenvironment in tissues, the dynamic interactions between multiple cell types, as well as the 'flux' of the dynamic states that the cells undergo as the immune response unfolds. For many years, our understanding of the localisation and cell-cell interactions within tissues has largely relied on information provided by light and electron microscopy, the mainstay techniques that allow 'snapshots' of immune events to be glimpsed.

In their application to living tissues, immunofluorescence single-photon confocal microscopy has limited practical use beyond ~20μm of tissue depth due to heavy scattering of light, resulting in high levels of background and blurry images. Increasing fluorescence excitation to improve fluorescence signal causes phototoxicity and photobleaching. Thus, the introduction of two-photon microscopy nearly two decades ago constituted a breakthrough in the capability of imaging living biological tissues (Denk et al., 1990; Piston, 1999).

Two-photon excitation is achieved when two photons are simultaneously absorbed by a single fluorophore. This confers several advantages over conventional single-photon confocal microscopy: a) due to the low probability of two-photon absorption, excitation is effectively confined to the focal volume of the excitation region and reduces background noise from out-of-focus light scattering typically encountered with confocal microscopy; b) the longer excitation wavelength used (deep red and near infrared) allows deeper penetration into tissues of interest due to less scattering; and c) lower energy photons produce less phototoxicity and permit prolonged imaging periods.

Consequently, adoption of two-photon microscopy by immunologists more than a decade ago has led to a proliferation of studies examining the complex

interplay of cellular dynamics during immune response *in vivo*. Nevertheless, there are limits to this technology: despite significantly improved penetration depth, background noise can still render imaging of deep regions impractical (we could achieve up to 250-300μm under LN capsule and 200μm into the dermis of the skin). Furthermore, simultaneous imaging of multiple fluorescent probes (more than 5) is still not possible without significant compromises.

In short, two-photon microscopy has opened up new avenues for investigating the dynamic nature of the immune system, which is crucial for understanding of how immune cells cooperate and coordinate at a cellular level in order to drive critical immune decision towards forming optimal immunity or tolerance.

1.3.2 IMMUNE SURVEILLANCE: FROM ANTIGEN DELIVERY TO ANTIGEN PRESENTATION

During an infection, the route by which a pathogen is introduced can influence the dissemination and acquisition of antigen by antigen-presenting cells (APC). This is of critical relevance to the immune system to mount defences against all forms of pathogenic attacks. For example, the spleen filters the blood and serves as a reactive centre of primary immune response generation during systemic infections where pathogens have gained access to the circulatory system. On the other hand, a localised infection where pathogen dissemination is limited to the peripheral tissues often requires the transport of antigen by APC to the draining LN, where the kinetics and magnitude of the immune response, abundance of antigen, as well as the inflammatory milieu that influences lymphocyte differentiation can differ substantially.

How pathogens enter the immune surveillance network

In some infections, pathogens gain access to the lymphatics and are carried to the draining LN via lymph flow (**Fig. 1.2A**). $CD169^+$ macrophages that line the SCS and medulla form a filtering layer, capture lymph-borne antigens and transfer them to B cells and DCs in proximity for antigen presentation (Junt et al.,

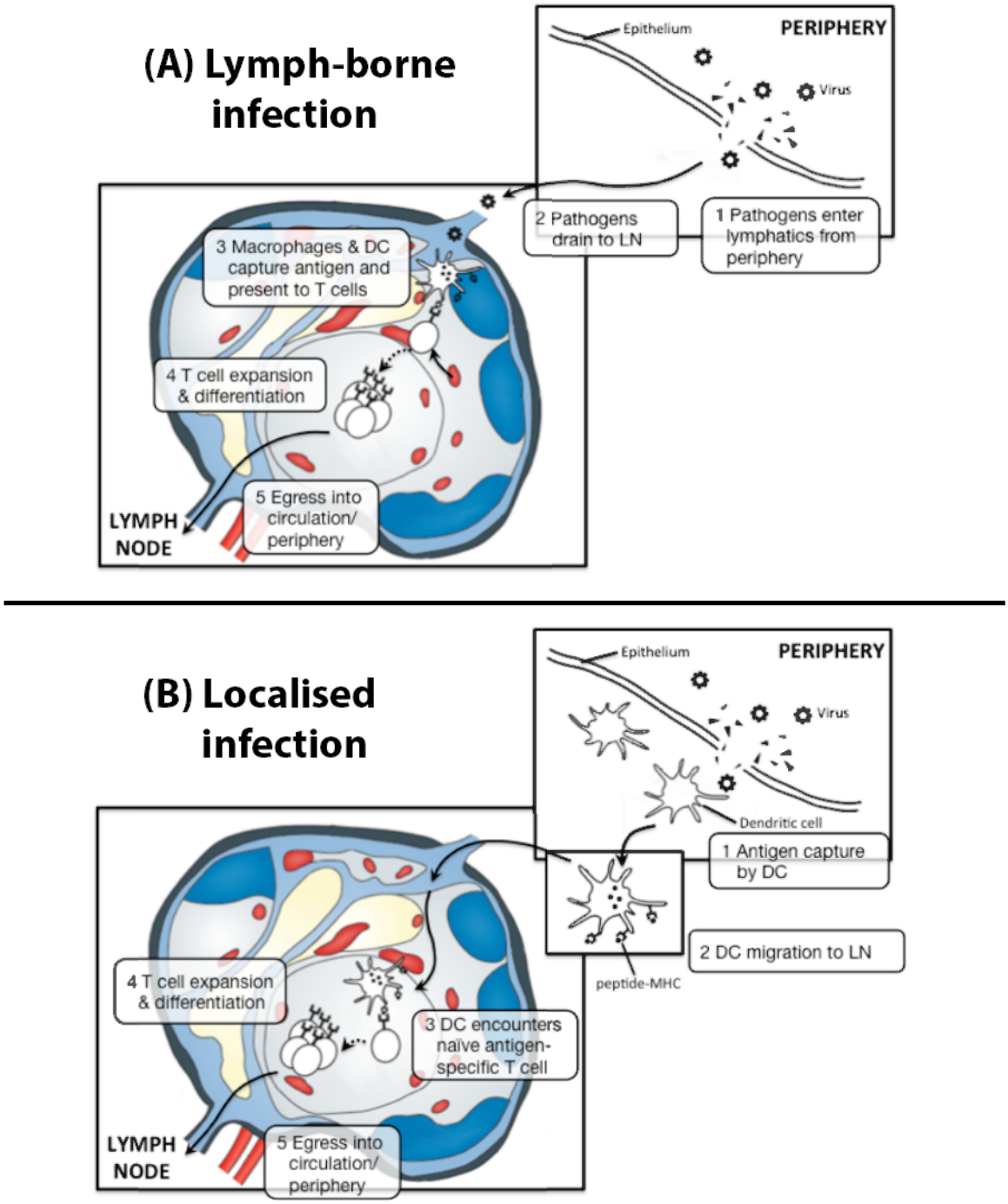

Figure 1.2. Initiation of cell-mediated immunity during peripheral infection: from antigen delivery to antigen presentation.
(A) Upon penetrating the anatomical barrier in the periphery (e.g. epithelium in the skin), pathogens can access the lymphatic sinuses draining the peripheral sites, and are carried to the local draining LN with the lymph. Macrophages and lymphatic-sinus DC that line the SCS floor sample the lymph-borne pathogens and present the antigen to T cells, which can re-localise from the T cell zone to the LN periphery.
(B) Alternatively, migratory DC patrolling the periphery capture pathogens, leading to their maturation and migration to draining LN. Upon arriving in the LN, DC present antigen to and activate antigen-specific T cells in the T cell zone. Antigen transfer to LN-resident DC may also occur at this stage. Activated T cells undergo proliferation and differentiation into effector cells, and egress the LN via efferent lymphatics to access the circulation and home to inflamed tissues.

2007; Phan et al., 2009; Hickman et al., 2011). Soluble antigens from the SCS also diffuse into the follicles to be acquired by B cells (Pape et al., 2007). Additionally, low molecular weight molecules (proteins <70 kDa) can be delivered to LN cortex via conduits formed by reticular fibres (Gretz et al., 1997; Gretz et al., 2000), and dendritic processes of DCs can penetrate the basement membrane of these conduits to sample the fluid for antigen (Sixt et al., 2005). A recently identified specialised $CD11b^+$ DC population residing under the SCS, termed lymphatic sinus associated (LS)-DC, was shown to sample particulate antigens from lymph fluid through protruding dendritic processes across the lymphatic lumen and facilitate early priming of $CD4^+$ T cells (Gerner et al, 2015). Some vaccination strategies and experimental settings, where pathogens are introduced via subcutaneous injection (e.g. footpad injection), also resemble this type of antigen delivery route. This route of infection is rapid and pathogens usually arrive at draining LN within minutes after injection (Junt et al., 2007; Hickman et al., 2008; Gonzalez et al., 2010).

In other peripheral infections, such as influenza virus of the lung and herpes virus infection of the skin, however, pathogen spread is typically contained within the infected site with little to no direct access to the draining LN (Belz et al., 2004; Mueller et al., 2002b; Allan et al., 2006; Lee et al., 2009). In this case, antigen delivery in the form of APC represents the primary means through which the immune response can be initiated (**Fig. 1.2B**). Therefore, the tissue tropism of the pathogen, the accessibility of APC to antigen, the functional differences between different APC subsets and their geographical segregation in both the peripheral tissue and the lymphoid organs, as well as the evasion mechanism employed by pathogen can influence the kinetics and magnitude of the initiation of an immune response.

In the following section, focus will be given to immune surveillance in the skin, as it is most relevant to the cutaneous herpes simplex virus type 1 (HSV-1) infection model employed in this thesis.

Immune surveillance in the skin

Apart from keratinocytes that form the protective barrier against pathogens beyond the skin and their ability to secrete inflammatory cytokines in response to pathogen invasion, various myeloid and lymphoid cell types, including γδ T cells, also populate the skin and perform immune surveillance (Nestle et al., 2009).

The DC subsets in the skin can be categorised based on their phenotypes and location in distinct regions of the skin. Langerhans cells (LC) are the main DC subset that populates the epidermis, while dermal DCs (dDC) localise to the dermis below the dermal-epidermal junction of the skin. LC have long been regarded as the principal DC subset responsible for capturing skin antigen. This is of particular relevance to cutaneous HSV-1 infection as the virus infects only epidermal cells and has limited dissemination to the dermal layer underneath (Shukla and Spear, 2001).

However, studies have provided evidence that LCs are significantly delayed in their arrival to the LN following immunisation or during skin HSV infection (Kissenpfennig et al., 2005; Allan et al., 2006) and, surprisingly, do not contribute to antigen presentation to HSV-specific $CD8^+$ T cells (Allan et al., 2003). On the contrary, $CD11b^+$ dDCs that reside in the dermis were shown to be the primary antigen carrier, despite their geographical exclusion from the epidermis (Allan et al., 2006). An additional $langerin^+$ $CD103^+$ $CD8\alpha^-$ dDC subset that was shown to cross-present skin-associated self antigens to $CD8^+$ T cells was also found to capture and present HSV-1 antigens late in infection but, surprisingly, did not contribute to the early wave of presentation required for priming (Bedoui et al., 2009). Early presentation to $CD8^+$ T cells was instead mediated by $CD8^+$ lymph node-resident DC (Allan et al., 2006).

The mechanism by which dDC acquire antigen in the epidermis is not known. Using transgenic OVA protein-expressing keratinocyte mouse model, it was shown that LC are dispensable for $CD103^+$ dDC-mediated cross-presentation of OVA, arguing against the possibility of antigen transfer from LC to dDC (Henri et

al., 2011). Bursch et al. (2007) noted that $CD103^+$ dDC in the dermis could reach their dendrites across the basement layer and probe the epidermal cells within hair follicles (which is contiguous with the surface epidermal layer and also a site of replication for HSV), providing a possible mechanism for antigen acquisition by dDC.

Neutrophils bridging the innate and adaptive immune systems

In addition to various DC subsets surveying the skin for foreign antigen, other innate immune cells are also involved during inflammatory response in the skin. Skin-resident macrophages, neutrophils, inflammatory monocytes and mast cells are known to trigger inflammatory cascades in the event of tissue damage or infection and promote further recruitment of innate immune cells through inflammatory cytokines and chemokines expressed by neutrophils and monocytes such as CXCR2 and CCR1 ligands (Soehnlein and Lindbom, 2010; Abraham & St. John, 2010).

Neutrophils are short-lived innate cells rapidly recruited to the inflammation site and are known for their phagocytic and antimicrobial activity through respiratory bursts of reactive oxygen intermediates (ROI) after engulfing pathogen, forming neutrophil extracellular traps (NETs), as well as secreting inflammatory cytokines to augment the recruitment of immune cells (Nathan, 2006). Due to their prominent role as pro-inflammatory cells, neutrophils usually undergo apoptosis by responding to increasing level of tumour necrosis factor (TNF) produced by macrophages and monocytes (Meszaros et al., 2000; van den Berg et al., 2001). Apoptotic neutrophils signal their own ingestion by macrophages and promote the resolution of inflammatory response (Lauber et al., 2003).

Of particular interest here, the traditionally-defined role of neutrophils as inflammatory cells has recently been re-examined and expanded as new evidence suggests neutrophils may also be involved in modulating the adaptive immune response (Mantovani et al., 2011). In this thesis, we investigated neutrophil functions as potential antigen carrier, and also as mediator of

crosstalk between innate and adaptive arms of the immune system during localised viral infection (Chapter 3). Studies have found that after ear skin injection with *Mycobacterium bovis* BCG or Modified Vaccinia virus Ankara (MVA), pathogen-containing neutrophils were detected in the draining auricular LN within hours, preceding the arrival of migratory DC (Abadie et al., 2005; Abadie et al., 2009). These findings implicated antigen shuttling capacity of neutrophils, and may therefore allow the LN early access to antigen for mounting rapid immune response. More recently, neutrophil recruitment from ear skin to draining LN after *Staphylococcus aureus* infection was shown to modulate proliferation of T and B cells (Hampton et al., 2015). Additionally, neutrophils were also found to transport MVA to the bone marrow, allowing $CD8^+$ T cells to be primed in this site (Duffy et al., 2012). Another study reported the ability of neutrophils to cross-prime $CD8^+$ T cells *in vivo* (Beauvillain et al., 2007). Thus, the rapid recruitment of neutrophils to the infected site and to the LN suggests a previously unidentified antigen shuttling capacity prior to peripheral DC migration, as well as immunomodulatory role associated with the generation of adaptive immune response.

DC maturation and migration to the draining LN

Immature DCs distribute throughout the peripheral tissues such as the skin to sample the microenvironment for foreign antigens. These DCs express inflammatory chemokine receptors CCR1, CCR2, CCR5 and CXCR1, which allow them to respond to inflammatory stimuli such as LPS and TNF-α (Sallusto et al., 1998).

During the steady state, only a limited number of DCs migrate to the draining LN from the periphery (Tomura et al., 2008). However, during inflammation, immature DC respond to inflammatory stimuli and undergo a maturation process that is associated with increased expression of MHC-II, chemokine receptors including CCR7 and CXCR4, as well as costimulatory molecules (such as CD80, CD86 and CD40) while at the same time inflammatory chemokine receptors such as CCR1, CCR2 and CCR5 are downregulated (Dieu et al., 1998; Sallusto et al., 1998; Sozzani et al., 1997; Förster et al., 1999). Mature DC from

the periphery can respond to the CCR7 ligands CCL19 and CCL21 and be guided towards the draining LN. Indeed, lymphatic endothelial cells (LECs) in the periphery were found to increase CCL21 expression during inflammation, suggesting a mechanism by which DCs can rapidly locate the exit point on their path towards the draining LN from the periphery (Martin-Fontecha et al., 2003). DCs enter the lymphatic vessels through preformed portals, allowing rapid entrance instead of integrin-mediated intravasation through sealed junctions of lymphatic cell layers (Pflicke and Sixt, 2009). Once in the LN, migrant DCs initially localise to the cortical ridge where HEVs are abundant but begin to disperse throughout the T cell zone over time and become integrated into the sessile DC network. (Lindquist et al., 2004)

Mode of antigen presentation

$CD8^+$ T cells can be activated either through direct or cross presentation, which refers to the presentation of endogenous or exogenous peptides through MHC-I, respectively. While MHC-I molecules constitutively present antigens sampled from the cytosol and allow $CD8^+$ T cells to be primed in the presence of foreign antigen in transformed or infected cells, a distinct pathway by which exogenously acquired antigen can be loaded on to MHC-I – cross-presentation – is important for protection against intracellular pathogens that do not infect APC (Heath and Carbone, 2001).

Various DC subsets exhibited differential cross-presentation ability. DCs derived from the Batf3-IRF8-Id2 transcription factor lineage consist of LN-resident $CD8\alpha^+$ DC as well as migratory $CD103^+$ DC. Recently, the chemokine receptor XCR1 has been identified as a unique expression marker on DC ontologically derived from this lineage in mice and its equivalent in humans (Dorner et al., 2009; Bachem et al., 2010; Bachem et al., 2012). These DCs have demonstrated superior cross-presentation capacity compared to $CD8\alpha^-$ DC subsets (Schnorrer et al., 2006; Bedoui et al., 2009). $CD8\alpha^+$ DC were found to have an enhanced ability to capture dead cells (Schulz and Reis e Sousa, 2002; Iyoda et al., 2002) and their expression of the C-type lectin CLEC9A (DNGR-1) has been implicated as vital for sensing necrotic cells and facilitating their cross-presentation by

$CD8\alpha^+$ DCs (Sancho et al., 2009; Zhang et al., 2012). On the other hand, splenic $CD8^-$ DCs were shown to be more efficient at presenting to $CD4^+$ T cells through MHC-II (Dudziak et al., 2007).

The requirement for cross-presentation to mount effective immune responses varies between pathogens. For some infections, such as vaccinia virus, direct presentation is sufficient for effective CTL response (Hickman et al., 2008; Xu et al., 2010). On the other hand, robust CTL responses against viruses such as Sendai virus, West Nile virus, influenza virus as well as HSV require $CD8^+$ T cells to be cross-primed. (Hildner et al., 2008; Edelson et al., 2010; GeurtsvanKessel et al., 2008; Allan et al., 2006; Singh et al., 2010). Immune responses against certain parasitic infections such as *Toxoplasma gondii* also rely on cross presentation for effective defense (John et al., 2009).

1.3.3 INITIATION OF ADAPTIVE IMMUNE RESPONSES (I): T CELL-APC ENCOUNTER

Geographical distribution of DC in the LN

Apart from the functional differences between various DC subsets in terms of their antigen presentation capacity, DC subsets may also occupy distinct anatomical regions within the SLO. In the spleen, $CD8\alpha^+$ $DEC205^+$ DCs were shown to occupy the T cell zone, while $CD8\alpha^-$ $33D1^+$ DCs occupied the red pulp and marginal zone (Dudziak et al., 2007). In the LN, after skin irritant application, LC and dDC localised to geographically distinct regions: LC in the deep paracortex and dDC in the outer paracortex (cortical ridge) (Kissenpfennig et al., 2005). Recent histo-cytometric analysis of steady state LN also revealed a similar pattern, with LN-resident $CD11b^+$ DC residing in the lymphatic region of the LN, migratory dDC localising to the interfollicular regions and outer paracortex, whereas migratory LC, $CD103^+$ DC as well as LN-resident $CD8a^+$ DC occupied the deep paracortex (Gerner et al., 2012). Indeed, some studies have reported that migratory DCs situated in the outer paracortex were the first to present antigen to naïve T cells, likely because of their proximity to HEVs where naïve lymphocytes arrive (Bajenoff et al., 2003; Katakai et al., 2004).

The functional significance of such geographical segregation remains elusive. However, it has been suggested that different DC subsets with varying properties (such as MHC presentation capacity, maturation state and inflammatory cytokine expression profile) respond to spatially distinct cues, resulting in their preferential localisation in different compartments (Gerner et al., 2012). In light of the finding that different DC subsets are highly specialised in their functions, this segregated distribution may imply an evolutionary strategy that optimises their encounter with respective cells of interest.

Furthermore, recent findings that central memory and naïve $CD8^+$ T cells respond to different chemokine cues, with the former expressing chemokine receptor CXCR3 and responding to its ligand CXCL9, and therefore preferentially

localise to the LN periphery during lymph-borne infection while naïve $CD8^+$ T cells remained in paracortex (Sung et al., 2012; Kastenmuller et al., 2013). These findings suggest previously unappreciated roles of such spatial segregation where different T cell subsets undergo priming and differentiation.

Improving the odds of T cell-DC encounter

Since the endogenous pool of T cells with a particular antigen specificity can be as low as 50-500 per adult mouse (Moon et al., 2007), which translates to approximately 1-10 T cells per LN (Germain et al., 2008), the successful encounter between a rare antigen-specific T cell and its cognate antigen-bearing DC, which can also be relatively scarce especially early after infection, is a challenging task.

DC migrating from the periphery as well as those resident in the LN form a network distributed across the T cell zone filled with FRC-ensheathed conduits. Naïve T cells traversing through the LN are therefore provided with ample opportunities to make contact with DCs as they crawl along the FRC network (Lindquist et al., 2004). The positioning of DCs on the reticular fibre network allows them to maximise scanning efficiency by passing T cells for potential cognate interaction (Lindquist et al., 2004).

Indeed, it is estimated that each DC can probe 500-5000 T cells per hour, suggesting the presence of a highly efficient scanning mechanism (Bousso et al., 2003; Miller et al., 2004b; Beltman et al., 2007). Miller et al. (2004b) computed the estimated parameters and showed that given the presence of 100 antigen-bearing DCs in a LN, the probability of encountering an antigen-specific T cell out of every 10^6 cells through random T cell migration is 95% within 6 hours. Similarly, modelling data estimates a T cell scanning rate of ~100 different DCs per hour (Beltman et al., 2007).

A recent study also demonstrated that at steady state, naïve $CD8^+$ and $CD4^+$ T cells survey DCs by employing different strategies: $CD4^+$ T cells spend less time dwelling in LN and passage through the LN twice as fast as $CD8^+$ T cells, and scan

on average less DCs than $CD8^+$ T cells (Mandl et al., 2012). It was suggested that this strategy might compensate for the lower precursors of $CD4^+$ T cells by decreasing their retention time in each LN (Moon et al., 2009; Obar et al., 2008; Mandl et al., 2012).

During inflammation, LN can increase T cell dwelling time by restricting egress in a phenomenon known as "LN shutdown." Inflammatory cytokines, chiefly type I interferons, can trigger the upregulation of CD69 in T cells, which in turn negatively regulates the expression of $S1P_1$ and restricts their ability to exit the LN (Shiow et al., 2006). The partial collapse of sinus vessels due to decreased cellular transmigration also reduces the flow pressure, further limiting T cell exit from the LN (Grigorova et al., 2010). Meanwhile, blood flow into the node is increased to promote lymphocyte entry (Soderberg et al., 2005). Activated $CD4^+$ T cells have been implicated in the remodelling the arterioles that supply the LN, through as yet unknown mechanism involving DCs, and promote the influx of naïve lymphocytes into the reactive node (Kumamoto et al., 2011).

Furthermore, activated $CD4^+$ T cells have been shown to induce CCL3 and CCL4 production in the reactive LN and promote the upregulation of CCR5 in naïve $CD8^+$ T cells (Castellino et al., 2006). This provides a mechanism for drawing naïve $CD8^+$ T cells toward antigen-bearing DC as well as $CD4^+$ T cell-DC conjugates, thereby allowing T cell help to take place, which requires cognate interactions. Hugues et al. (2007) demonstrated that activated $CD8^+$ T cells can also mediate a similar antigen-independent CCR5-dependent mechanism that prolongs the transient interaction between naïve $CD8^+$ T cells and mature DCs that have previously interacted with antigen-specific $CD8^+$ T cells.

As such, various strategies regulating structural and biochemical changes within the LN effectively improve the chances of cognate T cell-DC encounter during inflammation.

1.3.4 INITIATION OF ADAPTIVE IMMUNE RESPONSES (II): SPATIOTEMPORAL DYNAMICS OF T CELL ACTIVATION

Upon TCR recognition of cognate peptide-MHC complexes, and coupled with binding of costimulatory molecules, naïve T cells initiate a cascade of intracellular signalling that results in activation. The dynamics of T cell-DC interactions that lead into T cell activation will be explored in this section.

The question of whether transient or stable interactions lead to T cell activation had remained unresolved for many years. Long-lived stable interactions between naïve T cells and APC through the formation of immunological synapses (IS) are mediated by integrin- and Ca^{2+}-dependent mechanisms that lead to T cell arrest (Negulescu et al., 1996; Dustin et al., 1997; Dustin, 2008). Some early studies using *in vitro* models showed that stable T cell-DC interactions (synapse formation) were required for full activation (Huppa et al., 2003; van Stipdonk et al., 2003). Others studies provided contrary evidence that activation signalling is achieved prior to IS formation, and long-lived interactions are therefore not needed for full activation (Lee et al., 2002). Moreover, some studies have reported full $CD4^+$ T cell activation where transient interactions dominate, presumably through signal integration from serial transient interactions (kinapse formation) (Gunzer et al., 2000; Faroudi et al., 2003; Dustin, 2008).

The temporal aspect of T cell priming

With the advent of intravital two-photon imaging, Mempel et al. (2004) first examined T cell priming after subcutaneous injection of peptide-pulsed DCs *in vivo* and proposed a three-phase priming model: during the first phase, $CD8^+$ T cells form transient contacts with antigen-bearing DCs for up to 8 hours and expressed early activation markers CD69 and CD44; for the next 16 hours, the second phase consists of stable T cell-DC conjugates that last for hours, concurrent with IL-2 and IFN-γ production as well as CD25 expression; finally, T cells dissociate from DC during the third phase and begin division while maintaining transient contacts with DC. These observations suggest that priming

is sequential and that stable interactions with DC are required for functional T cell activation.

On the other hand, Miller et al. (2004a) also performed similar experiment with $CD4^+$ T cells and noted similar but a five-phase priming events, consisting of both transient and stable phases as well as a swarming phase after dissociation from DC. However, in contrast to Mempel et al. (2004), the multiphasic interaction observed by Miller et al. was cognate. It is not clear whether the observed disparity represents intrinsic differences between $CD4^+$ and $CD8^+$ T cell modes of activation or a discrepancy as a consequence of different experimental setups.

Others reported that the duration of the first phase of T cell-DC interactions can be variable and in some cases the transient phase was abrogated as T cells formed stable clusters with DC almost immediately (Shakhar et al., 2005; Celli et al., 2007; Azar et al., 2010), including during experiments involving certain live pathogens (Hickman et al., 2008). Later studies then revealed that the duration of "phase one" transient T cell-DC interactions can be dictated by factors such as the overall antigen dose, density of pMHC complex on the DC surface (Henrickson et al., 2008), potency of peptide ligands (Skokos et al., 2007), as well as frequency of T cell precursors (Garcia et al., 2007).

Celli et al. (2007) also established that at least 6 hours of continuous signalling is needed for full $CD4^+$ T cell activation. Recently, Moreau et al. (2012) showed that TCR ligand affinity is directly correlated with both the duration of T cell-DC contact as well as TCR signalling strength. Peptide ligands with high and low TCR affinities promoted synapse (stable interaction) and kinapse (motile interaction) formation, respectively, although only high affinity ligands resulted in activation. Interestingly, a peptide ligand with intermediate affinity for the TCR showed a mixture of both synapse and kinapse formation, but was able to trigger activation (Moreau et al., 2012). These findings suggest that both stable interactions and serial transient interactions can lead to T cell activation as long as the signalling threshold can be reached. It is less clear, however, whether the

presence of inflammatory stimuli in the context of live pathogen infection can also influence T cell-DC contact duration and stability.

The spatial aspect of T cell priming

Early imaging studies utilising peptide injection or peptide-pulsed DCs determined that T cells are initially primed at the cortical ridges of the LN, where HEV are abundant (Bajenoff et al., 2003; Mempel et al., 2004). This is in agreement with the observation that the strategic placement of migratory DCs at the cortical ridges allows them to efficiently scan naïve lymphocytes emerging from the HEV (Katakai et al., 2004).

However, recent studies employing injection of live pathogens have revealed that naïve $CD8^+$ T cells re-distribute to the LN periphery within hours, particularly the interfollicular region near the capsule when LN is infected (Norbury et al, 2002; Hickman et al., 2008; John et al., 2009). This dramatic redistribution of T cells that customarily reside within the LN paracortex appears to correlate with the antigen load in the LN (Hickman et al., 2008). Interestingly, in a recent study, viral drainage to the LN did not induce migration of naïve $CD8^+$ T cells to the superficial region of the LN as had been reported previously (Kastenmuller et al., 2013). Instead, central memory $CD8^+$ T cells preferentially localise to the LN periphery to allow for rapid contact with infected cells (further discussed below in **Section 1.3.7**). This has been attributed to the different virus strains used and therefore the actual mechanism that causes the change in T cell localisation behaviour remains unresolved.

Dynamics of CD4 help provision

The requirement for T cell help to promote effective CTL responses has been controversial. Antigen-bearing DC were shown to require "help" from activated $CD4^+$ T cells in a cognate- and CD40-dependent manner for effective CTL priming (Bennett et al., 1998; Ridge et al., 1998; Schoenberger et al., 1998). Certain studies have also demonstrated that T cell help is crucial for $CD8^+$ T cell memory development by inhibiting a TRAIL-mediated cell death pathway, but is dispensable for primary CTL responses (Shedlock and Shen, 2003; Janssen et al.,

2003). Similarly, CD4 help appears to be vital for CTL responses during chronic lymphocytic choriomeningitis virus (LCMV) and HIV infections (Williams and Bevan, 2007).

During primary responses to many pathogens including influenza and LCMV, CTL priming is CD4 help-independent (Bevan, 2004). Nonetheless, some studies have reported the requirement for $CD4^+$ T cell help to generate primary CTL responses. Serre et al. (2006) showed that T cell help is required for effective CTL priming against vesicular antigen. Similarly, Smith et al. (2004) demonstrated the dependence for T cell help to prime HSV-specific $CD8^+$ T cells through DC 'licensing'. This has been attributed to the lower level of inflammation induced and therefore requires help to promote robust priming. A recent study by Greyer at al. (2016) suggested that CD4 help is crucial in amplifying suboptimal innate signals in DC, such as IL-15 during HSV-1 infection, for efficient CTL priming.

The dynamics of $CD4^+$ T cells providing help – when and how $CD4^+$ T cells deliver help – remains largely unresolved. Owing to the cognate nature of help provision, whereby both antigen-specific $CD4^+$ and $CD8^+$ T cells must interact with the same APC, the question hinges upon whether both $CD4^+$ and $CD8^+$ T cells need to simultaneously engage with the same DC, or if $CD4^+$ T cells can successively 'license' multiple DCs through transient interactions, which would then allow the 'licensed' DC to activate $CD8^+$ T cells after the helper $CD4^+$ T cell has already disengaged.

The simplest model is the three-cell cluster model, which suggests that both $CD4^+$ and $CD8^+$ T cells form a ternary cluster with the antigen-bearing DC (**Fig. 1.3A**). This model would support findings that paracrine signalling by cytokines such as IL-2 by $CD4^+$ T cells affects $CD8^+$ T cell expansion, or that close interaction allows $CD4^+$ T cells to directly stimulate $CD8^+$ T cells via CD40 (Bourgeois et al., 2002). However, whether these mechanisms are truly essential for the outcome of $CD4^+$ T cell help are not clear, as other studies cast doubt on

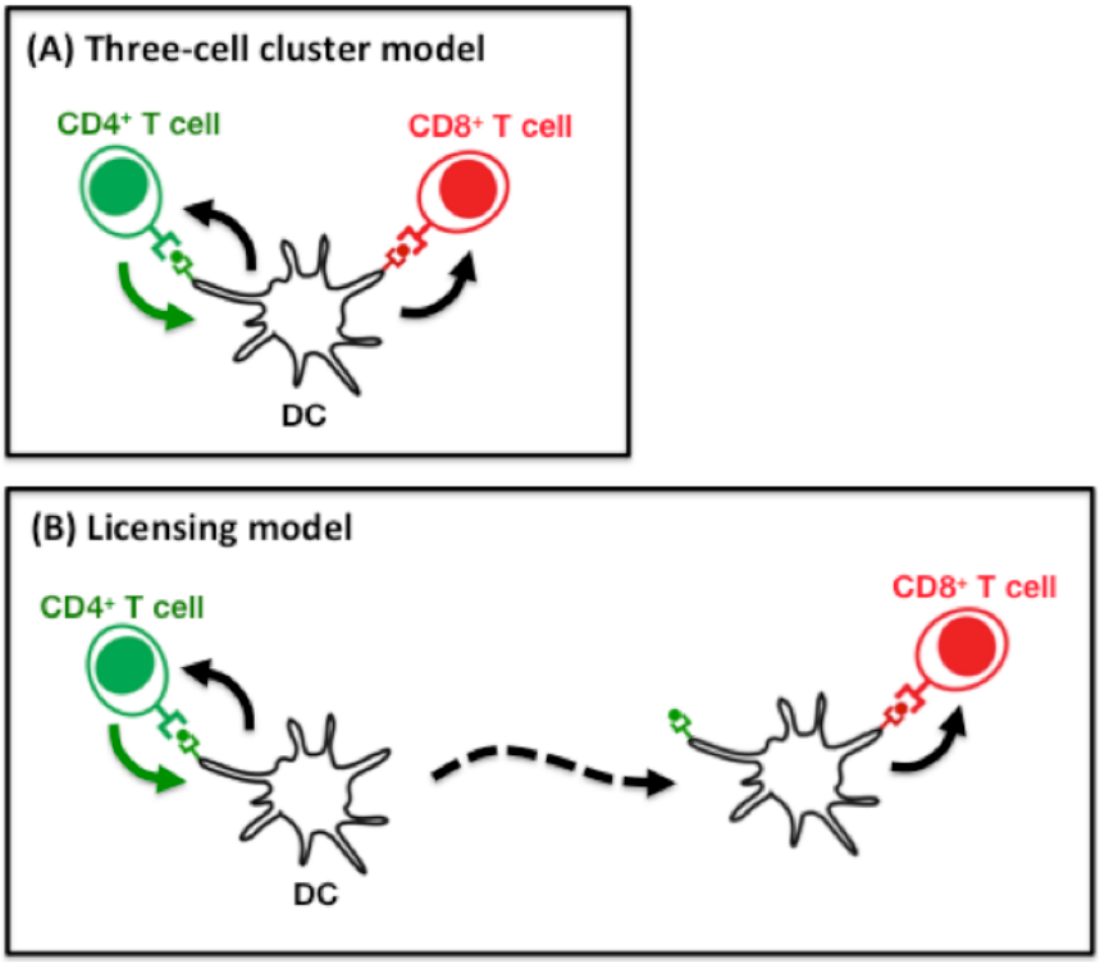

Figure 1.3. Models of CD4 help provision.
(A) Three-cell cluster model: both $CD4^+$ and $CD8^+$ T cells engage with the same APC simultaneously. The proximity of both T cell subsets enables paracrine signalling from $CD4^+$ T cells. However, the probability of both rare antigen-specific T cells to encounter the same APC via random migration is considered to be highly unlikely.
(B) Licensing model: $CD4^+$ T cells 'license' DC, which acquire the capacity to fully activate $CD8^+$ T cells, even without continuous interaction of DC with helper $CD4^+$ T cells. This model permits help signals to be rapidly distributed, and substantially broaden the time period for rare $CD8^+$ T cells to successfully encounter helped, antigen-bearing DC.

their roles (Sun & Bevan, 2004; Lee et al., 2003). More recently, Feau et al. (2011) demonstrated that instead of paracrine secretion by $CD4^+$ T cells, it was the autocrine IL-2 signalling by $CD8^+$ T cells themselves that was crucial for sustaining effector cell proliferation and differentiation *in vivo*. Rather, $CD4^+$ T cells deliver 'help' via CD40 signalling, which allows the 'helped' APC to then help $CD8^+$ T cells through CD70-CD27 signalling (Feau et al., 2011; Feau et al., 2012). In addition to CD40 signalling, lymphotoxin β receptor (LTβR) expressed on DC has also been implicated in the provision of help signals, where LTαβ-expressing $CD4^+$ T cells interact with LTβR-expressing DC to influence CTL expansion via a type I IFN-dependent mechanism (Summers deLuca et al., 2010). Together, these studies showed that multiple signalling pathways likely contributed to enhancing CTL expansion and memory-forming capacity via CD4 help through contact-dependent mechanisms to transmit 'help' signals to DC.

Nevertheless, for at least two rare antigen-specific T cells to encounter the same APC in roughly similar time periods would exponentially decrease the probability of such encounter, and would be a highly inefficient strategy for the provision of help. Thus, the alternative model would involve multiple transient interactions by activated $CD4^+$ T cells with different DC to rapidly 'license' a large number of DC in a shorter period (Ridge et al., 1998), though this has yet to be formally demonstrated *in vivo* (**Fig. 1.3B**).

It is important to appreciate that non-random migration of T cells could also improve the probability of $CD4^+$ and $CD8^+$ T cells encountering the same DC, as Castellino et al. (2006) demonstrated that naïve $CD8^+$ T cells can be guided via CCR5-mediated migration to $CD4^+$ T cell-DC conjugate producing CCR5 ligands CCL3 and CCL4. Therefore, instead of random encounter, it is likely that specific mechanisms are in place to facilitate the meeting of rare antigen-specific $CD4^+$ and $CD8^+$ T cells with their antigen-bearing APC, which could help resolve the paradoxical notion that a three-cell cluster is too unlikely to be formed in a timely manner.

1.3.5 DIFFERENTIATION OF ACTIVATED T CELLS

Clonal expansion and differentiation of activated T cells can produce a heterogeneous pool of effector cells with diverse functional and cytokine expression profiles. Cell fate studies using single-cell transfer and cellular barcoding experiments have established that the diverse progeny produced by a single naïve T cell cannot be explained through pre-programming during thymic development alone (Stemberger et al., 2007; Gerlach et al., 2010). Asymmetric partitioning of cellular contents during mitosis, such as the transcription factor T-bet, and thereby the unequal inheritance of signals by the daughter cells has been proposed as a mechanism for the resultant diversity (Chang et al., 2007; Chang et al., 2011). Modification of epigenetic landscapes has also been implicated to contribute to the diverse effector and memory differentiation (Yamanaka et al., 2013).

Apart from late-stage differentiation mechanisms, Beuneu et al. (2010) found that initial interactions between T cells and DC produce variable efficiencies of IFN-γ gene activation despite having the same TCR specificity. Furthermore, these qualitatively distinct activation signals generated diversity in functional outcomes by the activated T cells in terms of cytokine profile. This questions whether the duration of T cell-DC interactions and the associated signal strength during early activation can also influence T cell fate. Additionally, the time at which $CD4^+$ and $CD8^+$ T cells enter the LN has also been demonstrated to impart distinct differentiation pathways, with late-arriving cells exhibiting the tendency to differentiate into memory subsets, possibly due to changes in the LN microenvironment following infection (Catron et al., 2004; van Faassen et al., 2005; D'Souza et al., 2006). Therefore, the early events of activation can have a profound influence on the eventual fate of lymphocyte activation.

1.3.6 EFFECTOR T CELL HOMING AND FUNCTIONS

Upon entering the lymphatic system and draining into the circulation, effector T cells migrate to sites of inflammation guided by mechanisms mediated by various molecular interactions including integrins, selectins and chemokine receptors. According to the "area code" hypothesis, the ability of T cells to gain entrance to distinct tissues is regulated by endothelial display of unique combinations of chemokines and cell adhesion molecules (including integrins and selectins), which then allows effector T cells expressing the matching surface molecules to roll, stick and then diapedese (Springer, 1994). Further migration towards the inflammatory region is guided by chemokine gradient along the interstitial tissues.

While $CD4^+$ T follicular helper cells (T_{FH}) upregulate CXCR5 to migrate intranodally into B follicles (Ma et al., 2012), programming of T cell homing to specific organs during priming and differentiation results in the acquisition of chemokine receptors and specific ligands to cell adhesion molecules. For example, intestinal mucosal entry is regulated by the integrin α4β7 and the chemokine receptor CCR9 (Johansson-Lindom and Agace, 2007), whereas P-selectin, E-selectin, as well as chemokine receptors CCR4 and CCR10 mediate cutaneous entry (Austrup et al., 1997; Reiss et al., 2001).

However, numerous studies have concluded that T cell homing to peripheral sites is most likely multifactorial and context-dependent: the LN in which the T cell received activation, timing of T cell activation, inflammatory milieu, presence of metabolites, the DC subsets that provided signals to T cells, types of inflammation as well as the pathogen all appear to influence the molecular signatures displayed by T cells after differentiation to guide them into specific tissues (Masopust and Schenkel, 2013). Furthermore, studies have demonstrated that environmental factors also allow for the fine-tuning of these homing and tissue residence capabilities through acquisition of new homing receptors following the entry of T cells into effector sites (Liu et al., 2006).

Coordinated responses by $CD4^+$ and $CD8^+$ T cells are critical for optimal protection against foreign invading microorganisms. The majority of $CD4^+$ and $CD8^+$ T cells have to travel to infected tissues to perform their effector functions. The primary function of $CD8^+$ T cells is to deliver lytic granules into infected APC upon forming an immunological synapse via TCR-pMHC-I-dependent interaction, which leads to the killing of infected cells. The kinetics of killing by effector $CD8^+$ T cells reported thus far, however, have been fairly diverse. Although $CD8^+$ T cells could eliminate infected cells within a few minutes after contact *in vitro*, intravital imaging studies using tumour model as well as liver stage malaria infection failed to observe such rapid killing by $CD8^+$ T cells (Breart et al., 2008; Cockburn et al., 2013). Instead, $CD8^+$ T cells formed stable interactions with infected cells spanning at least a few hours prior to the destruction of infected cells. During cutaneous vaccinia virus infection, $CD8^+$ T cells were shown to rapidly kill infected inflammatory monocytes at the periphery of the lesion while having restricted access into the epidermal keratinocytic foci (Hickman et al., 2013). These functions were taken over by neutrophils penetrating the foci instead, thus highlighting synergistic relationship between innate and adaptive immune cells in the control of pathogen spread. More recently, Halle et al. (2016) showed that in skin murine cytomegalovirus (MCMV) and MVA infection models, rather than forming stable interaction, $CD8^+$ T cells engaged with infected cells in motile, transient kinapses and disrupted the cells within 20-120 minutes after initial contact. Interestingly, individual $CD8^+$ T cell contact often did not lead to a sustained perforin-dependent Ca^{2+} flux and target cell death, and multiple CTLs were seen to cooperate in the killing process, where a higher number of CTL contacts significantly increased the probability of target cell death. Therefore, it appears that the dynamics of $CD8^+$ T cell killing can vary depending on the type of pathogen and environmental context.

Both $CD4^+$ and $CD8^+$ T cells produce cytokines that recruit immune cells as well as activate immune mechanisms that facilitate clearance or containment of pathogens. While it is known that cytokine signalling can occur in a paracrine fashion over long distance *in vitro*, using a hepatic Bacillus Calmette–Guérin (BCG) model, Egen et al. (2011) showed that delivery of IFN-γ by $CD4^+$ T cells *in*

vivo is highly localised to the immunological synapse at the T cell-APC interface. While this might suggest a mechanism whereby individual interaction with infected cells is required for effective clearance, a later study employing cutaneous *Leishmania major* infection model demonstrated that while effector $CD4^+$ T cells only formed stable interaction with a minority of infected cells, such limited IFN-γ signalling could exert bystander effector activity over a cytokine gradient of more than 80μm distance (Muller et al., 2012). As such, the study implicated that an efficient, widespread response can be achieved with $CD4^+$ T cells contacting as few as 10% of the infected cells. In epicutaneous HSV-1 infection, a broad dissemination of $CD4^+$ T cells in the infected epithelia was also observed whereas $CD8^+$ T cells localised specifically to the infected epidermal cells, further supporting the idea that $CD4^+$ T cells exert their cytokine activity over intermediate ranges while $CD8^+$ T cells deliver their lytic granules and cytotoxicity via direct contact with infected cells (Macleod et al., 2014).

1.3.7 T CELL MEMORY FORMATION

Successful clearance of an invading pathogen and resolution of inflammation is associated with the death of the majority of effector T cells. However, a hallmark feature of the adaptive immune system is immunological memory, which provides anamnestic response and protects the host against secondary challenges. Though up to 90 to 95% of effector T cells undergo apoptosis, a small number of these T cells survive and form heterogeneous pools of memory T cells.

Memory T cells are classified as central memory (T_{CM}) or effector memory (T_{EM}) cells, based on their broad distribution and functional specialisation (Sallusto et al., 2004). T_{CM} express lymph-node homing molecules CCR7 and CD62L, which allow their recirculation into lymphoid tissues, and exhibit superior proliferative capacity and production of IL-2. In contrast, T_{EM}, which do not express CCR7 and CD62L, circulate in the peripheral tissues instead and have been shown to produce effector cytokines such as IFN-γ. Thus, both subsets of memory T cells provide complementary roles of protective immunity through distinct migration patterns and functional properties.

Recent studies also demonstrated that $CD8^+$ T_{CM} are recruited to LN periphery (SCS, interfollicular region and medulla) through CXCR3-mediated mechanism during LCMV infection, leading to enhanced activation, proliferation and IFN-γ production compared to naïve T cells in the LN (Sung et al., 2012). Similarly, in another study using MVA infection, $CD8^+$ T_{CM} preferentially localised near the LN periphery, which allowed their rapid migration to infected cells in the LN (Kastenmuller et al., 2013). Interestingly, the augmented IFN-γ production by activated $CD8^+$ T_{CM} also drives CXCL9 production (ligands for CXCR3) through local myeloid cells to facilitate further recruitment in a feed-forward loop.

A distinct population of memory T cells also persists in peripheral tissues, such as the skin and intestine, and does not re-enter the circulation. Termed tissue-resident memory T cells (T_{RM}), these cells establish residence in antigen-challenged peripheral tissues for very long periods of time, possibly indefinitely. T_{RM} cells can function as an early warning system in the female genital mucosa and the skin – a role traditionally attributed to innate immune sentinel cells such as macrophages – and activate a broad range of immune functions through prompt release of IFN-γ upon pathogen encounter. This was shown to result in amplification of lymphocyte recruitment as well as innate immune cell-driven inflammation (Schenkel et al., 2014; Ariotti et al., 2014). In the skin after HSV-1 infection, memory $CD8^+$ T_{RM} preferentially lodge in the epidermis (where the virus infects) and exhibit highly dendritic-like morphology, squeezing between the keratinocytes that populate the epidermal layer (Gebhardt et al., 2011). In contrast, memory $CD4^+$ T cells localise to the dermal layer and are highly motile. Unlike their $CD8^+$ counterparts, these memory $CD4^+$ T cells re-enter the circulation and do not permanently reside in the skin. In this thesis, we wanted to further examine if cytoskeletal organising capability during lymphocyte migration affects formation of T_{RM} in the skin, the results are shown in Chapter 6.

Nonetheless, a recent study has reported on the formation of persisting $CD4^+$ T_{RM} in the genital mucosa after HSV-2 infection (Iijima & Iwasaki, 2014). Using parabiotic mice, $CD4^+$ T_{RM} were shown to reside in previously infected tissues

and did not re-circulate. Interestingly, these $CD4^+$ T_{RM} preferentially form clusters (termed 'memory lymphocyte cluster') in distinct microanatomical regions enriched in CCL5 produced by macrophages, which was dependent on IFN-γ expression in the tissues. It should be noted that the geographical distribution of $CD4^+$ T_{RM} is markedly different than that of $CD8^+$ T_{RM}, which have been found in both the epithelium and the 'memory lymphocyte cluster'. The proximity of $CD4^+$ T_{RM} to regions susceptible to re-infection allows immediate antiviral defense through high level of IFN-γ secretion, a critical temporal advantage over the delayed infiltration of circulating memory $CD4^+$ T cells.

1.4 HERPES SIMPLEX VIRUS

Herpes simplex virus-1 (HSV-1), the prototypical member of *Herpesviridae*, is a large enveloped DNA virus and a highly prevalent human pathogen, with up to 50-65% of the population being seropositive in the United States and Europe. As with all herpesviruses, the virus life cycle consists of both lytic and latent phases. In the case of HSV-1, it infects the epithelial cells during the lytic phase and establishes latency in the trigeminal and dorsal root ganglia (DRG). Typical clinical presentation includes lesion in the orofacial region (cold sores) and although initial infection is cleared relatively quickly in healthy people, the infection is potentially lethal in newborns and immune-compromised patients. Furthermore, recurrent infections can occur as a result of viral reactivation from latency, with an estimated 80% of the population having at least one recurrent episode by adulthood (Schillinger et al., 2004).

Viral structure

The viral DNA genome is enclosed within an icosahedral nucleocapsid, which is in turn surrounded by an amorphous proteinaceous tegument. A lipoprotein envelope encapsulates the tegument, and glycoprotein spikes decorate the envelope surface. Of the more than 40 known viral proteins, 23 populate the tegument and are mostly responsible for nuclear transport of the capsid, immune evasion, as well as transcriptional regulation (Loret et al., 2008). Additionally, there are at least 13 viral glycoproteins that mediate virus binding of host cell surface receptors as well as its entry mechanism.

Viral pathogenesis

HSV-1 enters permissive cells through a series of entry mechanism mediated by its surface glycoproteins. gB and gC bind to heparan sulphate chains, a type of glycosaminoglycan (GAG) chain on cell surface proteoglycans (Shieh et al., 1992; WuDunn and Spear, 1989). Although binding to heparan sulphate is not essential for viral entry, as gB and gC deficient viruses have been shown to infect cells, infectivity is substantially reduced (Herold et al., 1991; Herold et al., 1994). A

second interaction between gD and its target receptors facilitate viral entry by triggering fusion of the virion envelope with cell membrane. gD binds to three classes of cell surface receptors: HVEM (herpesvirus entry mediator), nectin-1 and nectin-2, as well as specific sites of heparan sulphate generated by 3-O-sulfotransferases. For HSV-1, HVEM, nectin-1 and 3-O-sulphate-modified heparan sulphate are preferentially bound by gD. To facilitate viral entry, structurally conserved glycoproteins, especially gB and gH-gL heterodimer are also required in addition to gD binding to its receptor. It has been postulated that while gD may not be an immediate component of the fusion machinery, gD engaging its receptor may cause a conformational change and allow interaction with gB or gH-gL heterodimers, which in turn cause the fusogenic activity (Spear and Longnecker, 2003).

The expression of gD receptors thus determines the cellular tropism of HSV-1. HSV-1 infects predominantly epithelial cells and sensory neurons. Epithelial cells express both HVEM and nectin-1, whereas neurons express only the latter. HSV-1 has been reported to preferentially enter polarised epithelial cells from the basolateral surface (Schelhaas et al., 2003), and this observation is consistent with an earlier study showing that nectin-1 co-localised with adherans junctions of polarised cells (Yoon and Spear, 2002). This implies tissue disruption of the epithelia is required to expose certain virus entry receptors for robust infection.

Upon viral fusion with cell membrane, the nucleocapsid containing viral genome is transported to the nucleus. Viral gene transcription is a tightly regulated process and gene expression can be classified based on temporal kinetics: α (immediate early/IE), β (early), and γ (late) genes (Weir, 2001). Late genes are typically transcribed during virus replication and are also further subdivided into a) γ1 (leaky late) genes, where expression begins prior to viral DNA replication but is only maximal during the replication phase; and b) γ2 (late) genes where expression is only initiated during replication. Thus, synthesis of viral proteins occurs in sequential stages: in each stage, transcriptional and translational regulators promote gene expression of later phases, as well as inhibiting earlier gene transcription. Structural proteins for progeny viral

particles, as well as proteins integrated into the tegument, are synthesised during late gene expression and are assembled in the nucleus into capsids together with replicated viral genomes. The newly assembled virions then bud through the nuclear envelope containing viral glycoproteins, before being released as vesicles, or through cell lysis (Melchjorsen et al., 2009).

1.4.1 IMMUNE RESPONSES AGAINST HSV INFECTION

Both innate and adaptive arms of the immune system are crucial in host defence against HSV-1 infection. An important component of innate immunity against HSV-1 is type I interferon (IFN), a key antiviral cytokine produced by innate immune cells such as NK cells and plasmacytoid DCs (pDC). Type I IFN signalling leads to the transcription of IFN stimulated genes (ISG), which are critical for mitigating viral replication, inducing an antiviral state among infected and nearby cells as well as augmenting inflammation (reviewed in Schneider et al., 2014). Mice deficient in receptors for type I IFN are highly susceptible to infection and survive poorly during HSV-1 infection (Leib et al., 1999; Luker et al., 2003). Furthermore, recombination activating gene (RAG)-deficient mice, which lack mature T and B cells but retain type I IFN responses showed resistance against HSV-1 during the first few days of infection (Vollstedt et al., 2004). These studies underscored the indispensable role of innate immunity in controlling acute HSV-1 infection.

Innate immunity against HSV

pDC were first reported as the innate immune cell type primarily responsible for type I IFN production during HSV infection in humans (Siegal et al., 1999). While sharing a common progenitor with classical DC, pDC appear to play a minimal role in antigen presentation but are specialised in amplifying type I IFN production after sensing viral or self nucleic acid presence via TLR7 and TLR9 (Swiecki and Colonna, 2015). Indeed, pDC were shown to recognise HSV-2 during genital infection through TLR9 sensing (Lund et al., 2003), though TLR9-independent pathways may be utilised depending on tissue from which pDC

were isolated (Hochrein et al., 2004). Mice lacking TLR9 or pDC also showed poorer survival compared to wildtype mice, thereby implicating pDC for defence against HSV (Lund et al., 2006).

However, the virus has equally remarkable immune evasion strategies that limit IFN production and signalling. Furthermore, viral proteins such as ICP47 (Fruh et al., 1995; Hill et al., 1995) and *vhs* (virion host shut-off) (Hill et al., 1994; Tigges et al., 1996) inhibit antigen presentation on MHC-I by host cells through interfering with TAP (transporter associated with antigen processing), as well as intracellular MHC-I transport, respectively. This can be counteracted by NK cells, via expression of NK inhibitory receptors that recognise viral-mediated downregulation of MHC-I in infected cells, leading to NK-mediated lysis. While a number of studies have demonstrated the importance of NK cells during HSV infection, the evidence remains largely inconclusive (Chew et al., 2009). This may in part be due to the difference in TAP disruption efficiency across species by viral proteins, where TAP function seemed to be less impaired in mouse compared to human (Tomazin et al., 1998), and thus murine models of HSV may not reflect the full extent of the roles played by NK cells.

Adaptive immunity against HSV-1

Antibody responses are also important for protective immunity against HSV infection (Awasthi et al., 2013; Belshe et al., 2014), and studies have shown the antigenic potential of glycoproteins critical for viral entry into host cells (Whitbeck et al., 1999; Cairns et al., 2006). Additionally, neutralising antibodies may also be important for mitigating the axonal spread of virus (Mikloska et al., 1999). Nonetheless, it remains unclear whether antibody is essential for clearance and protection against HSV. Passive transfer of immune serum into SCID or B-cell-deficient mice showed that despite decreased disease severity, viral replication did not appear to be impacted (Morrison et al., 2001). Interestingly, HSV gE can function as Fcγ receptor that binds IgG, while gC binds to and interrupts complement component C3, the combined effect of which could substantially reduce the efficacy of antibody-mediated responses against HSV infection (Lubinski et al., 2002; Lubinski et al., 2011). It seems that optimal

protection against genital HSV-2 infection, despite high antibody titres, requires T cell-mediated immunity (Milligan et al., 1998).

Involvement of T cells during HSV infection has been described by numerous studies and has been extensively investigated as potential vaccine candidate. Both virus-specific $CD4^+$ and $CD8^+$ T cells can be found in HSV-infected skin lesions and ganglia; however, the exact contribution of each T cell subset in providing protective immunity is not well understood, with some studies arguing that either T cell subset is adequate for protection (Smith et al., 1994; Milligan et al., 1998; Ghiasi et al., 1999). To a certain extent, cooperation between $CD4^+$ and $CD8^+$ T cells is indispensable for optimal immunity. In murine HSV-1 infection, 'licensing' of DC by activated $CD4^+$ T cells is a prerequisite for generating robust primary $CD8^+$ T cell responses (Smith et al., 2004). $CD4^+$ T cells may also enhance effector $CD8^+$ T cell recruitment via IFN-γ production (Nakanishi et al., 2009).

IFN-γ is a key antiviral cytokine produced by T cells and NK cells. Although IFN-γ alone is not sufficient for complete viral clearance, it has been implicated in augmenting T cell-mediated clearance of HSV infection (Milligan and Bernstein, 1997). $CD4^+$ T cells are the predominant cellular source of IFN-γ, and the CD4-mediated IFN-γ response has been demonstrated to act upon stromal but not haematopoietic cells to actively suppress viral replication (Iijima et al., 2008).

Apart from delivery of cytolytic granules to eliminate infected cells, $CD8^+$ T cells also produce IFN-γ albeit to a lesser extent compared to $CD4^+$ T cells during genital HSV-2 infection (Milligan and Bernstein, 1997). Interestingly, NK cells, which contribute to early IFN-γ responses, did not appear to significantly affect the rate of viral clearance upon their depletion (Milligan and Bernstein, 1997; Iijima et al., 2008). Furthermore, $CD4^+$ but not $CD8^+$ T cell-depleted mice exhibited delayed clearance of virus, thus highlighting the essential role of $CD4^+$ T cells in protecting against genital HSV-2 and ocular HSV-1 infections (Milligan and Bernstein, 1997; BenMohamed et al., 2003). However, it is possible that

reduced $CD8^+$ T cell responses in the absence of $CD4^+$ T cell help contributed to these observations.

HSV also infects and establishes latency in sensory ganglion, and $CD8^+$ T cells have been found to infiltrate and persist in ganglionic sites after infection in both mice and humans (Liu et al., 1996; Khanna et al., 2003; van Lint et al., 2005; Theil et al., 2003). $CD8^+$ T cells are thought to be effective in controlling latent HSV infection, as ablation of $CD8^+$ T cells in mice resulted in widespread killing of ganglionic neurons by virus (Simmons and Tscharke, 1992). Furthermore, adoptive transfer of activated virus-specific $CD8^+$ T cells into immunocompromised $RAG^{-/-}$ mice significantly improved viral clearance and survival, suggesting that $CD8^+$ T cells alone could provide protective immunity against both skin and ganglionic HSV infection (van Lint et al., 2004). Nonetheless, activated $CD8^+$ T cells did not prevent the virus from establishing latency in the sensory ganglia, and only attenuated viral copy number through partial clearance of virus in the skin (Wakim et al., 2008). This likely reflects the rapid skin-to-nerve transmission of the virus. Additionally, persistence of $CD4^+$ T cells has also been reported in latently infected ganglia (Cantin et al., 1995; Johnson et al., 2008). $CD4^+$ T cells control latent HSV infection via cytolytic-independent pathways, with IFN-γ being suggested as a predominant form of antiviral mechanism in preventing viral spread (Johnson et al., 2008).

1.4.2 MURINE CUTANEOUS HSV-1 INFECTION MODEL

To investigate the immune response to peripheral infection, many studies have utilised subcutaneous injection in the mouse footpad, flank skin, or ear skin, which – while closely resembling certain drug or vaccine delivery methods – is confounded by the simultaneous delivery of pathogens to the draining LN via lymphatic vessels. Instead, we wished to approximate the natural route of skin infection to study the activation of cell-mediated immunity during peripheral viral infection.

In the present study, a well-characterised mouse model of cutaneous HSV-1 infection was employed (van Lint et al., 2004). In this model, a small scarification site on the flank skin of C57BL/6 mouse is induced through light abrasion, which allows the virus to infect the exposed epidermal keratinocytes in the disrupted tissue (**Fig. 1.4**). From the epidermis, HSV-1 also establishes latency by entering the innervating sensory neurons and is transported to the DRG via retroaxonal flow. Virus continues to replicate and spread to other neurons within the ganglia innervating the dermatome, and at around 3 days after initial infection, re-emerges in the skin from the sensory nerves, effectively spreading to the entire dermatome (Blyth et al., 1984). The viral recrudescence leads to band-like vesicular lesions that are visibly formed on the skin of the innervated dermatome. Viral titres in the skin peak at around day 5 p.i. and virus is cleared around days 7-8 p.i., coinciding with the skin infiltration of CTL a couple days prior (van Lint et al., 2004). Persistent tissue-resident memory T cells form at the sites of infection long after viral clearance in the skin to provide long-lasting protection against secondary challenge (Gebhardt et al., 2009; Gebhardt et al., 2011).

Importantly, viral spread in the skin is highly localised to the epidermal layer. In contrast, footpad inoculation leads to transient detection of virus in the draining LN (Mueller et al., 2002b). Excision of the infection site at 2 hr after skin infection (which allows ample time for viral particles drainage, but before the arrival of migratory DC in the LN) showed complete abrogation of CTL responses (Stock et al., 2004). Furthermore, pharmaceutical blockage of DC emigration from skin similarly resulted in severely impaired CTL responses (Allan et al., 2006). Together, these studies suggest that antigen transport is predominantly mediated by migratory dDC, while direct drainage of virions (if there is any) contributes minimally to CTL priming.

During localised infection, only the LN that drains the site of infection will receive antigen, become inflamed and support the activation and expansion of pathogen-specific T cells. Due to the limited size of scarified area in our mouse

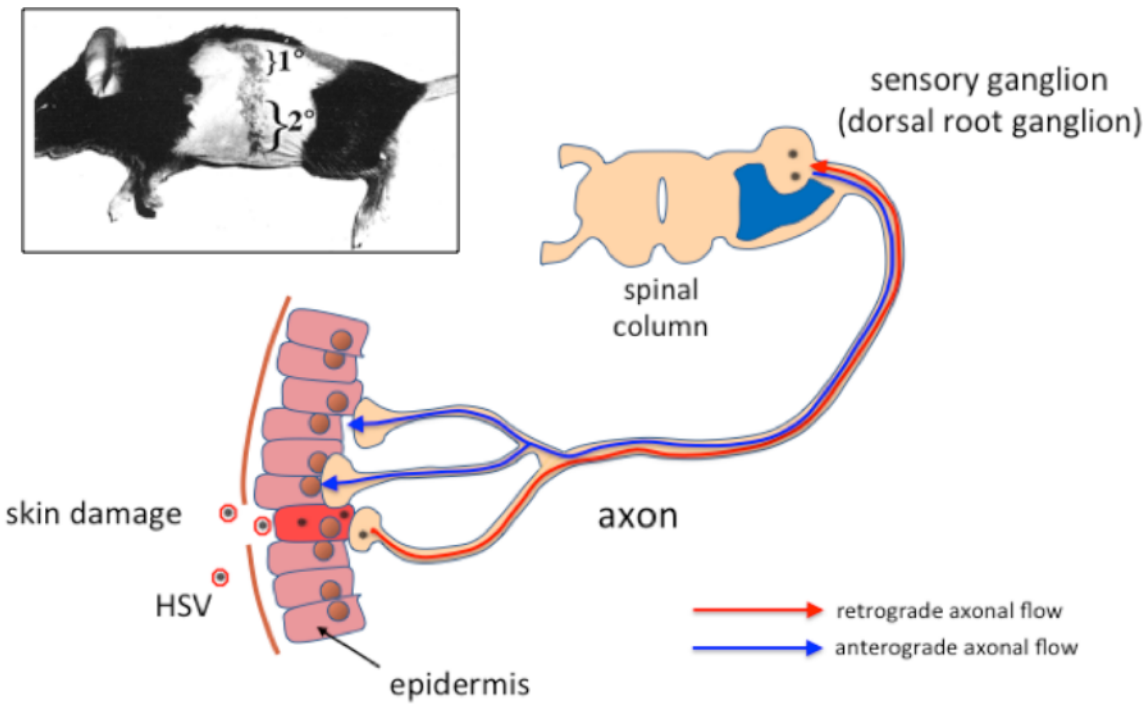

Figure 1.4. Flank scarification HSV-1 infection model.
Scarification is induced on a small area of the flank skin, removing the outermost *stratum corneum* and exposing the epidermal keratinocytes. HSV-1 infects the keratinocytes and replicates locally, but also accesses innervating sensory neurons and travels to the dorsal root ganglion for further replication (red arrow). HSV-1 from the ganglia eventually re-emerges at the skin innervated by the same ganglion via anterograde axonal transport (blue arrows) and results in viral spread to the entire skin dermatome. Inset shows formation of band-like vesicular lesions on secondary site (2°) after viral recrudescence from ganglia.

HSV-1 skin infection model, the brachial LN (bLN) situated under the forelimb drains the scarified cutaneous site where the dorsal tip of spleen is visible under the skin (dorsal flank of the skin; van Lint et al., 2004). Conversely, axillary LN (aLN) drains the lower flank of the skin and is only involved in T cell priming after viral recrudescence from D3 p.i., when virus spreads to the lower flank of the skin from the innervating ganglion (Bedoui et al., 2009).

Both bLN and aLN are lymphatically connected and comprise part of a lymphatic chain, with the aLN situated downstream of bLN. As such, cells exiting the bLN will pass through the aLN before draining into the common jugular vein (Kawashima et al., 1964). Following activation and expansion in the bLN, T cells egress the LN from lymphatic medullary sinuses into the lymphatic system and are eventually drained into the circulation (including further proliferation in the spleen) (Girard et al., 2012). From the bloodstream, differentiated T cells can now infiltrate inflamed sites via various chemokinetic and tissue-homing cues (Masopust and Schenkel, 2013).

Several unique features of this model allow investigation of immune priming during localised viral infection. First, with migratory DC as the primary source of antigen, we could minimise contributions from antigen presentation by LN-resident DC acquiring virus from the lymph. This is in contrast to most other infection models that involve subcutaneous injection. Second, the availability of both $CD4^+$ and $CD8^+$ TCR transgenic T cells specific for immunodominant HSV epitopes (gD-specific $CD4^+$ and gB-specific $CD8^+$ T cells) allows *in vivo* tracking and visualisation of the dynamics of T cell priming (Mueller et al., 2002a; Wallace et al., 1999; Bedoui et al., 2009). Finally, induction of the primary $CD8^+$ T cell response is help-dependent (Smith et al., 2004) and is invaluable for elucidating the as yet elusive nature of the dynamics of DC 'licensing'.

1.5 AIMS AND EXPERIMENTAL APPROACH

This thesis aims to investigate the spatiotemporal dynamics of the priming of cell-mediated immunity during localised viral infection. Specifically, to:

1) Explore whether neutrophils play an immunomodulatory role on T cell priming and migration of effector T cells (Chapter 3).

2) Characterise the factors contributing to the spatiotemporal dynamics of $CD4^+$ and $CD8^+$ T cell priming (Chapter 4).

3) Visualise the priming dynamics of $CD4^+$ and $CD8^+$ T cells, as well as dissecting the dynamics of T cell-APC interactions (Chapter 5).

4) Explore whether the protein Dedicator of Cytokinesis 8 (DOCK8) is required for the migration, formation and survival of $CD8^+$ T_{RM} cells in the skin (Chapter 6).

CHAPTER TWO:
MATERIALS AND METHODS

2.1 MATERIALS

2.1.1 Mice

Strain	Description	Reference
C57BL/6	Inbred animals expressing MHC class II I-A^b and MHC class I H-2^b	
B6.SJL-*Ptprc^{a}Pep3^b*/ BoyJ (B6.Ly5.1)	Congenic mice expressing T cell surface antigen CD45.1 (Ly5.1) *Ptprc^a* (protein tyrosine phosphate, receptor type c, a allele). This marker has been used to distinguish cells from these mice and cells from C57BL/6 mice expressing CD45.2 (Ly5.2)	
gBT-I.1	H-$2K^b$ restricted, TCR transgenic (Vα2/Vβ8.1$^+$), specific for HSV-1 glycoprotein B peptide ($gB_{498\text{-}505}$, SSIEFARL)	(Mueller et al., 2002a)
gBT-I.1 x B6.Ly5.1	F1 generation of heterozygous/homozygous gBT-I.1 and B6.Ly5.1 breeding. Haematopoeitic cells express both CD45.1/Ly5.1 and CD45.2/Ly5.2 markers.	
gBT-I.1 x B6.uGFP	F1 generation of heterozygous/homozygous gBT-I.1 and B6.uGFP breeding. Cells express enhanced green fluorescent protein (EGFP) under the control of ubiquitin promoter.	
gBT-I.1 x B6.DsRed	F1 generation of heterozygous/homozygous gBT-I.1 and B6.DsRed breeding. Cells express red fluorescent protein (DsRed) under the control of chicken beta-actin promoter.	
gDT-II	I-A^b restricted, TCR transgenic (Vα3.2 Jα16/Vβ2 Dβ2.1 Jβ2.1$^+$), specific for HSV-1 glycoprotein D peptide (IPPNWHIPSIQDA)	
gDT-II x B6.Ly5.1	F1 generation of heterozygous/homozygous gDT-II and B6.Ly5.1 breeding. Haematopoeitic cells express both CD45.1/Ly5.1 and CD45.2/Ly5.2 markers.	
gDT-II x B6.uGFP	F1 generation of heterozygous/homozygous gDT-II and B6.uGFP breeding. Cells express enhanced green fluorescent protein (EGFP) under the control of ubiquitin promoter.	
OT-I	H-$2K^b$ restricted, TCR transgenic (Vα2/Vβ5.2$^+$), specific for $OVA_{257\text{-}264}$ peptide (SIINFEKL)	(Hogquist et al., 1994)

OT-I x B6.Ly5.1	F1 generation of heterozygous/homozygous OT-I and B6.Ly5.1 breeding. Haematopoeitic cells express both CD45.1/Ly5.1 and CD45.2/Ly5.2 markers.	
OT-I x B6.uGFP	F1 generation of heterozygous/homozygous OT-I and B6.uGFP breeding. Cells express enhanced green fluorescent protein (EGFP) under the control of ubiquitin promoter.	
OT-II	I-A^b restricted, TCR transgenic (Vα2/Vβ5.1$^+$), specific for $OVA_{323-339}$ peptide (KISQAVHAAHAEINEAG)	(Barnden et al., 1998)
OT-II x B6.Ly5.1	F1 generation of heterozygous/homozygous OT-II and B6.Ly5.1 breeding. Haematopoeitic cells express both CD45.1/Ly5.1 and CD45.2/Ly5.2 markers.	
OT-II x B6.DsRed	F1 generation of heterozygous/homozygous OT-II and B6.DsRed breeding. Cells express red fluorescent protein (DsRed) under the control of chicken beta-actin promoter.	
P14	H-$2D^b$ restricted, TCR transgenic (Vα2Jα_{TA31}/Vβ8.1DβJβ2.4$^+$), specific for LCMV $glycoprotein_{33-41}$ peptide (KAVYNFATM)	(Pircher et al., 1989)
P14 x B6.Ly5.1	F1 generation of heterozygous/homozygous P14 and B6.Ly5.1 breeding. Haematopoeitic cells express both CD45.1/Ly5.1 and CD45.2/Ly5.2 markers.	
P14 x B6.DsRed	F1 generation of heterozygous/homozygous P14 and B6.DsRed breeding. Cells express red fluorescent protein (DsRed) under the control of chicken beta-actin promoter.	
SMARTA	I-A^b restricted, TCR transgenic (Vα2/Vβ8.3$^+$), specific for LCMV $glycoprotein_{61-80}$ peptide (GLKGPDIYKGVYQFKSVEFD)	(Oxenius et al., 1998)
SMARTA x B6.uGFP	F1 generation of heterozygous/homozygous SMARTA and B6.uGFP breeding. Cells express enhanced green fluorescent protein (EGFP) under the control of ubiquitin promoter.	
Itgax-venus	Also CD11c-EYFP. Transgenic mouse expressing enhanced yellow fluorescent protein (EYFP) under the control of CD11c promoter, resulting in fluorescent CD11c$^+$ DC upon excitation.	(Lindquist et al., 2004)

XCR1-venus	Transgenic mouse expressing fluorescent Venus protein under the control of XCR1 promoter, resulting in fluorescent XCR1$^+$ DC upon excitation.	(Yamazaki et al., 2013)
LysM-EGFP	Transgenic mouse expressing enhanced green fluorescent protein (EGFP) under the control of Lysozyme M promoter, resulting in fluorescent neutrophils, monocytes and macrophages. Neutrophils express higher level of reporter and are distinguished as brightly fluorescent cells.	(Faust et al., 2000)
Ab^o	Transgenic mouse lacking functional MHC class II (IA$^-$ IE$^-$) through disruption of Aβ loci by homologous recombination in an embryonic stem cell line D3 derived from strain 129 mouse, which carries a defective Eα gene promoter. Progeny carrying the mutation was subsequently backcrossed to C57BL/6.	(Cosgrove et al., 1991)
B6 x KAEDE	Transgenic mouse expressing photoconvertible KAEDE fluorescent proteins in all cells under the control of CAG promoter. KAEDE proteins change colour from green to red upon exposure to violet light	(Tomura et al., 2008)

2.1.2 Viruses

Virus	Description	Reference
HSV-1 KOS	Herpes Simplex Virus Type 1 KOS strain. Donated by S. Person, John Hopkins University, USA.	(Rawls et al., 1968)
LCMV Armstrong	Lymphocytic Choriomeningitis Virus Armstrong strain	
VV-OVA	Recombinant Vaccinia Virus expressing OVA epitope. Donated by D. Tscharke, Australian National University, Australia	
HKx31-gB/gD	Recombinant influenza virus HKx31 strain expressing $gB_{498\text{-}505}$ or $gD_{315\text{-}327}$ epitope.	

2.1.3 Bacteria

Bacterium	Description	Reference
***S. aureus* JKD6009 GFP**	Recombinant GFP-expressing vancomycin-susceptible *S. aureus* strain JKD6009	(Howden et al., 2010)

2.1.4 Cell lines

Cell	Description
Vero	African green monkey kidney cells
BHK-21	Baby hamster kidney cells
293T	Human embryonic kidney cells encoding SV40 T antigen
MDCK	Madin-Darby Canine kidney cells

2.1.5 Peptides

Peptide	Description	Reference
SSIEFARL	H-2K^b restricted HSV-1 glycoprotein B peptide gB$_{498-505}$	(Hanke et al., 1991; Bonneau et al., 1993)
IPPNWHIPSIQDA	I-A^b restricted HSV-1 glycoprotein D peptide gD$_{315-327}$	

2.1.6 Tissue culture reagents

Minimal Essential Media (MEM)	Media Preparatory Unit, Department of Microbiology & Immunology, University of Melbourne
Dulbecco's Modified Eagles Medium (DMEM)	Gibco BRL, Victoria, Australia
RPMI 1640	Gibco BRL, Victoria, Australia
Phosphate buffered saline (PBS)	Media Preparatory Unit, Department of Microbiology & Immunology, University of Melbourne
Dulbecco's phosphate buffered saline (D-PBS)	Sigma Co., St. Louis, MO, USA
Hanks Balanced Salt Solution (HBSS)	Media Preparatory Unit, Department of Microbiology & Immunology, University of Melbourne
Fetal Calf Serum (FCS)	Gibco BRL, Victoria, Australia
Dimethyl sulphoxide (DMSO)	Sigma Co., St. Louis, MO, USA
Trypsin/EDTA	Gibco BRL, Victoria, Australia
Gentomycin sulfate (G418)	Gibco BRL, Victoria, Australia
LPS from E. coli	Sigma Co., St. Louis, MO, USA
Recombinant human IL-2	Peprotech Inc., Rocky Hill, NJ, USA
Tissue culture plates (6, 24, 96 wells)	Greiner Labortechnik GmbH, Frickenhausen, Germany
Tissue culture flasks (T25, T75, T175)	Greiner Labortechnik GmbH, Frickenhausen, Germany
Tissue culture petri dishes (90mm, 30mm)	Corning, NY, USA
Falcon tube (50ml)	BD Bioscience, Bedford, MA, USA
Haemacytometer	Reichert, Buffalo, NY, USA
Trypan Blue solution (0.4%)	Sigma Co., St. Louis, MO, USA
Streptomycin	Gibco BRL, Victoria, Australia
L-glutamate	Gibco BRL, Victoria, Australia
2-mercaptoethanol	Sigma Co., St. Louis, MO, USA
HEPES	Merck Millipore, Billerica, MA, USA
Sodium azide	Ajax Finechem Pty. Ltd., Taren Point, NSW, Australia
Ammonium chloride	Sigma Co., St. Louis, MO, USA
Sodium hydrongen carbonate	Ajax Finechem Pty. Ltd., Taren Point,

	NSW, Australia
Tris UltraPure	ICN Biochemicals, Aurora, OH, USA
Heart Infusion (HI) broth	Media Preparatory Unit, Department of Microbiology & Immunology, University of Melbourne
Heart Infusion (HI-CM) plate	Media Preparatory Unit, Department of Microbiology & Immunology, University of Melbourne
Media 199	Gibco BRL, Victoria, Australia
L-15 Medium	Gibco BRL, Victoria, Australia

2.1.7 Transfection reagents

FUGENE® 6 Transfection Reagent	Promega Co., Madison, WI, USA
TPCK-treated trypsin	Worthington Biochemical Corp., Lakewood, NJ, USA

2.1.8 Media and solutions

MEM-10: 10% FCS, 5% SC for DMEM in MEM

MEM-2: 2% FCS, 5% SC for DMEM in MEM

DMEM-10: 10% FCS, 5% SC for DMEM in DMEM

RPMI-10: 10% FCS, 5% SC for RPMI in RPMI 1640

RPMI-5: 5% FCS, 5% SC for RPMI in RPMI 1640

RPMI-2: 2% FCS, 5% SC for RPMI in RPMI 1640

RPMI-1: 1% FCS, 5% SC for RPMI in RPMI 1640

HBSS-2.5: 2.5% FCS in HBSS

Supplementum Complementum (SC): 2mg/ml Steptomycin, 1000U/ml Penicillin, L-glutamine (40mM for RPMI, 80mM for DMEM), 1mM 2-mercaptoethanol, 100mM HEPES, made to 1L with RPMI 1640 or DMEM

Red Blood Cell lysis buffer: 7.8g/L NH_4Cl, 1.0g/L $NaHCO_3$, 50mM EDTA made in MilliQ water

Tris EDTA (TE): 100mM Tris-Cl, 10mM EDTA (pH 8.0) made in MilliQ water

FACS buffer: D-PBS/2% FCS/5mM EDTA/0.1% NaN_3

2.1.9 PFU assay reagents

Toluidine blue (0.1%)	Sigma Co., St. Louis, MO, USA
Molecular grade agarose (powder)	Bioline, London, UK
Formaldehyde (10% formalin)	Ajax Finechem Pty. Ltd., NSW, Australia
Tissue culture plates (6 well)	Greiner Bio-One GmbH, Kremsmunster, Austria
Polytron PT 2100 homogeniser with 7.5mm aggregate	Kinematica AG, Lucerne, Switzerland
Neutral red	Sigma Co., St. Louis, MO, USA
	Merck Millipore, Billerica, MA, USA

2.1.10 Flow cytometry reagents and materials

Collagenase type III (Clostridium histolyticium)	Worthington Biochemical Corp., Lakewood, NJ, USA
Bovine serum albumin (BSA) grade IV	Sigma Co., St. Louis, MO, USA
EDTA	Gibco BRL, Victoria, Australia
Polypropylene round-bottom FACS tubes (5ml)	Becton Dickinson, Franklin Lakes, NJ, USA
Propidium Iodide (PI)	Sigma Co., St. Louis, MO, USA
SPHERO black calibration particles (6-6.4µm)	BD Bioscience, Bedford, MA, USA
Metal mesh, 0.25mm thick	Sefar Metal Mesh, Australia
Nylon mesh, 75µm	Clear Edge Filtration (Australia) Pty Ltd, Victoria, Australia
Nylon mesh, 30µm	Clear Edge Filtration (Australia) Pty Ltd, Victoria, Australia
Tissue culture plates (96 well, round bottom)	Greiner Bio-One GmbH, Kremsmunster, Austria
Trypan Blue (0.4%)	Sigma Co., St. Louis, MO, USA
Haemocytometer	Reichert, Buffalo, NY, USA

2.1.11 Flank scarification infection

Ketamine	Parnell Laboratories, Alexandria, NSW, Australia
Ilium Xylazil	Troy Laboratories, Smithfield, NSW, Australia
Micropore surgical tape	3M Healthcare, St. Paul, MN, USA
Transpore surgical tape	3M Healthcare, St. Paul, MN, USA
Veet hair remover	Reckitt Benckiser, West Ryde, NSW, Australia
Opsite Flexigrid	Smith and Nephew, Hull, England
Needle, 26G	Terumo Corporation, Tokyo, Japan
Syringe, 1mL	Terumo Corporation, Tokyo, Japan
Lacri-Lube® lubricating eye ointment	Allergen Australia, NSW, Australia
Wahl clipper	Wahl Clipper Co., Sterling, IL, USA
Dremel Multipro rotary tool	Dremel, Mount Prospect, IL, USA
3.2mm grind stone	Dremel, Mount Prospect, IL, USA
150mm cotton-tipped wooden applicators	Livingstone International Pty. Ltd., NSW, Australia

2.1.12 Cell isolation, dye labelling and adoptive transfer

Cell strainer, 70µm	Corning, NY, USA
Cell strainer, 40µm	Corning, NY, USA
ATC Red Cell Lysis Buffer	Sigma Co., St. Louis, MO, USA
Biomag Goat anti-Rat IgG beads	QIAGEN, Hilden, Germany
Bovine Serum Albumin (BSA)	Sigma Co., St. Louis, MO, USA
Carboxyfluorescein succinimidyl ester (CFSE)	Invitrogen Co., Carlsbad, CA, USA
Detach-a-Bead® Mouse CD4	Invitrogen Co., Carlsbad, CA, USA
Dynabeads® Mouse CD4	Invitrogen Co., Carlsbad, CA, USA
CellTrace Violet	Molecular Probes, Eugene, OR, USA
CellTracker Deep Red	Molecular Probes, Eugene, OR, USA
29½G insulin needle	Becton Dickinson, Franklin Lakes, NJ, USA

2.1.13 Epidermal sheet T cell and LN DC isolation

Collagenase type III	Worthington Biochemical Corp., Lakewood, NJ, USA
DNase I from bovine pancreas, grade II	Roche Diagnostics GmbH, Mannheim, Germany
Dispase® II (neutral protease, grade II)	Roche Diagnostics GmbH, Mannheim, Germany
EDTA, tetrasodium salt dihydrate	Sigma Co., St. Louis, MO, USA

2.1.14 Confocal and two-photon microscopy

Paraformaldehyde (PFA) (8%, 16%)	Electron Microscopy Science, Hatfield, PA, USA
Sodium periodate ($NaIO_4$)	BDH Chemicals; VWR International, Radnor, PA, USA
Sodium dihydrogen orthophosphate, monohydrate ($NaH_2PO_4.H_2O$) (monobasic)	BDH Chemicals; VWR International, Radnor, PA, USA
di-Sodium hydrogen orthophosphate, anhydrous (Na_2HPO_4) (dibasic)	Ajax Finechem Pty. Ltd., NSW, Australia
L-lysine	Sigma Co., St. Louis, MO, USA
Acetone	Chem Supply, Gillman, SA, Australia
Cryomold (Standard, Intermediate, Biopsy)	Tissue-Tek, Sakura Finetek, CA, USA
Glass Coverslips, No. 1.5 (24x50mm)	ProSciTech, Queensland, Australia
Hoechst 33258	Invitrogen Co., Carlsbad, CA, USA
Isoflurane	Cenvet, NSW, Australia
Normal Donkey Serum (NDS)	Jackson ImmunoResearch Laboratories Inc., West Grove, PA, USA
O.C.T. Compound	Tissue-Tek, Sakura Finetek, CA, USA
Pap pen	Daido Sangyo Co. Ltd., Tokyo, Japan
Prolong® Gold antifade reagent	Invitrogen Co., Carlsbad, CA, USA
Protein Block	Dako, Glostrup, Denmark
Superfrost® Plus microscope slide (25x75x1.0mm)	Gerhard Menzel GmbH, Braunschweig, Germany
Vacuum Grease	Dow Corning, Midland, MI, USA
Vetbond tissue adhesive	3M Healthcare, St. Paul, MN, USA

Durapore™ surgical tape	3M Healthcare, St. Paul, MN, USA
Sucrose	Chem Supply, Gillman, SA, Australia

PLP Fixative (pH7.4): 1% PFA, P-buffer 0.1M pH7.4 (0.2M NaH_2PO_4, 0.2M Na_2HPO_4 in water), L-lysine 0.2M pH7.4 dissolved in P-buffer, $NaIO_4$ (Sodium periodate)

2.1.15 *in situ* TRITC painting

Tetramethylrhodamine-5-(and-6)-isothiocyanate	Life Technologies, Carlsbad, CA, USA
Acetone	Chem Supply, Gillman, SA, Australia
Dimethyl sulphoxide (DMSO)	Sigma Co., St. Louis, MO, USA

2.1.16 DNFB painting

2,4-Dinitrofluorobenzene (DNFB)	Sigma Co., St. Louis, MO, USA
Olive oil, 100% Pure	Colavita, Roma, Italy

2.1.17 RT-PCR reagents

RNAlater® solution	QIAGEN, Hilden, Germany
RNeasy Mini Kit	QIAGEN, Hilden, Germany
UltraPure™ DNase/RNase-free distilled water	Invitrogen Co., Carlsbad, CA, USA
Superscript® VILO™ cDNA Synthesis Kit	Invitrogen Co., Carlsbad, CA, USA
TaqMan® Fast Advanced Master Mix	Applied Biosystems, Foster City, CA, USA

2.1.18 Thick LN section imaging

Razor blades, single edge, No. 9 (0.22mm)	VWR International, Radnor, PA, USA
Tissue culture plates (96 well, round bottom)	Corning, NY, USA
Tissue culture plates (24 well, flat bottom)	Greiner Bio-One GmbH, Kremsmunster, Austria
Superfrost® Plus microscope slide (25x75x1.0mm)	Gerhard Menzel GmbH, Braunschweig, Germany

Glass Coverslips, No. 1.5 (24x50mm)	ProSciTech, Queensland, Australia
Molecular grade agarose	Sigma Co., St. Louis, MO, USA
Vetbond tissue adhesive	3M Healthcare, St. Paul, MN, USA
Gelatin from porcine skin	Sigma Co., St. Louis, MO, USA
Glycerol for molecular grade, ≥ 99%	Sigma Co., St. Louis, MO, USA
Dumont No. 5 forceps	Fine Science Tools Inc., Foster City, CA, USA
Scissors, straight, sharp	Roboz Surgical Instrument Co., Inc., Galthersburg, MD, USA

2.1.19 Antibodies and tetramer

Antibody	**Clone**	**Source**
Rat α-mouse B220-Pacific Blue	RA3-6B2	BioLegend
Armenian hamster α-mouse CD3ε-PerCP-Cy5.5	145-2C11	eBioscience
Rat α-mouse CD4-Alexa Fluor 700	RM4-5	BD Pharmingen
Rat α-mouse CD4-Brilliant Violet 605	RM4-5	BioLegend
Rat α-mouse CD4-PE-Cy7	RM4-5	BD Pharmingen
Rat α-mouse CD4-Quantum Dot 605	RM4-5	Life Technologies
Rat α-mouse CD8α-APC-eFluor780	53-6.7	eBioscience
Rat α-mouse CD8α-Pacific Blue	53-6.7	BD Pharmingen
Rat α-mouse CD8α-PerCP-Cy5.5	53-6.7	eBioscience
Rat α-mouse CD11b-APC-Cy7	M1/70	BD Pharmingen
Rat α-mouse CD11b-Brilliant Violet 711	M1/70	BioLegend
Armenian hamster α-mouse CD11c-Brilliant Violet 785	N418	BioLegend
Armenian hamster α-mouse CD11c-PE-Cy7	N418	eBioscience
Rat α-mouse CD19-PerCP-Cy5.5	1D3	BD Pharmingen
Rat α-mouse CD25-APC	PC61.5	BioLegend
Rat α-mouse CD44-PE-Cy7	IM7	eBioscience
Rat α-mouse CD44-Alexa Fluor 700	IM7	eBioscience
Mouse α-mouse CD45.1-APC	A20	eBioscience
Mouse α-mouse CD45.1-APC-Cy7	A20	eBioscience
Mouse α-mouse CD45.1-FITC	A20	eBioscience
Mouse α-mouse CD45.1-PE	A20	BD Pharmingen
Mouse α-mouse CD45.1-PE-Cy7	A20	eBioscience
Rat α-mouse CD62L-PE	MEL-14	BD Pharmingen
Rat α-mouse CD62L-PerCP-Cy5.5	MEL-14	eBioscience
Goat α-mouse CD69	polyclonal	R&D Systems
Armenian hamster α-mouse CD69-APC	H1.2F3	BD Pharmingen
Armenian hamster α-mouse CD69-PE	H1.2F3	BD Pharmingen
Armenian hamster α-mouse CD103-APC	2E7	BioLegend
Rat α-mouse CD205-APC	205yekta	eBioscience

Rat α-mouse F4/80-APC	BM8	eBioscience
Rabbit α-Herpes Simplex Virus Type 1 (HSV-1)	polyclonal	Dako Australia
Rat α-mouse Ly6C-APC	AL-21	BD Pharmingen
Rat α-mouse Ly6C-FITC	AL-21	BD Pharmingen
Rat α-mouse Ly6C and Ly6G (Gr-1)-APC	RB6-8C5	BD Pharmingen
Rat α-mouse Ly6C and Ly6G (Gr-1)-PE	RB6-8C5	BD Pharmingen
Rat α-mouse Ly6G	1A8	BioXCell
Rat α-mouse Ly6G-PE	1A8	BD Pharmingen
Rat α-mouse Ly6G-Alexa Fluor 647	1A8	BioLegend
Rat α-mouse Ly6G-V450	1A8	BD Horizon
Rabbit α-mouse LYVE1	polyclonal	Abcam
Rat α-mouse MHC II (I-A/I-E)-Alexa Fluor 700	M5/114.15.2	eBioscience
Rat α-mouse MHC II (I-A/I-E)-APC-eFluor780	M5/114.15.2	eBioscience
Mouse α-mouse NK1.1-PerCP-Cy5.5	PK136	BD Pharmingen
Rat α-mouse PNAd-Alexa Fluor 488	MECA-79	eBioscience
Armenian hamster α-mouse TCRβ-APC-Cy7	H57-597	BD Pharmingen
Rat α-mouse Vα2-Alexa Fluor 700	B20.1	BD Pharmingen
Rat α-mouse Vα2-PE-Cy7	B20.1	BD Pharmingen
Rat α-mouse Vα3.2-biotin	RR3-16	BD Pharmingen
Rat α-mouse Vα3.2-PE	RR3-16	BioLegend
Purified Rat α-mouse CD16/CD32 (Mouse BD Fc BlockTM)	2.4G2	BD Pharmingen
Donkey α-rabbit IgG (H+L) Alexa-Fluor 647	polyclonal	Life Technologies
Streptavidin APC-Cy7	-	BD Pharmingen

Tetramer	**Source**
H2-K^{b}-gB SSIEFARL -PE	Provided by Dr. Jie Lin, A. Brooks Laboratory, Department of Microbiology and Immunology, University of Melbourne, Australia

2.2 METHODS

2.2.1 Cell lines

Vero cells were grown in MEM-10, and BHK-21 cells were grown in DMEM-10. Both cells were cultured at 37°C in a humidified atmosphere with 6.5% CO_2.
MDCK cells were cultured in RPMI 1640 with added gentamycin (24μg/mL) and penicillin/streptomycin (100U/mL) at 37°C with 5% CO_2.

2.2.2 Viruses

2.2.2.1 HSV-1

Working stock of HSV-1 KOS strain was cultured and propagated in Vero cells. Confluent Vero cells were infected with HSV master stock at 1:300 m.o.i. for 1 hr at room temperature, and were then incubated for 3-4 days at 37°C at 6.5% CO_2 until significant CPE. The supernatant and cell debris were collected and centrifuged at 2000 rpm for 10 min at 4°C (Beckman Coulter Allegra X-12R). The supernatant (SV) fraction was then spun at 12000 rpm for 2 hr at 4°C (Sorvall centrifuge) and the pellet resuspended. Cell-associated (CA) virus was released through sonication of cellular debris in ice-cold water bath for 5 min prior to centrifugation at 2000 rpm for 10 min at 4°C. The supernatant (CA-1) was collected, and the pellet resuspended in MEM-10, sonicated for 5 min and further centrifuged as above. The supernatant (CA-2) was pooled with other supernatant aliquots (SV, CA-1) and stored at -70°C until required. Each working virus stock was titred using standard plaque forming unit (PFU) assay on Vero cell monolayers.

For UV-inactivation of HSV, virus resuspended in D-PBS was pipetted into a 30 mm petri-dish, which was placed ~10cm from a UV light source for 30 min. Inactivation was confirmed with PFU assay using samples collected before and after UV-irradiation.

2.2.2.2 LCMV

For LCMV, T25 flasks each containing $5x10^5$ BHK-21 cells were grown to ~75% confluency. Frozen virus plaques resuspended in DMEM were thawed quickly in a 37°C water bath, vigorously vortexed and 1mL suspension were added to cell monolayers in rocking T-25 flasks to ensure even coating. Flasks were then incubated at 37°C for 1 hr with intermittent rocking of the flasks, and were further incubated for 3 days after adding 5mL of pre-warmed DMEM-10. The 'P1' (Passage 1) stock was then harvested, aliquoted in 1mL volume and frozen at -80°C. Viral titre was determined with PFU assay on Vero cell monolayers, and high titre P1 stocks were then further passaged in T175 flasks containing $5x10^6$ BHK-21 cells each with ~0.2-0.5 m.o.i. at 37°C for 1 hr, with regular rocking of the flasks. After adding 40mL of pre-warmed DMEM-10 and 48 hr of incubation at 37°C, media from the flasks were collected (P2) and centrifuged at 800rpm for 5 min. Supernatant from all flasks were pooled, aliquoted and frozen at -80°C until required. Each P2 working stock was then titred using PFU assay on Vero cell monolayers.

2.2.2.3 HKx31

Recombinant HKx31 expressing $gB_{498-505}$ or $gD_{315-327}$ epitope on neuraminidase stalk was generated using reverse genetics. Transfection mix was prepared by addition of 1µg of each plasmid (NP, NS2, PB2, M, PA, PB1, HA, NA) and 3µl of FUGENE6 (Roche) / µg of DNA, before incubation at room temperature for 45 min. Transfection was performed on 293T cells in 6-well plates for 6 hr at 37°C with 10% CO_2. Transfection media were then removed and replaced with Easy flu media, and further incubated for 18-30 hr at 37°C with 10% CO_2. After incubation, Easy flu media containing 1µg TPCK-treated trypsin (Worthington) was added for another 48-72hr while checking for CPE. With positive CPE, supernatant was collected and stored at -70°C until required, and was used to infect embryonated eggs. Virus was titred with PFU assay on MDCK cell monolayers.

2.2.3 Virus infections

2.2.3.1 Flank scarification infection

Mice were anaesthetised with 1:1 mixture of Ketamine and Xylazil (10μL/g of body weight) by i.p. injection with a 26G needle (1mL syringe). Lubricating eye gel was applied to eyes of anaesthetised mice to prevent ocular dehydration. Hair was removed from the flank using a clipper (Wahl) and depilated with Veet (Reckitt Benckiser). Scarification was performed by lightly abrading the flank skin (2-3mm^2) for ~10 s using a Dremel™ powertool with fine grindstone attachment. For spleen tip infection, scarification was induced on the skin area covering the dorsal tip of the spleen. For imaging experiments, scarification was performed at the hind flank, near the transition of torso-hind limb region to allow drainage to inguinal LN.

10μL of 10^6 pfu HSV-1 was applied to the scarified site, which was then covered with a strip of Opsite Flexigrid adhesive (Smith & Nephew) longitudinally to contain the virus at the scarified area. To protect the infection site from physical disruption, mice were bandaged around midsection with Micropore™ tape (3M), and then with Transpore™ tape (3M). Mice were kept warm in the cage placed on heat pad until they regain consciousness. Bandages were removed at day 2 p.i.

2.2.3.2 Footpad subcutaneous infection

Mice were anaesthetised with isoflurane and 10^6 or 10^7 pfu HSV-1, or $5x10^4$ pfu HKx31-gB and HKx31-gD each, in 20μL volume was injected s.c. into the hind footpad using 29½G insulin syringe.

2.2.3.3 Flank intradermal infection

Mice were anaesthetised and shaved as described in *2.2.3.1 Flank scarification infection*. Virus was diluted to 10^6 or 10^7 pfu / 20μL, and intradermally injected into skin covering the tip of spleen with a 29½G insulin syringe.

2.2.4 Bacteria infection

2.2.4.1 Flank intradermal infection of *S. aureus*

S. aureus JKD6009 GFP was grown in Heart Infusion (HI) broth at 37°C on an agitator to mid-log phase, and then washed twice and resuspended in PBS. Using a spectrophotometer, concentration was determined by measuring optical density at 600nm (OD_{600}) and bacterial suspension diluted with PBS accordingly to achieve the desired concentration (5 x 10^7 or 5 x 10^8 CFU/mL, for 1 x 10^6 or 1 x 10^7 CFU/20µL injection). Inoculum was also plated on HI-CM plates to verify the colony-forming unit (CFU) on the following day.

For intradermal injection of bacteria, mice were anaesthetised with Ketamine/Xylazil and hair shaved and depilated as per *2.2.3.1 Flank scarification infection*. With a 29½G insulin syringe, 1 x 10^6 or 1 x 10^7 CFU bacteria in 20µL was injected intradermally into skin covering the tip of spleen. Mice were then allowed to recover in a cage placed on heat pad.

2.2.5 Peptide immunisations

For peptide injections, equal concentrations of $gB_{498\text{-}505}$ (SSIEFARL) and $gD_{315\text{-}327}$ (IPPNWHIPSIQDA) peptides diluted in D-PBS were mixed 1:1 and injected s.c. into hind footpad of anaesthetised mice in 20µL volume using 29½G insulin syringe.

2.2.6 T cell enrichment, labelling and adoptive transfer

T cells were enriched from naïve LNs and/or spleens of female transgenic mice. Cell suspensions were prepared from LNs and/or spleens harvested in HBSS-2.5 through mechanical disruption and passaging through wire mesh. If spleen was included, cells were treated with 3mL ATC Red Cell Lysis Buffer for 3 min and were washed in 20mL HBSS-2.5.

2.2.6.1 CD8 T cell enrichment

For CD8 gBT-I and OT-I T cells, cells were resuspended in CD8 T cell negative enrichment antibody cocktail (anti-erythrocytes [Ter119], anti-I-A/E [M5/114],

anti-CD4 [GK1.5], anti-Gr1 [RB6-8C5], anti-Mac-1 [M1/70], anti-F4/80 [F4/80]) for 30 min on ice prior to washing and incubation with Biomag sheep anti-rat IgG-coupled magnetic beads (used at 6:1 bead:cell ratio) in round bottom FACS tubes for 20 min on an angled rotor at 4°C. Enriched CD8 T cells were obtained by collecting supernatant from tubes loaded on magnet. Purity was determined via flow cytometry by co-staining for anti-CD8 and anti-Vα2 (for gBT-I and OT-I), with >90% purity typically achieved.

2.2.6.2 CD4 T cell enrichment

For CD4 OT-II T cells, the procedure was performed as described in *2.2.6.1 CD8 T cell enrichment*, except incubated with CD4 T cell negative enrichment antibody cocktail (anti-erythrocytes [Ter119], anti-I-A/E [M5/114], anti-CD8 [53-6.7], anti-Gr1 [RB6-8C5], anti-Mac-1 [M1/70], anti-F4/80 [F4/80]). Purity was determined by co-staining for anti-CD4 and anti-Vα2, with an expected purity of >80%.

For CD4 gDT-II T cells, 6mL Biomag beads ($4x10^8$ beads/mL) were used for each mouse (LNs and spleen). After negative magnetic enrichment as described in *2.2.6.1 CD8 T cell enrichment*, a further positive magnetic enrichment was performed where cells were resuspended at $1x10^7$ cells/mL and incubated with anti-CD4 Dynabeads® (25µL/10^7 cells; Invitrogen) for 20 min on an angled rotor at 4°C. After application to a magnetic column, the supernatant was discarded and bead-bound cells were released via incubation with Detach-a-Bead® (Invitrogen) on an angled rotor at room temperature for 45 min. Purified CD4 T cells were then collected as supernatant while loaded to magnetic column. Purity was determined by co-staining for anti-CD4 and anti-Vα3.2, with an expected purity of 50-60%.

2.2.6.3 Dye labelling and adoptive transfer

For labelling with CFSE (1µM) or CellTrace Violet (5µM), cells were resuspended in 0.1% BSA/PBS at 10^7 cells/mL. Dye solution was added to cell suspensions and vortexed immediately to ensure even mixing, prior to incubation at 37°C for 10 min. At the end of incubation, cells were washed with HBSS-10.

For labelling with CellTracker Deep Red, cells were resuspended in PBS at 10^7 cells/mL and incubated with 1:1 mixture of 0.5μM dye and Pluronic F-127 (1:10 dilution) for 15 min, and further incubated with complete medium (HBSS-10) for another 15 min. Cells were washed in HBSS-10 after incubation.

Prior to adoptive transfer, a viable cell count was performed through trypan blue exclusion and counted using a haemocytometer. 0.5-5 x 10^5 T cells, resuspended in HBSS, were then adoptively transferred intravenously into recipient mice prior to infection.

2.2.7 Flow cytometry

2.2.7.1 Sample preparation

Spleen and LN

Spleen and LNs were collected in HBSS-2 and single cell suspensions prepared by mechanical disruption and passaging through wire mesh. For spleen, cells were also resuspended in 2mL Red Blood Cell Lysis Buffer for 3 min, and washed in HBSS-2. Viable cell counts were performed via trypan blue exclusion and 2-4 x 10^6 cells were transferred into round bottom FACS tubes containing 1mL FACS buffer.

For DC isolation, LNs were disrupted using scalpel blade and 1mg/mL collagenase type III (containing 20μg/mL DNase) in RPMI-2 was added to the tubes and mixed vigorously by pipetting up and down for 20 min, prior to addition of 0.1M EDTA. Cells were then further mixed for 5 min, filtered with 70μm nylon mesh, and resuspended as above for antibody staining.

Skin

For experiments involving skin neutrophil, 1 x 1 cm^2 skin was excised using a scalpel blade and placed into 1mL collagenase type III (3mg/mL in RPMI-5). Skin samples were finely chopped by hand with scissors and incubated at 37°C for 90 min. Following incubation, the cells in digestion media were transferred into

5mL RPMI-10 and vigorously mixed with a Pasteur pipette to release cells into suspension.

For experiments involving detection of epidermal T cells, 2 strips of 0.5 x 1.5 cm^2 (covering the infection site) were excised and placed into 2mL dispase, and incubated at 37°C for 90 min. Epidermal sheets were then carefully separated using forceps, and transferred into 1mL trypsin. The remaining skin was placed into 1mL collagenase type III, and chopped into small pieces with scissors. Both epidermis/trypsin and dermis/collagenase samples were incubated at 37°C for 30 min, before transferring into 5mL RPMI-10 and pipetted up and down.

Cell debris was filtered out by passing cells through 70μm nylon mesh. After resuspension in 1mL FACS buffer, cells were placed into round bottom FACS tube by filtering through 30μm nylon mesh.

2.2.7.2 Antibody and tetramer staining

Surface marker staining with monoclonal Abs

Samples transferred into round bottom FACS tube containing 1mL FACS buffer were pelleted at 1600 rpm for 5 min and incubated for 30 min in the dark with antibody cocktails in 50μL volume. Cells were washed with FACS buffer and resuspended in 150μL FACS buffer. For tetramer staining, cells were first incubated with tetramers after washing (see below) before resuspension in 150μL volume. For skin samples, approximately 20,000 blank calibration beads were also added to each sample. Propidium iodide was added to samples prior to acquisition by flow cytometry to allow exclusion of dead PI^+ cells. Flow cytometric acquisition was performed with BD FACS Canto or BD Fortessa, and data were analysed using Flowjo software (Treestar).

Surface marker staining with tetramer

Cells were washed in 2% FACS buffer and incubated with 40μL tetramer (PE-conjugated K^b-gB) for 45 min at 37°C in the dark. Cells were then washed twice and stained for surface markers with monoclonal Abs as described above, before resuspending in 150μL FACS buffer for flow cytometric analysis.

2.2.8 *in vitro* activation of transgenic T cells

2.2.8.1 *in vitro* activation of CD8 gBT-I T cells

Transgenic gBT-I splenocytes (gBT-I/Ly5.1 or gBT-I/DOCK8/uGFP) were cultured with peptide-pulsed C57BL/6 splenocytes for four days at 37°C with 6.5% CO_2. C57BL/6 splenocytes were first pulsed with gB peptide (SSIEFARL) at 0.1µg/mL concentration at 37°C for 45 min, washed twice in HBSS, resuspended in RPMI-10 and were added to T75 flask containing transgenic gBT-I splenocytes in a total volume of 40mL RPMI-10 and 6µg LPS per flask. Cell cultures were split 1:2 on days 2 and 3 with fresh media containing 12.5U/mL human recombinant IL-2. On day 4, the cells were harvested, pooled, washed twice with HBSS and viable cell counts performed. Cells were resuspended in HBSS and adjusted to appropriate concentration (1 x 10^7 cells/200µL) prior to adoptive transfer via intravenous tail vein injection using 29½G insulin syringe.

2.2.8.2 *in vitro* activation of CD4 gDT-II T cells

Transgenic gDT-II cells from LN and spleen were enriched as described in *2.2.6.2 CD4 T cell enrichment.* C57BL/6 splenocytes were pulsed with 10µM gD peptide (IPPNWHIPSIQDA) and 2µg LPS in 2mL HBSS for 45 min at 37°C. After incubation the pulsed splenocytes were irradiated at 3000 rad for 15 min prior to washing with HBSS. Irradiated splenocytes were then cultured with enriched gDT-II cells in a T75 flask in a total volume of 20mL RP-10 and 2µg LPS. On day 2, 20mL fresh RPMI-10 was added to the flask, and were split and diluted on days 2 and 4. 25 U/mL recombinant human IL-2 was also added on days 2 and 4. On day 5, cells were harvested, pooled, washed twice in HBSS and viable cell count performed. A small aliquot of cells were stained with anti-Vα3.2 and anti-CD4 to determine purity, and concentration adjusted appropriately (1 x 10^6 cells/200µL) prior to adoptive transfer via intravenous tail vein injection using 29½G insulin syringe.

2.2.9 *in situ* dye painting

Tetramethylrhodamine-5-isothiocyanate (TRITC) was dissolved in DMSO and diluted to 0.5% (v/v) in acetone. Mice were anaesthetised with Ketamine/Xylazil (10µL/g bodyweight) via i.p. injection and hair removed and depilated as per *2.2.3.1 Flank scarification infection.* 10µL TRITC dye/acetone mix was slowly applied to a 1cm-diameter area of the flank skin and allowed to dry. Mice were then kept in a cage placed on heat pad until conscious. HSV infection was performed 4-6 hr after TRITC application.

For tracking neutrophils in flank-infected mice, at 6hr p.i., mice were anaesthetised again with Ketamine/Xylazil and bandages removed to allow application of TRITC dye on area covering the infection site. 10µL PBS was applied to the scarified site prior to re-bandaging as described in *2.2.3.1 Flank scarification infection.*

For intradermally infected mice, mice were anaesthetised with isoflurane and TRITC dye applied on the skin area containing the infection site, prior to returning the mice to their housing cages.

2.2.10 KAEDE photoconversion

For tracking neutrophil migration from skin, photoconversion was performed at 6 hr p.i. Mice were anaesthetised with Ketamine/Xylazil and bandages removed as described in *2.2.9 in situ dye painting*. Using an aluminium foil with a 1cm^2 window to cover the mouse, laid on a heat pad, the skin area containing the infection site exposed by the foil window was then exposed to violet light (placed ~10cm from the skin) for a duration of 400 s. 10µL PBS was applied to the infection site prior to re-bandaging the mouse. Mice were then allowed to recover in a cage placed on a heat pad.

2.2.11 DNFB painting

Mice were anaesthetised with Ketamine/Xylazil, shaved and depilated as per *2.2.3.1 Flank scarification infection.* 15µl 0.5% DNFB in acetone/olive oil (4:1) was then applied to a 1 x 1.5 cm² skin area and allowed to dry. Flank infection of mice with HSV-1 was performed ~30 days post-DNFB treatment, dorsal of the DNFB-treated patch.

2.2.12 *in vivo* depletion of neutrophils

Mice were injected i.p. with 500µg anti-Ly6G (1A8) depleting antibodies in 200µL PBS at indicated time points. Depletion efficiency was determined at the experiment endpoint by co-staining for anti-Ly6C and anti-Gr-1 to detect neutrophils ($Ly6C^{int}$ $Gr\text{-}1^{hi}$).

2.2.13 Intradermal lodgement of T cells

Mice were anaesthetised with Ketamine/Xylazil, shaved and depilated as per *2.2.3.1 Flank scarification infection.* 1 x 10^6 *in vitro* activated transgenic gBT-I/Ly5.1 and gBT-I/DOCK8/uGFP cells each were mixed to 1:1 ratio *(see 2.2.7 in vitro activation of CD8 gBT-I T cells)* and intradermally injected into recipient mice in 5 x 2µL injections over a 1 x 1.5 cm^2 skin area of the mouse flank.

2.2.14 RT-PCR

2.2.14.1 Whole LN RNA extraction

LNs harvested from sacrificed mice were stored immediately in RNAlater (QIAGEN) at -20°C to prevent RNA degradation. For RNA extraction, tissues were transferred into cryovials containing RLT/2-β-mercaptoethanol solution and homogenised prior to centrifugation at 12000g for 2 min. 1 volume of 70% DNA-grade ethanol was added to cleared lysate, and samples briefly pulsed at 12000g for 15 s. With RNA bound to the membrane, spin columns were washed with RW1 buffer by brief pulsing at 12000g. DNase digestion was performed by adding DNAse/RDD solution to the column and incubated for 15 min at room temperature, and spin columns were subsequently washed with RPE buffer at 12000g, once for 15 s and then for 2 min to dry the membrane to prevent

carryover of ethanol during elution. RNA was obtained through elution by adding RNase-free water and centrifuging at 12000g for 1 min. Purity and concentration of eluted RNA were determined using a spectrophotometer (Nanodrop).

2.2.14.2 cDNA synthesis

cDNA was synthesised using SuperScript VILO cDNA synthesis kit (Invitrogen). Briefly, 11µL mRNA from each sample was mixed with 2µL oligo(dT)/10mM dNTP mix, and heated at 65°C for 5 min (hot start) before cooling to 50°C. mRNA samples then were incubated on ice for 1 min and were pulsed briefly. 7µL of SuperScript III RT mixture (containing 0.1M DTT, RNase inhibitor and SuperScript III reverse transcriptase in First-Strand buffer) were added to each tube, and the samples returned to a heating block at 50°C. After 30-60 min incubation, the reaction was terminated by heating to 70°C for 15 min. Samples from each tube were resuspended with 400µL molecular-grade H_2O, and stored at -20°C until required.

2.2.14.3 Quantitative RT-PCR

Quantitative RT-PCR experiments were performed using StepOnePlus Real-Time PCR system (Applied Biosystems) with TaqMan Gene Expression Assays and TaqMan Fast Advanced Master Mix (Applied Biosystems). Threshold cycle (Ct) of gene transcripts for each sample as determined by RT-PCR was normalised to the geometric mean of Ct values of housekeeping genes *B2m*, *Pgk1* and *Hprt* from the corresponding samples to obtain ΔCt values. ΔΔCt was calculated from ΔCt_{sample} - $\Delta Ct_{control}$, where $\Delta Ct_{control}$ is the averaged ΔCt of naïve samples of the gene of interest. Fold change was then determined using $2^{-\Delta\Delta Ct}$ method for each gene of interest (Livak & Schmittgen, 2001).

The TaqMan Gene Expression Assays used were *Ccl2* (*Mm00441242_m1*), *Ccl5* (*Mm01302427_m1*), *Ccl19* (*Mm00839967_g1*), *Ccl20* (*Mm01268754_m1*), *Ccl21a* (*Mm03646971_gH*), *Ccl27a* (*Mm04206819_gH*), *Cxcl9* (*Mm00434946_m1*), *Cxcl10* (*Mm00445235_m1*), *Cxcl16* (*Mm00469712_m1*), *Xcl1* (*Mm00434772_m1*), *B2m* (*Mm00437762_m1*), *Pgk1* (*Mm01225301_m1*) and *Hprt* (*Mm03024075_m1*).

2.2.15 Plaque assay

2.2.15.1 HSV-1

Skin samples were obtained from sacrificed mice through excision of 2 strips of 0.5 x 1.5 cm^2 skin covering the infected area and kept in cryovials containing 1mL MEM-2. Skins were finely chopped with scissors and homogenised with a Polytron homogeniser (with a 7.5mm aggregate attached) for 30 s. The homogenised samples were stored at -70°C until required.

For plaque assay, the frozen samples were thawed and pelleted via centrifugation at 1600 rpm for 5 min. Serial dilutions (1:2 and ten-fold from 10^{-2} to 10^{-6}) of the supernatant were performed in serum-free (SF) MEM and added to confluent Vero cell monolayers in 6-well plates (one dilution per well). Vero cells were rinsed with SF-MEM twice prior to addition of supernatant. After 1 hr incubation at room temperature with occasional swirling, 3mL 1% agarose in MEM-2 was added into each well and allowed to set, and Vero cells were further incubated for 3-4 days in a 37°C incubator at 6.5% CO^2 until plaque formation was observed.

At the end of the incubation, 4mL 10% formalin was added to each well for 1 hr at room temperature to fix the Vero cells and neutralise virus. Agarose overlays were then removed with spatula and each well stained with 0.1% Toluidine blue and then rinsed with water to visualise plaques, which can be discerned as clear plaques against blue background. Viral plaques were counted by eye, aided by a dissecting microscope. Two wells, each containing 10-100 viral plaques, were counted and averaged for calculation. The virus concentration was calculated with the formula:

Number of plaques / (dilution factor x 0.9) = pfu/mL

Viral titre per sample was calculated by multiplying the concentration with volume of the sample. The viral titre obtained was also further adjusted for each cm^2 skin.

2.2.15.2 LCMV

6-well plates were seeded with ~$7.5x10^5$ Vero cells per well and incubated overnight at 37C to achieve confluency. Serial dilutions (10^{-1} to 10^{-8}) of virus samples were performed in 300µL volume with RPMI-1. 200µL of virus samples were then added to each well and incubated at 37°C for 1 hr, prior to addition of 3-4mL 2% agarose in 2x199 media (1:1 mix). Agarose in wells was allowed to set and cells further incubated at 37°C for 4 days.

At the end of the incubation, 2mL 1:1 1% agarose/2x199 mixture containing neutral red solution was added to each well, and plates covered with aluminium foil for incubation overnight at 37°C. Viral plaques were counted on light box, and agarose overlays removed to inspect for hidden plaques.

Virus concentration was calculated with the following formula:

Number of plaques x 5 x dilution factor = pfu/mL

Viral titre per sample was calculated by multiplying the concentration with volume of the sample. Two wells, each containing 10-100 viral plaques, were counted and averaged for final calculation.

2.2.15.3 HKx31

6-well plates were seeded with ~$5x10^9$ MDCK cells in each well and incubated overnight at 37°C, 5% CO_2 overnight until confluent. Cell monolayers were then washed and bathed in RPMI plus gentamycin (24µg/mL) and penicillin/streptomycin (100U/mL) and placed in a 37°C incubator with 5% CO_2. Virus stocks were serially diluted (in ½ log dilutions from 10^{-4} to $10^{-7.5}$) and were added to MDCK monolayers (each dilution per well) for 45 min at 37°C, 5% CO_2 with occasional shaking. At the end of incubation, L15 medium mixed with 1.8% agarose (1:1 mix) with added trypsin was added to each well at room temperature until set. The cells were then further incubated at 37°C, 5% CO_2 for another 3 days and viral plaques counted to determine virus concentration.

2.2.16 Immunofluorescence and confocal microscopy

LNs and spleens were harvested and fixed in PLP fixative or 4% (v/v) PFA for 6-8 hr, washed twice in PBS for 10 min and incubated in 20% sucrose overnight at 4C. For skin, tissues were fixed in PLP and incubated in sucrose for 10 min each. Fixed tissues were then embedded in OCT compound and frozen at -80°C until required.

For cryosectioning of tissue samples, LN sections were cut at 12µm thickness and skin sections at 18µm thickness with a cryostat and air-dried before fixation in acetone for 5 min, dried and then blocked for 20 min at room temperature. Sections were then stained with primary antibodies at room temperature for 1.5 hr, washed in PBS for 10 min and stained with secondary antibodies for 30 min at room temperature. Sections were then washed in PBS for 5 min and mounted on glass slides using Prolong Gold antifade reagent. Images were acquired using an LSM700 or LSM710 confocal microscope (Zeiss) and analysed using Imaris 7 (Bitplane), ImageJ (NIH) and Photoshop (Adobe).

Determination of LN compartments was performed using masks for different regions that were generated semi-automatically using ImageJ based on anti-B220 and anti-LYVE1 staining. Cells were detected using "analyse particles" function in ImageJ and were masked using each region generated above. Percentage was calculated based on number of cells per region over cells detected in all regions.

2.2.17 Thick LN section imaging

Harvested LNs were either fixed in PLP fixative or 2% (v/v) PFA at 4°C for 2-6 hr, or left unfixed, prior to embedding in 2% agarose. Agarose blocks containing tissues were trimmed carefully into cuboid shape with razor blade and were sliced using a VT1200 S vibratome (Leica) into 200-250µm thick sections (~0.03mm/s blade speed with ~1.6mm amplitude). Cut slices were transferred into wells in a 96-well round-bottom plate filled with cold PBS. For antibody staining, tissue slices were blocked for 1.5-2 hr before incubating with primary antibodies in 2.5% NDS for 8-16hr at 4°C. Slices were then washed in PBS for up

to 2 hr before staining with secondary antibody at 4°C, followed by washing in PBS. Tissue slices were then mounted on glass slides, using Prolong Gold antifade reagent and a 1:1 mix of gelatin and glycerol. Images were acquired on a LSM710 NLO multiphoton microscope (Zeiss) with Chameleon Vision II Ti:sapphire laser (Coherent) tuned to 800nm to detect fluorochrome-conjugated antibodies and cell tracker dyes and 880nm to detect TRITC and GFP. Imaging volumes were typically 100-150µm thick with intervals of 2µm in the Z-axis. Post-acquisition processing was performed in Imaris 7 (Bitplane).

For cluster detection, spots were created with built-in spot detection function in Imaris and clusters detected using custom MATLAB scripts interfaced with Imaris XT (**Appendix A.1**). A cluster was defined as a minimum of 3 cells aggregating within a distance of 15µm measured from the centroid of each cell. To determine the composition of gDT-II and gBT-I within each cluster, spots from different fluorescence channels were examined using a custom MATLAB script on clusters with a minimum of 4 cells aggregating with a 15µm centroid-to-centroid distance threshold (**Appendix A.2**).

2.2.18 Intravital two-photon microscopy

2.2.18.1 Skin surgical preparation for imaging

Mice anaesthetised with isoflurane (2.5% for induction, 1-1.5% for maintenance, vaporised in 80:20 mixture of O_2 and air) were shaved on the left flank with a clipper (Wahl) and hair depilated with Veet (Reckitt Benckiser). Two incisions (~15mm apart) were made longitudinally along the left flank, cutting through the dermis, before separated from the peritoneum by cutting away the connective tissues underneath. A 18mm-wide x 1mm thick stainless steel platform was inserted under the exposed dermis, and Vetbond tissue adhesive was used to glue the underside of the dermis to the steel platform. The edges of the skin were lined with vacuum grease, upon which a glass coverslip was placed. Moist gauze was placed around the incisions to prevent dehydration.

2.2.18.2 LN surgical preparation for imaging

Mice were anaesthetised with isoflurane (2.5% for induction, 1-1.5% for maintenance, vaporised in 80:20 mixture of O_2 and air). Surgically exposed left inguinal LNs were prepared for intravital imaging using a modified version of a published protocol (Miller et al., 2003; Qi et al., 2006). Briefly, mice were shaved on the left flank with a clipper (Wahl) and hair depilated with Veet. A ventral midline incision was made through the skin and diagonal incisions from both ends of the midline incision to the left hindlimb and the dorsal flank next to left forelimb. Skin was carefully detached from the peritoneum, exposing the adipose pad covering the left inguinal LN. The skin flap was then glued with Vetbond tissue adhesive to a raised platform. With a dissecting microscope, a circular skin flap superficial to the LN was excised and adipose tissue carefully removed using microscissors to expose the cortical side of LN. A rectangular ring of vacuum grease was placed around the margins of the skin flap and the enclosing space filled with warm PBS before being partially covered with a glass coverslip, which has hydrophobic barriers drawn by pap pen on 3 sides to contain PBS on top of coverslip during imaging. As the vacuum grease enclosed region was only partially sealed, warm PBS was added periodically during long imaging period. Moist gauze was placed around incisions to prevent dehydration.

2.2.18.3 Intravital imaging

For intravital imaging, animals were placed in an environment chamber built to accommodate a multiphoton microscope, maintained at 35°C with heated air. Using an upright LSM710 NLO multiphoton microscope (Zeiss) with a 20x/1.0 NA water immersion objective, fluorescence excitation was provided by a Chameleon Vision II Ti:sapphire laser (Coherent) with dispersion correction and fluorescence emission detected using external non-descanned photomultiplier tubes. EGFP and DsRed were excited at 940nm, EYFP and TRITC at 880nm and fluorescent probes excited at 800nm. Collagen-rich dermis of the skin and the LN capsule were visualised by second harmonic generation (SHG). The following emission filters were used for NDD channels: Blue/SHG (BP 380-425nm), Green (BP 500-550nm), Red (BP 565-610nm), and Far red (BP 640-710nm). A typical imaging volume of the LN was 300x300x50µm acquired ~200-250µm below LN

capsule in the outer T cell zone, with 2µm intervals in the z-axis. For four-dimensional data sets, three-dimensional stacks were captured every 30-45 s (LN) or 30 s (skin) for 30-90 min.

Raw imaging data were processed with Imaris 7 (Bitplane) and drift corrected. Autofluorescence was removed using channel arithmetic function from Imaris XT. Briefly, a fluorescence channel containing no fluorescent probe of interest was used to capture autofluorescent signal during image acquisition. The obtained autofluorescent signal was then subtracted from the channel of interest with the following formula:

$$Channel_{COMP} = Channel_{DET} - Channel_{AUTOF} \times (R_{DET/AUTOF})$$

,where $Channel_{DET}$ is the intensity initially acquired through the detector, $Channel_{AUTOF}$ is the intensity from autofluorescence channel, and $R_{DET/AUTOF}$ is the ratio of intensity of an autofluorescent region from initial detector to the intensity of the same region from the autofluorescence channel.

Cellular motion was tracked semi-automatically using built-in tracking functions aided by manual corrections. Tracks with a duration of <3 min were filtered out. Mean track velocities were calculated for each cell population and were normalised relative to the mean velocities of their respective population in uninfected mice to facilitate ready comparison of the different populations. Data were plotted using Prism (Graphpad). Confinement ratio was calculated as track displacement divided by track length.

For tracking contact duration, spots and surfaces were generated for T cells and $TRITC^+$ cells, respectively, and were tracked using custom MATLAB scripts interfaced with Imaris XT (**Appendices A.3**, **A.4**). Briefly, contact threshold was defined by distances of <8µm between centroid of T cell spot objects to the rendered surface of $TRITC^+$ objects. Movies were generated in Imaris (Bitplane) and composed in After Effects (Adobe).

CHAPTER THREE:

IMMUNOMODULATORY ROLES OF NEUTROPHILS IN ADAPTIVE IMMUNITY DURING EPICUTANEOUS HSV INFECTION

3.1 INTRODUCTION

Innate and adaptive immunity were once thought to be separate arms of the immune system. However, recent development in our understanding of immunology has increasingly blurred the delineation of the two branches, with mounting evidence suggesting close cooperation between immune cells of innate and adaptive immunity. Neutrophils are the principal innate immune cells to rapidly infiltrate peripheral tissues in response to infection and tissue damage. Sensing of pathogen-associated molecular patterns (PAMP) or danger-associated molecular pattern (DAMP) released by infected or damaged cells leads to secretion of inflammatory factors by tissue-resident macrophages and mast cells, triggering neutrophil recruitment to the foci of inflammation (Sadik et al., 2011; Williams et al., 2011).

Neutrophils have long been established as terminally differentiated cells responsible for the inflammatory response as well as pathogen clearance through phagocytosis and degranulation of reactive oxygen species. More recently, neutrophils were reported to perform immunomodulatory functions and engage in crosstalk between the innate and adaptive immune systems (Mantovani et al., 2011).

In particular, neutrophils have been implicated in transporting bacterial antigens to draining LN during *M. bovis BCG* inoculation of the ear pinna (Abadie et al., 2005), and their migration to the LN from skin after *S. aureus* injection may influence humoral and cell-mediated responses (Hampton et al., 2015), raising the possibility that their numerical advantage and rapid infiltration into infected sites could provide prompt delivery of antigen to the lymphoid tissues and enhance antigen presentation, especially when the initial antigen load is low. Furthermore, neutrophils were shown to interact with B cells and plasma cells in the LN to regulate humoral immunity (Kamenyeva et al., 2015), thus demonstrating their contribution in the shaping of adaptive immunity.

Studies investigating the role of neutrophils during peripheral viral infections, including influenza virus in the lung, and HSV-1 in the skin, have reported their recruitment to sites of infection at the peak of infection, but have not examined their role early in the initiation of adaptive immunity (Tate et al., 2012; Wojtasiak et al., 2010b). Functional studies showed that neutrophils enhanced $CD8^+$ T cell responses against influenza virus in the lung, but had no effect on the viral load nor the severity of disease during both intranasal and epicutaneous HSV-1 infections (Tate et al., 2012). The relationship between neutrophils and priming of T cells during skin HSV-1 infection, however, was not assessed.

We investigated whether neutrophils can (1) help transport antigen to the draining LN and (2) if they are pivotal in the priming, expansion and migration of $CD4^+$ and $CD8^+$ T cells during cutaneous HSV-1 infection. In this chapter, we showed that neutrophils infiltrate both the skin and draining LNs early after dermal scarification, but were dispensable as antigen carriers and modulators of primary T cell responses.

3.2 RESULTS

3.2.1 Early virus-independent recruitment of neutrophils and monocytes to HSV-infected skin.

To visualise neutrophil infiltration into infected skin, we used two-photon microscopy and performed intravital flank skin imaging of transgenic LysM-EGFP mice after epicutaneous HSV-1 infection. In LysM-EGFP mice, neutrophils and monocytes/macrophages can be distinguished through their bright and dim expression of enhanced green fluorescent protein (EGFP), respectively. As early as 2 hr p.i., neutrophils entered the dermis of the scarified site, localising predominantly to the edge of the scarified region, where exposed epidermal keratinocytes were infected (**Fig. 3.1A**, **Movie R1**).

Accumulation of neutrophils at the scarified site continued over the next few hours, and by 8 hr p.i. the entire perimeter of the scar was illuminated by bright aggregates of $EGFP^+$ neutrophils (**Fig. 3.1B**). Our intravital imaging data thus demonstrated a rapid, early infiltration of neutrophils into the infected site and their localisation near infected keratinocytes in the epidermis, which indicated opportunity to interact with infected cells and to acquire viral antigens.

To further characterise the kinetics of neutrophil infiltration into infected skin, we used flow cytometry to follow the recruitment of neutrophils into the skin. At 6 hr p.i., significant influx of two myeloid populations was observed: neutrophils ($Ly6G^{hi}$ $Ly6C^{int}$) and inflammatory monocytes ($Ly6C^{hi}$ $Ly6G^{lo}$) (**Fig. 3.2A**). Although there was variation in the number of cells between mice, both neutrophils and monocytes increased significantly in number compared to untreated skin (**Fig. 3.2B, E**), and represented ~30% and ~20% of $CD11b^+$

Movie R1 Neutrophil infiltration into HSV-infected skin (LINK)
LysM-EGFP mice were infected with HSV-1 on the flank and imaged at 2 hr p.i. onwards. Shown are examples of two time points (2 hr and 4 hr p.i.) at the scarified edge of the infection site. Neutrophils are distinguished through their bright EGFP (green) expression. Second harmonic generation (SHG) was shown in blue, indicating the collagen-rich dermal layer of the skin.

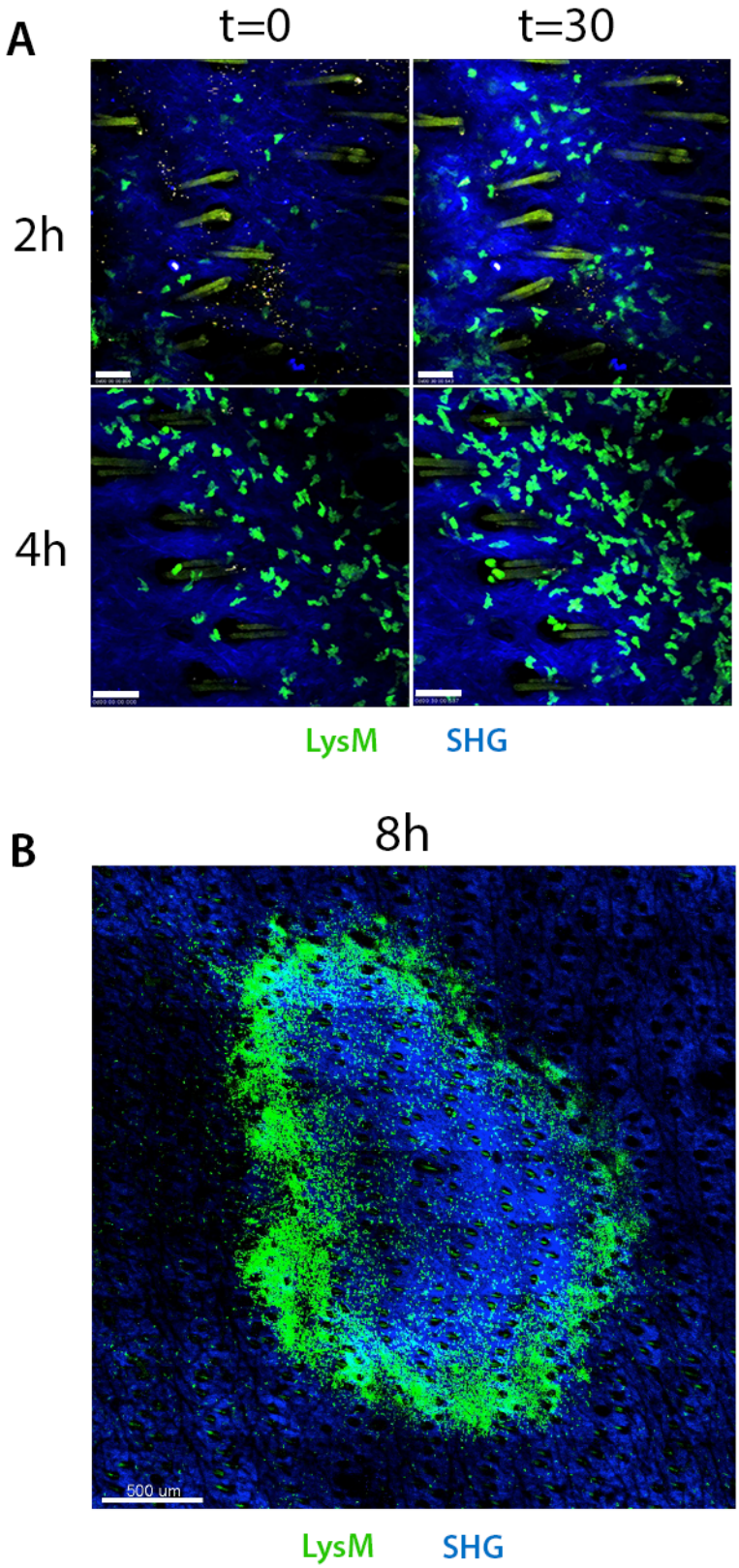

Figure 3.1 Neutrophils infiltrate the skin early after HSV-1 infection.
LysM-EGFP mice, which express brightly fluorescent neutrophils (green) were scarified dermally and inoculated with HSV-1 for at least 1 hour before surgical preparation for intravital two-photon microscopy of the scarified skin.
(A) Time lapse snapshots depicting two areas of scarified skin (2 hours, top row and 4 hours, bottom row after HSV-1 infection) at the start of imaging period (t = 0) and 30 minutes after (t=30). Neutrophils are shown in bright green against the dermal background (blue) as illuminated by second harmonic generation. Macrophages and monocytes are visible as dim green fluorescent cells. Scale bars denote 50μm. See also **Movie R1**.
(B) Snapshot of the entire scarified region at 8 hours after HSV-1 infection, showing localisation of neutrophils (bright green) in relation to the scarified area. Scale bar denote 500μm.

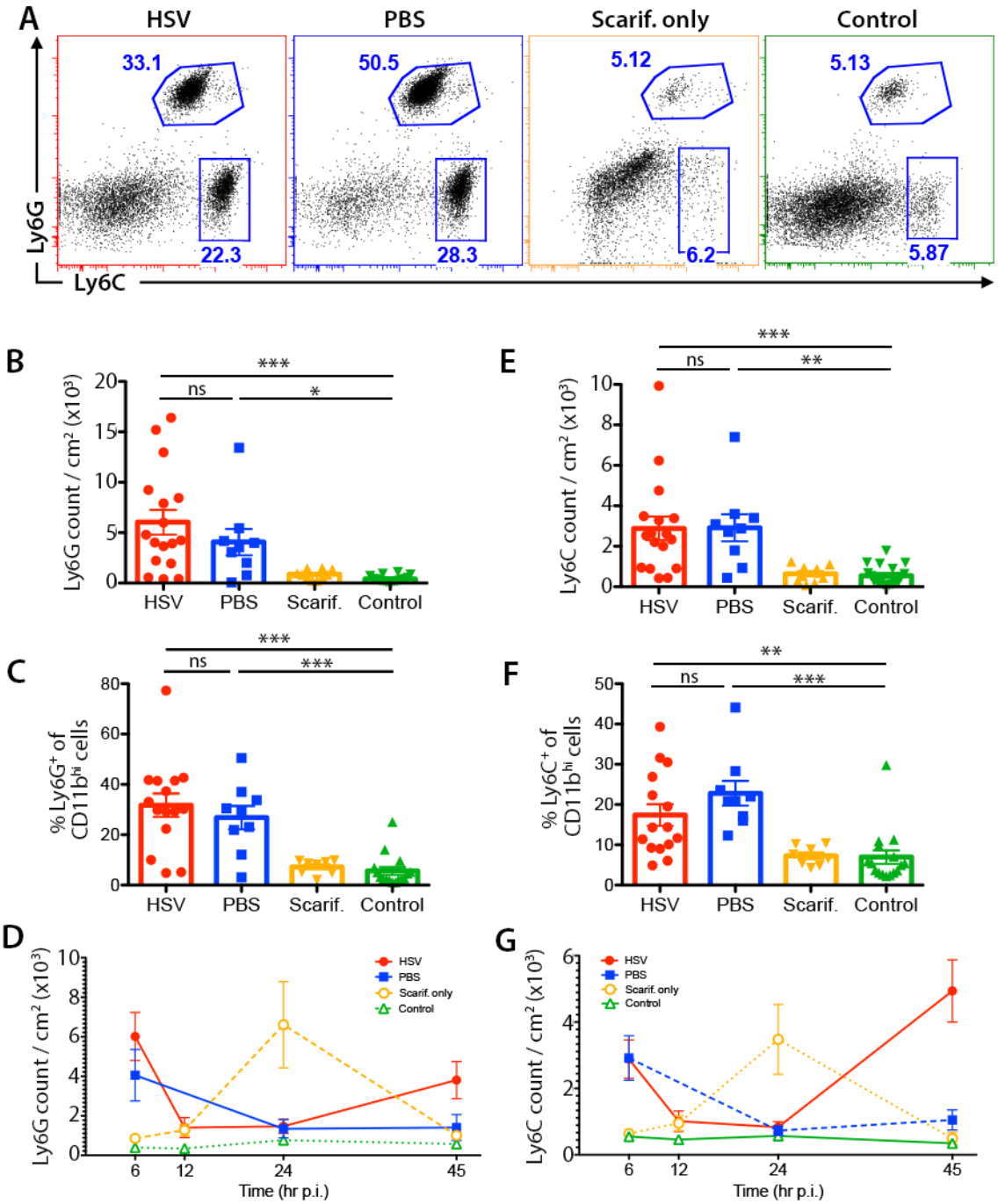

Figure 3.2 Kinetics of neutrophil and monocyte recruitment to the skin during early HSV-1 infection.

(A) C57BL/6 mice were dermally scarified and treated with either HSV-1 (red box), PBS (blue box), scarified but left untreated (orange box) or left intact (green box). 1cm² skin containing the scarified area were excised for flow cytometric analysis at various time points. Representative dot plots of CD11b⁺ cells in the skins treated under different conditions at 6 hr post-scarification were shown in (A), also depicting gating strategies for neutrophils (Ly6G^{hi} Ly6C^{int}) and monocytes (Ly6C^{hi} Ly6G^{lo}).

(B, E) Total number of Ly6G^{hi} neutrophils (B) and Ly6C^{hi} monocytes (E) recovered from 1cm² skin at 6 hr post-scarification, as shown in (A).

(C, F) Proportion of Ly6G^{hi} neutrophil (B) and Ly6C^{hi} monocytes (F) population amongst CD11b⁺ cells at 6hr post-scarification, as shown in (A).

(D, G) Time course depicting total number of Ly6G^{hi} neutrophil (D) and Ly6C^{hi} monocyte (G) population from 6 hr to 45 hr post-scarification.

Data pooled from 2-5 independent experiments, n=8-15 mice per group. Error bars represent mean ± SEM. *p<0.05, **p<0.01, ***p<0.001, one-way ANOVA, Tukey's multiple comparisons. ns, not significant.

myeloid cells in the skin, respectively (**Fig. 3.2C, F**). However, we also observed comparable accumulation of both cells in mock-infected (saline-treated) mice, suggesting that the recruitment might be triggered independent of viral-derived cues.

Interestingly, an early increase in both neutrophils and monocytes was not detected in mice treated only by scarification, without application of virus or saline. This might indicate a role of moisture in the damaged skin for recruitment of inflammatory cells, which could lead to more rapid healing compared with dry wounds (Junker et al., 2013). Alternatively, low levels of endotoxin typically found in phosphate-buffered saline (PBS, also used in the reconstitution of virus supernatant) might be sufficient to elicit an inflammatory response. To address the latter possibility, we also analysed skin samples from mice mock-infected with saline solution containing very low endotoxin level (<0.1%) and observed comparable amounts of neutrophil and monocyte recruitment to the skin (data not shown), suggesting that endotoxin in the virus diluent was unlikely to be the cause of the non-specific neutrophil recruitment.

Following the kinetics of neutrophil and monocyte recruitment to the skin over the first 45 hr of infection, we found that this early influx of myeloid cells at 6 hr p.i. represented a transient wave of recruitment, as their numbers began to decline by 12 hr p.i., reaching baseline level at around 24 hr p.i. before increasing again at 45 hr p.i (**Fig. 3.2D, G**). For the neutrophils this secondary wave of recruitment was expected to continue and peak at around Day 5 p.i. at a higher magnitude compared to the earlier wave of infiltration that peaks at 6 hr p.i., as has been reported previously (Wojtasiak et al., 2010b). On the contrary, mice receiving only scarification showed delayed infiltration of neutrophils and monocytes, peaking at 24 hr p.i. This further suggests that moisture in the scarified tissue favoured more rapid recruitment of inflammatory cells to tissue injury.

Thus, following HSV infection, we observed an early, transient wave of neutrophil and inflammatory monocyte infiltration into the scarified site that was presumably driven by inflammatory cues released by tissue damage.

3.2.2 Concurrent infiltration of neutrophils and monocytes into draining LN following dermal scarification.

In addition to the skin, we also examined the draining brachial LNs (bLN) and noted an influx of neutrophils and inflammatory monocytes into the LN (**Fig. 3.3A**). Both neutrophils and monocytes were recovered from LN in greater numbers at 6 hr p.i. compared to those enumerated in the corresponding skin samples (**Fig. 3.3B, E**). Also similar to the skin, both neutrophils and monocytes represented ~15-20% of total CD11b$^+$ myeloid cells in bLN (**Fig. 3.3C, F**). Saline-treated mice showed slightly fewer neutrophils and monocytes than HSV-infected mice, but this was not statistically significant.

While neutrophil numbers began to decline by 12 hr p.i., paralleling the skin, monocytes remained at a relatively high number in the bLN (**Fig. 3.3D, G**). Interestingly, non-draining axillary LN (aLN), which is situated downstream of bLN, showed an increase in neutrophil numbers at 24 hr p.i. It was not clear if this reflected egress of neutrophils from bLN into efferent lymphatics and their subsequent arrival at the downstream aLN, or drainage of inflammatory factors into aLN that induced the infiltration of neutrophils from blood.

Nonetheless, the simultaneous influx of neutrophils into the skin and LN suggested either an independent recruitment of the cells to both tissues concurrently, or a continuity where neutrophils first entered the skin, and from there migrated into the draining bLN.

To explore if there was a connection between neutrophils in the skin and LN, we performed immunofluorescence microscopy on bLN sections at 6 hr p.i., at the peak of neutrophil migration into LN. By staining for high endothelial venules (HEVs) and lymphatic vessels, we wished to determine the localisation of these cells in bLN. Neutrophils situated in the SCS could indicate entry from the

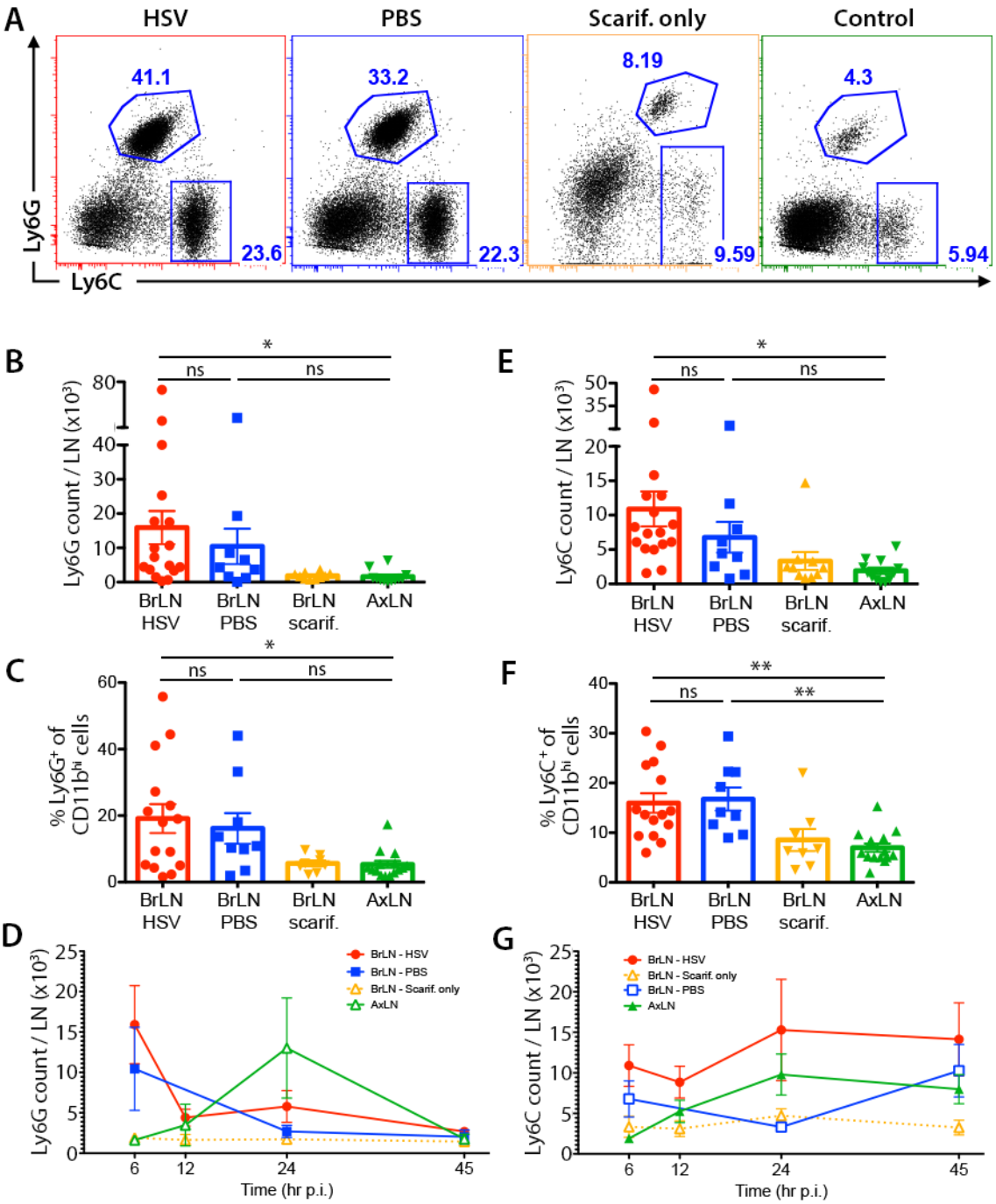

Figure 3.3 Kinetics of neutrophil and monocyte recruitment to the draining LN during early HSV-1 infection.

(A) Draining bLNs of skins corresponding to **Fig. 3.2** were harvested and analysed using flow cytometry. (A) shows representative dot plots of CD11b⁺ cells in bLN draining the skin treated with HSV-1 (red box), PBS (blue box), scarified only (orange box) or left untreated (green box). Also shown were gating strategies for neutrophils (Ly6G^{hi} Ly6C^{int}) and monocytes (Ly6C^{hi} Ly6G^{lo}).

(B, E) Total number of Ly6G^{hi} neutrophils (B) and Ly6C^{hi} monocytes (E) recovered from bLN at 6 hr post-scarification, as shown in (A).

(C, F) Proportion of Ly6G^{hi} neutrophil (C) and Ly6C^{hi} monocyte (F) population amongst CD11b⁺ cells at 6 hr post-scarification, as shown in (A).(D, G) Time course depicting total number of Ly6G^{hi} neutrophil (D) and Ly6C^{hi} monocyte (G) population from 6 hr to 45 hr post-scarification.

Data pooled from 2-5 independent experiments, n=8-15 mice per group. Error bars represent mean ± SEM. *p<0.05, **p<0.01, one-way ANOVA, Tukey's multiple comparisons. ns, not significant.

afferent lymphatics, possibly from the peripheral tissues. In contrast, neutrophils from the bloodstream would enter from HEVs.

We found that most neutrophils distributed to the medullary regions of bLN in both virus- and saline-treated mice, where lymphatic sinuses are abundant and many of which intertwined with HEVs in the medullary region (**Fig. 3.4A**). Many neutrophils were situated within the medullary lymphatic sinuses as well as around and within HEVs (**Fig. 3.4B**). Interestingly, neutrophil localisation occurred almost exclusively around medullary HEVs, rather than paracortical HEVs. Nonetheless, based on confocal microscopy data, we could not determine if the neutrophils entered the LN via HEVs or afferent lymphatics, although we also observed some neutrophils in the SCS. Very few neutrophils were found within T or B cell zones at the time point examined, which suggested that there were probably minimal interaction with T and B cells.

3.2.3 Minor contribution of HSV in neutrophil recruitment to the skin.

Our data indicated that both neutrophils and monocytes infiltrated the skin and LN in response to tissue damage cause by scarification. It was not clear if virus-induced inflammation also contributed to their recruitment, which might have been obfuscated by inflammation triggered by scarification. To investigate if viral-derived factors contribute to neutrophil and monocyte recruitment, we injected mice with either HSV-1 (10^6 pfu or 10^7 pfu) or saline intradermally and analysed the skin and dLN. Intradermal injection creates minimal tissue damage compared to scarification, while delivery of virus into the dermis prevents epidermal lesions due to the strict epidermal tropism of HSV.

We performed two independent experiments and found that at 6 hr p.i., although there were minor increases in neutrophil numbers in HSV-injected skins, they appeared to be statistically non-significant when compared to saline-injected skins (**Fig. 3.5A**). Interestingly, in the dLN there was no increase in neutrophil numbers (**Fig. 3.5B**).

Figure 3.4 Spatial distribution of neutrophil in draining LN during early HSV-1 infection.

C57BL/6 mice were scarified in the skin and treated with either HSV-1 or PBS. Draining bLNs were harvested at 6hr p.i. for immunofluorescence microscopy.

(A) Confocal images of bLN sections stained with anti-B220 (blue), anti-PNAd (green), anti-LYVE1 (red) delineating B cells, HEVs, and lymphatic vessels respectively. Localisation of neutrophils was visualised using anti-Ly6G (white).

(B) Close-up of medullary region of bLN from HSV-1 infected mouse (top) showing location of neutrophils (white) in both HEVs (green) and lymphatic sinuses (red).

Data representative of 2 independent experiments, n=4-6 mice per group.

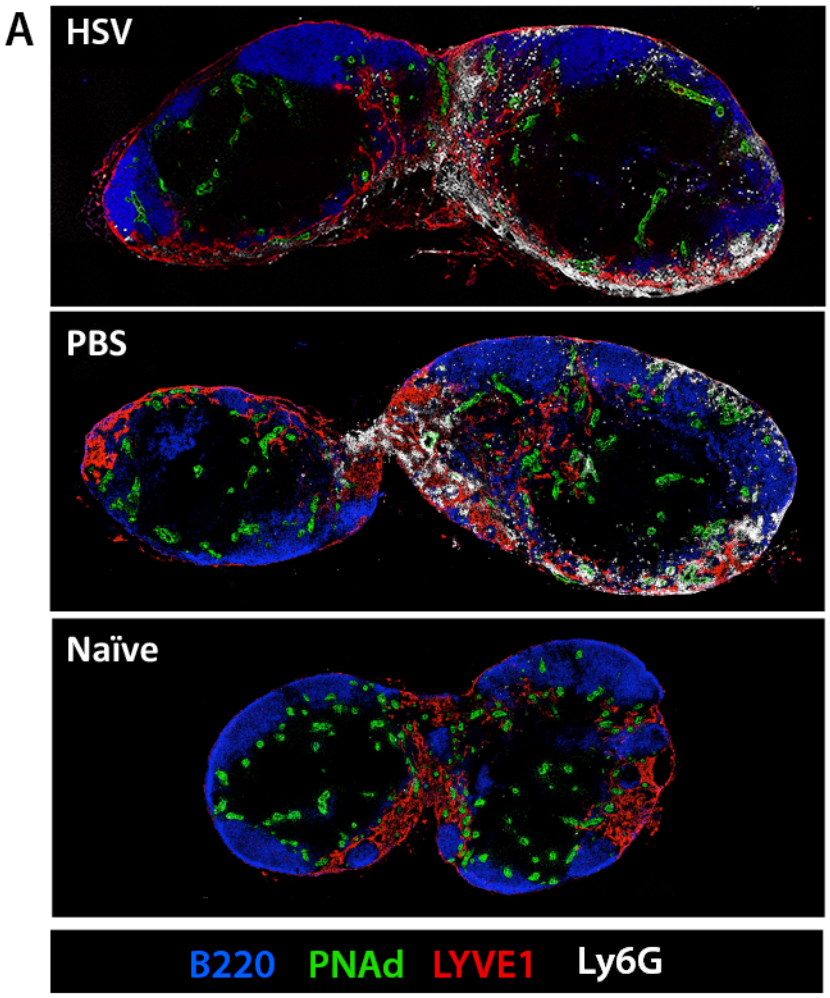
A
HSV
PBS
Naïve
B220 PNAd LYVE1 Ly6G

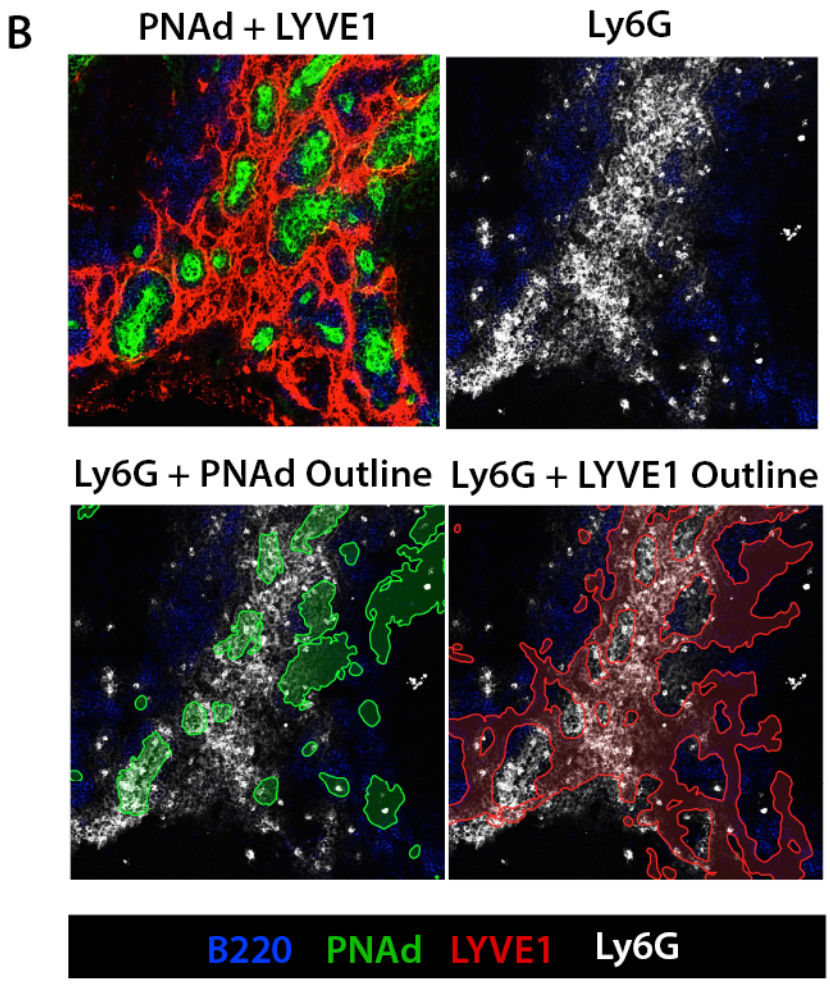
B
PNAd + LYVE1
Ly6G
Ly6G + PNAd Outline
Ly6G + LYVE1 Outline
B220 PNAd LYVE1 Ly6G

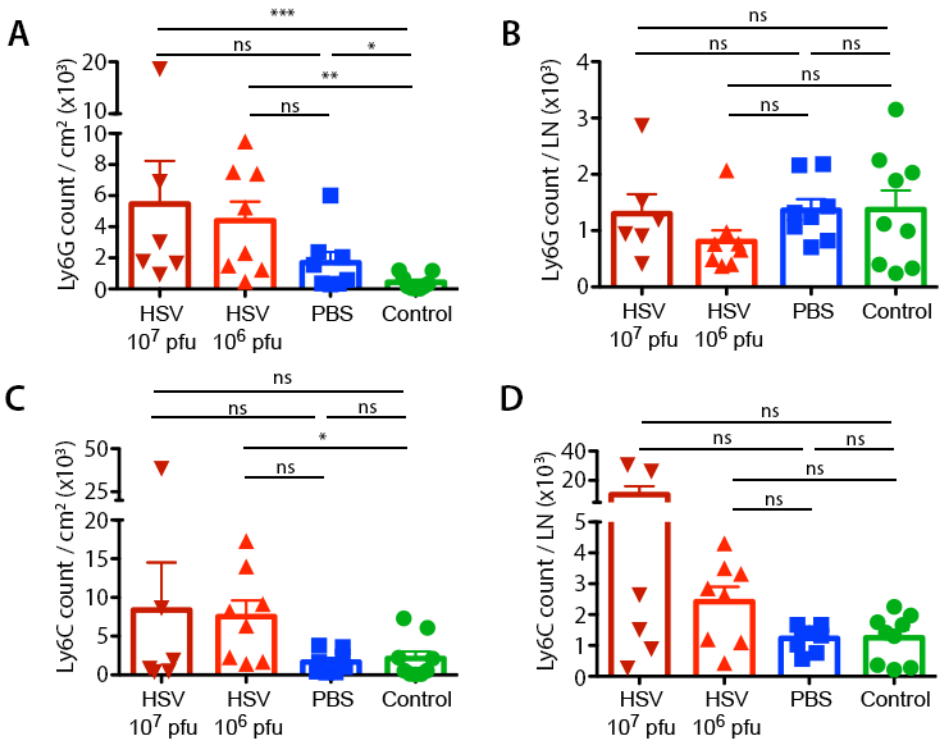

Figure 3.5 Minor contribution of viral-derived factors to neutrophil and monocyte infiltration to skin and LN.

C57BL/6 mice were intradermally injected with HSV-1 (10^7 pfu, dark red or 10^6 pfu, red) or PBS (blue). 1cm² skin containing the injection site as well as the draining bLN were excised at 6 hr p.i. for flow cytometry analysis.

(A, C) Total count of Ly6G^{hi} neutrophils (A) and Ly6C^{hi} monocytes (C) recovered from 1cm² skin at 6 hr p.i.

(B, D) Total count of Ly6G^{hi} neutrophils (B) and Ly6C^{hi} monocytes (D) recovered from draining bLN at 6 hr p.i.

Data pooled from 2 independent experiments, n=6-9 samples per group.

Error bars represent mean ± SEM. *p<0.05, **p<0.01, ***p<0.001, one-way ANOVA, Tukey's multiple comparisons on log transformed values. ns, not significant.

For Ly6C^{hi} monocytes, the changes in their number in the skin (**Fig. 3.5C**) and dLN (**Fig. 3.5D**) were less clear, with inconsistent changes observed between different groups. Overall, our data suggested that there might be slight increase in monocytes in the skin after intradermal HSV-1 injection but not in dLN.

In short, our data showed that while there might be a minor contribution of virus-induced inflammation to the recruitment of neutrophils and monocytes to the skin, unlike scarification, there was an absence of their infiltration into dLN. Since the only time point we examined was 6 hr p.i., it remains to be determined if some of these cells migrated to the dLN at a later time point.

As a control, we also compared the extent of neutrophil and monocyte infiltration into the skin and dLN with a bacterial pathogen. It is well documented that *S. aureus* infection of ear skin induces robust neutrophil recruitment to the injection site (Abtin et al., 2014). However, it was not clear if intradermal lodgement of the pathogen in the flank skin would also induce similar levels of cellular recruitment.

As with the preceding experiment, we enumerated neutrophil and monocyte recovered from flank skin 6 hr after intradermal injection with either 10^6 CFU or 10^7 CFU *S. aureus*. Despite large variability in absolute numbers, in two experiments we observed substantial increases in neutrophils in the skin regardless of infectious dose (**Fig. 3.6A**). There was, however, no difference in the increase of Ly6C^{hi} monocyte numbers in the skin (**Fig. 3.6C**). Unlike with HSV-1, *S. aureus* infection induced a substantial increase in neutrophil numbers in the dLN (**Fig. 3.6B**). Increased monocyte infiltration into dLN was also observed, but occurred to a lesser extent compared to neutrophils (**Fig. 3.6D**).

Together, our data showed that viral-derived factors only minimally stimulated recruitment of neutrophils, and to a lesser extent monocytes, to the skin in the absence of damage induced by scarification. There was also no corresponding increase in the total number of these cells in the dLN. In contrast, introduction of

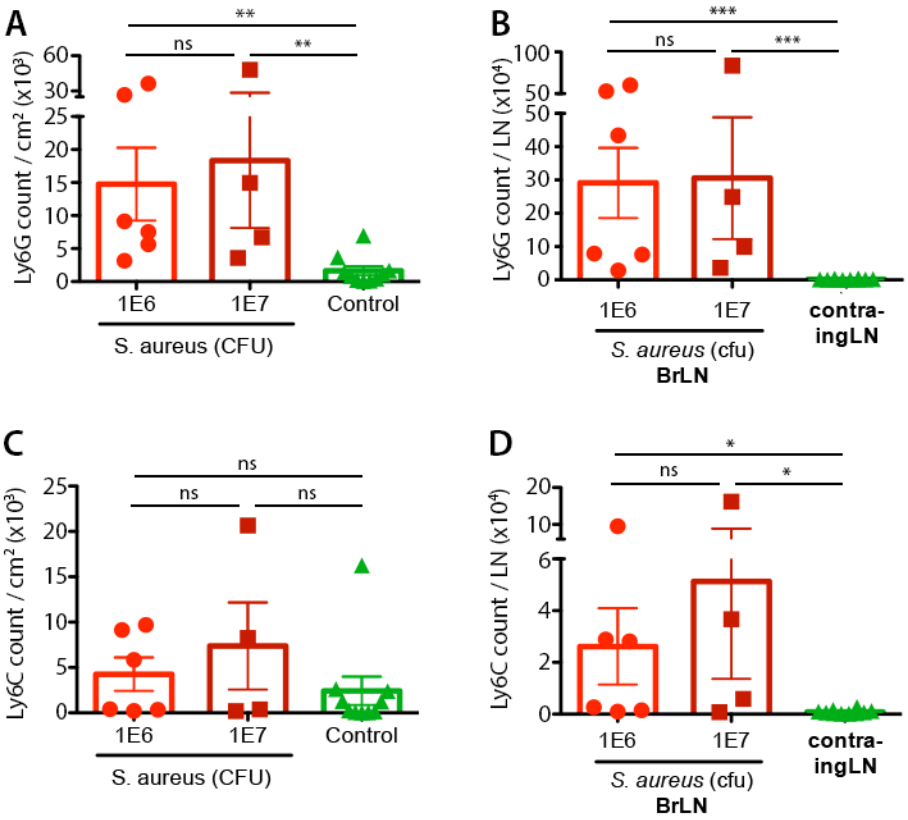

Figure 3.6 Neutrophil and monocyte infiltration to the skin after intradermal *S. aureus infection*.

C57BL/6 mice were intradermally injected with *S. aureus* (10^7 CFU, dark red or 10^6 CFU, red) or left untreated (green). 1cm² skin containing the injection site as well as the draining bLN were excised at 6 hr p.i. for flow cytometry analysis.

(A, C) Total count of Ly6G^{hi} neutrophils (A) and Ly6C^{hi} monocytes (C) recovered from 1cm² skin at 6 hr p.i.

(B, D) Total count of Ly6G^{hi} neutrophils (B) and Ly6C^{hi} monocytes (D) recovered from draining bLN at 6 hr p.i.

Data pooled from 2 independent experiments, n=4-10 samples per group.

Error bars represent mean ± SEM. *p<0.05, **p<0.01, ***p<0.001, one-way ANOVA, Tukey's multiple comparisons on log transformed values. ns, not significant.

S. aureus intradermally induced their recruitment to both the skin and dLN. To what extent both pathogens drained to the dLN from the skin remains to be determined. Nonetheless, our results implied that the early wave of robust neutrophil influx to the dLN observed after skin HSV infection might be predominantly caused by inflammation induced from scarification and/or that infection of epidermal cells during epicutaneous HSV infection contributed to the production of inflammatory stimuli in the LN.

3.2.4 Minimal migration of neutrophils from the skin to dLN after HSV infection.

Although the influx of neutrophils and monocytes into the dLN after epicutaneous HSV infection might be recruited independently of those infiltrating the skin, the localisation of neutrophils to the SCS and medullary sinuses of the dLN (**Section 3.2.2**) suggested that some could have migrated from the skin. We wanted to examine if this was the case and if infiltrating cells could potentially serve as carriers of antigen to the dLN.

To track their migration from the skin, we painted the infection site with the red fluorescent dye TRITC at ~6 hr p.i., during the peak recruitment of neutrophils and monocytes to the skin (**Section 3.2.1**), and analysed the dLN at 13 hr p.i. after allowing sufficient time for migration (**Fig 3.7A**). As bacterial infections can induce neutrophil migration to the dLN from the ear skin injected with killed *S. aureus* bioparticles (Hampton et al., 2015), we also examined intradermal *S. aureus* infection of the flank skin for comparison purposes.

Only very low numbers of TRITC$^+$ cells were recovered in the draining bLN (less than 100 cells on average) after epicutaneous HSV or saline treatment, and these cells were mostly comprised of migratory dermal DC (dDC) (~60%) as identified by their CD11c$^+$ MHC-II^{hi} expression (**Fig. 3.7B, E, G**). Conversely, CD11c$^+$ MHC-II^{int} LN-resident DC were not TRITC$^+$ (**Fig. 3.7F**). This ruled out the possibility of dye capture by APC in the LN via lymphatic drainage.

Figure 3.7 Tracking neutrophil and monocyte migration from infected skin to draining LN.
(A) Schematic showing the procedure for tracking neutrophils migrated from skin in bLN using flow cytometry. C57BL/6 mice were scarified and treated with either 10^6 pfu HSV-1 or PBS, or i.d. injection with 10^6 CFU *S. aureus*. Mice were painted with fluorescent dye TRITC and re-bandaged at 6.5 hr post-scarification prior to sacrifice at 13 hr post-scarification.
(B) Contour plots showing gating strategy for TRITC$^+$ cells in draining bLN. TRITC$^+$ population was further gated on CD11c$^+$ MHC-II^{hi} migratory dDC (red), CD11c$^+$ MHC-II^{int} LN-resident DC (black), Ly6C^{hi} monocytes (blue), and Ly6G^{hi} neutrophils (green).
(C-F) Total count of the TRITC$^+$ Ly6G^{hi} neutrophils (C), Ly6C^{hi} monocytes (D), CD11c$^+$ MHC-II^{hi} migratory dDC (E), and CD11c$^+$ MHC-II^{int} LN-resident DC (F) in bLN as gated in (B) under various conditions.
(G) Proportion of TRITC$^+$ Ly6G^{hi} neutrophils (green), Ly6C^{hi} monocytes (blue), and or CD11c$^+$ MHC-II^{hi} migratory dDC (red) amongst all TRITC$^+$ cells in bLN of either HSV-1-, *S. aureus*- or PBS-treated mice at 13 hr p.i.
(H) Proportion of TRITC$^+$ cells of total Ly6G^{hi} neutrophils per bLN of either HSV-1- (red), S. aureus- (yellow) or PBS-treated mice (blue) at 13 hr p.i.
Data pooled from 2 independent experiments, n=4-10 LN per group. Error bars represent mean ± SEM.
(I) KAEDE mice were scarified and treated with 10^6 pfu HSV-1 or PBS prior to photoconversion at 6 hr p.i., and sacrificed at 12 hr p.i. for flow cytometry analysis of draining bLN. Each data point represents number of photoconverted (KAEDE red) CD11c$^+$ MHC-II^{hi} migratory dDC (red), CD11c$^+$ MHC-II^{int} LN-resident DC (black), Ly6C^{hi} monocytes (blue), and Ly6G^{hi} neutrophils (green) from pooled bLNs.
Data from 1 experiment, n=2 LN per group. Error bars represent mean ± SEM.

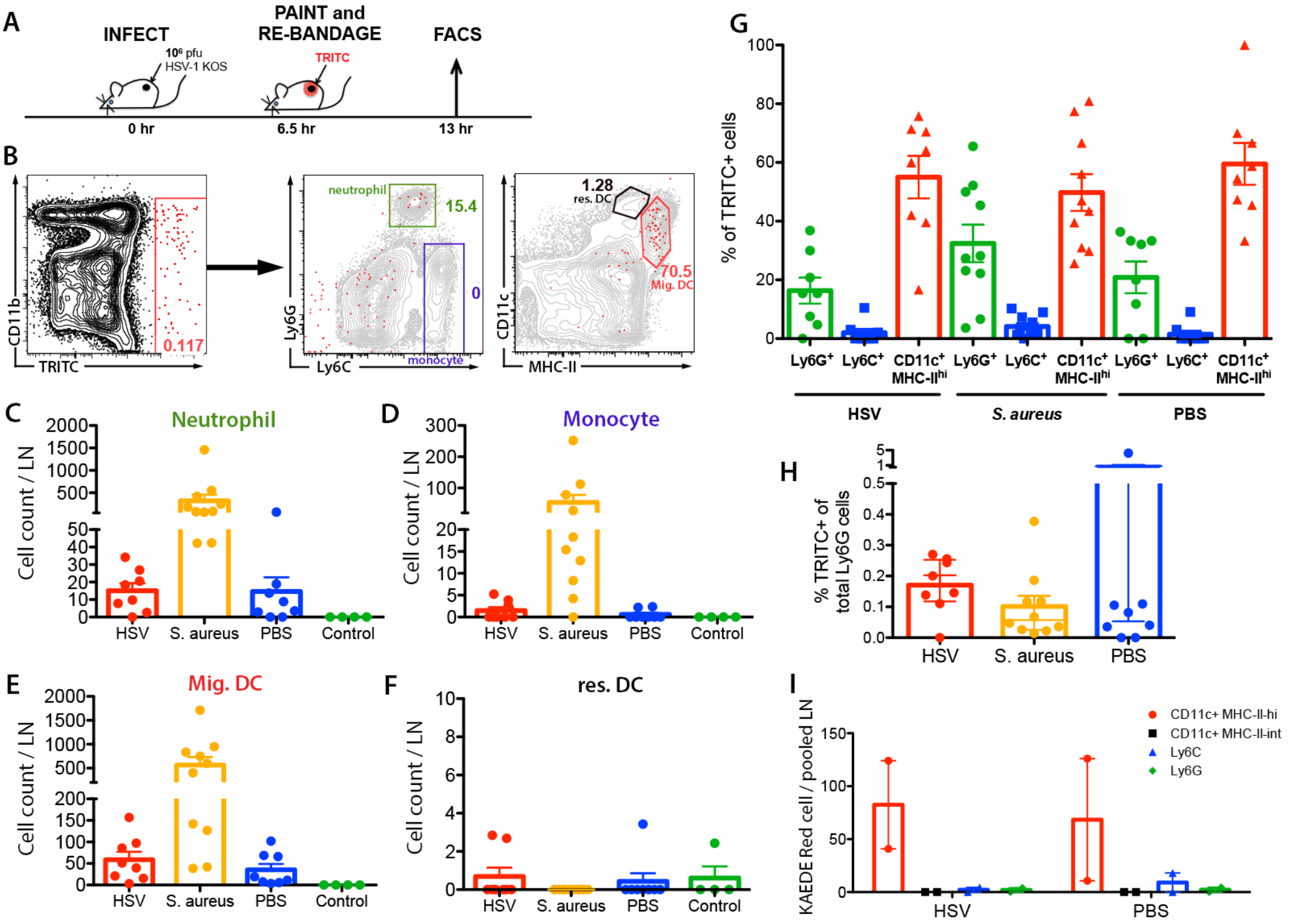
A
INFECT
10⁶ pfu
HSV-1 KOS
PAINT and
RE-BANDAGE
TRITC
FACS
0 hr
6.5 hr
13 hr
B
CD11b
TRITC
0.117
neutrophil
15.4
Ly6G
Ly6C
monocyte
0
CD11c
MHC-II
1.28
res. DC
70.5
Mig. DC
G
% of TRITC+ cells
Ly6G+
Ly6C+
CD11c+ MHC-IIhi
HSV
S. aureus
PBS
C
Neutrophil
Cell count / LN
HSV
S. aureus
PBS
Control
D
Monocyte
E
Mig. DC
F
res. DC
H
% TRITC+ of total Ly6G cells
I
KAEDE Red cell / pooled LN
CD11c+ MHC-II-hi
CD11c+ MHC-II-int
Ly6C
Ly6G

We detected only a very low level of TRITC$^+$ Ly6G^{hi} neutrophils (averaged less than 20 neutrophils per LN) after HSV infection, which was equivalent to the saline-treated group (**Fig. 3.7C**). These migrant neutrophils contributed to ~20% of the total TRITC$^+$ cells (**Fig. 3.7G**). Surprisingly, there was a near absence of Ly6C^{hi} monocytes migrating to dLN (**Fig. 3.7D**), in contrast to studies suggesting antigen transport by monocytes from peripheral tissues to the LN following intranasal administration of OVA or anthrax spores (Jakubzick et al., 2013).

Injection of 10^6 CFU *S. aureus* induced a higher number of migrating neutrophils, monocytes and dDC to the dLN, amounting to ~250 neutrophils, ~100 monocytes and ~500 migratory dDC per LN (**Fig. 3.7C, D, E**). Interestingly, the proportions of TRITC$^+$ neutrophils and dDC amongst total TRITC$^+$ cells were similar to those of HSV and saline-treated groups (**Fig. 3.7G**), indicating that different infections induced a similar proportion but different magnitude of cell migration from skin to dLN. It should also be noted that TRITC$^+$ neutrophils represented only ~0.1% of total neutrophils in the draining bLN under all conditions tested (**Fig. 3.7H**). This demonstrated that the majority of dLN-infiltrating neutrophils arrived from the blood. Thus, our results suggest that only very low numbers of neutrophils migrate to dLN early during viral and bacterial infection.

To determine if TRITC dye painting was adequately sensitive for detection of migratory cells, we repeated the experiment using transgenic mice expressing photoconvertible KAEDE proteins. We detected a lower amount of photoconverted migratory dDC in the dLN than mice painted with TRITC dye, and failed to detect the presence of migrant neutrophils in these mice (**Fig. 3.7I**). Due to a very small sample size, further experiments should be conducted to validate the data presented here.

It should be noted that despite robust neutrophil recruitment to the skin following intradermal injection of GFP-expressing *S. aureus*, we detected only ~15-20% of GFP$^+$ neutrophils at 6.5 hr p.i. in the skin, indicating that the

majority of recruited neutrophils remained uninfected, or did not phagocytose the bacteria (**Fig. 3.8A, B**). Similarly, in the dLN, we detected only very low numbers of GFP$^+$ cells at 6.5 hr and 13 hr p.i. (**Fig. 3.8C, D, E**) However, almost none of the S*. aureus*-containing GFP$^+$ cells were TRITC$^+$. Instead, they appeared to be TRITC$^-$ Ly6G^{hi} neutrophils (**Fig. 3.8D, F**), suggesting that these neutrophils might have entered the LN from bloodstream and subsequently ingested bacteria drained to the LN.

Taken together, we demonstrated minimal level of neutrophil migration from the skin to dLN after cutaneous HSV-1 infection. When compared to a skin bacterial infection model, we also failed to observe their skin-to-LN migration. These observations suggested that neutrophils likely do not function as antigen carrier during flank skin infection.

3.2.5 Neutrophils are dispensable for CD4$^+$ and CD8$^+$ T cell priming and expansion during cutaneous HSV-1 infection.

Neutrophils migrating from the skin to LN have been implicated in modulating T cell expansion during skin *S. aureus* infection (Hampton et al., 2015). To investigate whether neutrophils play vital roles in T cell priming and proliferation, we co-transferred CellTrace Violet-labelled HSV-specific CD4$^+$ gDT-II and CD8$^+$ gBT-I T cells into recipient mice, then depleted neutrophils from the mice with anti-Ly6G antibodies at Days -1, 1 and 2 p.i. (**Fig. 3.9A**) Following epicutaneous HSV-1 infection, draining bLNs were examined at 72 hr p.i. to assess expression of activation markers as well as cell division as measured by CellTrace Violet dilution.

To determine depletion efficiency, we co-stained bLN cells with antibodies against Ly6C and Gr-1 to detect neutrophils and found almost complete ablation in the treated group (**Fig. 3.9B, C**). However, both CD4$^+$ and CD8$^+$ T cell expansions as well as the extent of divisions were largely comparable between treated and untreated groups, suggesting that neutrophils did not markedly affect T cell expansion (**Fig. 3.9D-I**). Furthermore, expressions of cell surface markers associated with T cell activation: CD69, CD62L and CD44 were similar in

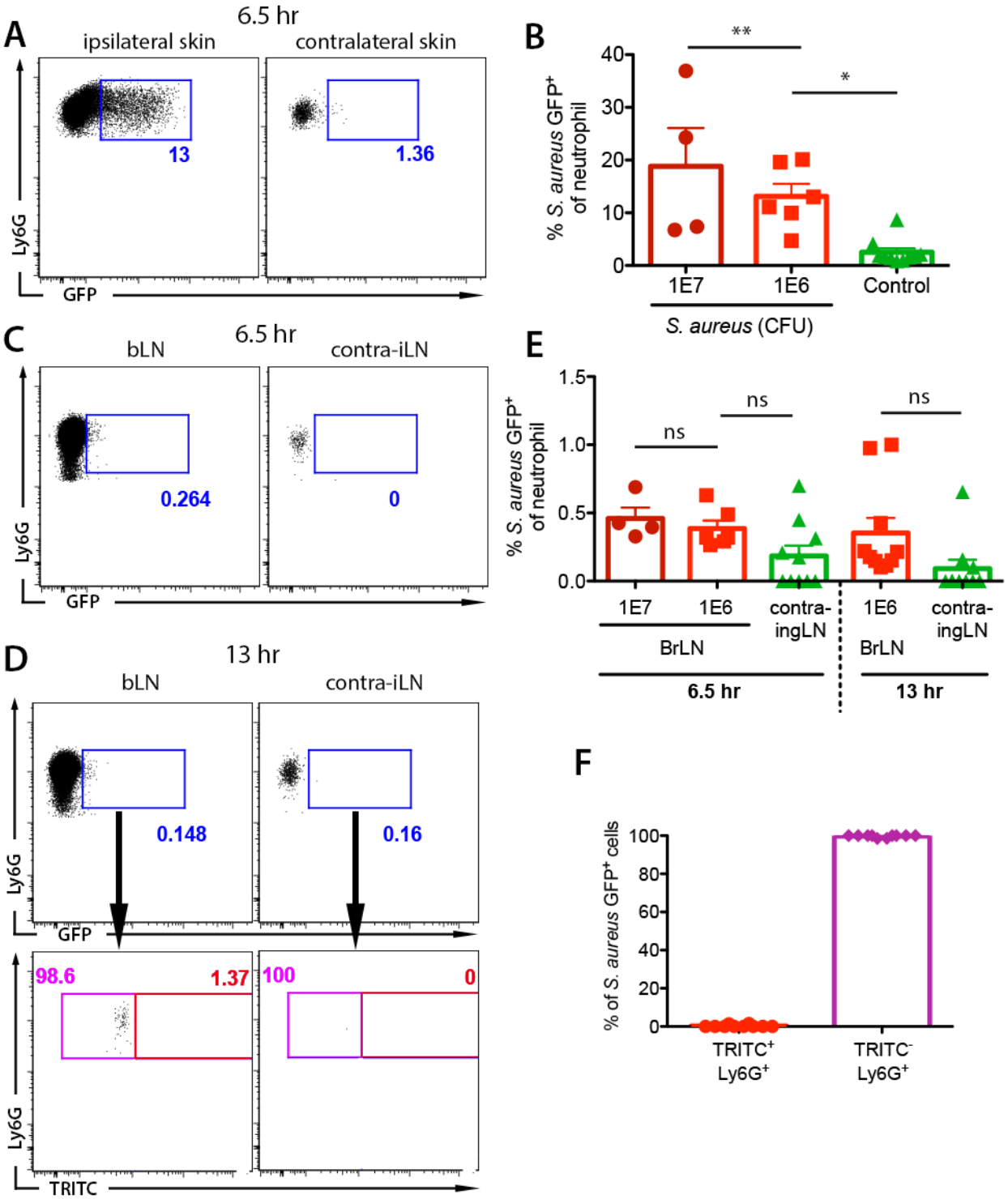

Figure 3.8 Minimal migration of *S. aureus*-containing neutrophils into draining LN.
C57BL/6 mice were intradermally injected with GFP-expressing *S. aureus* (10^7 CFU, dark red or 10^6 CFU, red). 1cm² skin containing the injection site as well as the draining bLN were excised at 6.5 hr p.i. for flow cytometry analysis. Some mice were painted with TRITC at 6.5 hr p.i. and draining bLN harvested at 13 hr p.i. for analysis.
(A) Representative dot plots showing gating of GFP⁺ Ly6G^{hi} neutrophils in the skin (infected, left; control; right) at 6.5 hr p.i.
(B) Proportion of *S. aureus* GFP⁺ cells of all neutrophils per cm² skin at 6.5 hr p.i.
(C, D) Representative dot plots showing gating of GFP⁺ Ly6G^{hi} neutrophils in the LN (draining bLN, left; non-draining iLN, right) at 6.5 hr (C) and 13 hr p.i. (D). Bottom panels of (D) show further separation of GFP⁺ Ly6G^{hi} cells into TRITC⁺ (red) and TRITC⁻ (magenta).
(E) Proportion of *S. aureus* GFP⁺ cells of all neutrophils per LN at 6.5 hr and 13 hr p.i.
(F) Proportion of TRITC⁺ or TRITC⁻ GFP⁺ Ly6G^{hi} neutrophils per LN at 13 hr p.i.
Data pooled from 2 independent experiments, n=4-13 LN per group. Error bars represent mean ± SEM. *p<0.05, **p<0.01, one-way ANOVA, Tukey's multiple comparisons. ns, not significant.

Figure 3.9 Neutrophil depletion does not affect HSV-specific $CD4^+$ and $CD8^+$ T cell expansion.

(A) Schematic showing the strategy for neutrophil depletion. $5.0x10^5$ CellTrace Violet-labelled $CD4^+$ gDT-II and $CD8^+$ gBT-I cells each were adoptively transferred into C57BL/6 mice 2 days before epicutaneous infection with 10^6 pfu HSV-1. 500µg of 1A8 (anti-Ly6G) depleting antibodies were injected i.p. into mice from the depleted group 1 day before, and 1 and 2 days after infection. Mice were sacrificed at Day 3 p.i. for flow cytometry analysis.

(B) Representative dot plots showing neutrophil depletion efficiency as indicated by co-staining for Ly6C and Gr-1.

(C) Total number of neutrophils recovered in draining bLN in both non-depleted and anti-Ly6G depleted groups based on gating shown in (B).

(D, E) Total count of $CD4^+$ gDT-II (D) and $CD8^+$ gBT-I (E) T cells recovered from bLN in non-depleted (open bars) and anti-Ly6G depleted (filled bars) groups.

(F, G) Total number of divided (CellTrace $Violet_{lo}$) $CD4^+$ gDT-II (F) and $CD8^+$ gBT-I (G) T cells recovered from bLN in non-depleted (open bars) and anti-Ly6G depleted (filled bars) groups.

(H, I) Proportion of divided (CellTrace $Violet_{lo}$) $CD4^+$ gDT-II (H) and $CD8^+$ gBT-I (I) T cells in non-depleted (open bars) and anti-Ly6G depleted (filled bars) groups.

Data pooled from 3 independent experiments, n=14-15 mice per group. Error bars represent mean ± SEM. **$p<0.01$, unpaired Student t test. ns, not significant.

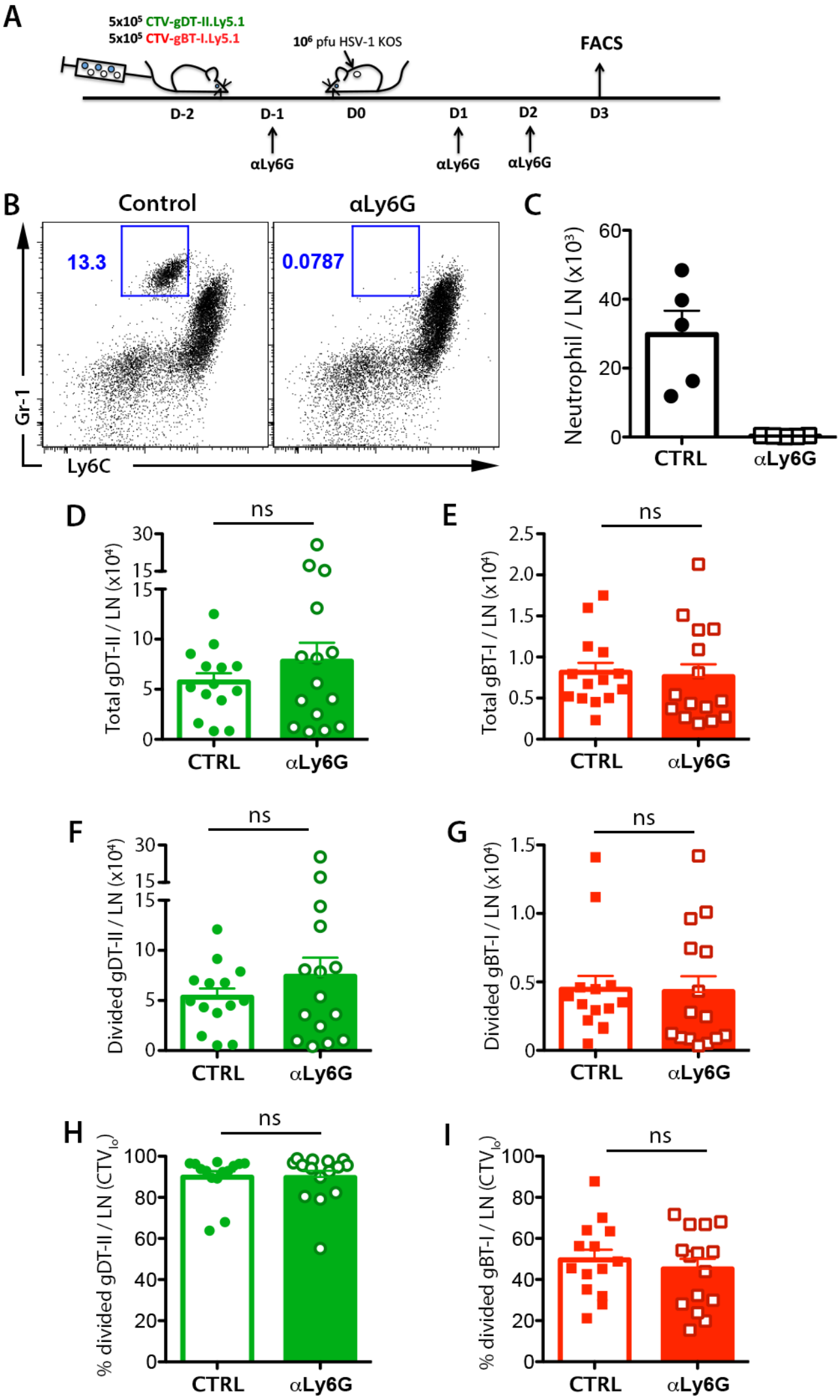
A
5x10⁵ CTV-gDT-II.Ly5.1
5x10⁵ CTV-gBT-I.Ly5.1
10⁶ pfu HSV-1 KOS
FACS
D-2
D-1
D0
D1
D2
D3
αLy6G
αLy6G
αLy6G
B
Control
αLy6G
13.3
0.0787
Gr-1
Ly6C
C
Neutrophil / LN (x10³)
CTRL
αLy6G
D
Total gDT-II / LN (x10⁴)
ns
CTRL
αLy6G
E
Total gBT-I / LN (x10⁴)
ns
CTRL
αLy6G
F
Divided gDT-II / LN (x10⁴)
ns
CTRL
αLy6G
G
Divided gBT-I / LN (x10⁴)
ns
CTRL
αLy6G
H
% divided gDT-II / LN (CTV$_{lo}$)
ns
CTRL
αLy6G
I
% divided gBT-I / LN (CTV$_{lo}$)
ns
CTRL
αLy6G

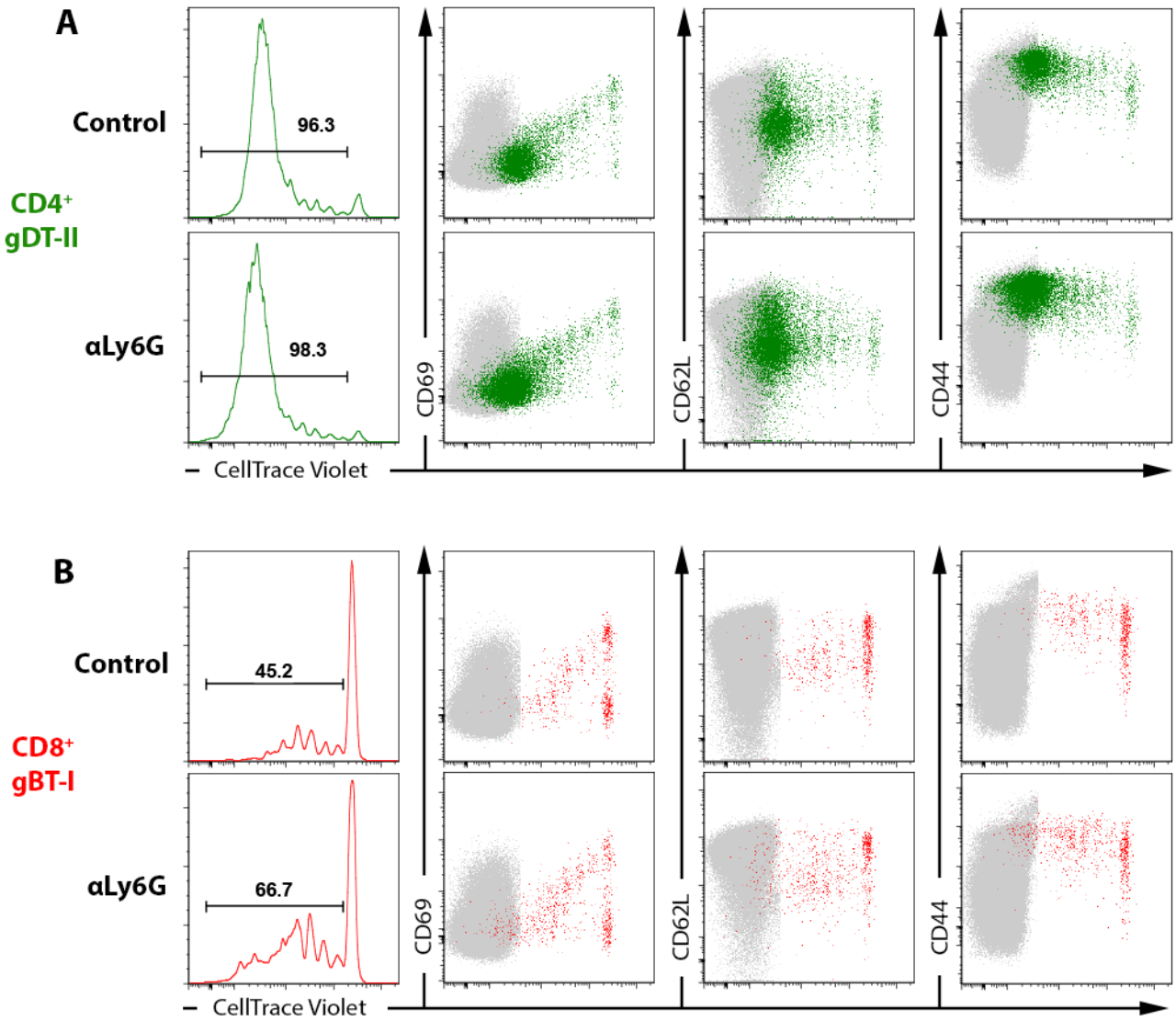

Figure 3.10 Expression of activation markers in HSV-specific CD4⁺ and CD8⁺ T cells after neutrophil depletion.

(A, B) Representative dot plots depicting the division and expression of activation markers CD69, CD62L and CD44 in CD4⁺ gDT-II (A) and CD8⁺ gBT-I (B) T cells between non-depleted (top row) and anti-Ly6G depleted (bottom row) groups at Day 3 p.i. corresponding to **Fig. 3.9**. Data representative of 2 independent experiments.

both groups (**Fig. 3.10A, B**). Together, these results support the view that neutrophils are dispensable for T cell priming and early proliferation after skin HSV-1 infection.

3.2.6 Neutrophils do not contribute to effector CD4⁺ and CD8⁺ T cell homing to the skin after HSV-1 infection.

Neutrophils have also been found to influence CD8⁺ T cell migration into influenza-infected lungs via deposition of CXCL12 chemokine trails from blood vessels to the infected region (Lim et al., 2015). We wanted to investigate if neutrophils are also crucial for the homing of effector T cells into skin during HSV-1 infection. To compare effector cell numbers in the skin, we co-transferred $5x10^4$ congenically-marked HSV-specific CD4⁺ gDT-II and CD8⁺ gBT-I T cells into recipient mice before infection, depleted neutrophils at Days 1, 3 and 5 p.i. with anti-Ly6G antibodies, and analysed the infected skin at D6 p.i. (**Fig. 3.11A**). While we noticed a more than 10-fold decrease in neutrophils in the skin of depleted mice, an increase in Ly6C⁺Gr-1⁺ cells in treated mice prevented reliable gating of neutrophils in the skin (**Fig. 3.11B, C**).

Enumerating CD4⁺ gDT-II and CD8⁺ gBT-I T cells in the skin 6 days after infection, from four independent experiments, we noted almost equivalent numbers in both depleted and undepleted groups (**Fig. 3.11D, E**). Similarly, there was no difference in T cell numbers after neutrophil depletion when examined a day later on day 7 post-infection (**Fig. 3.11F, G**). Examining the lymphoid tissues, the numbers of CD4⁺ gDT-II and CD8⁺ gBT-I cells in both draining bLN (**Fig. 3.11H, I**) and the spleen (**Fig. 3.11J, K**) were also very similar between both groups at D6 p.i., indicating that HSV-specific T cell expansion was unaffected by the ablation of neutrophils.

Together, our results suggested that neutrophils do not contribute to effector CD4⁺ and CD8⁺ T cell recruitment to the skin after HSV infection.

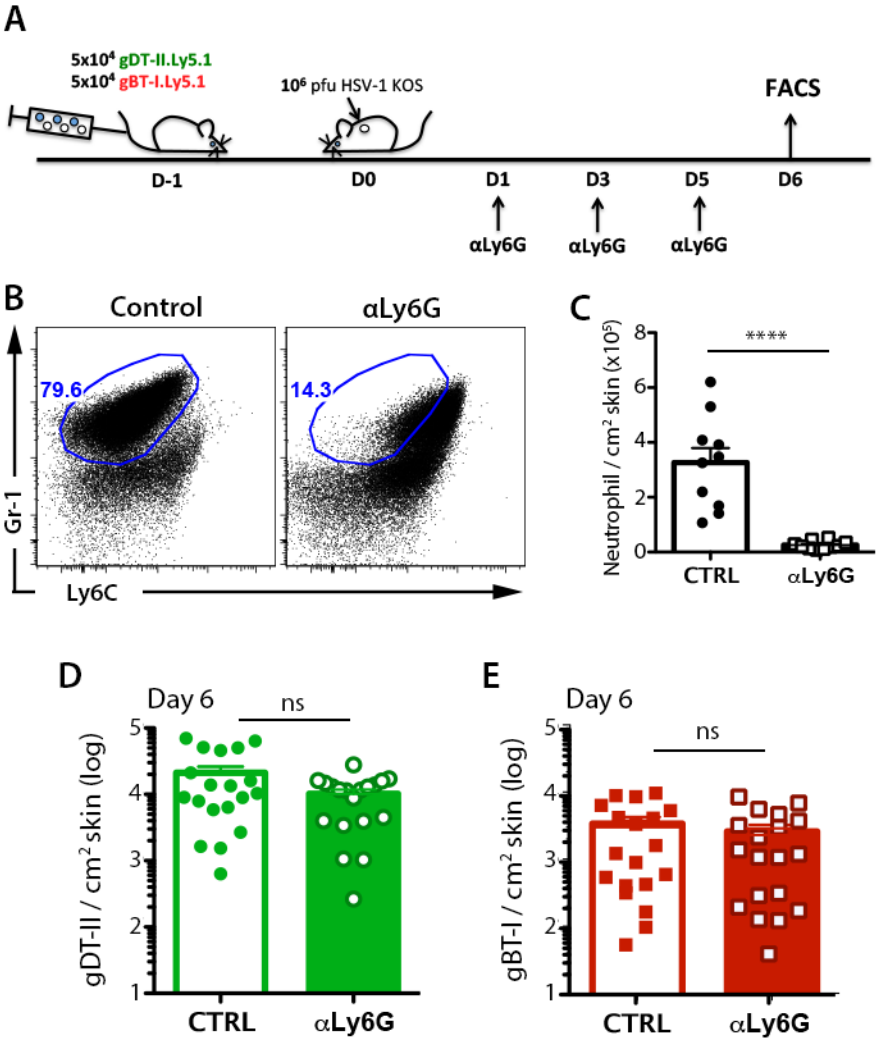

Figure 3.11 Neutrophil depletion does not affect HSV-specific CD4⁺ and CD8⁺ T cell migration to the effector site.

(A) Schematic showing neutrophil depletion strategy. 5x10⁴ CD4⁺ gDT-II and CD8⁺ gBT-I T cells each were adoptively transferred into C57BL/6 mice prior to epicutaneous HSV-1 infection. Mice received 3 doses of 500µg 1A8 (anti-Ly6G) depleting antibodies i.p. at Days 1, 3 and 5 p.i. and were sacrificed at Day 6 or Day 7 p.i. 1.5cm² skins containing the herpes lesion were excised and analysed via flow cytometry. Draining bLN and spleens were also harvested for analysis.

(B) Representative dot plots showing neutrophil depletion efficiency in the skin as indicated by co-staining for Ly6C and Gr-1.

(C) Number of neutrophils in 1cm² skin of both non-depleted and anti-Ly6G depleted groups based on gating shown in (B).

(D-E) Total count of CD4⁺ gDT-II (D) and CD8⁺ gBT-I (E) T cells per cm² of excised Day 6 skin in non-depleted (open bars) and anti-Ly6G depleted (filled bars) groups. Data pooled from 4 independent experiments, n=18-19 mice per group.

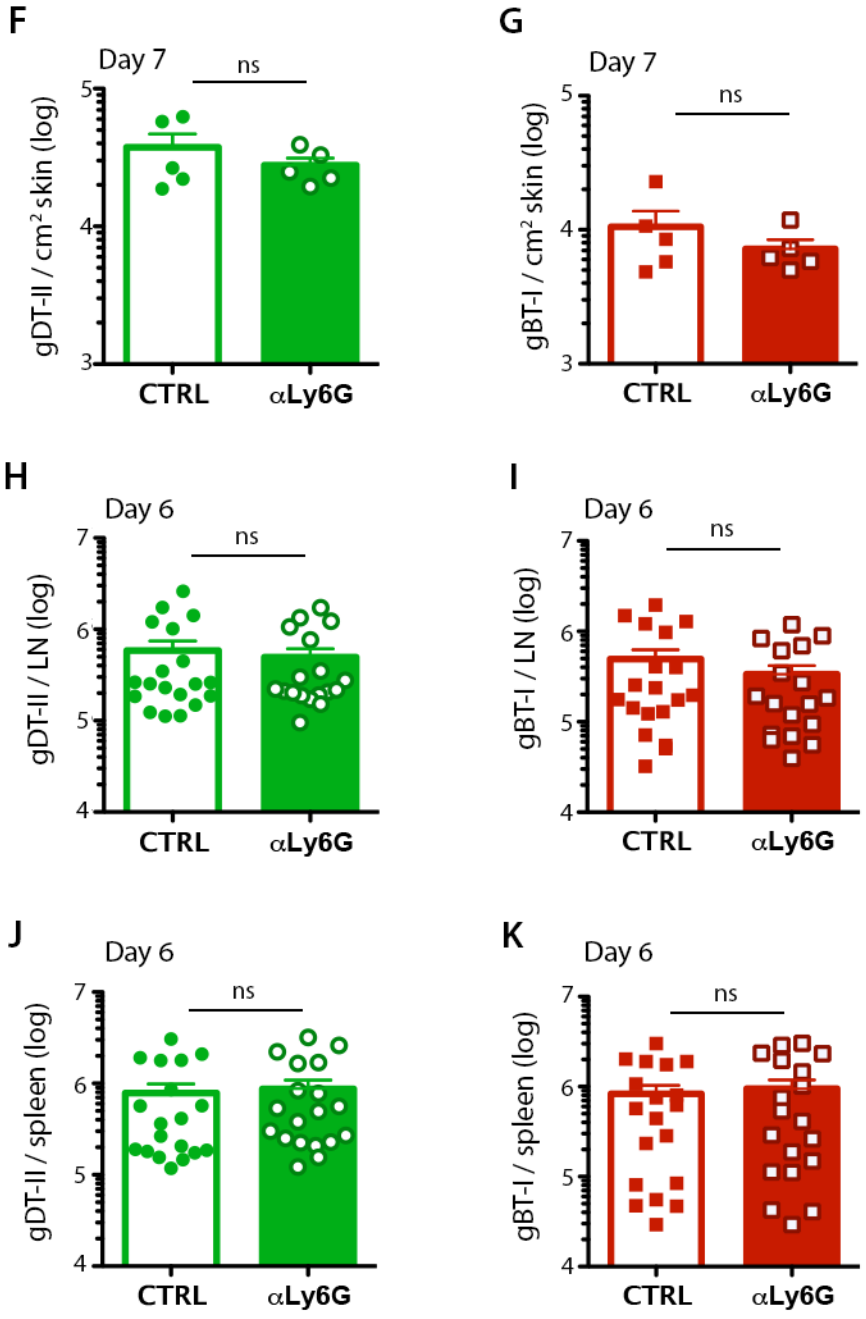

(F, G) Total count of CD4⁺ gDT-II (F) and CD8⁺ gBT-I (G) T cells per cm² of excised Day 7 p.i. skin in non-depleted (open bars) and anti-Ly6G depleted (filled bars) groups.
Data from 1 experiment, n=5 mice per group.
(H, I) Total count of CD4⁺ gDT-II (H) and CD8⁺ gBT-I (I) T cells recovered from Day 6 p.i. bLN in non-depleted (open bars) and anti-Ly6G depleted (filled bars) groups.
(J, K) Total count of CD4⁺ gDT-II (J) and CD8⁺ gBT-I (K) T cells recovered from Day 6 p.i. spleen in non-depleted (open bars) and anti-Ly6G depleted (filled bars) groups.
(H-K) Data pooled from 4 independent experiments, n=18-19 mice per group.
Error bars represent mean ± SEM. ****p<0.001, unpaired Student t test. ns, not significant.

3.3 DISCUSSION

Data presented here describe a previously unidentified early, transient accumulation of neutrophil in the skin of HSV-1 infected mice that preceded a more robust, secondary wave of neutrophil influx later during infection (Wojtasiak et al., 2010b). The entry of neutrophils into both the skin and dLN was accompanied by Ly6C^{hi} monocytes, and agrees with a recent study that identified a transient, concomitant infiltration of both neutrophils and monocytes into skin wounds (Rodero et al., 2014).

It is well established that early innate immune responses are triggered by the activation of pathogen recognition receptors (PRRs) through detection of PAMPs in the case of microbial entry, or DAMPs during sterile injury by tissue macrophages and mast cells, which leads to extravasation of neutrophils from the blood into the site of inflammation. HSV glycoproteins and its viral genomic DNA have been reported to activate TLR2, also the receptor for bacterial cell wall and glycolipids, and TLR9 respectively (Leoni et al., 2012; Sørensen et al., 2008; Sato et al., 2006). Similarly, damaged epidermal cells release DAMPs such as mitochondrial DNA that can induce neutrophil recruitment (Zhang et al., 2010).

Although we showed that immune sensing of viral-derived factors could contribute to early influx of neutrophils, as evident after intradermal HSV-1 injection, it was likely that sensing of tissue damage was the predominant cause of neutrophil recruitment to the skin and draining LN after HSV-1 infection following scarification, as there was no difference in the level of neutrophil recruitment between HSV- and saline-treated mice.

Interestingly, we found that neutrophil and monocyte infiltration into the skin was delayed following scarification without saline and bandaging. This observation is similar to a study demonstrating LTβ4-dependent neutrophil recruitment in tape-stripped skin (Oyoshi et al., 2012), but another study employing skin biopsy punch reported rapid infiltration of neutrophils to the damaged tissue (Kim et al., 2008). This suggests that light abrasion of the skin is

insufficient to induce robust neutrophil recruitment unless accompanied by additional signals. Our results agree with the current view on wound treatment that a moist environment promotes autolytic debridement, which relies on neutrophils and macrophages cleaning up necrotic cells (Ramundo, 2012). In short, moist wounds prevent desiccation of tissue macrophages that are crucial in the production of inflammatory cytokines and chemoattractants responsible for recruiting neutrophils to the inflamed sites, as well as growth factors for tissue healing.

Neutrophils entering infected tissues also present ample opportunity for interactions with pathogens and infected cells. Studies have shown that neutrophils can modulate $CD8^+$ T cell responses during lung influenza virus infection (Tate et al., 2012), and that infected neutrophils may present antigen to effector $CD8^+$ T cells in the lung (Hufford et al., 2012). Additonally, neutrophils have also been reported to act as antigen carriers after intradermal BCG and MVA infections to the draining LN and bone marrow, respectively (Abadie et al., 2005; Duffy et al., 2012). Our data using intravital microscopy suggested that neutrophils accumulated in dermis just underneath the infected epidermal layer, indicating possible interactions with virus-infected keratinocytes. However, by tracking neutrophil migration from the skin, we found that only very small numbers of neutrophils migrated to draining LN. Although we labelled the skin at the peak of neutrophil recruitment to mark the infiltrating neutrophils, it was possible that we did not capture the optimal window that represented maximal migration.

Hampton et al. (2015), using transgenic mice expressing photoconvertible KAEDE proteins, showed that during intradermal *S. aureus* injection in ear skin, at 8 hr p.i. up to 4% of neutrophils in the draining LN migrated from the injected skin. To directly compare with HSV-1 infection, we also infected mice intradermally in the flank skin with *S. aureus* but observed a much lower number of migrated neutrophils (~0.1% of all neutrophils in LN). Although we found ~15% of *S. aureus*$^+$ neutrophils in the skin at 6.5 hr p.i., only very few *S. aureus*$^+$ cells were found in the dLN at either 6.5 hr or 13 hr p.i. Our observation is thus

different from those reported by Hampton et al. (2015) where up to 20% of *S. aureus*$^{+}$ neutrophils were detected in both the skin and dLN.

Although the discrepancies might be attributable to the time point selected (we chose 13 hr p.i. to match our HSV-1 experiments), a number of factors could have contributed to the difference in our observations. First, instead of utilising heat-killed *S. aureus* bioparticles, we administered live bacteria. *S. aureus* employs a variety of immune evasion strategies that confer resistance to phagocytosis and killing by neutrophils, and secrete a whole host of cytolytic toxins that kill leukocytes and innate immune cells (Spaan et al., 2013; Thammavongsa et al., 2015). For example, Staphylococcal complement inhibitor (SCIN) interferes with complement activation through inhibition of C3 convertase, a key component that facilitates neutrophil-mediated phagocytosis of *S. aureus* (Jongerius et al., 2007). Similarly, all strains of *S. aureus* can produce a number of leukocidins, which are cytolytic toxins that could directly lyse innate immune cells, including neutrophils (Thammavongsa et al., 2015). Thus, we speculate that live bacteria could resist phagocytosis and even interfere with neutrophil functions to a better extent than killed bacterial bioparticles.

Additionally, differences in the sites of bacterial injection (ear pinna vs. flank skin) might also influence leukocyte recruitment and migration. We noted far fewer neutrophils infiltrating the flank skin as compared to data published by other groups employing ear skin model (Abtin et al., 2014). A study found Langerhans cell dependence for CTL priming during epicutaneous immunisation with ovalbumin in the flank but not in the ear, implicating the presence of distinct conditions between anatomical sites of the skin (Wang et al., 2008). These differences have been attributed to the much thinner dermis of the ear skin (Romani et al., 2010). Interestingly, studies examining administration of DNA vaccine found that intradermal delivery of vaccine into ear pinna provided superior gene transfection and elicited stronger cell-mediated response compared to administration into abdominal skin (Forg et al., 1998; Vandermeulen et al., 2015).

Additionally, a recent study found significantly higher number of mast cells in the ear skin compared to back skin (Tong et al., 2015), which could sense peptidoglycan from *S. aureus* via TLR2 (Supajatura et al., 2002). Mast cell activation could also induce and enhance neutrophil recruitment (Galli et al., 2011; Abraham & St. John et al., 2010), and thus could result in pronounced neutrophil infiltration to ear skin after tissue damage and infection.

Furthermore, while Abadie et al. (2005) observed neutrophil migration to draining LN following inoculation of ear pinna with *M. bovis* BCG, another study utilising the same pathogen to infect the footpad failed to detect neutrophils migrating to the draining LN (Bollampalli et al., 2015). Taken together, these findings suggest that distinct regions of inoculation in the skin can have variable immunological outcomes. We speculate that the much thinner ear pinna may have allowed more lymphatic drainage than the flank skin, and consequently better flow of inflammatory factors and recruitment of innate immune cells to the inflamed site.

Although we were unable to assess the efficiency of TRITC dye uptake by cells in the skin, our initial experiment using photoconvertible KAEDE systems detected an even lower number of migratory cells, further suggesting that neutrophil migrations from the skin to dLN is rare after HSV infection.

Studies reporting neutrophil migration from sites of inflammation to the LN have demonstrated that neutrophils appeared to enter the lymphatics via a CD11b-dependent pathway (Gorlino et al., 2014; Hampton et al., 2015), and preferentially localised to SCS and interfollicular regions (Kamenyeva et al., 2015; Hampton et al., 2015). We examined the distribution of neutrophils in draining LN at 6 hr p.i., where the majority of cells were associated with lymphatic and HEV structures located in the medullary region. This was similarly reported by Gorlino et al. (2014) showing that neutrophils enter the LN post-immunisation from the blood vessels and lymphatics. Nonetheless, it was less clear if these cells entered the LN from medullary HEV, as we have observed in

our experiments. It remains to be determined whether there are any biological significance in their distinct localisation to the medullary region.

A number of studies have demonstrated an immunomodulatory role by neutrophils in both B cell and T cell responses during infection. Hampton et al. (2015) showed that neutrophils migrating from skin altered both B and T cell proliferation, while implicating antigen shuttling and production of inflammatory cytokines as possible mechanisms that modulate lymphocyte expansion. Similarly, neutrophils were also shown to directly interact with B cells and regulating antibody production possibly through a TGFβ-dependent mechanism (Kamenyeva et al., 2015). Neutrophils also potentially interact with APC in the peripheral tissues. In one study employing *M. tuberculosis* infection, neutrophils facilitated early $CD4^+$ T cell activation through helping non-infected DC to acquire antigen, as infected DCs themselves were impaired in migration (Blomgran & Ernst, 2011). On the other hand, neutrophils may also control the magnitude of $CD4^+$ T and B cell responses through immunosuppressive effects (Yang et al., 2013).

In the case of epicutaneous HSV-1 infection, a previous study showed that neutrophil depletion did not alter the viral load or lesion severity throughout the course of infection (Wojtasiak et al., 2010b). Here we showed that ablation of neutrophils did not diminish nor enhance $CD4^+$ or $CD8^+$ T cell priming. The magnitude of expansion and the degree of proliferation by D3 p.i., as well as the expression of activation markers were unchanged in depleted mice. This suggested that neutrophils did not significantly alter antigen presentation to T cells. Tate et al. (2012) reported that neutrophil depletion during influenza virus infection did not affect antigen presentation to $CD8^+$ T cells, but showed diminished $CD8^+$ T cell expansion as well as impaired antiviral cytokine expression.

Finally, neutrophils have been implicated in influencing migration of effector $CD8^+$ T cells to peripheral tissues, including the skin (Dilulio et al., 1999; Engeman et al., 2004). Recently, Lim et al. (2015) showed that neutrophils leave

behind CXCL12-enriched trails in their migratory paths in influenza-infected lungs, which in turn directed the migration of effector $CD8^+$ T cells (Lim et al., 2015). Following neutrophil depletion, we found no significant difference in the number of effector $CD8^+$ T cells recruited to HSV-infected skin. However, for $CD4^+$ T cells we observed impaired recruitment to the skin in neutrophil-depleted mice in one experiment, with slight but insignificant difference in the other experiment. During mucosal HSV-2 infection it has been shown that $CD4^+$ T cells infiltrate infected tissues and promote local CXCL9 and CXCL10 production, which in turn facilitates $CD8^+$ T cell accumulation, demonstrating distinct stages of $CD4^+$ and $CD8^+$ T cell recruitment to the infected tissues (Nakanishi et al., 2009). Thus, with multiple chemokine pathways regulating effector T cell recruitment, it was possible that in the case of HSV-1, only early $CD4^+$ T cell entry was affected by neutrophil-dependent CXCL12-mediated migration, but $CD8^+$ T cells entering the tissue later might be less influenced by CXCL12 due to the presence of other chemokine cues such as CXCL9 and CXCL10, likely acting in a redundant manner.

In summary, we report an early, transient wave of neutrophil migration to both HSV-infected skin and LN, triggered by tissue damage in the skin. We detected only minimal migration of neutrophil from the skin to its draining LN, ruling out a role as antigen carrier that promotes early antigen presentation to T cells. Neutrophils were found to be dispensable for $CD4^+$ and $CD8^+$ T cell priming, as well as being non-essential for effector T cell migration to infected sites later during the immune response.

CHAPTER FOUR:

CHARACTERISATION OF THE SPATIOTEMPORAL KINETICS OF HSV-SPECIFIC $CD4^+$ AND $CD8^+$ T CELLS ACTIVATION DURING EPICUTANEOUS INFECTION

4.1 INTRODUCTION

Priming of the adaptive immune system is complex. The process of mounting effective cell-mediated defence against pathogens requires cooperation between an elaborate set of immune cells. In addition to antigen-specific encounters between T lymphocytes and their cognate antigen-bearing APCs, clearance and protection against many types of infection depend on the coordinated responses of helper $CD4^+$ and cytotoxic $CD8^+$ T cells (Bousso, 2008; Bevan, 2004; Castellino and Germain, 2006).

Efficient immune responses against pathogenic challenge require swift encounter between rare-antigen specific lymphocytes and their APC (Germain et al., 2008). The secondary lymphoid organs (SLO) including the spleen and LNs have evolved advanced immunosurveillence mechanisms to allow prompt detection of foreign antigen. During systemic and lymph-borne infections, pathogens disseminating to the SLO are readily captured by macrophages and dendritic cells (DC) lining the lymphatic sinuses (Norbury et al., 2002; Hickman et al., 2008; Chtanova et al., 2009; Germer et al., 2015). In contrast, during localised infection, where pathogens are highly confined to peripheral tissues and are effectively excluded from the lymph surveillance network, migratory APC from the periphery play a pivotal role in the sampling and transport of antigen to the local draining LN (Allan et al., 2006; Randolph et al., 2008).

Upon activation in the secondary lymphoid organs, T cells divide and differentiate into effector cells. Proliferating to large numbers, these effector T cells then migrate into the lymphatics for re-circulation to the spleen and inflamed sites to perform their effector functions. As infection subsides, the immune response undergoes contraction, whereupon most effector cells die by apoptosis, while some form memory cells to protect against secondary challenge (Williams and Bevan 2007; Brachiale and Hahn 2013).

We wished to examine the cooperative relationship between $CD4^+$ and $CD8^+$ T cells during priming in the context of localised infection. In this chapter, we

began by investigating the spatiotemporal aspects of $CD4^+$ and $CD8^+$ T cells during peripheral viral infection – the intranodal positioning of T cells over the course of infection. Using mouse cutaneous HSV-1 infection model, we mapped the distribution of fluorescently-labelled HSV-specific TCR transgenic $CD4^+$ and $CD8^+$ T cells in the reactive LN and followed their migration through various tissues. We found that $CD4^+$ T cells migrated out of the reactive node and entered the infected skin earlier than $CD8^+$ T cells, and that this could be attributed to the staggered nature of their priming kinetics.

We next investigated the mechanisms that underlie the differential priming kinetics of $CD4^+$ and $CD8^+$ T cells after skin HSV infection by examining various possible determinants including the TCR transgenic T cells, viral protein expression, routes of infection, types of viruses and dependence on $CD4^+$ T cell help. The factors contributing to delayed $CD8^+$ T cell priming appear to be complex and may involve multiple variables such as *de novo* synthesis of viral proteins by infected cells and the segregated roles of presenting DC subsets.

4.2 RESULTS

4.2.1 Spatiotemporal distribution of CD4⁺ and CD8⁺ T cell expansion in lymphoid tissues after HSV infection.

We wanted to examine the spatiotemporal distribution of HSV-specific CD4⁺ and CD8⁺ T cells during priming, across the lymphoid tissues. To track T cell expansion and migration, we adoptively transferred $5x10^4$ congenically marked HSV-specific CD4⁺ gDT-II and CD8⁺ gBT-I T cells into recipient B6 mice prior to infection. We chose to transfer a relatively small number of naïve transgenic T cells, i.e. $5x10^4$ cells, so that we could track early T cell proliferation without altering the kinetics of the response, as is the case with abnormally high precursor numbers (Stock et al., 2007). Harvesting the skin-draining LN (brachial LN [bLN] and axillary LN [aLN], as well as the contralateral cervical LN [cLN]) and the spleen from D3 to D7 p.i., we determined the number of recovered CD4⁺ gDT-II and CD8⁺ gBT-I cells in each lymphoid tissue through flow cytometry. A marked increase in T cell numbers, denoting antigen-specific expansion, was first detected in CD4⁺ gDT-II cells in the bLN at D3 p.i., culminating in a peak at D5 p.i. prior to declining afterwards (**Fig. 4.1A**). In contrast, expansion of CD8⁺ gBT-I cells in the bLN lagged by at least a day compared to CD4⁺ gDT-II cells but also peaked at roughly D5 p.i. before their decrease in number by D7 p.i. (**Fig 4.1A**)

Examining the aLN revealed that CD4⁺ gDT-II cell numbers began to increase at D4 p.i., a day after their initial detection in the bLN, and gradually increased over the next few days (**Fig. 4.1B**) A similar increase was also observed in the spleen from D4 p.i. (**Fig. 4.1C**), while small amount of CD4⁺ gDT-II also entered the non-draining cLN by D4-5 p.i. (**Fig. 4.1D**) In all three cases, CD8⁺ gBT-I cells also lagged behind CD4⁺ gDT-II cells by ~1 day. This suggested that CD4⁺ gDT-II cells expanded to a greater number in the reactive bLN than CD8⁺ gBT-I cells and also entered the downstream aLN and the spleen earlier than CD8⁺ gBT-I cells. However, this does not preclude the possibility of additional CD4⁺ T cell

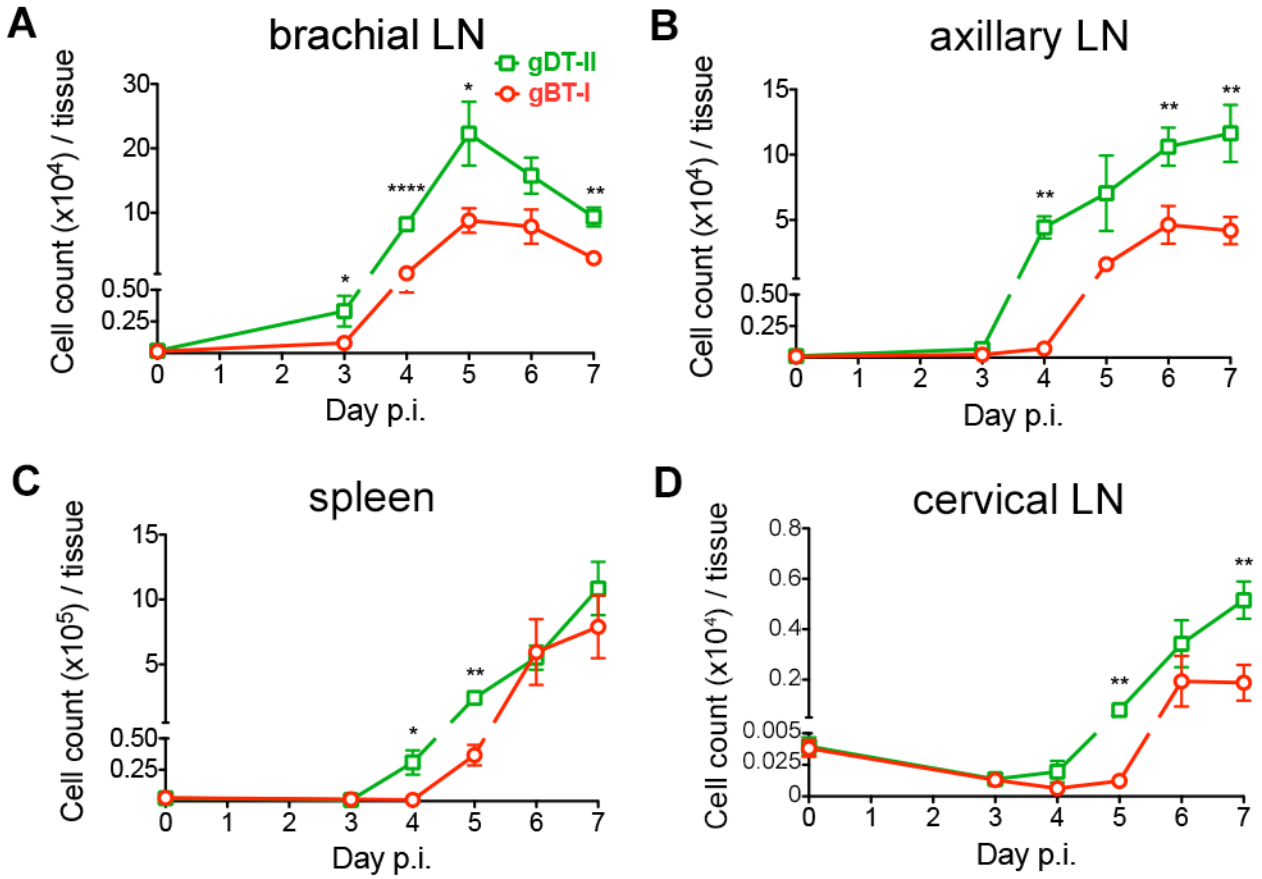

Figure 4.1 HSV-specific CD4⁺ and CD8⁺ T cell expansion and distribution in secondary lymphoid tissues during epicutaneous HSV-1 infection

5x10⁴ CD4⁺ gDT-II.Ly5.1 and CD8⁺ gBT-I.Ly5.1 were co-transferred into recipient C57BL/6 mice 1 day prior to receiving cutaneous HSV-1 infection on the flank skin. (A-D) Total number of CD4⁺ gDT-II (green) and CD8⁺ gBT-I (red) cells recovered from draining brachial LN (A), downstream axillary LN (B), spleen (C), and non-draining cervical LN (D) at D0 and D3-7 p.i. Data pooled from 2 independent experiments; n = 5-7 mice for each time point. Error bars represent mean ± SEM. *p<0.05, **p<0.01, ****p<0.0001, paired Student t test.

expansion in the aLN, because viral spread to the lower flank also allows the axillary node to receive antigen after D3 p.i. (Bedoui et al., 2009)

4.2.2 CD4+ T cells egress the draining brachial LN and enter the downstream node before CD8+ T cells.

To further examine whether the increase in number in the aLN was due to activated T cells entering the node after their egress from the reactive bLN, or that the increase reflected the expansion of antigen-specific T cells in the aLN after viral recrudescence, we performed immunofluorescence confocal microscopy on frozen bLN and aLN sections. Transgenic CD4+ gDT-II and CD8+ gBT-I cells were visualised using fluorescent proteins, by crossing these transgenic mouse strains with either EGFP- or DsRed-expressing mice. $5x10^4$ CD4+ EGFP.gDT-II cells and a similar number of CD8+ DsRed.gBT-I cells were adoptively transferred into recipient B6 mice prior to HSV-1 infection and LN sections from D3, D3.5, D4 and D5 p.i. were examined. The localisation of T cells enabled determination of whether CD4+ gDT-II cells egressed the bLN earlier than CD8+ gBT-I cells and migrated to the aLN and the spleen. Exiting T cells will migrate into the efferent lymphatic sinuses of the upstream node (bLN) and will be apparent in the afferent lymphatics of the downstream node (aLN). In contrast, T cell proliferation customarily takes place in the deep paracortex, and as such the intranodal positioning of the T cells within both lymphatically-connected LNs would further indicate the nature of expanded T cell number in the axillary node.

Staining for lymphatic vessels (anti-LYVE1) revealed more CD4+ gDT-II cells compared to CD8+ gBT-I cells at D3 p.i. in the T cell zone of draining bLN. This may indicate an earlier expansion of CD4+ gDT-II cells consistent with our observation via flow cytometry. However, CD4+ gDT-II cells were first observed to localise into the lymphatic sinuses in the medullary region of the node at D3.5 p.i. (data not shown), and their progressive migration into the medullary sinuses continued into D4 and D5 p.i. (**Fig. 4.2A**) Starting D4 p.i., these CD4+ T cells were also situated within the SCS, interfollicular regions and B cell follicles, while at the same time the initially densely packed T cell zone was continuously cleared,

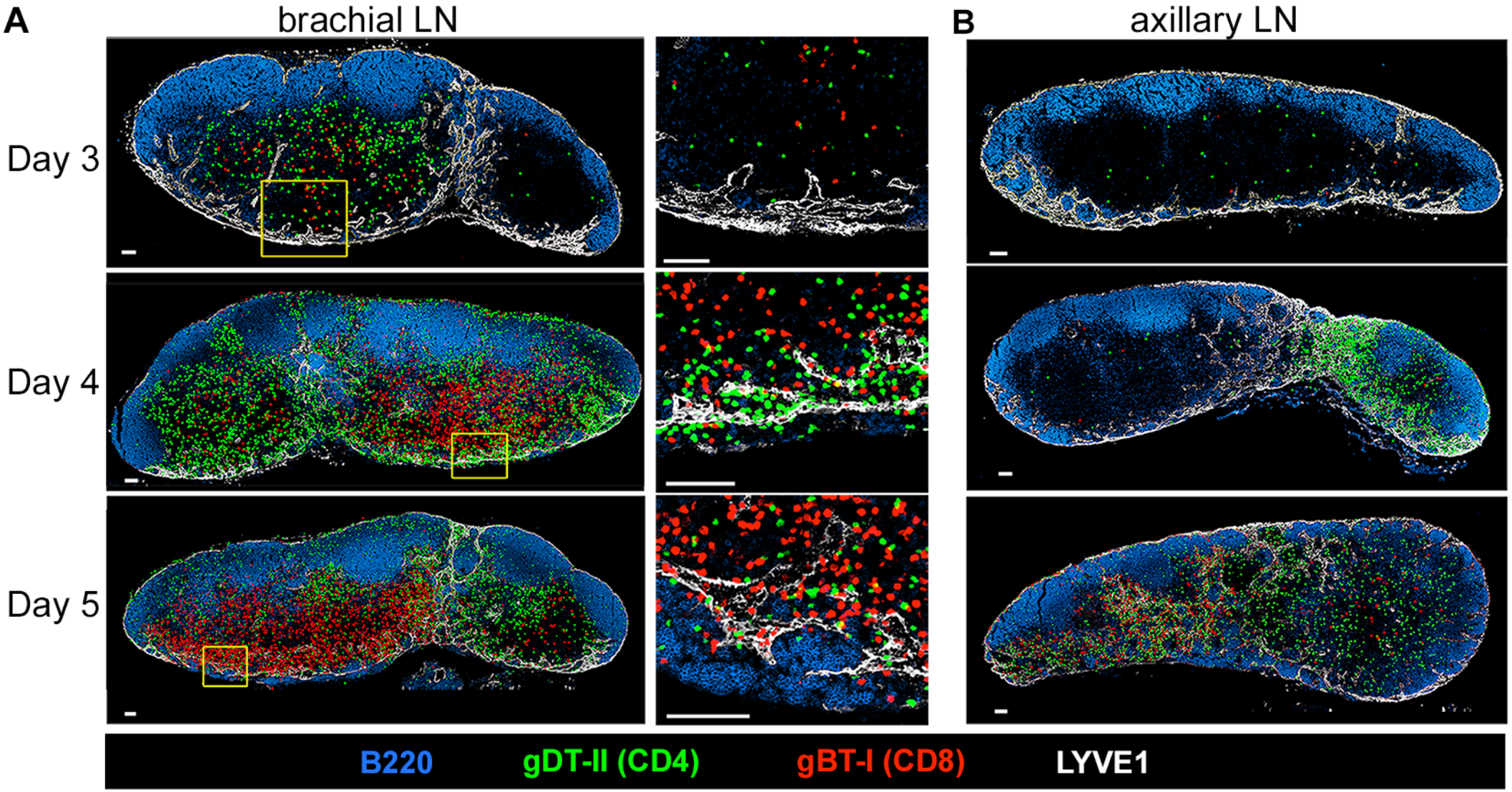

Figure 4.2 HSV-specific CD4⁺ T cells egress from draining brLN and enter downstream LN preceding CD8⁺ T cells
5x10⁴ CD4⁺ gDT-II.EGFP and CD8⁺ gBT-I.DsRed were co-transferred into recipient C57BL/6 mice prior to epicutaneous HSV-1 infection. (A) Confocal images showing spatial distribution of CD4⁺ (green) and CD8⁺ (red) T cells in the draining brachial LN at D3 (top), D4 (middle), and D5 (bottom) p.i. Magnified regions are shown in the panels to the right. B220⁺ B cells and LYVE-1⁺ lymphatic vessels are stained in blue and white, respectively.
(B) Confocal images showing infiltration of CD4⁺ (green) and CD8⁺ (red) T cells into the downstream axillary LN of the corresponding draining brachial LN at D3 (top), D4 (middle), and D5 (bottom) p.i. All scale bars denote 100μm.

indicating outward migration of T cells from the deep T cell zone. $CD8^+$ gBT-I cells followed the same pattern but were delayed by at least 12 hr compared to their $CD4^+$ counterparts, again paralleling our observations from flow cytometry.

To quantitate the shifting distribution of these T cells within different anatomical compartments of the reactive node over time, we divided bLN sections into five compartments based on B cell (anti-B220) and lymphatic vessel (anti-LYVE1) staining: SCS, B follicles, interfollicular region (IFR), T cell zone as well as the medulla (**Fig. 4.3A**). By calculating the proportion of $CD4^+$ and $CD8^+$ T cells within each region at each time point, our results showed that in the medulla, $CD4^+$ gDT-II cells increased in proportion between D3 and D4 p.i, (**Fig. 4.3C**). This was paralleled by their reciprocal decrease in the T cell zone over the same period (**Fig. 4.3B**). This suggested that the changing positioning of T cells between each time point was likely due to migration of differentiated T cells, having acquired the appropriate homing receptors, from T cell zone into the medulla in order to egress from the reactive node. It should also be noted that, as described earlier, increases in $CD4^+$ gDT-II cells in B follicles, SCS and IFR were also observed from our quantitative analysis (**Fig. 4.3D-F**). Furthermore, $CD8^+$ gBT-I cells clearly entered the medulla at a later time point, and this supports the hypothesis that $CD4^+$ T cells exit the node earlier than $CD8^+$ T cells.

We also examined the aLN and, as expected, at D3.5 and D4 p.i., an influx of $CD4^+$ gDT-II cells were observed and the majority of these cells localised to the vessels in the afferent lymphatics, the region from which cells from an upstream node enter (**Fig. 4.2B**). At later time points (D4 and D5 p.i.), $CD8^+$ gBT-I cells were also observed in the afferent lymphatics, while some of the $CD4^+$ T cells had already penetrated the LN parenchyma. Together, by combining flow cytometry and immunofluorescence microscopy, our data suggested that HSV-specific $CD4^+$ and $CD8^+$ T cells egress with temporally distinct kinetics from the reactive node, with $CD8^+$ T cells lagging behind by half a day or so.

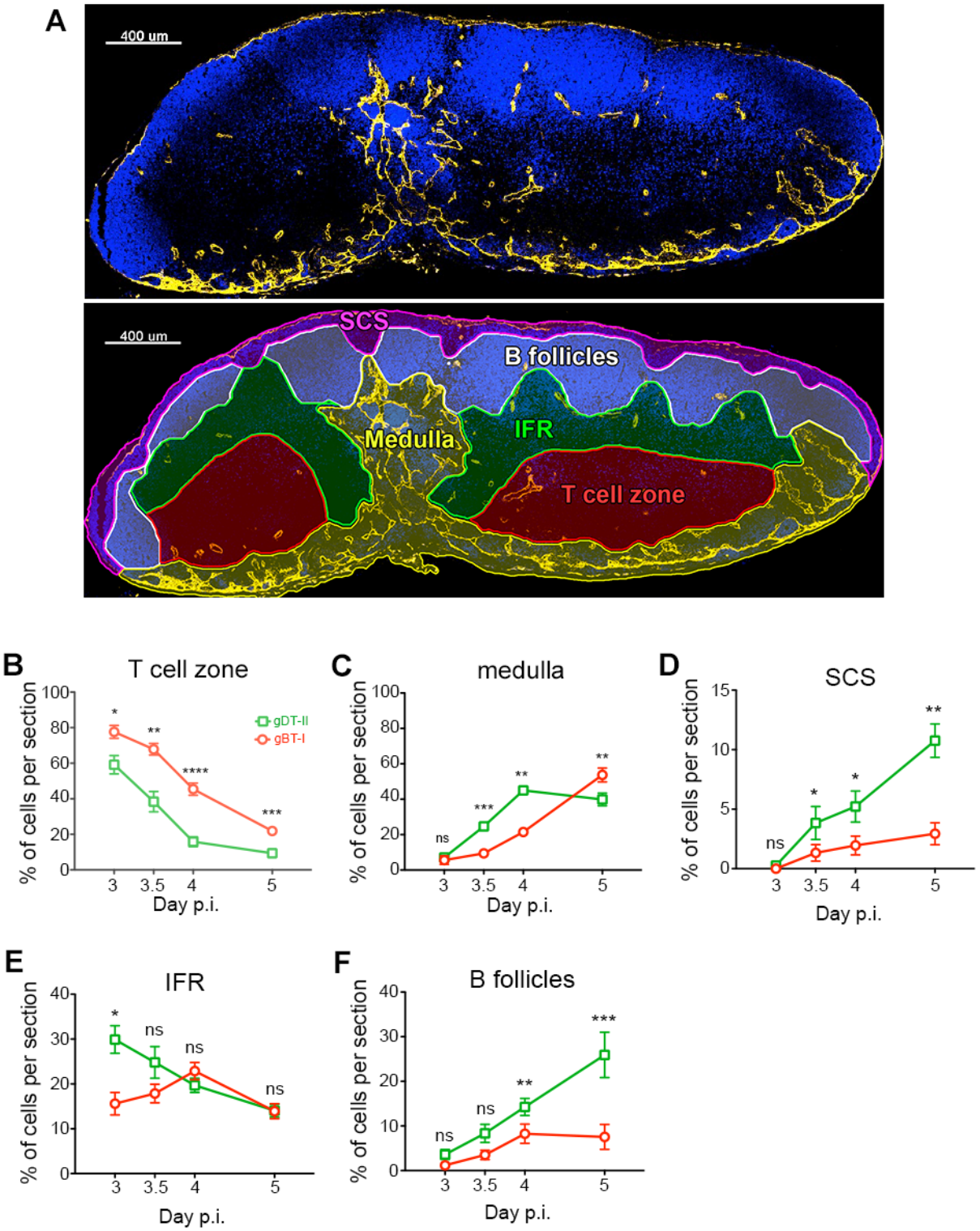

Figure 4.3 Quantitation of T cell localisation to draining LN compartments after HSV-1 infection

(A) Confocal images of LN sections from Figure 4.2 were delineated into five compartments: subcapsular sinus (SCS), B follicles, interfollicular region (IFR), T cell zone and medulla based on anti-B220 (B cell, blue) and anti-LYVE-1 (lymphatic vessels, yellow) staining.

(B-F) Proportion of $CD4^+$ gDT-II (green) and $CD8^+$ gBT-I (red) T cells occupying the T cell zone (B), medulla (C), SCS (D), IFR (E) and B follicles (F) from D3 to D5 p.i. Data pooled from 2 independent experiments; n = 5-7 mice for each time point. Error bars represent mean ± SEM. *p<0.05, **p<0.01, ***p<0.001, ****p<0.0001, paired Student t test. ns, not significant.

4.2.3 CD4+ T cells enter spleen and infected skin prior to CD8+ T cells.

Following the anticipated path of migration, we expected the T cells to enter the spleen and then the infected skin in succession – CD4+ T cells should be detected in both the spleen and the infected skin prior to CD8+ T cells. Examining spleen sections, most of the fluorescent T cells observed were CD4+ gDT-II cells at D4 p.i., whereas CD8+ gBT-I cells were only detected in substantial numbers at D5 p.i. (**Fig. 4.4A**)

Similarly, a very small number of CD4+ gDT-II cells could be seen in the infected skin at D4 p.i., situated mostly in the deeper subcutaneous region of the skin (**Fig. 4.4B**), which was otherwise undetectable in the contralateral (uninfected) skin (data not shown). By D5 p.i., both CD4+ and CD8+ T cells had infiltrated extensively into the dermis of the skin, with CD4+ T cells vastly outnumbering CD8+ T cells at this point. Thus, CD4+ T cells preceded the arrival of CD8+ T cells in the infected sites by at least 12-24 hours.

4.2.4 Changing LN chemokine expression during epicutaneous HSV-1 infection.

Intranodal positioning of lymphocytes can be guided by chemokine cues. That CD4+ and CD8+ T cells migrate to the medullary sinuses at different times might reflect changes in chemokine expression in the LN as well as differential timing in chemokine receptor expression by activated lymphocytes. We wanted to determine whether the distinct pattern of intranodal T cell migration could be attributed to changes in chemokine expression. First, we examined the total mRNA level of various chemokines in the draining bLN at 18 hr as well as D3.5 p.i. using RT-PCR. We found that a number of chemokines, including CCL2, CCL20, CXCL9 and CXCL10 increased in expression over the course of infection (**Fig. 4.5**). Activated T cells are known to express CXCR3, the receptor for CXCL9 and CXCL10 and have been demonstrated to influence the intranodal localisation of T cells after activation (Groom et al., 2012). In contrast, other chemokines such as CCL5, CCL21, CCL27, CXCL16 and XCL1 decreased in expression (**Fig. 4.5**). The cause and biological significance of these changes have yet to be ascertained, but are compatible with previously published findings that

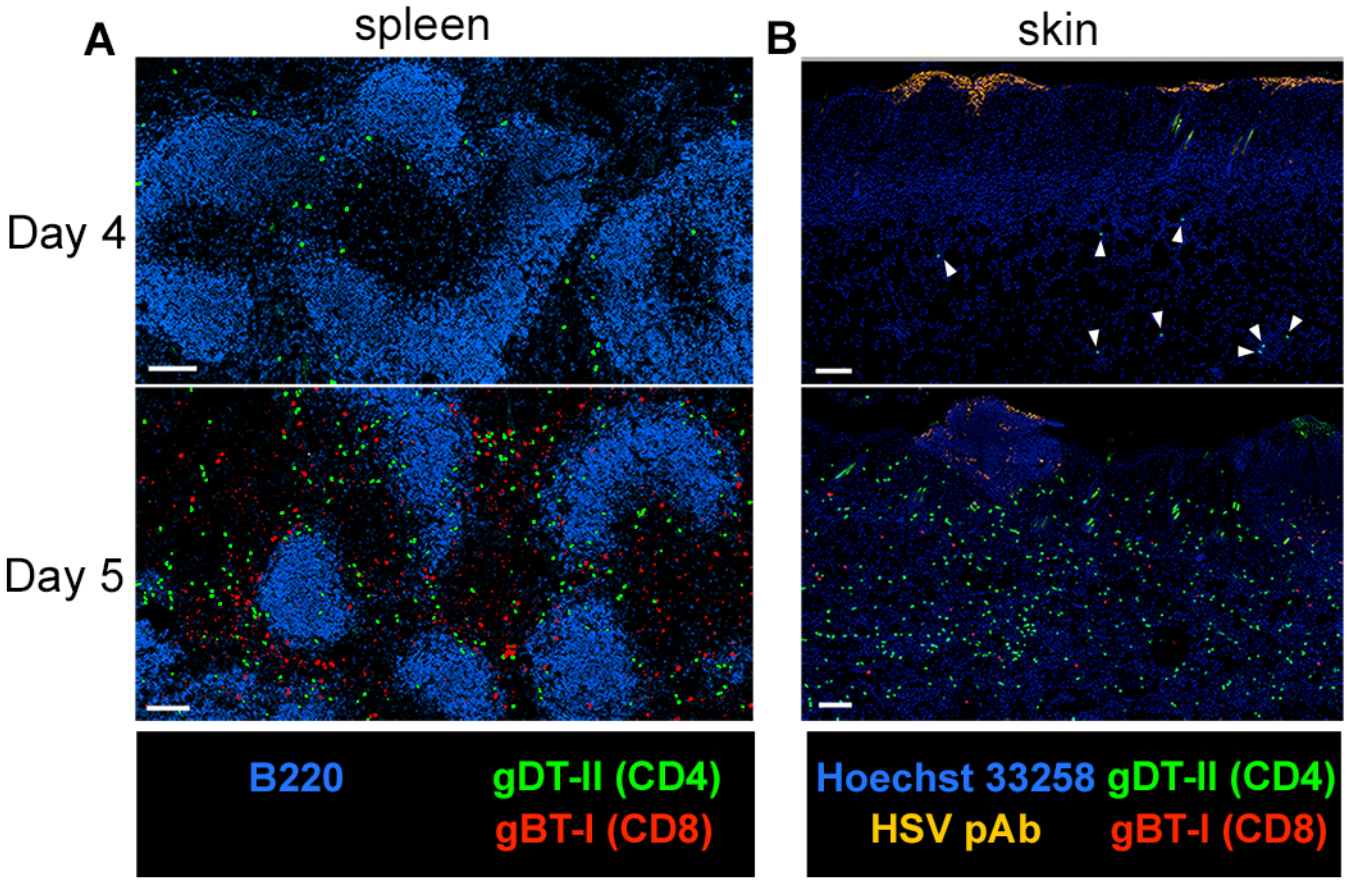

Figure 4.4 CD4⁺ T cells infiltrate the spleen and infected skin before CD8⁺ T cells

(A,B) Confocal microscopy showing localization of CD4⁺ gDT-II (green) and CD8⁺ gBT-I (red) cells of the spleen (A) and infected skin (B) sections of mice corresponding to Figure 4.2 at D4 (top) and D5 (bottom) p.i. B220⁺ B cells are stained in blue in (A). Cell nuclei (Hoechst 33258) and HSV antigen are stained in blue and yellow respectively in (B). White arrowheads denote position of CD4⁺ gDT-II cells (green) in infected skin at D4 p.i. Data representative of 2 independent experiments.

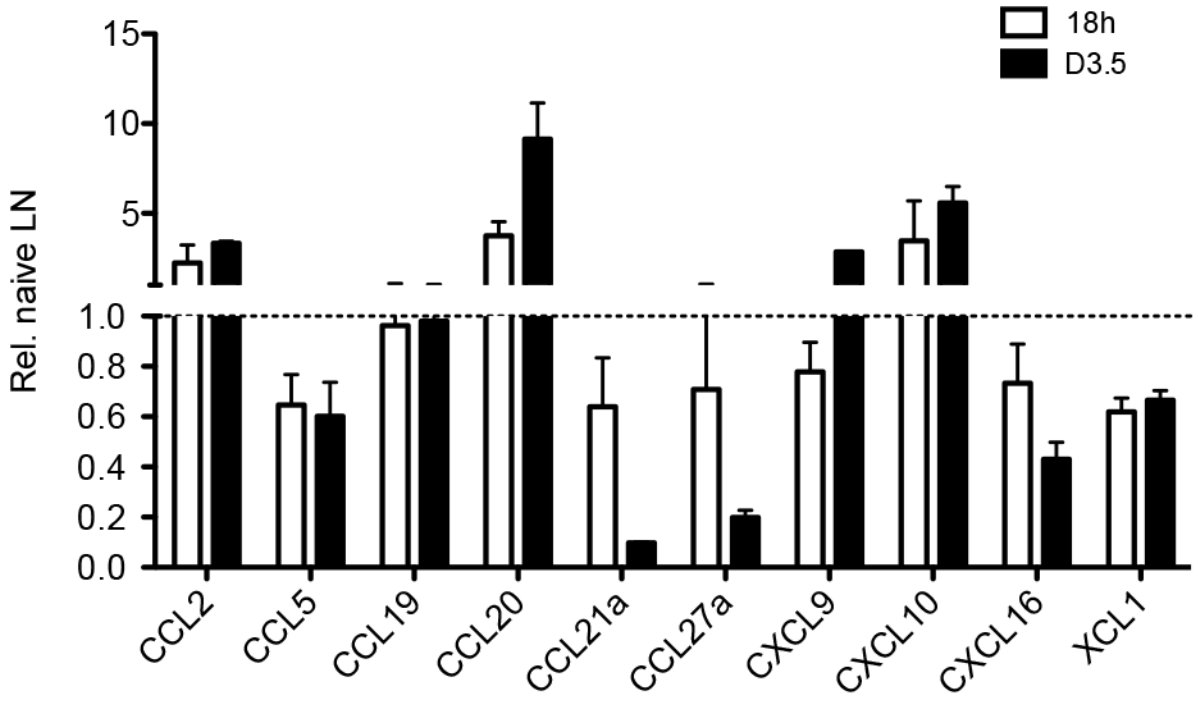

Figure 4.5 Measuring changes to chemokine levels in draining LN after HSV infection

Chemokine mRNA fold change relative to naïve LN were measured using RT-PCR at 18 hr (white bars) and D3.5 (black bars) p.i. Data representative of 1 experiment.

after infection, certain chemokines governing lymphocyte migration within LN, such as CCL19, CCL21 and CXCL13, are transiently downregulated (Mueller et al., 2007). Our results suggested that the LN undergoes substantial changes in chemokine expression but we did not identify the source of chemokine-producing cells, nor if activated $CD4^+$ and $CD8^+$ T lymphocytes responded differently to certain chemokines, dictating their motility. Further experiments examining the local changes in LN chemokine production as well as chemokine receptor expression on $CD4^+$ and $CD8^+$ T cells will be vital to address this question.

4.2.5 Differential priming kinetics of $CD4^+$ and $CD8^+$ T cells during epicutaneous HSV-1 infection.

Our results thus far indicated that $CD4^+$ T cells proliferated to a greater extent, exited the draining LN and infiltrated the effector sites earlier than $CD8^+$ T cells. This might suggest that $CD4^+$ T cells undergo an accelerated division and differentiation programme that enabled their early egress from the draining LN. On the other hand, $CD4^+$ and $CD8^+$ T cells may have asynchronous priming kinetics that result in staggered activation, proliferation and differentiation of both T cell subsets, as well as their eventual exit from the draining LN at different phases.

To investigate this possibility, we proceeded to establish the priming kinetics of $CD4^+$ gDT-II and $CD8^+$ gBT-I T cells over the first 72 hr after epicutaneous HSV-1 infection. $5x10^5$ $CD4^+$ gDT-II and an equal amount of $CD8^+$ gBT-I cells were adoptively transferred into recipient mice prior to infection. The transferred T cells were also labelled with CellTrace Violet dye to track their proliferation *in vivo*.

$CD4^+$ T cells in the draining bLN readily upregulated the early activation marker CD69 as early as 12 hr p.i. (**Fig. 4.6A, B**), which was otherwise undetectable in contralateral non-draining cLN (**Fig. 4.6D**). The increased expression of CD69 occurred concurrently with downregulation of CD62L as well as upregulation of CD44 (data not shown), suggesting antigen-specific activation of T cells.

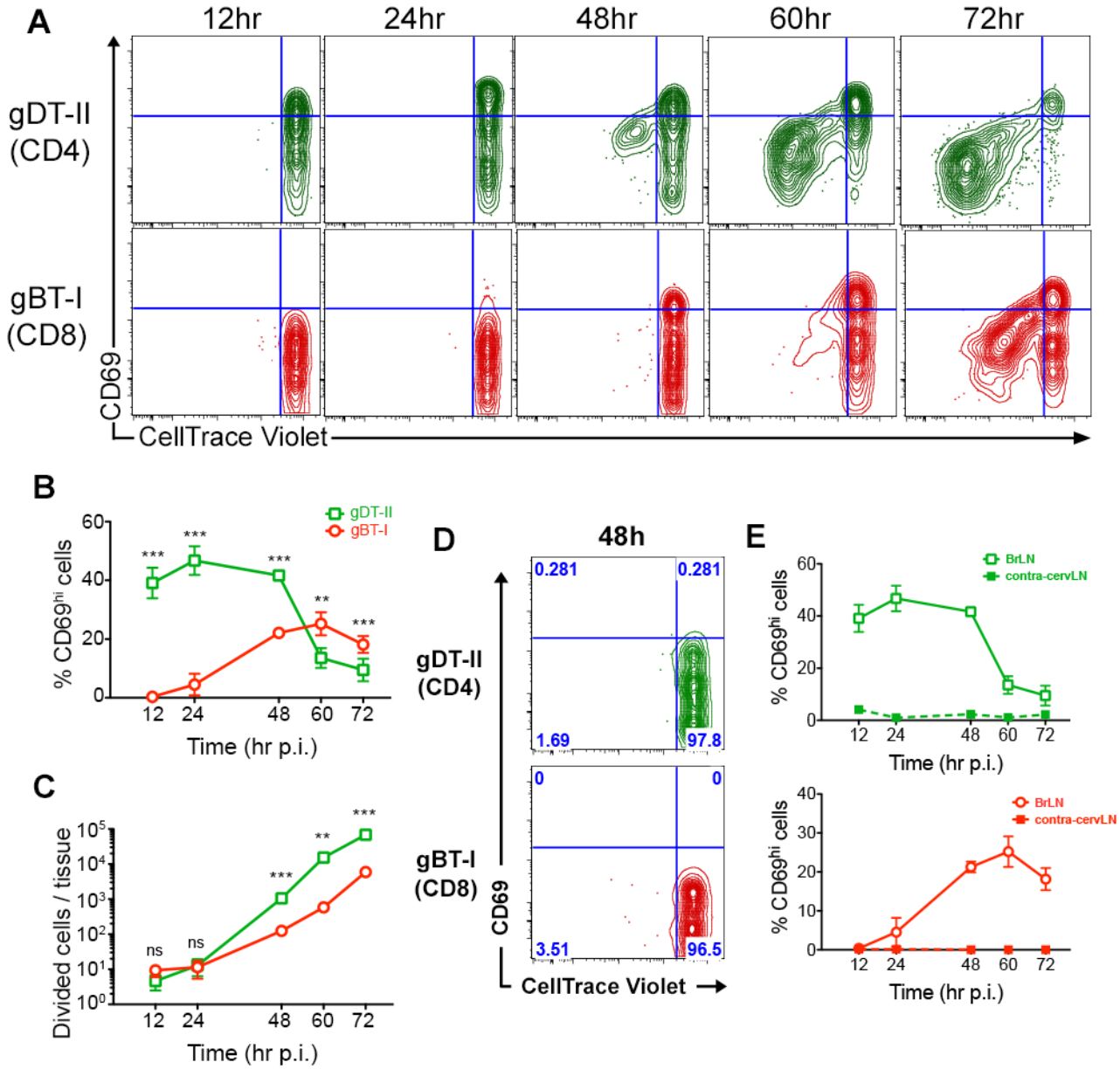

Figure 4.6 Differential priming kinetics of CD4⁺ and CD8⁺ T cells after cutaneous HSV-1 infection

5x10^5 CellTrace Violet-labelled CD4⁺ gDT-II.Ly5.1 and CD8⁺ gBT-I.Ly5.1 cells were adoptively transferred into recipient C57BL/6 mice 1 day prior to epicutaneous HSV-1 infection.

(A) Representative contour plots showing upregulation of early activation marker CD69 in CD4⁺ gDT-II (top row, green) and CD8⁺ gBT-I (bottom row, red) in draining brachial LN from 12 hr to 72 hr p.i.

(B) Proportion of CD69^{hi} CD4⁺ gDT-II (green) and CD8⁺ gBT-I (red) in draining brachial LN over 72 hr p.i.

(C) Number of divided cells (CellTrace Violet$_{lo}$) recovered per draining brachial LN over 72 hr p.i.

(D) Representative contour plots showing CD69 expression level in non-draining cervical LN at 48 hr p.i.

(E) Proportion of CD69^{hi} CD4⁺ gDT-II (top, green) and CD8⁺ gBT-I (bottom, red) in draining brachial LN (solid line) compared to non-draining cervical LN (dotted line) from 12 hr to 72 hr p.i.

Data pooled from 2-3 independent experiments; n = 6-12 mice per time point. Error bars represent mean ± SEM. **p<0.01, ***p<0.001, paired Student t test. ns, not significant.

Furthermore, when mice were transferred with non-specific CD4$^+$ OT-II and CD8$^+$ OT-I cells, CD69 expression in draining LN was essentially unchanged, similar to their counterparts in non-draining LN (data not shown), further indicating that such response were not due to the increased inflammation in the LN, which can also lead to elevated CD69 expression via type I interferon signalling (Shiow et al., 2006). In contrast to HSV-specific CD4$^+$ T cells, significant upregulation of CD69 in HSV-specific CD8$^+$ gBT-I cells was first observed at 48 hr p.i., a marked delay compared to their CD4$^+$ counterparts which already showed CD69 upregulation at 12 hr p.i. (**Fig. 4.6A, B**)

The onset of proliferation was also first observed in CD4$^+$ gDT-II cells, which began at 48 hr p.i., as indicated by the dilution of CellTrace Violet dye (**Fig. 4.6A**). CD8$^+$ gBT-I cells begun their division later, between 60-72 hr p.i. This led to an increase of divided CD4$^+$ gDT-II cells (CellTrace Violet$_{lo}$) by ~100 fold at 48 hr with at least an ~10 fold abundance over CD8$^+$ gBT-I cells, and continued to increase steadily over the course of our experiments (**Fig. 4.6C**). CD8$^+$ gBT-I cells followed a similar trend of cellular proliferation but were clearly delayed by ~12-24 hr compared to CD4$^+$ gDT-II cells. Taken together, the activation and division of CD4$^+$ and CD8$^+$ T cells appeared to be temporally staggered during skin HSV-1 infection.

4.2.6 Peptide injection invokes equal timing of CD4$^+$ and CD8$^+$ T cell activation.

While differential priming kinetics were observed in CD4$^+$ and CD8$^+$ T cells, it was not clear if this was a consequence of the TCR transgenic systems adopted. A multitude of factors influence activation of T cells, including TCR affinity for peptide-MHC complexes (Wulfing et al., 1997; Corse et al., 2011). As such, we wanted to determine if the early priming of CD4$^+$ gDT-II cells was due to higher sensitivity towards their pMHC ligand. To address this question we examined CD69 expression by both CD4$^+$ gDT-II and CD8$^+$ gBT-I transgenic T cells in the draining popliteal LN (pLN) after co-injection of their respective cognate peptides: gD$_{315-327}$ and gB$_{498-505}$. Equimolar concentration of both peptides were injected subcutaneously through the footpad at titrated doses of 0.1μM, 1μM and

10μM. At 3.5 hr post-injection, both CD4$^+$ gDT-II and CD8$^+$ gBT-I cells expressed high levels of CD69 at the 10μM peptide concentration. At lower concentrations, CD8$^+$ gBT-I cells consistently exhibited stronger responses compared to CD4$^+$ gDT-II cells (**Fig. 4.7**). Thus, our results showed that both CD4$^+$ gDT-II and CD8$^+$ gBT-I cells were capable of responding to peptide stimulation *in vivo* shortly after injection. Moreover, CD8$^+$ gBT-I cells upregulated CD69 to a greater extent than CD4$^+$ gDT-II cells. This was in contrast to our observation that CD4$^+$ T cells were primed earlier after HSV infection. These data suggested that CD8$^+$ gBT-I cells were potentially more sensitive to their pMHC ligand and, while various caveats apply, our results support the idea that the differential priming kinetics we observed could not simply be explained by the affinity of the TCR transgenic T cells alone.

4.2.7 CD8$^+$ T cells can be activated shortly after adoptive transfer.

We wanted to further rule out the possibility that the delay in antigen recognition by CD8$^+$ T cells during epicutaneous HSV infection resulted from differences between the adoptively transferred T cells. Since transgenic T cells were isolated and manipulated *ex vivo* prior to their transfer into recipient mice, this remained a possibility. However, if antigen presentation for CD4$^+$ and CD8$^+$ T cells does occur at different phases after HSV infection irrespective of the intrinsic characteristics of the transgenic T cells, then transferring the T cells at a later time (after antigen presentation to CD8$^+$ T cells is detectable) should result in synchronous activation of both T cells.

To examine this hypothesis, both CD4$^+$ gDT-II and CD8$^+$ gBT-I cells were adoptively transferred into HSV-infected mice at 36 hr p.i., when some CD8$^+$ T cells would normally be already activated, and CD69 expression on the transferred cells examined a further 12 hr later (at 48 hr p.i.) (**Fig. 4.8A**). Here, both CD4$^+$ gDT-II and CD8$^+$ gBT-I upregulated CD69 at 12 hr post-transfer, although the proportion of CD69^{hi} cells differed, with a larger proportion of CD4$^+$ gDT-II cells being CD69^{hi} compared to CD8$^+$ gBT-I cells (**Fig. 4.8B, C**). Thus, our data here demonstrated that both T cells were capable of being activated at the same time *in vivo*. As such, the delayed priming of CD8 T cells was unlikely to be

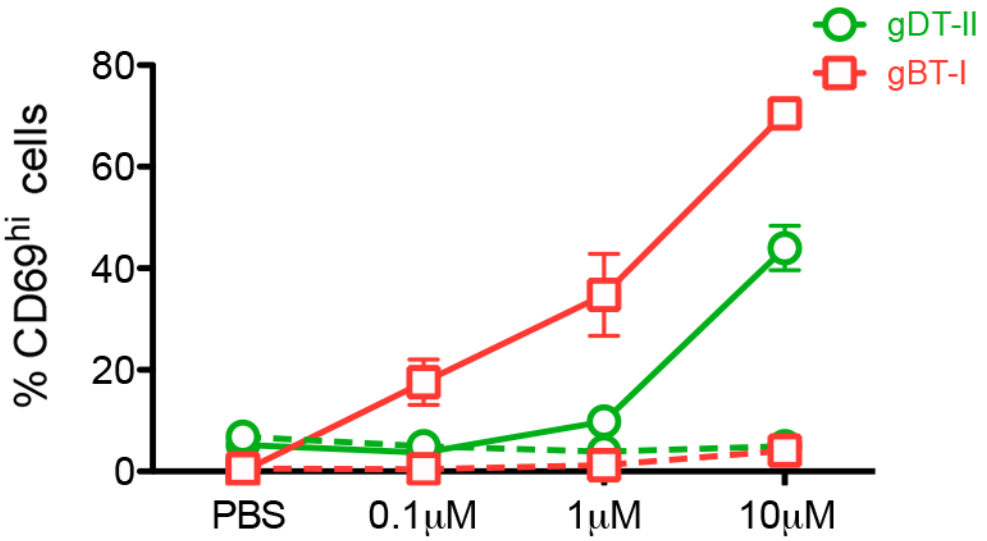

Figure 4.7 Peptide dose response of CD4+ gDT-II and CD8+ gBT-I
C57BL/6 mice received $5x10^5$ CD4+ gDT-II.Ly5.1 and CD8+ gBT-I.Ly5.1 cells 1 day prior to peptide injection. Equal amount of $gD_{315-327}$ and $gB_{498-505}$ peptides at titrated doses (0.1μM, 1μM, 10μM) were co-injected subcutaneously through footpad. Proportion of $CD69^{hi}$ CD4+ gDT-II (green) and CD8+ gBT-I (red) from draining popliteal LN (solid lines) and non-draining brachial LN (dotted lines) recovered at 3.5hr post-injection.
Data pooled from 1-2 independent experiments, n = 4-7 for popliteal LN; n = 1-4 for brachial LN per group. Error bars represent mean ± SEM.

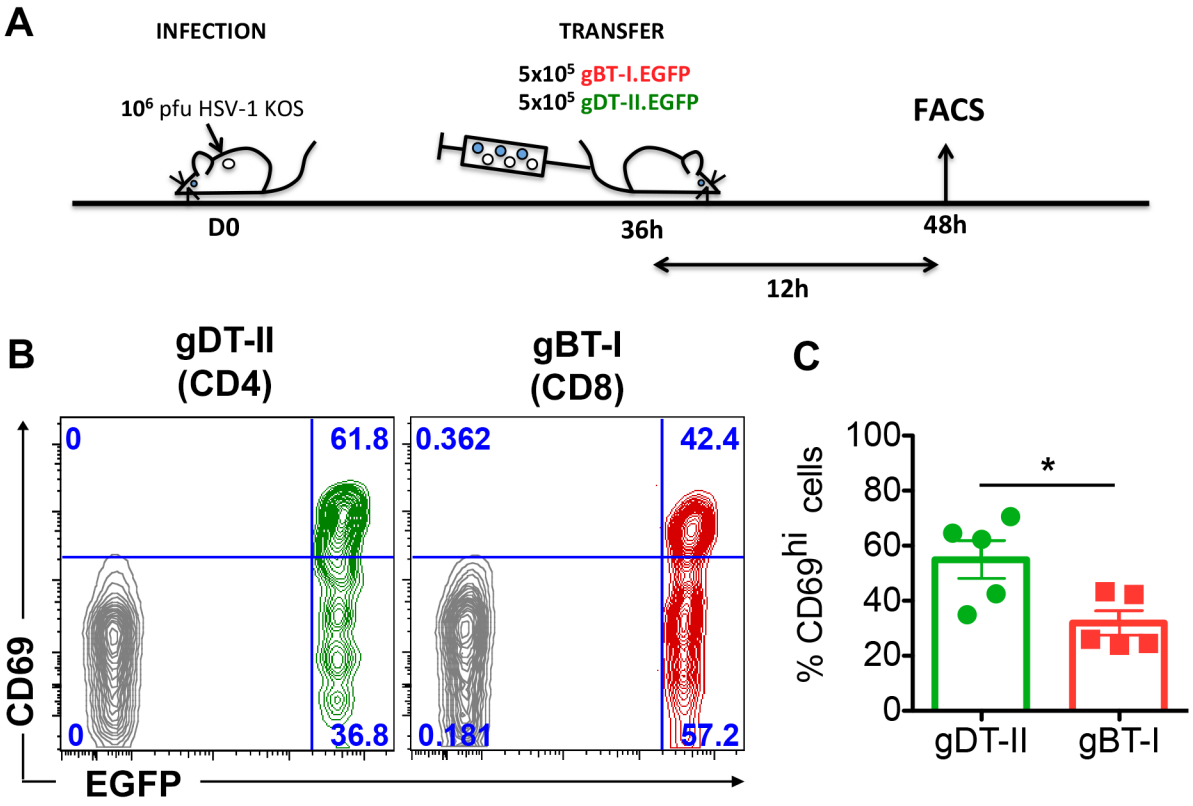

Figure 4.8 CD4⁺ and CD8⁺ T cells were activated shortly post-transfer during HSV-1 infection

(A) Schematics of experimental design: C57BL/6 mice were infected with HSV-1 epicutaneously and received 5x10^5 CD4$^+$ gDT-II.EGFP and CD8$^+$ gBT-I.EGFP at 36 hr p.i. At 12 hr post-transfer (48 hr p.i.) mice were sacrificed and draining brachial LN recovered for flow cytometry analysis.

(B) Representative contour plots showing CD69 upregulation of CD4$^+$ gDT-II (left, green) and CD8$^+$ gBT-I (right, red) in draining brachial LN at 12 hr post-transfer. CD69 level of endogenous CD4$^+$ and CD8$^+$ T cells are shown in grey in each plot respectively.

(C) Proportion of CD69^{hi} CD4$^+$ gDT-II (green) and CD8$^+$ gBT-I (red) in draining brachial LN at 12 hr post-transfer.

Data representative of 1 experiment, n = 5 mice. Error bars represent mean ± SEM. *p=0.0159, paired Student t test.

an intrinsic difference between the transgenic T cells. That more $CD4^+$ T cells upregulated CD69 also suggested that the quantity of antigen being presented on MHC-I versus MHC-II in this phase of the response might be different.

4.2.8 Virus with equal antigen expression triggers equal timing of $CD4^+$ and $CD8^+$ T cell activation.

Although we demonstrated that peptide injection induced T cell activation *in vivo*, this approach did not take into account the intricacies involved in antigen transport, processing and presentation during viral infection. Peptides were delivered directly to the LN, thereby circumventing the complex machinery associated with antigen processing and presentation that might influence the kinetics of antigen presentation (Babbitt et al., 1986; Adorini et al., 1988). Therefore, whole viral proteins should be introduced into the LN instead to ensure that peptides are generated via proteolytic degradation and loaded through pathways as would be expected during infection. Furthermore, we wished to normalise the amount of viral proteins introduced into the system to exclude bias that might have resulted from disparity in the quantity of protein contained within the virion.

To address this, we employed recombinant influenza virus strains where the epitopes of either HSV glycoproteins ($gD_{315\text{-}327}$ or $gB_{498\text{-}505}$) were expressed in the neuraminidase stalk, designated as HKx31-gD and HKx31-gB, respectively. Since both epitopes were expressed under the same promoter, the amount of antigen on both variants (gD and gB) was expected to be roughly equal.

Mice were transferred with $5x10^5$ antigen-specific $CD4^+$ gDT-II and $CD8^+$ gBT-I cells prior to co-infection with 1:1 ratio of HKx31-gD and HKx31-gB ($5x10^4$ pfu each) via subcutaneous footpad injection. At 14.5 hr and 24 hr p.i., both $CD4^+$ gDT-II and $CD8^+$ gBT-I upregulated CD69 with the same kinetics (**Fig. 4.9A, B**). Interestingly, CD69 expression by $CD4^+$ gDT-II and $CD8^+$ gBT-I was roughly similar at both time points, in contrast to epicutaneous HSV-1 infection (**Fig 4.9C**). This suggested that when the quantity and kinetics of antigen expression are equal, both $CD4^+$ and $CD8^+$ T cells are activated to a similar extent

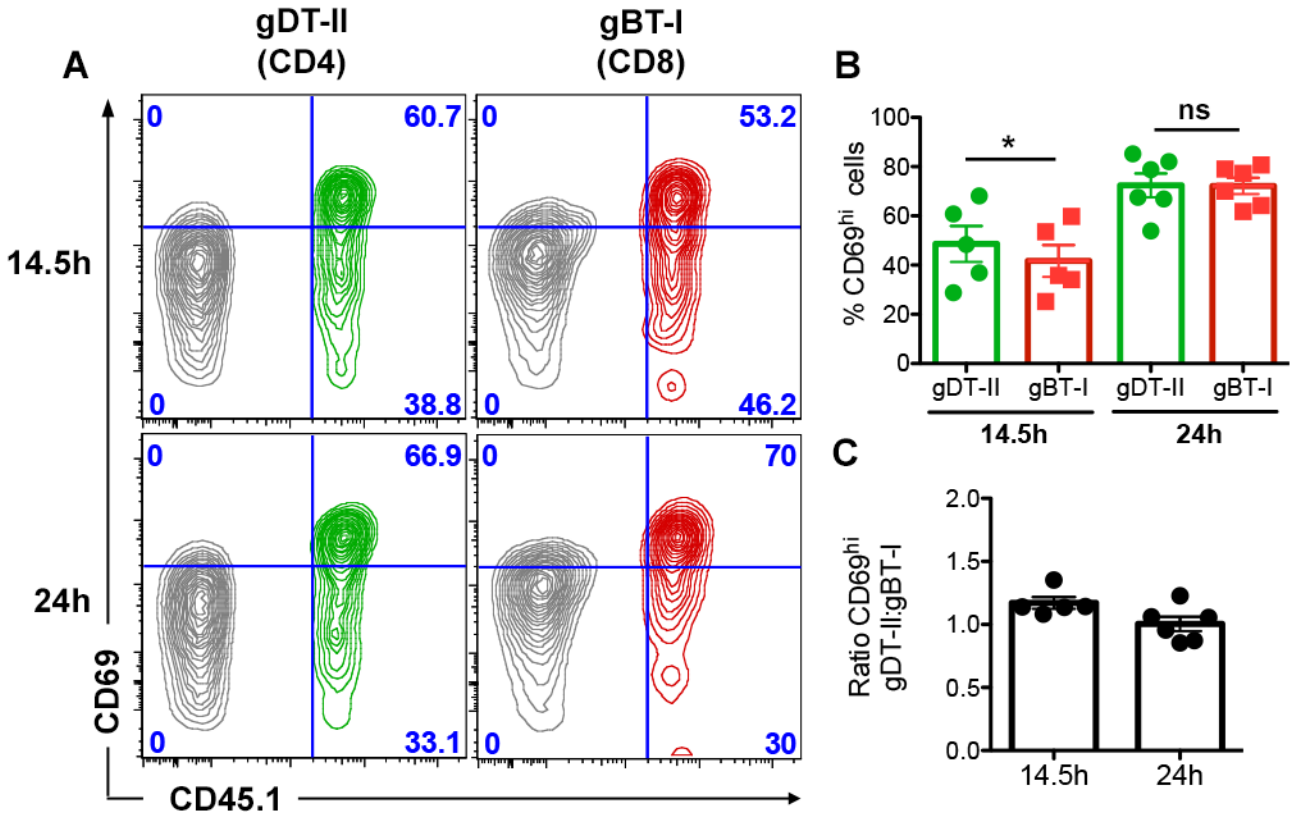

Figure 4.9 Equal antigen expression induces equal activation of CD4⁺ and CD8⁺ T cells

C57BL/6 mice receiving 5x10⁵ CD4⁺ gDT-II.Ly5.1 and CD8⁺ gBT-I.Ly5.1 were infected with 5x10⁴ pfu HKx31-gB and HKx31-gD subcutaneously.

(A) CD69 expression of CD4⁺ gDT-II (green, left) and CD8⁺ gBT-I (red, right) in draining popliteal LN at 14.5 hr (top row) and 24 hr (bottom row) p.i. CD69 expression of endogenous CD4⁺ (left) and CD8⁺ T cells (right) are shown in grey.

(B) Proportion of CD69^{hi} CD4⁺ gDT-II (green) and CD8⁺ gBT-I (red) at 14.5 hr and 24 hr p.i.

(C) Ratio of CD69^{hi} CD4⁺ gDT-II:CD8⁺ gBT-I at 14.5 hr and 24 hr p.i.

Data representative of 1 experiment, n = 4-6 per time point. Error bars represent mean ± SEM. *p<0.05, paired Student t test. ns, not significant.

temporally. Because different antigen processing pathways are required for the presentation of both peptide epitopes for $CD4^+$ and $CD8^+$ T cells, this also implied that the timing difference in activation of $CD4^+$ and $CD8^+$ T cells may not be due to the use of distinct processing pathways.

4.2.9 UV-inactivated virus impairs $CD8^+$ but not $CD4^+$ T cell priming response.

It has been reported that priming of HSV gB-specific $CD8^+$ T cells requires *de novo* synthesis of the viral antigen (Mueller et al., 2003). Virus devoid of replicative capacity after UV irradiation, as well as virus defective in gB synthesis, failed to stimulate IFN-γ production of antigen-specific $CD8^+$ T cells. This implied that gB associated with virions alone was insufficient to prime $CD8^+$ T cells. As such, the temporal requirement for viral protein synthesis, together with their transport to the draining LN by migratory DC, could substantially delay antigen presentation for $CD8^+$ T cells.

We hypothesised that unlike $CD8^+$ T cells, $CD4^+$ T cells could respond to gD antigen present in the virus inoculum, and thereby gain a kinetic advantage in priming compared to $CD8^+$ T cells. To test this, mice were adoptively transferred with $5x10^5$ CellTrace Violet-labelled $CD4^+$ gDT-II and $CD8^+$ gBT-I cells prior to epicutaneous infection with either live or UV-irradiated HSV-1. We chose to examine at 72 hr p.i. since robust priming as well as proliferation of $CD8^+$ gBT-I cells could be reliably detected at this point. Here, $CD4^+$ gDT-II cells were primed (CD69 upregulation) and proceeded to divide (CellTrace Violet dye dilution) in both mice infected with either live or UV-inactivated virus (**Fig. 4.10A**). Although $CD4^+$ T cells in the UV-inactivated virus group exhibited slightly lower CD69 expression and fewer divided cells (~10^5 cells vs. 10^4 cells) (**Fig. 4.10B, C**), this was likely due to the absence of viral replication and consequently reduced overall inflammatory and antigen level. In the case of $CD8^+$ T cells, however, priming and proliferation were abrogated in the UV-inactivated virus group (**Fig. 4.10A-C**). Therefore, one of the factors contributing to delayed priming of $CD8^+$ T cells may be attributable to the requirement for infected cells to synthesise viral

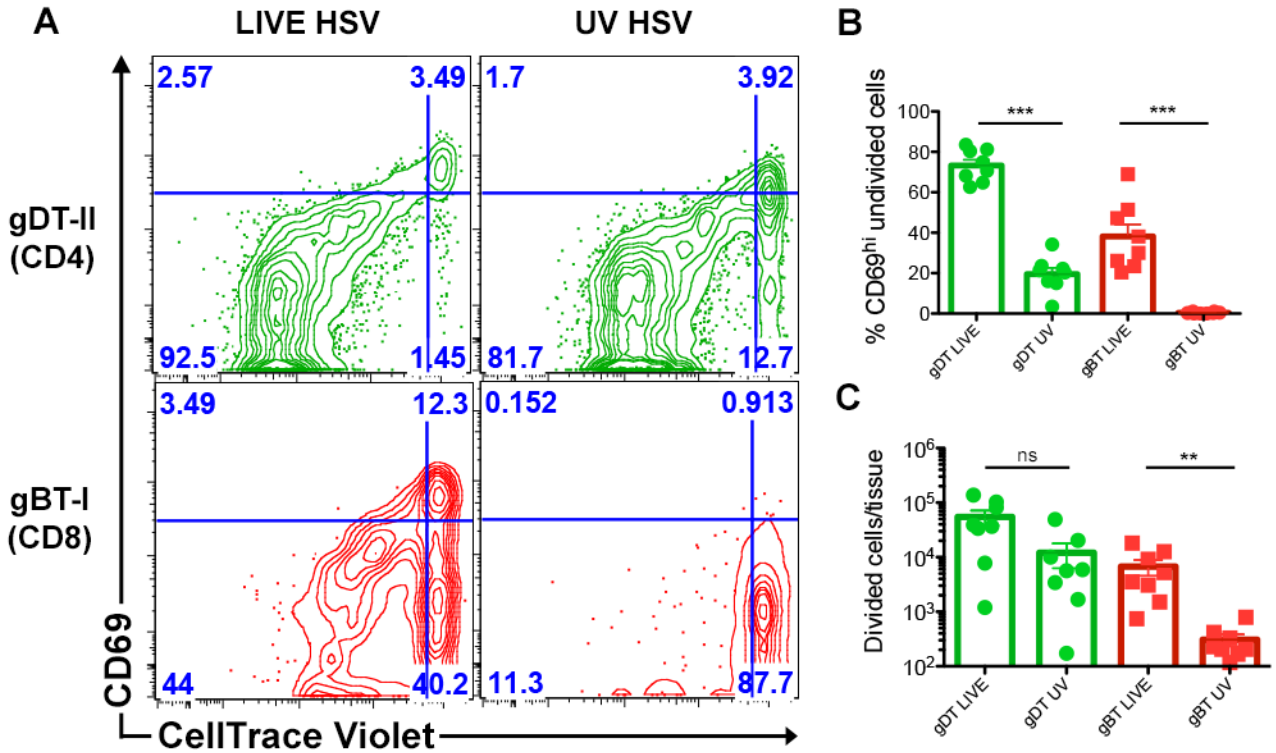

Figure 4.10 UV-inactivated virus impairs CD8⁺ but not CD4⁺ T cell priming
$5x10^5$ CellTrace Violet-labelled CD4⁺ gDT-II and CD8⁺ gBT-I cells were adoptively transferred into recipient C57BL/6 mice prior to epicutaneous infection with either live or UV-inactivated HSV.
(A) Representative contour plots of CD69 expression in CD4⁺ gDT-II (green, top row) and CD8⁺ gBT-I (red, bottom row) from draining inguinal LN at 72 hr p.i. with live (left) or UV-irradiated virus (right).
(B) Proportion of $CD69^{hi}$ undivided CD4⁺ gDT-II (green) and CD8⁺ gBT-I (red) at 72 hr p.i. Error bars represent mean ± SEM. ***p<0.001, one-way ANOVA, Tukey's multiple comparisons.
(C) Number of divided ($CellTrace\ Violet_{lo}$) CD4⁺ gDT-II (green) and CD8⁺ gBT-I (red) recovered from draining iLN at 72 hr p.i. Error bars represent mean ± SEM. **p<0.01, one-way ANOVA, Tukey's multiple comparisons on log transformed values. ns, not significant.
Data pooled from 2 independent experiments, n = 8 mice per group.

antigen, whereas CD4$^+$ T cells can access antigen derived from viral particles in the initial inoculum.

4.2.10 Lymphatic drainage of HSV narrows the interval between CD4$^+$ and CD8$^+$ T cell priming.

Previous studies have reported that LN-resident CD8α$^+$ DC, rather than migratory CD11b$^+$ dermal DC (dDC), are primarily responsible for the cross-presentation of gB antigen to HSV-specific CD8$^+$ T cells (Allan et al., 2003; Bedoui et al., 2009). Since the delivery of antigen is mediated by dDC, it has been suggested that 'antigen transfer' between DC subsets is necessary for subsequent priming of CD8$^+$ T cells (Allan et al., 2006). We surmised that CD4$^+$ gDT-II have early access to antigen presentation from migratory dDC, whereas antigen presentation to CD8$^+$ gBT-I cells is only available after CD8α$^+$ DC have acquired antigens from migratory dDC. It is possible that a requirement for such transfer could also delay CD8$^+$ T cell priming.

We wished to explore the priming kinetics of both CD4$^+$ and CD8$^+$ T cells when virus drained directly to the LN. Subcutaneous injection of virus through the footpad results in detectable viral load in the draining LN, and hence was employed as an alternate route of infection to rapidly introduce the virus to both DC subsets in the draining LN (Mueller et al., 2002b). We established the priming kinetics of CD4$^+$ gDT-II and CD8$^+$ gBT-I cells up to 48 hr p.i. using a similar setup to our earlier experiments with the epicutaneous route of infection. When 10^6 pfu HSV-1 was injected subcutaneously, CD4$^+$ gDT-II cells still upregulated CD69 earlier than CD8$^+$ gBT-I cells, but the lag in priming was substantially reduced to a narrower ~6-12 hr difference (**Fig. 4.11A, B**). By 24 hr p.i., both CD4$^+$ gDT-II and CD8$^+$ gBT-I cells showed similar level of CD69 expression. Furthermore, the extent of proliferation was very similar between CD4$^+$ gDT-II and CD8$^+$ gBT-I cells at 48 hr p.i., suggesting largely equivalent priming and proliferative kinetics (**Fig. 4.11C**).

Interestingly, when the inoculating dose was increased to 10^7 pfu, CD69 expression by both CD4$^+$ gDT-II and CD8$^+$ gBT-I cells were amplified and

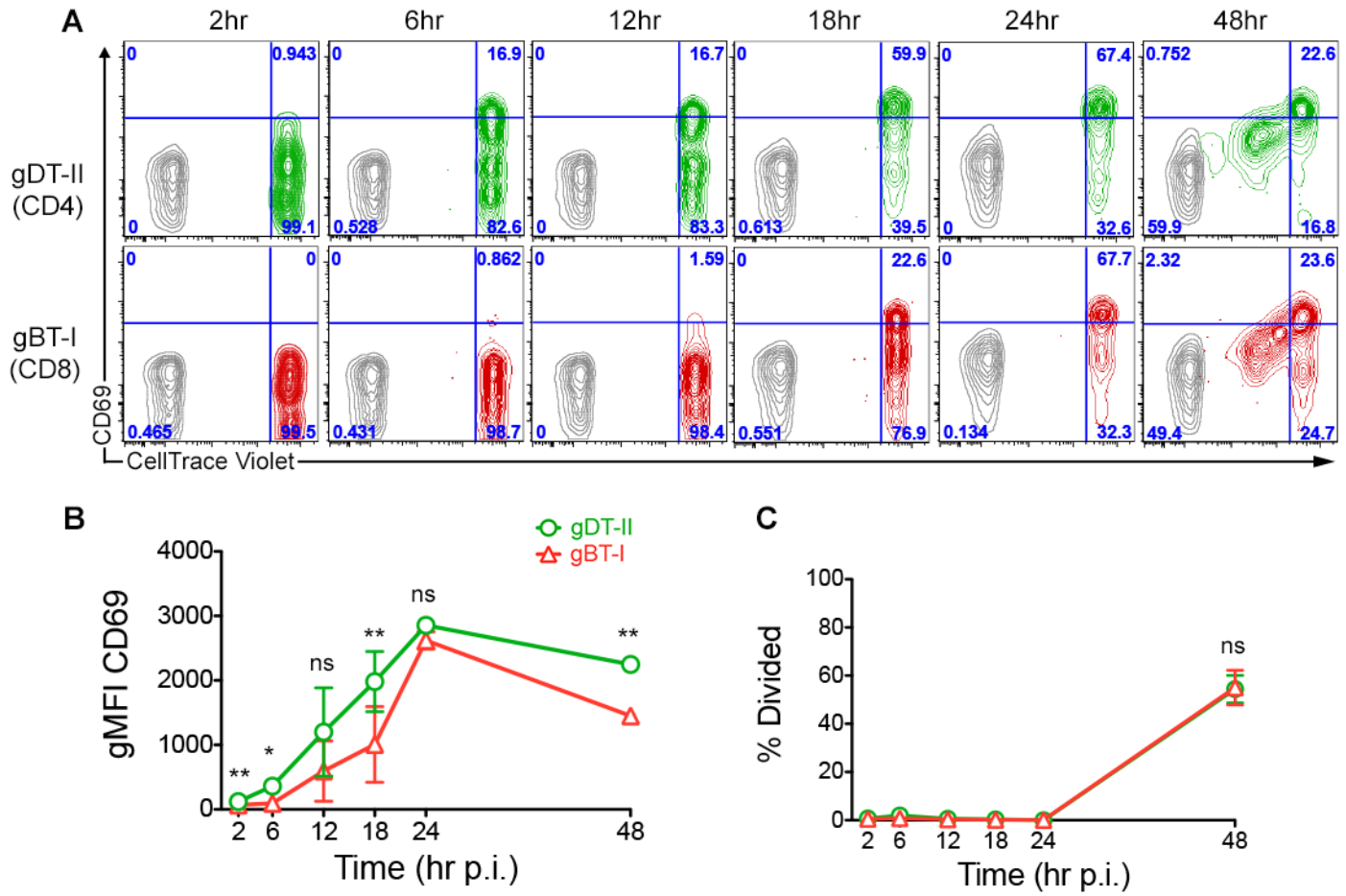

Figure 4.11 Priming kinetics of CD4⁺ and CD8⁺ T cells during subcutaneous HSV-1 infection

5x10^5 CellTrace Violet-labelled CD4⁺ gDT-II.Ly5.1 and CD8⁺ gBT-I.Ly5.1 cells were adoptively transferred into recipient C57BL/6 mice 1 day prior to subcutaneous footpad HSV-1 infection.

(A) Representative contour plots showing CD69 upregulation in CD4⁺ gDT-II (top row, green) and CD8⁺ gBT-I (bottom row, red) in draining popliteal LN from 2 hr to 48 hr p.i. CD69 expression of endogenous CD4⁺ (top row) and CD8⁺ (bottom row) T cells are shown in grey.

(B) Proportion of CD69^{hi} CD4⁺ gDT-II (green) and CD8⁺ gBT-I (red) in draining pLN over 48 hr p.i.

(C) Proportion of divided cells (CellTrace Violet$_{lo}$) in draining pLN over 48 hr p.i.

Data pooled from 2 independent experiments, n = 4-6 per time point. Error bars represent mean ± SEM. *p<0.05, **p<0.01, paired Student t test. ns, not significant.

although $CD4^+$ T cells still showed a greater proportion of $CD69^{hi}$ cells, CD8 gBT-I cells readily upregulated CD69 as early as 6hr p.i. (which was also first detectable at this time in $CD4^+$ gDT-II cells) (data not shown). However, it is not clear if such an accelerated response was a result of 'bystander activation' accentuated by the increased inflammatory milieu in the draining LN after high viral dose injection (Tough et al., 1996). An increase in CD69 expression by endogenous T cells, though not to the same extent as the transgenic T cells, appeared to support this notion.

Nevertheless, our results here showed that the activation as well as proliferative kinetics of both $CD4^+$ and $CD8^+$ T cells are influenced by different routes of infection, with subcutaneous infection – which allows virus to enter the LN directly – inducing more comparable kinetics of $CD4^+$ and $CD8^+$ T cell activation compared with epicutaneous infection.

4.2.11 Pre-transfer of activated $CD4^+$ T cells did not accelerate $CD8^+$ T cell priming.

Priming of HSV-specific $CD8^+$ T cells is CD4 help dependent (Smith et al., 2004). LN-resident $CD8\alpha^+$ DC need to be 'licensed' by $CD4^+$ T cells for the complete activation of $CD8^+$ T cells. Since the provision of help is contingent upon cognate interactions between activated $CD4^+$ T cells and antigen-bearing $CD8\alpha^+$ DC, we postulated that $CD4^+$ T cells needed to be activated first before priming of $CD8^+$ T cells could take place. We wanted to determine if this help requirement contributes significantly to the delayed priming of $CD8^+$ T cells.

$CD4^+$ gDT-II cells were first activated separately to bypass the time taken for priming $CD4^+$ T cells during infection. This was achieved through *in vitro* activation of $CD4^+$ gDT-II cells with peptide prior to adoptively transferring 10^6 of the activated T cells into recipient mice (**Fig. 4.12A**). The transfer of cells was performed 6 hr prior to infection to allow circulation of the activated lymphocytes to the lymphoid tissues. The mice additionally received $5x10^5$ CellTrace Violet-labelled virus-specific $CD8^+$ gBT-I as well as non-specific $CD8^+$ OT-I ~24 hr prior to epicutaneous infection with HSV-1.

At 25 hr p.i., some $CD4^+$ gDT-II (tracked using their congenic marker) could be detected in the draining LN (**Fig. 4.12B**). Nonetheless, there was no significant difference in terms of CD69 upregulation between mice receiving activated $CD4^+$ T cells and those that did not (**Fig. 4.12B, C**). Although we observed a slight increase in the mean fluorescence intensity (MFI) of CD69 on $CD8^+$ gBT-I, there was also a corresponding elevation in this marker by non-specific $CD8^+$ OT-I cells (**Fig. 4.12D**). Hence, the minor increase in CD69 expression may be attributable to an increased inflammatory milieu in the presence of transferred activated $CD4^+$ T cells in the LN, perhaps through secretion of inflammatory cytokines. However, this increase was not seen in non-draining LN (data not shown). Similarly, both groups showed comparable CD25 (IL-2Rα) expression (**Fig. 4.12E**), a molecule known to be induced upon help-dependent priming (Smith et al., 2004).

We also examined the draining LN at 60 hr p.i. for $CD8^+$ T cell division. Both groups showed similar numbers as well as proportion of divided $CD8^+$ gBT-I cells (**Fig. 4.12F-H**). Together, our data indicated that introduction of activated HSV-specific $CD4^+$ T cells prior to infection did not significantly alter the priming kinetics of $CD8^+$ T cells.

4.2.12 $CD8^+$ T cell priming is delayed in MHC-II knockout mice.

In addition to introducing activated $CD4^+$ T cells as a means to accelerate help, the opposite strategy is to negate the provision of help using MHC-II knockout transgenic mice. In the absence of MHC-II expression, cognate CD40-CD40L interaction – crucial for DC 'licensing' – between antigen-specific $CD4^+$ T cells and their antigen-presenting DC could not take place.

By measuring CD69 expression by $CD8^+$ gBT-I at 24, 48 and 72 hr p.i., we revealed that whereas $CD8^+$ gBT-I upregulated CD69 at 48 hr p.i. in wildtype mice, in MHC-$II^{-/-}$ this upregulation was delayed until 72 hr p.i. (**Fig. 4.13**) This indicated that the priming of $CD8^+$ T cells was further delayed in the absence of

Figure 4.12 Pre-activated CD4$^+$ T cells did not accelerate CD8$^+$ T cell priming

(A) Schematics of experimental design: 5x10^5 CellTrace Violet CD8$^+$ gBT-I and OT-I were co-transferred into recipient C57BL/6 mice. At 5-6 hr before infection, mice received either 10^6 *in vitro* activated CD4$^+$ gDT-II or left untreated prior to epicutaneous HSV-1 infection. Draining brachial LN were recovered at 25 hr and 60 hr p.i. for flow cytometry analysis.

(B) Representative contour plots showing CD69 upregulation of HSV-specific gBT-I (red, left) and non-specific OT-I (cyan, right) at 25 hr p.i. in draining brachial LN of mice transferred with (bottom row) or without (top row) pre-activated CD4$^+$ gDT-II. CD69 expression of endogenous CD8$^+$ T cells is shown in grey. Panel to the right show detection of CD4$^+$ gDT-II identified as EGFP$^+$ CD4$^+$ Vα3.2$^+$ population.

(C, E) Proportion of CD69^{hi} (C) and CD25^{hi} (E) gBT-I (red) and OT-I (cyan) in draining brachial LN at 25 hr p.i.

(D) Geometric mean fluorescence intensity (gMFI) of CD69 in gBT-I (red), OT-I (cyan), and endogenous CD8$^+$ T cells (orange) in draining brachial LN at 25 hr p.i.

(F) Representative histograms showing proliferation of gBT-I (red, left) and OT-I (cyan, right) as measured by dilution of CellTrace Violet at 60hr p.i. in draining brachial LN of mice treated with (bottom row) or without (top row) pre-activated CD4$^+$ gDT-II. Baseline CellTrace Violet level as measured from endogenous CD8$^+$ T cell is shown in grey. Panel to the right show detection of CD4$^+$ gDT-II identified as EGFP$^+$ CD4$^+$ Vα3.2$^+$ population.

(G) Proportion of divided (CellTrace Violet$_{lo}$) gBT-I (red) and OT-I (cyan) in draining brachial LN at 60 hr p.i.

(H) Number of divided gBT-I in draining brachial LN at 60 hr p.i.

Data pooled from 2 independent experiments, n = 10 per group. Error bars represent mean ± SEM. (C, D, G) One-way ANOVA, Tukey's multiple comparisons, (E, H) unpaired Student t test. ns, not significant.

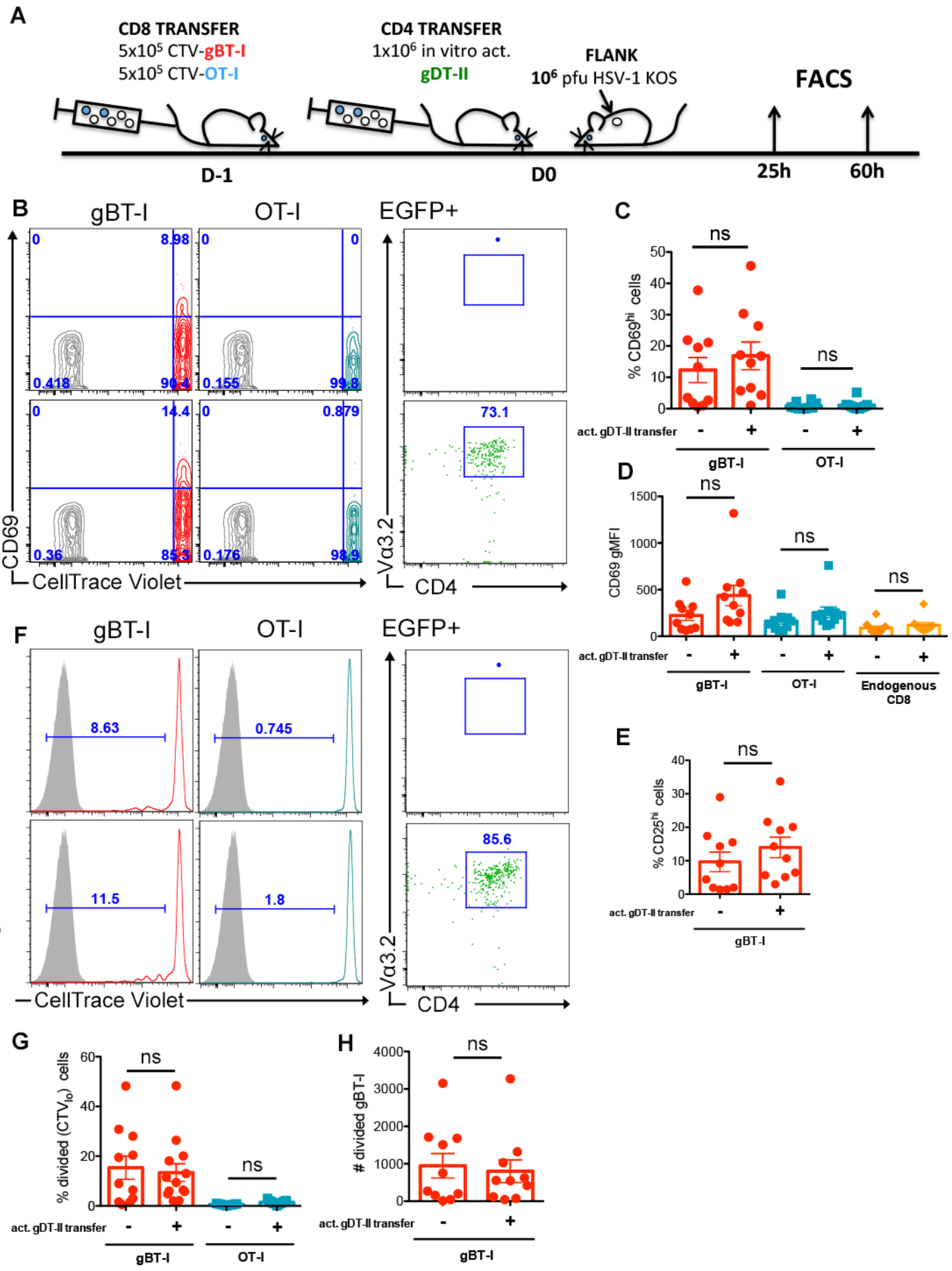
A
CD8 TRANSFER
5x10^5 CTV-gBT-I
5x10^5 CTV-OT-I
CD4 TRANSFER
1x10^6 in vitro act.
gDT-II
FLANK
10^6 pfu HSV-1 KOS
FACS
D-1
D0
25h
60h
B
gBT-I
OT-I
EGFP+
No transfer
+gDT-II
CD69
CellTrace Violet
Vα3.2
CD4
0
8.98
0.418
90.4
0.155
99.8
14.4
0.36
85.3
0.879
0.176
98.9
73.1
C
% CD69hi cells
ns
act. gDT-II transfer
gBT-I
OT-I
D
CD69 gMFI
Endogenous CD8
F
8.63
0.745
11.5
1.8
85.6
E
% CD25hi cells
G
% divided (CTVlo) cells
H
divided gBT-I

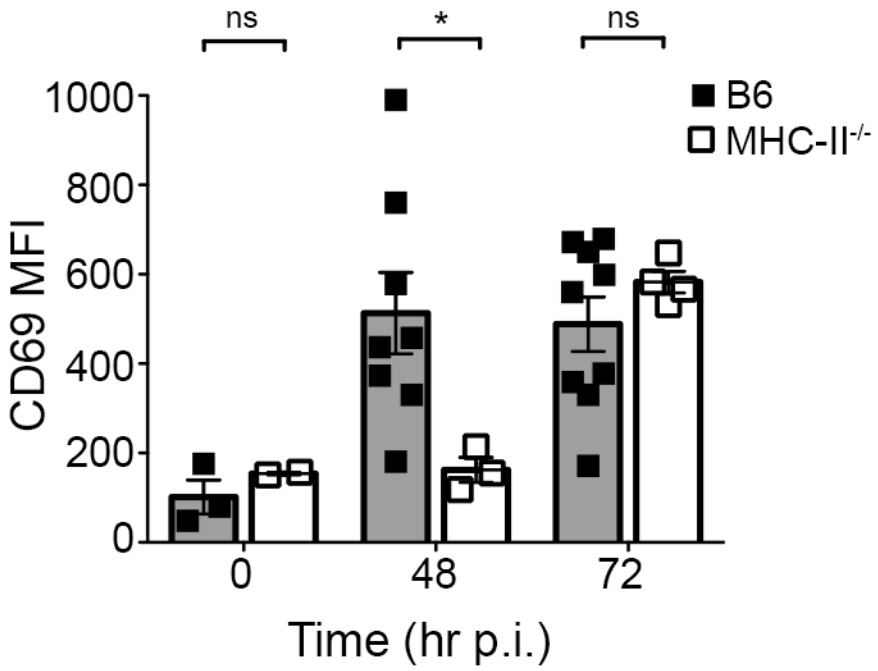

Figure 4.13 CD8⁺ T cell priming is delayed in MHC-II$^{-/-}$ mice
Wildtype or MHC-II$^{-/-}$ (AB^{o}) mice receiving 5x10^{5} CD8^{+} gBT-I cells were epicutaneously infected with HSV-1. Mean fluorescence intensity (MFI) of CD69 in CD8^{+} gBT-I recovered from draining brachial LN of wildtype (grey bars) or MHC-II$^{-/-}$ (white bars) at 0, 48 and 72 hr p.i. Error bars represent mean ± SEM. *$p<0.05$, one-way ANOVA, Tukey's multiple comparisons. ns, not significant.

$CD4^+$ T cell help. In short, our results suggest that multiple components of the immune response likely contributed to the delay of $CD8^+$ T cell activation.

4.2.13 Activation kinetics during skin LCMV and VV infections.

Our data from preceding sections suggested that following epicutaneous HSV-1 infection $CD8^+$ T cell priming was delayed relative to $CD4^+$ T cells. Few studies have examined the priming kinetics of both $CD4^+$ and $CD8^+$ T cells in infectious settings, and most of these studies have employed subcutaneous or intravenous routes of infection as their models. Such approaches allow pathogens to access the secondary lymphoid organs and thus may induce an altered set of priming conditions.

We wished to examine if differential $CD4^+$ and $CD8^+$ T cell priming kinetics during localised HSV-1 infection observed is also extended to other viral infections when introduced epicutaneously. To this end, mouse lymphocytic choriomeningitis virus (LCMV) as well as vaccinia virus (VV) were employed as infectious agents.

For LCMV infection, $CD4^+$ SMARTA and $CD8^+$ P14 TCR transgenic T cells specific for LCMV gp33 and gp61 epitopes respectively were employed to track the priming response of $CD4^+$ and $CD8^+$ T cells. $5x10^5$ CellTrace Violet-labelled $CD4^+$ SMARTA and $CD8^+$ P14 cells were adoptively transferred into recipient mice prior to infection with 10^6 pfu LCMV on scarified skin. While activation of $CD4^+$ SMARTA cells was clearly detectable by 12 hr p.i., $CD8^+$ P14 cells also upregulated CD69 as early as 18hr p.i. CD69 expression of both T cells peaked at 48 hr p.i., at which point these populations demonstrated almost synchronous division (**Fig. 4.14A, B**).

With VV infection, we used recombinant VV expressing OVA epitopes and tracked the T cell activation with $CD4^+$ OT-II and $CD8^+$ OT-I over the first 3 days of infection. Like LCMV, both $CD4^+$ and $CD8^+$ T cells showed similar profiles of activation and proliferative kinetics (**Fig. 4.14C, D**). Together, our data showed that $CD4^+$ and $CD8^+$ T cells did not appear to show distinct timing of activation

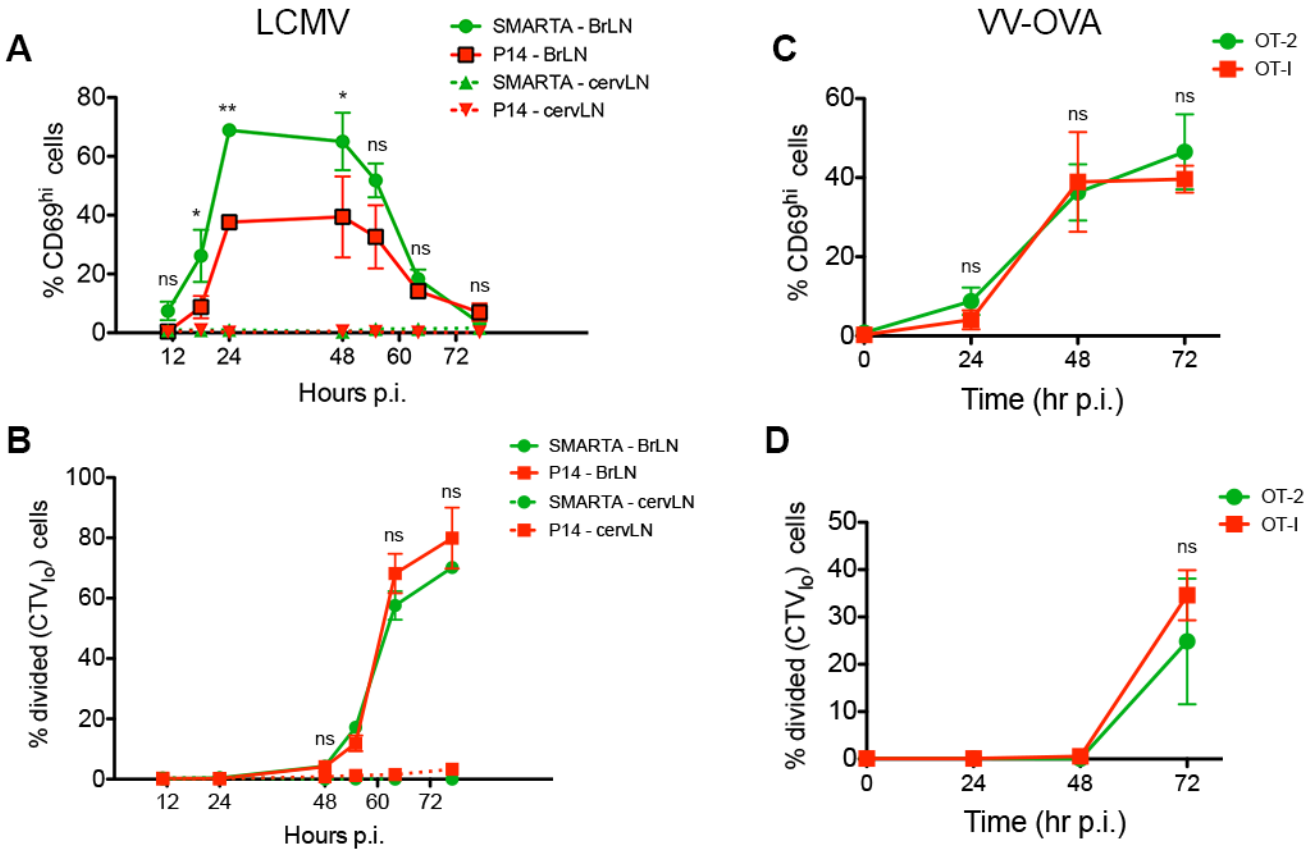

Figure 4.14 Priming kinetics of CD4⁺ and CD8⁺ T cells during epicutaneous LCMV and VV infection

(A, B) C57BL/6 mice transferred with CD4⁺ SMARTA.EGFP and CD8⁺ P14.Ly5.1 were epicutaneously infected with 10^6 pfu LCMV. Proportion of $CD69^{hi}$ (A) and divided cells ($CellTrace\ Violet_{lo}$) (B) in CD4⁺ SMARTA (green) and CD8⁺ P14 (red) from draining brachial LN (solid line) and non-draining cervical LN (dotted line) over 72 hr p.i.

Data from 1 experiment, n = 3-4 per time point.

(C, D) C57BL/6 mice were transferred with CD4⁺ OT-II.Ly5.1 and CD8⁺ OT-I.EGFP prior to epicutaneous infection with 10^6 pfu VV-OVA. Proportion of $CD69^{hi}$ (C) and divided cells ($CellTrace\ Violet_{lo}$) (D) in CD4⁺ OT-II (green) and CD8⁺ OT-I (red) from draining brachial LN over 72 hr p.i.

Data from 1 experiment, n = 3 per time point, n = 1 for D0.

Error bars represent mean ± SEM. *p<0.05, **p<0.01, paired Student t test. ns, not significant.

during both LCMV and VV infections as we did with HSV-1, but resembled more of the priming kinetics profile of subcutaneous HSV infection.

4.3 DISCUSSION

Coordination of $CD4^+$ and $CD8^+$ T cells is critical in providing protective immunity against many pathogens. It is well established that $CD4^+$ and $CD8^+$ T cells exhibit marked distinctions not only in their effector functions, but also in priming, proliferation, differentiation as well as migration. For example, though still heavily debated, proliferation of $CD8^+$ T cell is typically attributed to 'autopilot' programming upon sufficient TCR stimulation (Kaech and Ahmed, 2001; van Stipdonk et al., 2003), whereas $CD4^+$ T cells rely upon antigen persistence to maximise clonal expansion (Obst et al., 2005; Obst, 2015). Both T cells also adopt distinct surveillance strategies while traversing the LN in search of cognate antigen, resulting in different transit time and reliance on MHC interactions (Mandl et al., 2012). Furthermore, it has previously been proposed that during genital HSV-2 infection, effector $CD4^+$ T cells arrive at the infected mucosa and regulate entrance of effector CTLs via local cytokine and chemokine production (Nakanishi et al., 2009), underscoring a highly coordinated response in pathogen clearance.

Nonetheless, few studies have directly compared $CD4^+$ and $CD8^+$ T cell activation during infection. While the current paradigm on T cell priming presupposes synchronous activation of both T cell subsets upon immune challenge, here we demonstrated that during localised HSV-1 infection activation of $CD4^+$ and $CD8^+$ T cells was temporally staggered. This also helps to explain the separate entry of both T cells into effector sites. In this chapter, we sought to dissect the underlying mechanisms that contribute to the discordant timing of $CD4^+$ and $CD8^+$ T cell activation.

Priming of T cells is complex and often involves integration of a multitude of biochemical and cellular factors. One question regarding the timing of T cell priming was whether affinity of the TCR transgenic T cells contributed significantly to this observation. While Zehn et al. (2009) have shown that variations in peptide affinity affected the magnitude of expansion but not the initial proliferation of $CD8^+$ T cells, there is a paucity of studies that directly

compare CD4+ and CD8+ T cells for their TCR affinity. Our experimental endeavour through subcutaneous injection of viral peptides showed that contrary to epicutaneous infection, CD8+ gBT-I cells elicited a stronger activation phenotype than CD4+ gDT-II cells. Although our results suggest that the transgenic CD8+ gBT-I cells are equally if not more sensitive to their cognate peptide, this interpretation may be complicated by the fact that relatively stable peptide-MHC-II binding means cell surface exchange of peptide on MHC binding clefts is probably less efficient compared to MHC-I, resulting in a comparatively diminished display of peptide-MHC-II complexes (Neefjes et al., 2011). Nonetheless, our results argue that even at low peptide concentration, CD8+ gBT-I cells showed no signs of impaired antigen recognition.

Differential expression of virus proteins and the distinct presentation pathways on MHC-I and MHC-II may also influence the priming kinetics of CD8+ and CD4+ T cells. There is some evidence that HSV virion surface expression of glycoprotein D is ~11 times higher than glycoprotein B (Handler et al., 1996), though epitope presentation kinetics has been shown to be notoriously difficult to quantify, even more so when antigen is cross-presented (Croft et al., 2015; Tscharke et al., 2015). In our attempts to explore the contribution of these factors, we performed subcutaneous infection to deliver viruses directly to the draining LN, with either co-infection of recombinant flu viruses expressing gB or gD inserted into their neuraminidase stalk, as well as with HSV-1. With HSV-1, there was still a slight delay in CD8+ T cell priming (~6 hr), which may be attributable to the lower gB expression as noted above. In the case of subcutaneous flu infection, gB and gD were expressed under the same promoter (NA), theoretically equalising the amount of gD and gB antigen on virions. Indeed, we noted almost equal proportions of activated CD4+ and CD8+ T cells. Whether this represents equivalent processing and presentation kinetics on MHC-II and MHC-I, or that infection of LN cells contributed to direct presentation to CD8+ T cells is not clear. Influenza virus can enter macrophages via sialic acid-binding receptors, such as MMR (Upham et al., 2010), and although it usually leads to abortive infection, synthesis of viral polypeptide had been detected (Rodgers and Mims, 1981). Furthermore, the rate of viral protein expression is also different between

HSV and flu virus, and it is likely that the more rapid replicative kinetics of flu virus allows much higher expression of the gB epitope via direct presentation. Additionally, even with subcutaneous HSV-1 infection, cross-presentation appears to remain the dominant form of antigen presentation to CD8 T cells (Singh and Cresswell, 2010), though the infectious dose employed in this study was ~20 times lower than used in our experiments. This issue could perhaps be eliminated with an engineered HSV-1 where both gB and gD share the same promoter.

To further complicate matters, a previous study has reported that *de novo* synthesis of gB is required for priming of $CD8^+$ T cells in HSV-1 infection, as UV-irradiated non-replicative virus failed to induce their activation (Mueller et al., 2003). In our hands, $CD4^+$ T cell activation was not impaired using UV-inactivated virus, and in accordance with the previous report, activation of $CD8^+$ T cells was completely abrogated. This suggested that $CD4^+$ T cells might become activated from virion-derived antigen present in the inoculum, thereby resulting in their rapid activation. Whether the prerequisite for newly synthesised gB polypeptide stems from lower abundance of gB on the virions, or that virion-derived gB antigen is peculiarly unsuitable for antigen cross-presentation is not clear.

In short, while we could not definitively pinpoint the sources that led to asynchronous timing of $CD4^+$ and $CD8^+$ T cell activation during cutaneous HSV-1 infection, our results argue that synthesis of viral glycoprotein B by infected cells, the temporal requirement for antigen handover, as well as the dependence for help each contributed to the kinetic difference of $CD8^+$ T cell activation (Refer **Chapter 7** for further discussion).

Finally, we explored whether the staggered pattern of $CD4^+$ and $CD8^+$ T cell priming represents a unique aspect of skin infection. It should be noted that priming conditions could be vastly different in other peripheral organs, and a heterogeneous population of DC shapes the priming dynamics during infection depending on the tissues. For example, migratory $CD103^+$ DC play roles in early

cross-presentation to $CD8^+$ T cells during pulmonary influenza and poxvirus infections (GeurtsvanKessel et al., 2008; Beauchamp et al., 2010), and so too does a migratory $CD8\alpha^-$ population during HSV-2 infection of the genital mucosa (Lee et al., 2009). An equivalent tissue-derived DC, however, is absent during epicutaneous HSV-1 infection, and priming of $CD8^+$ T cells is reliant upon LN-resident $CD8\alpha^+$ DC (Bedoui et al., 2009). It was possible that a lack of cross-presenting $CD103^+$ DC contribution led to the delayed CTL priming, and thus we questioned if this was a distinct feature of flank skin immunity.

Our brief investigation of epicutaneous LCMV and VV infections suggested otherwise, as we found similar priming kinetics between $CD4^+$ and $CD8^+$ T cells. A number of possible factors might explain the differences between HSV and LCMV or VV. First, with lymphatic vessels lining the superficial dermis (Tal et al., 2011), it is conceivable that viruses gain entry to these vessels and allow them to infect the LN. Interestingly, attempts to detect HSV-1 in draining LN via plaque assay (data not shown), immunofluorescence microscopy (data not shown) as well as RT-PCR of LN DCs (Allan et al., 2006) were negative. HSV glycoproteins, which bind strongly to heparan sulfate chains (found abundantly in the epidermis) as well as dermatan sulfate (found in the dermis) of the host cellular receptors, may strictly limit the tissue tropism to the skin through binding of the virions to the epidermis and dermis. In contrast, LCMV binds to O-mannosylated α-dystroglycan (α-DG), which is ubiquitously expressed on many cell types and not restricted to epithelial cells (Cao et al., 1998, Imperiali et al., 2005). Indeed, preliminary experiments using plaque assay suggested LCMV-infected cells are detectable in the draining LN at 24 hr after epicutaneous infection (Y. Alexandre, personal communication). On the other hand, the entry receptor for VV has not been determined and it is purported to enter most mammalian cells (McFadden et al., 2005).

Second, HSV impairs migration of infected DC (Theodoridis et al., 2011; Puttur et al., 2010), and also induces DC apoptosis (Jones et al., 2003). These findings are consistent with the lack of HSV-infected cells observed in LN during epicutaneous infection as mentioned above. It remains unclear if LCMV- or VV-

infected DC could migrate to the dLN and prime CTL via direct presentation. Although LCMV strain Armstrong binds with low affinity to α-DG expressed on $CD11c^+$ cells (Sevilla et al., 2004), some DC could be infected and contribute to CTL priming. Finally, primary responses against both VV and LCMV are less dependent on CD4 T cell help (Rahemtulla et al., 1991), which may alter the kinetics of $CD8^+$ T cell activation. In short, differences in tissue tropism, viral pathogenesis and immune evasion may explain the differences in T cell priming kinetics observed.

In summary, in this chapter the spatiotemporal kinetics of $CD4^+$ and $CD8^+$ T cell priming and post-differentiation migration was characterised during localised infection with HSV-1. Our work demonstrated asynchronous timing of $CD4^+$ and $CD8^+$ T cell activation, which led to early expansion of $CD4^+$ T cells and their precession in infiltrating the effector sites.

CHAPTER FIVE:

CELLULAR DYNAMICS OF T CELL RESPONSES DURING HSV INFECTION

5.1 INTRODUCTION

The optimal induction of cell-mediated immunity critically relies upon rapid antigen-specific encounter between T lymphocytes and their APC, delivery of co-stimulatory and 'help' signals, as well as the presence of differentiation factors allowing for the acquisition of effector and memory-forming capabilities on the part of lymphocytes. This is typically regulated by a series of dynamic events within the reactive SLO involving a complex interplay between an array of immune cells, where integrative signalling influences the magnitude and quality of the resultant immune response.

In the preceding chapter, we demonstrated the temporally distinct activation kinetics of $CD4^+$ and $CD8^+$ T cells during localised HSV-1 infection. Since antigen presentation to $CD8^+$ T cells requires specialised LN-resident $CD8\alpha^+$ DC, the handover of antigen between migratory and resident DC and subsequent presentation to $CD4^+$ and $CD8^+$ T cells likely involves multiple subsets of DC (Allan et al., 2006; Bedoui et al., 2009). The requirement for $CD4^+$ T cell help, comprising cognate CD4-CD8-APC interactions, is also crucial for the robust generation of primary CTL responses to HSV (Smith et al., 2004). The dynamics of these cellular interactions, as the mounting of a primary response unfolds, has remained poorly defined.

With the advent of intravital imaging technologies, the cellular dynamics of T cell activation and differentiation can now be visualised and tracked throughout the course of infection. Employing two-photon microscopy, we wished to interrogate several key aspects of immune priming described above: first, we wanted to examine the spatial and temporal coordination of $CD4^+$ and $CD8^+$ T cell priming in the LN during localised viral infection; second, we investigated how diverse subsets of DC participate in contributing to this immunological puzzle; and finally, we hoped to elucidate the dynamic process that led to the cooperation between helper $CD4^+$ and cytotoxic $CD8^+$ T cells in mediating protective immunity, namely, how $CD4^+$ T cells deliver help and 'license' DC.

5.2 RESULTS

5.2.1 Establishing a hind flank infection model for imaging experiments.

Intravital imaging of the LN demands surgical preparation that exposes the living tissue and allows light to enter the tissue with minimal perturbation. The most common cutaneous LNs established for intravital microscopy are the inguinal LN [iLN] (situated under the hind flank) and popliteal LN [pLN] (situated within the knee of the hind limbs), due to their relatively accessible location for surgical manipulation.

The mouse model of epicutaneous HSV-1 infection that we have employed so far involves infection of an area of skin near the dorsal tip of the spleen, which drains to the brachial LN [bLN] in the forelimb "armpit". Difficulty in clearing soft tissues for exposure and stabilisation of the bLN prompted us to shift the infection site towards the hind flank (hind limb-torso transition), a position where lymph drains to the more accessible iLN . For clarity, the initial infection site is termed 'spleen tip' (ST) while the modified site is termed 'hind flank' (HF) (**Fig. 5.1A**).

To ascertain that the priming kinetics of the initial infection model can be reproduced, we established the activation and proliferative kinetics of both $CD4^+$ gDT-II and $CD8^+$ gBT-I cells in the hind flank model by measuring CD69 expression and CellTrace Violet dilution in the draining LNs. Similar to the experimental setup in **Section 4.2.5**, $5x10^5$ $CD4^+$ gDT-II and $CD8^+$ gBT-I cells each were adoptively transferred into two groups of recipient mice, each to be infected on the scarified site in either the hind flank or spleen tip regions. We examined the draining iLNs and bLNs (for 'hind flank' and 'spleen tip' infections respectively) at two nominated time points: 24 hr (early priming phase) and 74 hr (proliferation phase) p.i. At both time points, we observed comparable levels of CD69 upregulation in both $CD4^+$ gDT-II and $CD8^+$ gBT-I between 'hind flank' and 'spleen tip' infected mice, as is evident from the similar proportion of $CD69^{hi}$ cells (**Fig. 5.1B, C**). The division profiles of both T cells in 'hind flank' infected

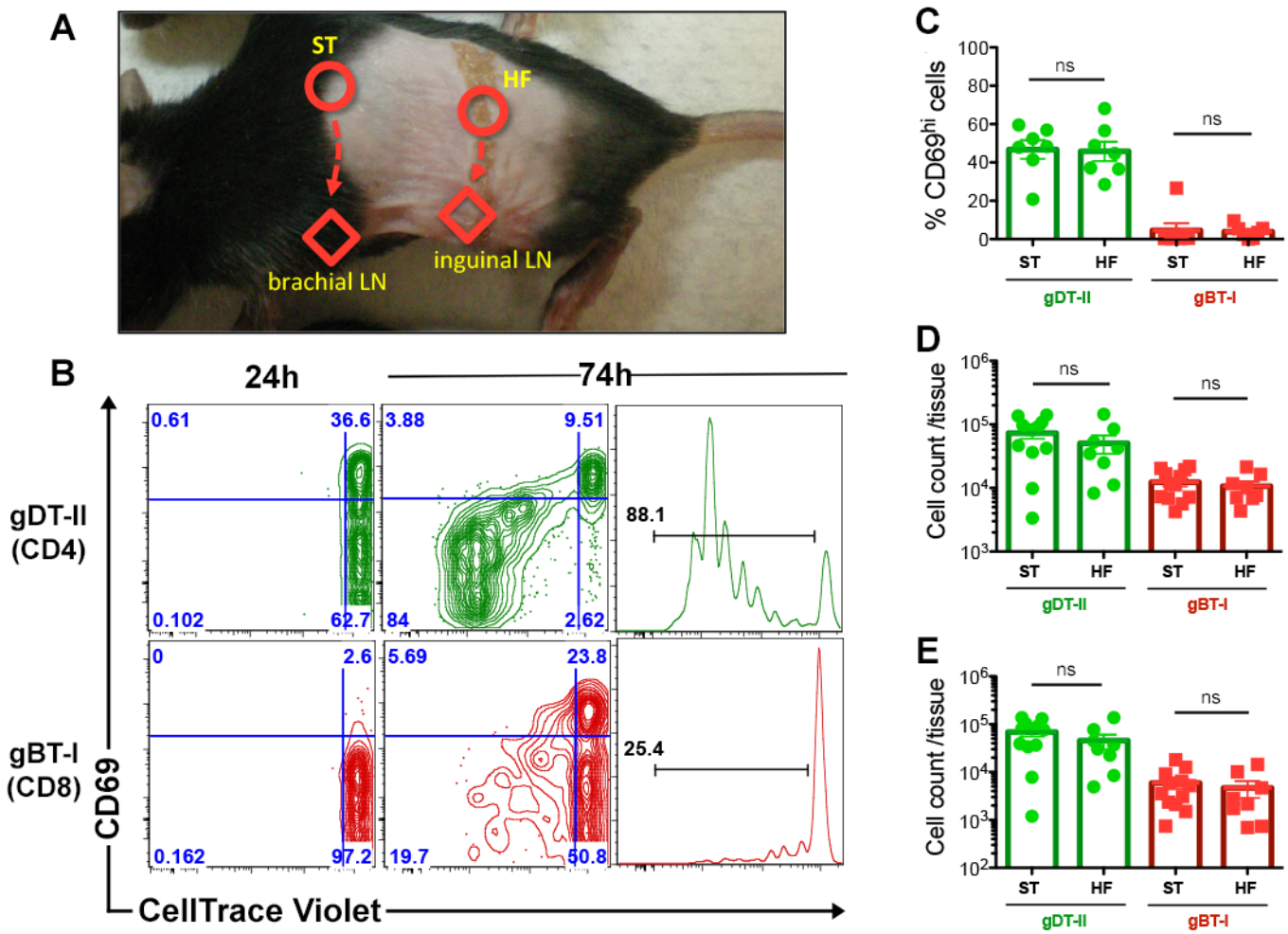

Figure 5.1 Characterisation of CD4⁺ and CD8⁺ T cell priming during 'hind flank' HSV-1 infection

5x10^5 CellTrace Violet-labelled CD4⁺ gDT-II.Ly5.1 and CD8⁺ gBT-I.Ly5.1 cells were adoptively transferred into recipient C57BL/6 mice 1 day prior to epicutaneous HSV-1 infection. Mice were either infected at the 'spleen tip' (ST) or 'hind flank' (HF) regions.

(A) Sites of infection together with their draining LN. ST drains to bLN, and HF drains to iLN.

(B) Representative contour plots showing upregulation of CD69 in CD4⁺ gDT-II (top row, green) and CD8⁺ gBT-I (bottom row, red) in draining iLN at 24 hr and 74 hr p.i. Histograms depicting CellTrace Violet dilution were shown to the right corresponding to the contour plot at 74 hr p.i.

(C) Proportion of CD69^{hi} cells in draining bLN (ST) and iLN (HF) at 24 hr p.i.

Error bars represent mean ± SEM. One-way ANOVA, Tukey's multiple comparisons. ns, not significant.

(D-E) Number of total (D) and divided cells (CellTrace Violet$_{lo}$) (E) recovered per draining LN at 74 hr p.i.

Data pooled from 2-3 independent experiments; n = 8-12 mice per time point. Error bars represent mean ± SEM. For (D), one-way ANOVA, Tukey's multiple comparisons and for (E), one-way ANOVA, Tukey's multiple comparisons on log transformed values. ns, not significant.

mice also paralleled those of the 'spleen tip' infected mice, exhibiting similar CellTrace Violet dilution as well as the number of total and divided cells (**Fig. 5.1B, D-E**). Therefore, we demonstrated the viability of this modified 'hind flank' HSV-1 infection model, which readily reproduces the differential priming kinetics as observed in the initial 'spleen tip' model (**Section 4.2.5**).

5.2.2 Cellular dynamics of CD4$^+$ and CD8$^+$ T cells in LN after epicutaneous HSV infection.

The ability to visualise migratory behaviour of T cells via intravital microscopy opens up new avenues for understanding the dynamic state changes undergone by T cells during priming and differentiation. At steady state, T cells migrate at high velocity while scanning for their cognate antigen through the formation of transient TCR-pMHC interactions with APC in the LN. Upon antigen recognition, T cells become arrested to engage in sustained interactions with APC (Mempel et al., 2004; Miller et al., 2004a).

Having established a 'hind flank' infection model suitable for imaging, we proceeded to characterise the migratory dynamics of CD4$^+$ and CD8$^+$ T cells in the draining iLN through *in vivo* visualisation by two-photon microscopy. Mice receiving 5x10^5 fluorescent CD4$^+$ gDT-II.EGFP and CD8$^+$ gBT-I.DsRed cells were left uninfected or infected with HSV-1 on the hind flank prior to iLN imaging.

In uninfected mice, both CD4$^+$ gDT-II and CD8$^+$ gBT-I cells migrated at relatively high velocity (**Fig. 5.2A, B**, **Movie S1A**). The mean velocities of these naïve T cells were used to establish baselines for comparison purpose (**Fig. 5.2C, D**). However, we noted a disparity of velocities between naïve CD4$^+$ gDT-II and CD8$^+$

Movie S1. Early clustering of HSV-specific CD4$^+$ T cells in the draining LN after infection. (LINK)

Mice were adoptively transferred with CD4$^+$ gDT-II and CD8$^+$ gBT-I T cells prior to intravital imaging of the inguinal LN. **S1A**, migration of naïve CD4$^+$ gDT-II (green) and CD8$^+$ gBT-I (red) T cells in uninfected mice. **S1B**, three examples of the clustering behavior of CD4$^+$ gDT-II T cells (green) and lack of clustering by CD8$^+$ gBT-I T cells (red) 16-24 hr after HSV-1 infection. Maximum intensity projection time series images were acquired by two-photon microscopy.

gBT-I cells (~14μm/min vs ~11μm/min) (**Fig. 5.2C**). This might reflect a difference in the innate disposition in migratory properties of these transgenic cells. In comparison, $CD4^+$ OT-II and $CD8^+$ OT-I cells averaged ~11μm/min and 12μm/min respectively (**Section 5.2.4**), although it should be noted that intranodal T cell motility can vary widely from ~10μm/min to ~15μm/min (Miller et al., 2003; Worbs et al., 2007) depending on the experimental setup. For comparison purpose, mean velocities were also normalised to observe relative change compared to naïve cells (**Fig. 5.2D**).

During infection, at 12-24 hr p.i., $CD4^+$ gDT-II cells demonstrated a marked reduction in migratory velocity compared to their naïve counterparts (~7μm/min vs ~14μm/min) and also formed dynamic clusters (**Fig. 5.2A-D**, **Movie S1B**). The clustering behaviour is typically attributed to those T cells engaging in long-lived, stable interaction with their APC upon encountering cognate antigen, and has been used as a readout for T cell activation in imaging studies (Mempel et al., 2004; Miller et al., 2004a).

On the contrary, during this phase (12-24 hr p.i.) $CD8^+$ gBT-I cells did not exhibit a significant change in their migratory velocity, which remained similar to naïve $CD8^+$ gBT-I cells (**Fig. 5.2C, D**, **Movie S1B**). The observation here corresponded to previous flow cytometric data that at this early time point, only $CD4^+$ T cells showed signs of activation via CD69 upregulation (**Section 4.2.5**). Hence, we categorised the period between 12-24 hr p.i. in which the movies were taken as the 'early priming phase.'

During the 'late priming phase,' starting at ~40 hr p.i., $CD8^+$ gBT-I cell clusters could also be detected in the T cell zone. Their mean migratory velocity also showed a significant reduction compared to naïve $CD8^+$ gBT-I cells, but not as pronounced as the difference observed for $CD4^+$ gDT-II cells (**Fig. 5.2C-D**, **Movie S2**). This may be accounted for by (i) fewer $CD8^+$ T cell clusters observed within our imaging volumes compared to $CD4^+$ T cell clusters; and (ii) the insufficient resolution in discriminating individual cells in dense clusters, resulting in an underestimation of the amount of cells present within the imaging volume.

Figure 5.2 Cellular dynamics of CD4⁺ and CD8⁺ T cell migration in draining LN during HSV-1 infection

$5x10^5$ CD4⁺ gDT-II.EGFP and CD8⁺ gBT-I.DsRed were co-transferred into recipient C57BL/6 mice prior to epicutaneous HSV-1 infection and iLN subjected to intravital two-photon imaging.

(A) Maximum intensity projection images depicting CD4⁺ gDT-II (green) and CD8⁺ gBT-I (red) clustering in the T cell zone of iLN (imaging depth ~150-200μm under LN capsure) at different phases of infection: uninfected (left), early (16 hr, middle), and late (40 hr, right). See also **Movies S1** and **S2**.

(B) Cell tracks of CD4⁺ gDT-II (top row) and CD8⁺ gBT-I (bottom row) colour-coded to display mean track velocity at the indicated time points. Red paths in tracks correspond to higher track velocities, while white paths show slower track velocities. Data from **Movies S1** and **S2**.

(C-D) Mean velocity of cell tracks showing actual velocity (C) or normalised to naïve cells (D). Each data point represents the mean velocity of all cell tracks per movie. Data pooled from at least 2 independent experiments; n=2-4 movies each from 2-6 mice per time point.

(E) Confinement ratio of cell tracks corresponding to (C) and (D).

(F) Proportion of clustering cells in iLN at different phases after infection. Each data point represents the proportion of clustering CD4⁺ gDT-II and CD8⁺ gBT-I cells in each imaging volume. Data pooled from 2 independent experiments; n = 4 mice per time point.

Error bars represent mean ± SEM. *p<0.05, **p<0.01, ***p<0.001, one-way ANOVA, Tukey's multiple comparisons. ns, not significant.

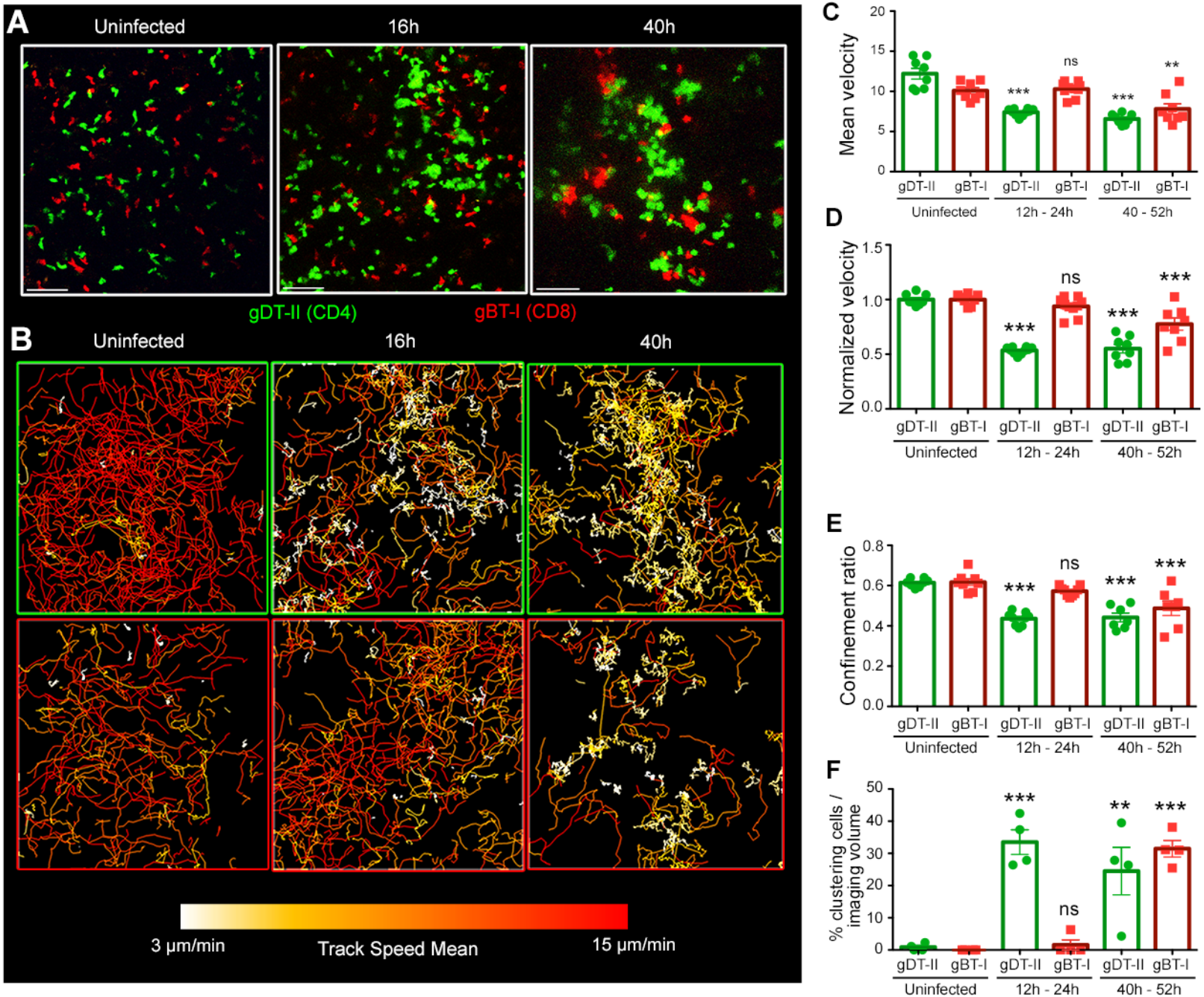
A
Uninfected
16h
40h
gDT-II (CD4)
gBT-I (CD8)
B
Uninfected
16h
40h
3 µm/min
Track Speed Mean
15 µm/min
C
Mean velocity
20
15
10
5
0
***
ns
***
**
gDT-II
gBT-I
Uninfected
12h - 24h
40 - 52h
D
Normalized velocity
1.5
1.0
0.5
0.0
***
ns
***
***
E
Confinement ratio
0.8
0.6
0.4
0.2
0.0
***
ns
***
***
F
% clustering cells / imaging volume
50
40
30
20
10
0
***
ns
**
***

Nonetheless, our results indicated that CD8$^+$ T cells only began to form clusters late in the response, mirroring the observation from our flow cytometric experiments.

Confinement ratios of the T cells were also calculated for each phase of infection, and the increased confinement observed for CD4$^+$ T cell migration during the early phase, as well as both CD4$^+$ and CD8$^+$ T cells during the late phase also agreed with the measures of their migratory velocities (**Fig. 5.2E**). This indicated increased retention of the T cells within an imaging volume, which was to be expected considering that many of these cells were visibly clustering.

To quantitate T cell clustering, we calculated the proportion of clustering T cells per imaging volume (**Movies S1**, **S2**). However, for reasons noted above, the lack of sufficient resolution prevented comprehensive tracking of clustering cells. Instead, we measured the proportion of clustering cells (defined as a minimum of 3 cells within 15μm cell centroid-to-centroid distance from each other) at snapshots every 10 minutes after manually correcting for cells not registered by the automated tracking function of our imaging processing software (Imaris), and averaged the measured proportions combined from all snapshots (time frames) (**Fig. 5.2F**). This revealed that a significant proportion of CD4$^+$ T cells formed clusters during the early phase whereas both CD4$^+$ and CD8$^+$ T cells clustered later. This closely corresponded with the decreased migratory velocities and increased confinement as measured above (**Fig. 5.2C-E**).

Interestingly, while both CD4$^+$ gDT-II and CD8$^+$ gBT-I cells clustered during >40 hr after infection, the majority of the clusters observed were relatively homogeneous (**Movie S2**). That is, the composition of the clusters was mostly

---

Movie S2. Late clustering of HSV-specific CD8$^+$ T cells in the draining LN after infection. (LINK)
Mice were adoptively transferred with CD4$^+$ gDT-II (green) and CD8$^+$ gBT-I T cells (red) prior to epicutaneous HSV-1 infection and intravital imaging of the inguinal LN. Three examples of the clustering behavior of CD4$^+$ gDT-II T cells (green) and CD8$^+$ gBT-I T cells (red) 40-48 hr after HSV-1 infection.

comprised of $CD4^+$ or $CD8^+$ T cells, with only a small number of the opposite cell type interacting transiently with the cluster (for example, a few $CD4^+$ T cells interacting with a cluster largely comprised of $CD8^+$ T cells). The formation of separate $CD4^+$ and $CD8^+$ T cell clusters was suggestive of their interaction with distinct cell types, perhaps with different DC subsets.

5.2.3 Migratory velocity of transgenic T cells was not affected by expression of different fluorescent proteins or dye labelling.

In the preceding section mice were transferred with fluorescent $CD4^+$ gDT-II.EGFP and $CD8^+$ gBT-I.DsRed T cells. Since we observed differences in the velocity of T cells from these two transgenic mice, a potential concern was that EGFP- and DsRed-expressing transgenic T cells may exhibit differential migratory behaviour (Xu et al., 2013).

To ascertain that both EGFP and DsRed variants of T cells were not compromised in their migratory behaviour, and since we did not have $CD4^+$ gDT-II cells expressing DsRed, we assessed the migration of $CD4^+$ OT-II as well as $CD8^+$ gBT-I cells expressing either colour. Equal numbers of $CD4^+$ OT-II.EGFP and OT-II.DsRed cells (or $CD8^+$ gBT-I cells for that matter) were adoptively transferred into recipient mice and their cellular movements recorded. Calculation of mean migratory velocities of the T cells showed highly comparable measurements regardless of the fluorescent proteins expressed (~10.5μm/min for both $CD4^+$ OT-II and $CD8^+$ gBT-I) (**Fig. 5.3A, B**).

In later experiments, we also utilised T cells labelled with fluorescent dyes including CellTracker Deep Red (far red emission) or CellTrace Violet (violet emission). Over-labelling of cells with dye may improve signal intensity, but the increased toxicity can also negatively affect their motility and impair normal cellular functions (Progatzky et al., 2013). To determine if dye labelling of cells affected their migratory behaviour, as with the above experiment, we co-transferred transgenic T cells expressing fluorescent protein as well as their dye-labelled counterparts. Using T cells with fluorescent proteins (EGFP or DsRed) as baseline measurements, the average velocities were compared with dye-labelled

T cells to determine if cellular motility was impaired.

With excessive dye concentration (high concentration of CellTracker Deep Red), we observed that migration of CD4+ gDT-II cells was severely impeded (data not shown). In contrast, labelling at lower concentrations (500nM and 250nM) resulted in migratory velocities comparable to T cells marked with EGFP (**Fig. 5.3C**). Similarly, labelling of CD8+ gBT-I cells with 5μM CellTrace Violet also showed comparable velocities with DsRed-expressing gBT-I cells (**Fig. 5.3D**).

Although we did not test every possible permutation, our results here indicated that differences in fluorescent proteins and dye labelling utilised in our experiments did not compromise or negatively influence their motility and migratory behaviour.

5.2.4 Clustering behaviour of T cells is antigen-specific.

To ascertain that the clustering of T cells that we observed in previous experiments was a result of antigen-specific interaction between T cells and their APC, we co-transferred both antigen-specific and non-specific T cells into recipient mice before infection. For CD4+ T cells, antigen-specific gDT-II and non-specific OT-II were transferred and the draining iLN examined via intravital microscopy early during priming (12-24 hr p.i.). For CD8+ T cells, antigen-specific gBT-I and non-specific OT-I were employed and the late phase of priming (40 hr+ p.i.) was examined. In both cases, we noted that only antigen-specific T cells clustered, confirming that the clustering behaviour of T cells involved TCR-pMHC engagement (**Fig. 5.4A, B**, **Movie S3**). The change in mean migratory velocities of the antigen-specific T cells between naïve and infected mice also agreed with our previous findings (**Fig. 5.4C, D**). Interestingly, there was a slight but significant reduction in migratory velocity by non-specific CD4+

Movie S3. Antigen specific T cell clustering during HSV-1 infection. (LINK)
Mice were adoptively transferred with either CD4+ gDT-II (green) and OT-II (red; left panel) or CD8+ gBT-I (green) and OT-I (red; right panel) T cells prior to epicutaneous HSV-1 infection and intravital imaging of the inguinal LN. Two examples of cell migration and clustering are shown for each condition.

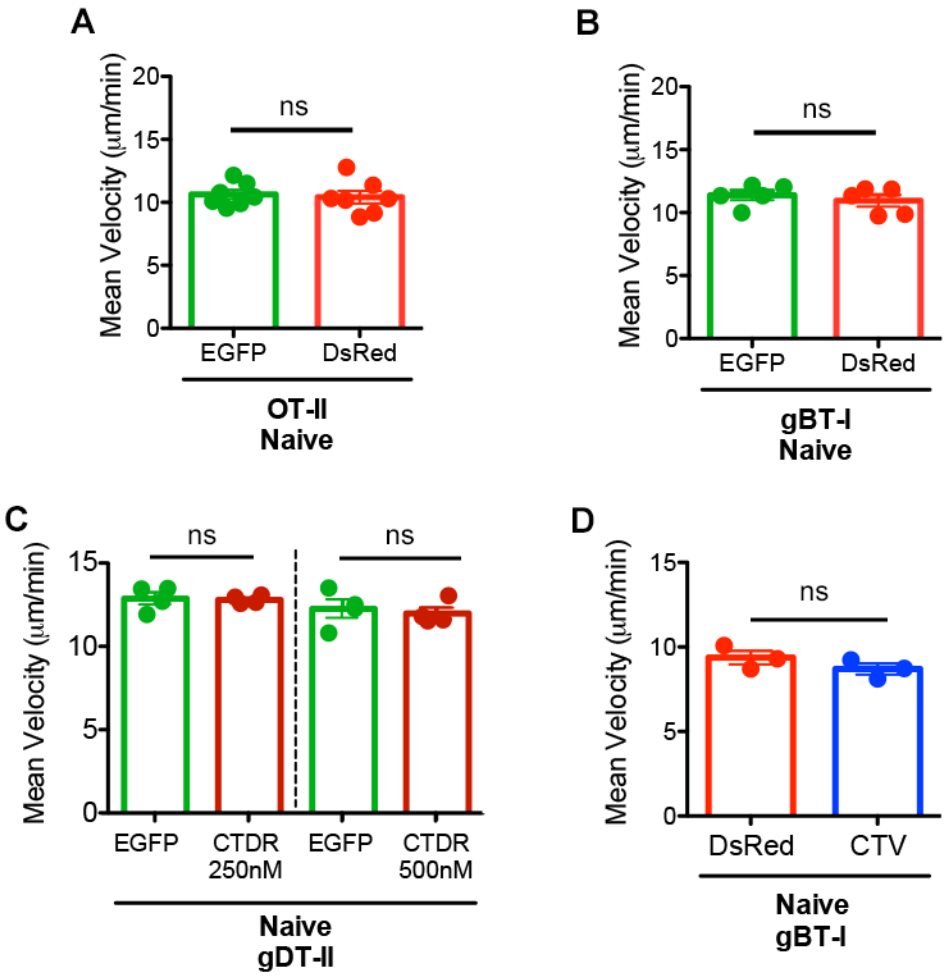

Figure 5.3 Characterisation of migration by T cells expressing fluorescent protein variants and cell tracking dyes

(A-B) $5x10^5$ EGFP- and DsRed-expressing variants of $CD4^+$ OT-II (A) or $CD8^+$ gBT-I (B) were co-transferred into recipient C57BL/6 mice.

(C) $5x10^5$ EGFP-expressing and CellTracker Deep Red-labelled $CD4^+$ gDT-II (250nM or 500nM) were co-transferred into recipient C57BL/6 mice.

(D) For $CD8^+$ gBT-I, DsRed-expressing and CellTrace Violet-labelled (5μM) cells were used instead.

Intravital two-photon imaging was performed on iLN of uninfected mice and mean migratory velocities of each cell population were calculated. Each data point represents the mean velocity of all cell tracks per move.

Data from 1 experiment; n = 2-3 movies each from 2 mice (A), 2-3 movies each from 3 mice (B), 2 movies each from 2 mice (C), 1-2 movies each from 2 mice (D). Error bars represent mean ± SEM. Paired Student t test. ns, not significant.

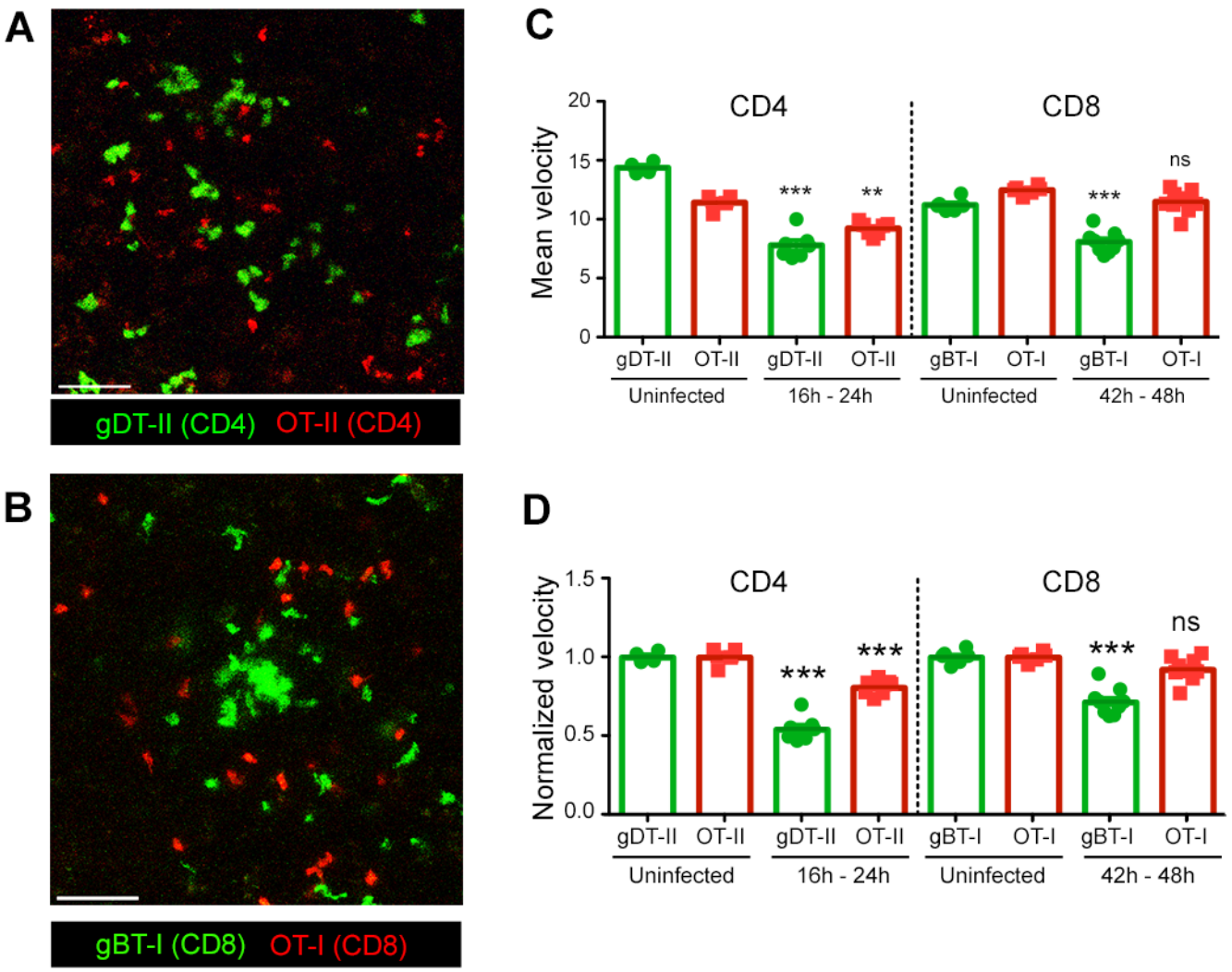

Figure 5.4 Clustering behaviour of T cells is antigen-specific

5x10^5 CD4$^+$ gDT-II.EGFP and OT-II.DsRed (A) or CD8$^+$ gBT-I.DsRed and OT-I.EGFP (B) were co-transferred into recipient C57BL/6 mice prior to epicutaneous HSV-1 infection and iLN subjected to intravital two-photon imaging.

(A-B) Maximum intensity projection images showing a snapshot of CD4$^+$ gDT-II and OT-II (A) or CD8$^+$ gBT-I and OT-I (B) in iLN after HSV-1 infection at 16 hr (A) and 42 hr (B) p.i. respectively.

(C-D) Mean velocity of cell tracks showing actual velocity (C) or normalised to naïve cells (D). Each data point represents the mean velocity of all cell tracks per movie. See also **Movie S3**.

Data pooled from at least 2 independent experiments; n=1-2 movies each from 4-7 mice per group. Error bars represent mean ± SEM. **p<0.01, ***p<0.001, one-way ANOVA, Tukey's multiple comparisons. ns, not significant.

OT-II cells compared to their naïve counterparts. This suggested that motility of $CD4^+$ T cells might in part be influenced by the inflammatory milieu of the LN during infection.

5.2.5 Localisation of T cells during early HSV infection.

Our intravital imaging data suggested that T cells were likely activated in the T cell zone during skin HSV-1 infection, since most of the clustering events occurred at least 100μm from the LN capsule. However, the limitation of light penetrating dense tissue such as a LN effectively restricted our imaging depth to no more than 300μm underneath the LN capsule from the cortical side. Furthermore, only small numbers of LN region were sampled, resulting in an incomplete picture of where T cells clustered. It was possible that $CD8^+$ T cells also formed clusters during the early phase but in the deeper paracortex, and thereby remained undetected by two-photon microscopy.

To address this, we imaged thick LN sections (of ~150μm thickness) that were sliced using a vibratome. With thicker sections, we hoped to capture the larger-sized clusters that are typically under-sampled in thinner sections imaged via conventional confocal microscopy. Longitudinal cross-sections of LN were used as they allowed visualisation of the cluster formation at various depths and in different LN compartments. Draining iLNs were harvested, sliced and imaged at 18 hr and 42 hr p.i. representing the early and late priming phases, respectively.

To facilitate detection and quantitation of clustering cells, we developed an analysis tool that allows automated detection of cell clusters (**Appendix A.1**). Interfacing the image processing software Imaris with MATLAB, which enables scripting of customised functions, this tool operates by calculating cell centroid-to-centroid distance from one another across the *xyz* dimensions. When a minimum of 3 cells falls within a proximity of 15μm from one another (the criteria of each parameter can be defined and adjusted manually by the user), these cells are then assigned to a cluster with a unique identifier. We chose a 15μm cell centroid-to-centroid distance by taking into account the approximate diameter of a lymphocyte (8-10μm). To establish baseline clustering frequencies

formed via random chance, LN sections from mock-infected mice were also used as controls.

With this method, we analysed LN sections from both early and late time points and calculated the proportion of clustering cells per LN section. In agreement with our intravital imaging experiments, only $CD4^+$ gDT-II clustered at 18 hr p.i. (early phase) whereas both $CD4^+$ gDT-II and $CD8^+$ gBT-I clustered at 42 hr p.i. (late phase) (**Fig. 5.5A-E**). In contrast, in mock-infected mice, there were virtually no detectable clusters in the LN (**Fig. 5.5E**). Thus, $CD4^+$ and $CD8^+$ T cell clustering was indeed temporally regulated and not due to the spatial limitation of our microscope in visualising deeper regions of the tissue.

Examining the localisation of T cell clusters in the LN cross-sections, we noted that most of the clusters were situated in the T cell zone, with very few $CD8^+$ T cell clusters forming in the periphery. This is in contrast to studies employing lymph-borne infection models where pathogens are delivered subcutaneously allowing their drainage to the LN, which results in activation of $CD8^+$ T cells in the interfollicular regions and under the SCS at the LN periphery (Hickman et al., 2008).

5.2.6 Cluster composition is relatively homogeneous.

As noted in **Section 5.2.2**, many of the T cell clusters observed appeared to be fairly homogeneous. We wanted to systematically examine the composition of the clusters detected using our cluster analysis tool as described in **Section 5.2.5** by measuring the relative homogeneity of these clusters. To aid in our quantitation task, we developed a tool to allow automated detection of a cluster (described in **Section 5.2.5**, but now defined as a minimum of 4 cells) that also calculates the proportion of $CD4^+$ and $CD8^+$ T cells within each cluster (**Appendix A.2**). The ratio of $CD4^+$:$CD8^+$ T cells per cluster was aggregated for each section and averaged values taken from all LNs were then plotted as a histogram to visualise the relative homogeneity of the cluster composition (homogeneous $CD4^+$ and $CD8^+$ T cell clusters are situated at either end of the histogram). If most clusters consist of randomly mixed $CD4^+$ and $CD8^+$ T cells, it

should result in histogram with a normal distribution; on the other hand, mostly homogeneous clusters should produce a bimodal distribution.

At 18 hr p.i. (early priming) the majority of clusters were exclusively composed of $CD4^+$ T cells as expected, showing a unimodal distribution that peaked only at the far right (homogeneous $CD4^+$ T cell clusters) (**Fig. 5.5F**). However, at 42 hr p.i. (late priming), dual peaks were observed that skewed toward either end of the histogram, indicating a bimodal-like distribution. Nonetheless, there were fewer $CD8^+$ gBT-I clusters in comparison to $CD4^+$ gDT-II clusters at this point. Hence, the analysis here confirmed our previous observation from intravital microscopy that those T cell clusters that formed were relatively homogeneous, which alluded to their interaction with distinct DC subsets.

An interesting note is that the locations that both $CD4^+$ and $CD8^+$ T cell clusters occupied within the LN region appeared to be comparatively segregated. The cause of this observation is currently not known, though we speculated that this might pertain to distinct geographical distribution and migration of different DC subsets within the lymphoid tissue. Further experiments employing spatial analysis tools as well as fluorescent markers for distinct DC and T cell subsets would be required to validate this observation.

5.2.7 T cell clustering after subcutaneous infection.

To provide a direct comparison with epicutaneous HSV-1 infection, we also performed immunofluorescence confocal microscopy on popliteal LN sections after subcutaneous HSV-1 injection in the footpad. While infecting with 10^6 pfu resulted in some drainage of virus to the LN and elicited some migration of $CD8^+$ gBT-I to the LN periphery at 6 hr p.i. (data not shown), infection with a higher dose (10^7 pfu) resulted in robust infection of cells in the LN periphery as is evident from the many cells situated near the SCS brightly stained with anti-HSV antibody (**Fig. 5.6A**). Consequently, a substantial proportion of $CD8^+$ gBT-I localised in the outer paracortex of the LN (near the periphery) and clustered with HSV^+ cells (**Fig. 5.6A, B**).

Figure 5.5 Spatial and temporal distribution of T cell clusters after cutaneous HSV-1 infection

$5x10^5$ $CD4^+$ gDT-II.EGFP and $CD8^+$ gBT-I.DsRed were adoptively transferred into recipient C57BL/6 mice prior to epicutaneous HSV-1 infection.

(A, C) Maximum intensity projection images of thick iLN sections (imaging volume ~100-120μm thickness) showing the distribution of $CD4^+$ gDT-II (green) and $CD8^+$ gBT-I (red) cells during early (A) and late (C) phases of infection. LN capsule was visualised through second harmonic generation (SHG) (blue).

(B, D) Location of clustering cells in iLN sections corresponding to (A) and (C), represented in green ($CD4^+$ gDT-II) or red ($CD8^+$ gBT-I) spots.

(E) Proportion of clustering cells per LN section. Each data point represents proportion of clustering cells within the scanned LN cross-section.

Data pooled from 2 independent experiments; n=8 mice per time point. Error bars represent mean ± SEM. *$p<0.05$, ***$p<0.001$, one-way ANOVA, Tukey's multiple comparisons. ns, not significant.

(F) Histograms depicting cluster composition at 18 hr (left) and 42 hr (right). Each cluster is defined as a minimum of 4 cells. A value of 1.0 represents homogenous (100%) $CD4^+$ gDT-II T cell clusters, while 0.0 represents 100% $CD8^+$ gBT-I T cell clusters. Data pooled from 2 independent experiments; n = 4-8 mice per time point.

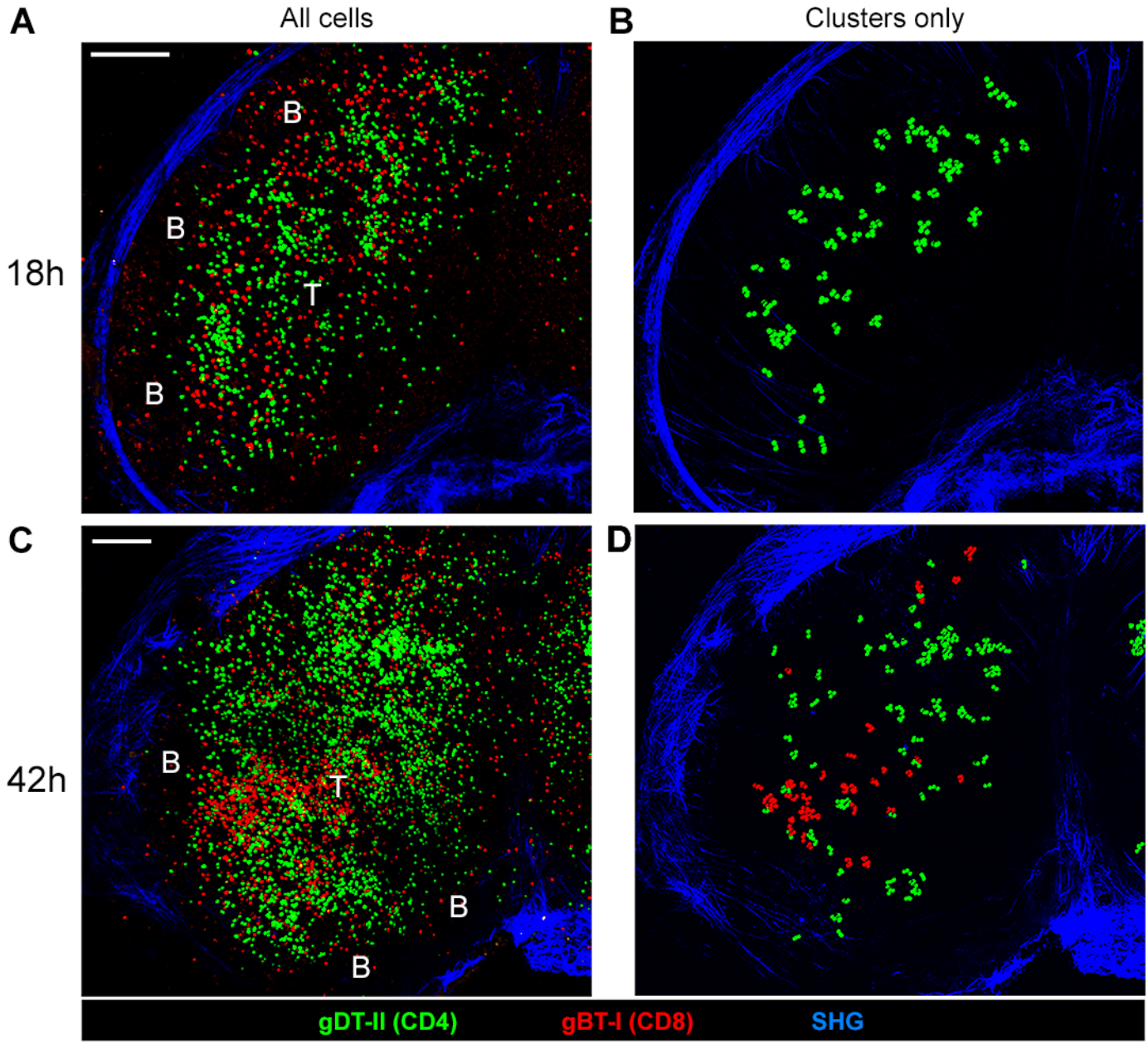
A
All cells
B
Clusters only
18h
B
B
T
B
C
D
42h
B
T
B
B
gDT-II (CD4)
gBT-I (CD8)
SHG

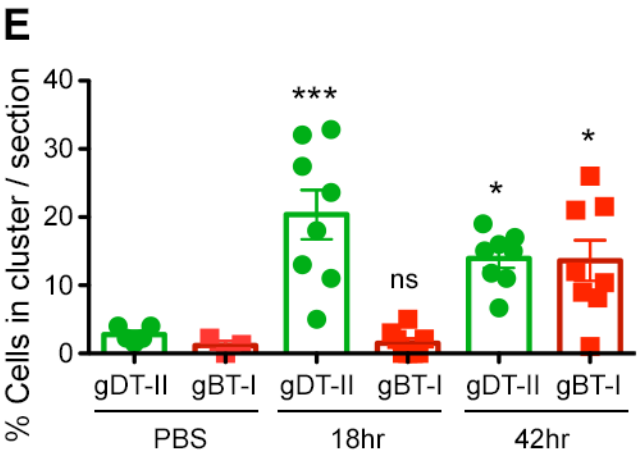
E
% Cells in cluster / section
40
30
20
10
0
***
ns
*
*
gDT-II
gBT-I
gDT-II
gBT-I
gDT-II
gBT-I
PBS
18hr
42hr

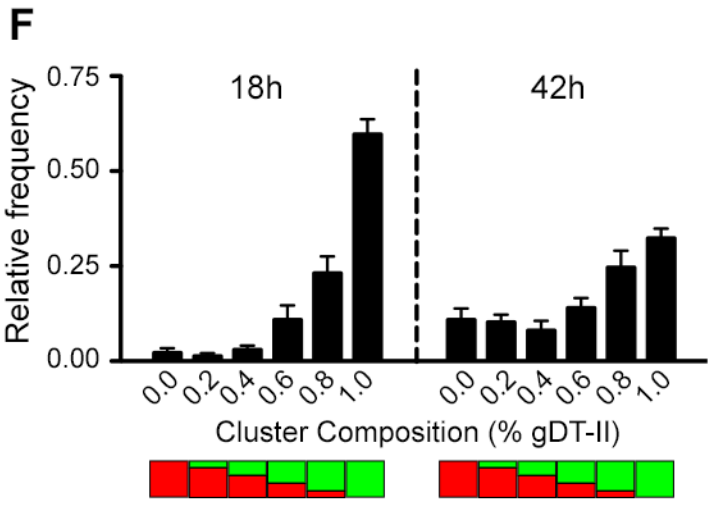
F
Relative frequency
0.75
0.50
0.25
0.00
18h
42h
0.0
0.2
0.4
0.6
0.8
1.0
0.0
0.2
0.4
0.6
0.8
1.0
Cluster Composition (% gDT-II)

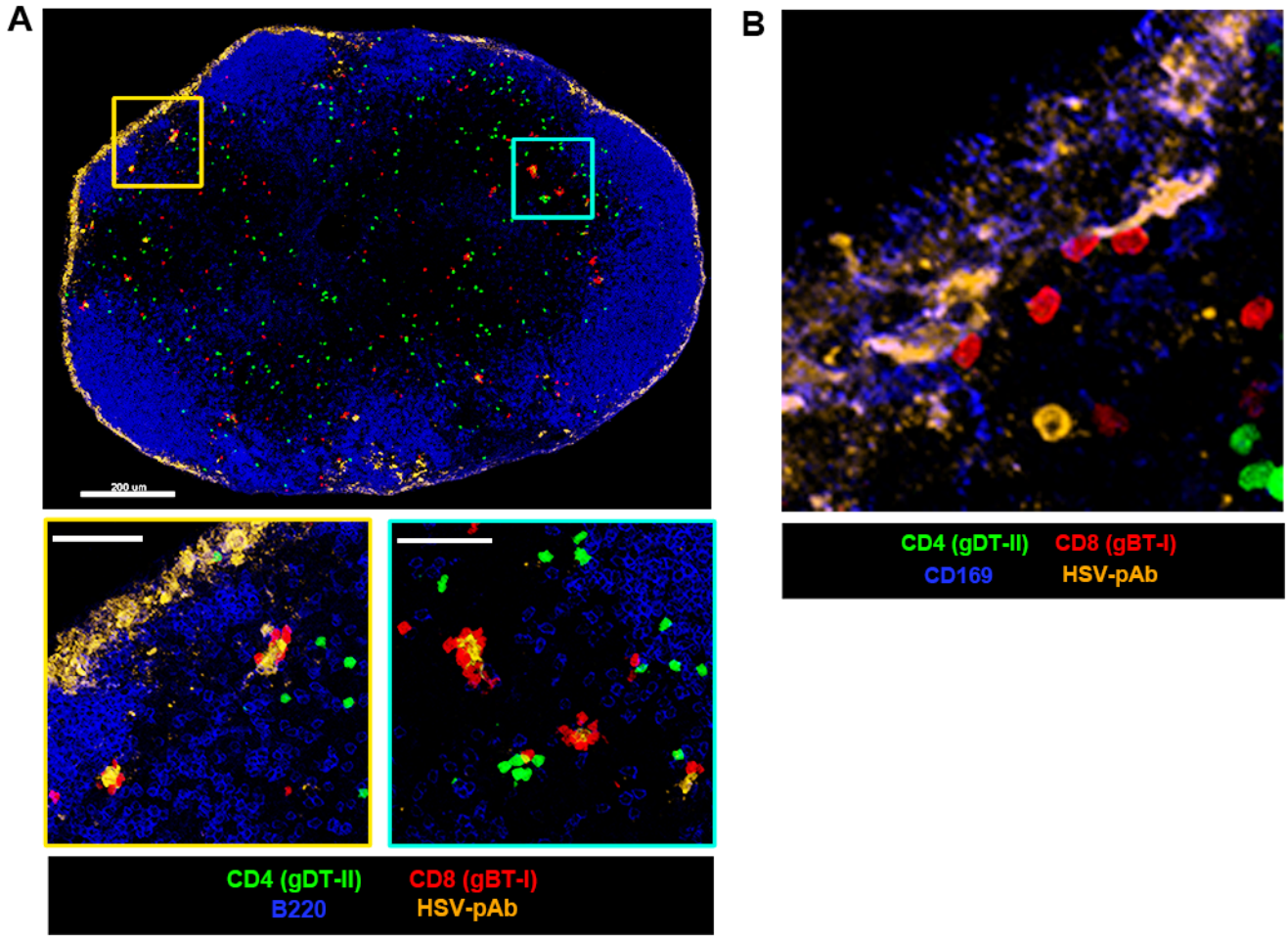

Figure 5.6 T cell clustering after subcutaneous HSV-1 infection
$5x10^5$ $CD4^+$ gDT-II.EGFP and $CD8^+$ gBT-I.DsRed were adoptively transferred into recipient C57BL/6 mice prior to subcutaneous footpad HSV-1 infection.
(A) Confocal image showing clusters of $CD4^+$ gDT-II (green) and $CD8^+$ gBT-I (red) in draining pLN at 6 hr p.i. B cells (anti-B220) and HSV antigen (anti-HSV) were depicted in blue and orange respectively. Bottom panels depict close up of selected regions.
(B) Close up image showing co-localisation of anti-HSV staining (orange) with $CD169^+$ macrophages (blue).

Interestingly, similar to epicutaneous infection, most of the T cell clusters remained fairly homogeneous. $CD8^+$ gBT-I predominantly clustered with HSV^+ cells, presumably infected cells presenting viral antigen via MHC-I, whereas $CD4^+$ gDT-II clustered around DC (identified with anti-CD11c staining, not shown), which did not stain positive for HSV (**Fig. 5.6A**). Thus, contrary to epicutaneous infection where $CD8^+$ T cell activation is delayed, our results here with lymph-borne HSV-1 infection suggested that $CD8^+$ T cells have early access to antigen presentation through infected cells in the LN.

5.2.8 Tracking DC migration into draining LN.

As discussed in the previous chapter, antigen presentation to $CD4^+$ and $CD8^+$ T cells may involve distinct DC subsets. While cross-presentation to $CD8^+$ T cells during HSV-1 infection is largely mediated by LN-resident $CD8\alpha^+$ DC (Allan et al., 2003), both $CD8\alpha^+$ DC and migratory $CD11b^+$ dDC can present antigens to $CD4^+$ T cells *ex vivo* (Bedoui et al., 2009). We hypothesised that $CD4^+$ T cells may be primed early by migratory $CD11b^+$ dDC via MHC-II presentation, while antigen transfer between migratory and LN-resident DC subsets, a requirement for *de novo* synthesis of viral glycoproteins and the dependence on help may contribute to the delayed priming of $CD8^+$ T cells *in vivo*.

To visualise migratory DC, we painted an area of the mouse flank skin with the red fluorescent dye, TRITC (Eidsmo et al., 2012). This labelled the DC in the skin and enabled visualisation of dye-labelled cells in the draining LN following scarification on the painted region of the skin and HSV-1 infection (**Fig. 5.7A**). Additionally, TRITC is highly photostable during two-photon excitation and allows cells to be tracked over prolonged imaging periods.

We observed a wave of DC migration from the skin into LN shortly after infection (**Fig. 5.7B**). At 18 hr p.i., most $TRITC^+$ cells were positioned near the cortical side of the node, which indicated their arrival from the afferent lymphatics. Later, at 42 hr p.i., many of these $TRITC^+$ cells accumulated in the LN medulla. Furthermore, most of the $TRITC^+$ cells exhibited dendritic-like morphology, suggesting that these cells are likely to be migratory DC from the skin. In short,

Figure 5.7 Tracking DC migration from skin into draining LN

(A) Schematics of experimental procedure showing painting with red fluorescent dye TRITC on flank skin prior to infection and imaging.

(B) Maximum intensity projection images of thick iLN sections showing localisation of $TRITC^+$ cells (red) at 18 hr (top) and 42 hr (bottom) p.i. Bars, 250μm.

(C) Flow cytometry analysis showing $TRITC^+$ cells in draining iLN at 26 hr p.i. and were divided into bright (red) and intermediate intensity (dark red). $TRITC^+$ cells were further subsetted into migratory DC (MHC-II^{hi} $CD11c^{int}$, red), LN-resident DC (MHC-II^{int} $CD11c^{hi}$, cyan), as well as MHC-II^{int} $CD11c^{int}$ cells (magenta). Further subsetting of $TRITC^+$ migratory DC into $CD11b^+$ DC (green), $CD103^+$ DC (orange), $CD8\alpha^+$ DC (black) and $CD11b^-$ $CD103^-$ $CD8\alpha^-$ cells (blue) were shown in last 2 columns from the right.

(D) Proportion of migratory DC (MHC-II^{hi} $CD11c^{int}$, red), LN-resident DC (MHC-II^{int} $CD11c^{hi}$, cyan), and MHC-II^{int} $CD11c^{int}$ cells (magenta) amongst $TRITC^+$ cells.

(E) Proportion of $CD11b^+$ DC (green), $CD103^+$ DC (orange), $CD8\alpha^+$ DC (black) and $CD11b^-$ $CD103^-$ $CD8\alpha^-$ cells (blue) amongst $TRITC^+$ MHC-II^{hi} $CD11c^{int}$ migratory DC.

(D-E) Data from 1 experiment, n=4 mice; Error bars represent mean ± SEM.

(F-G) Histograms depicting YFP intensity of various DC populations, with each subset colour-coded corresponding to (C-E).

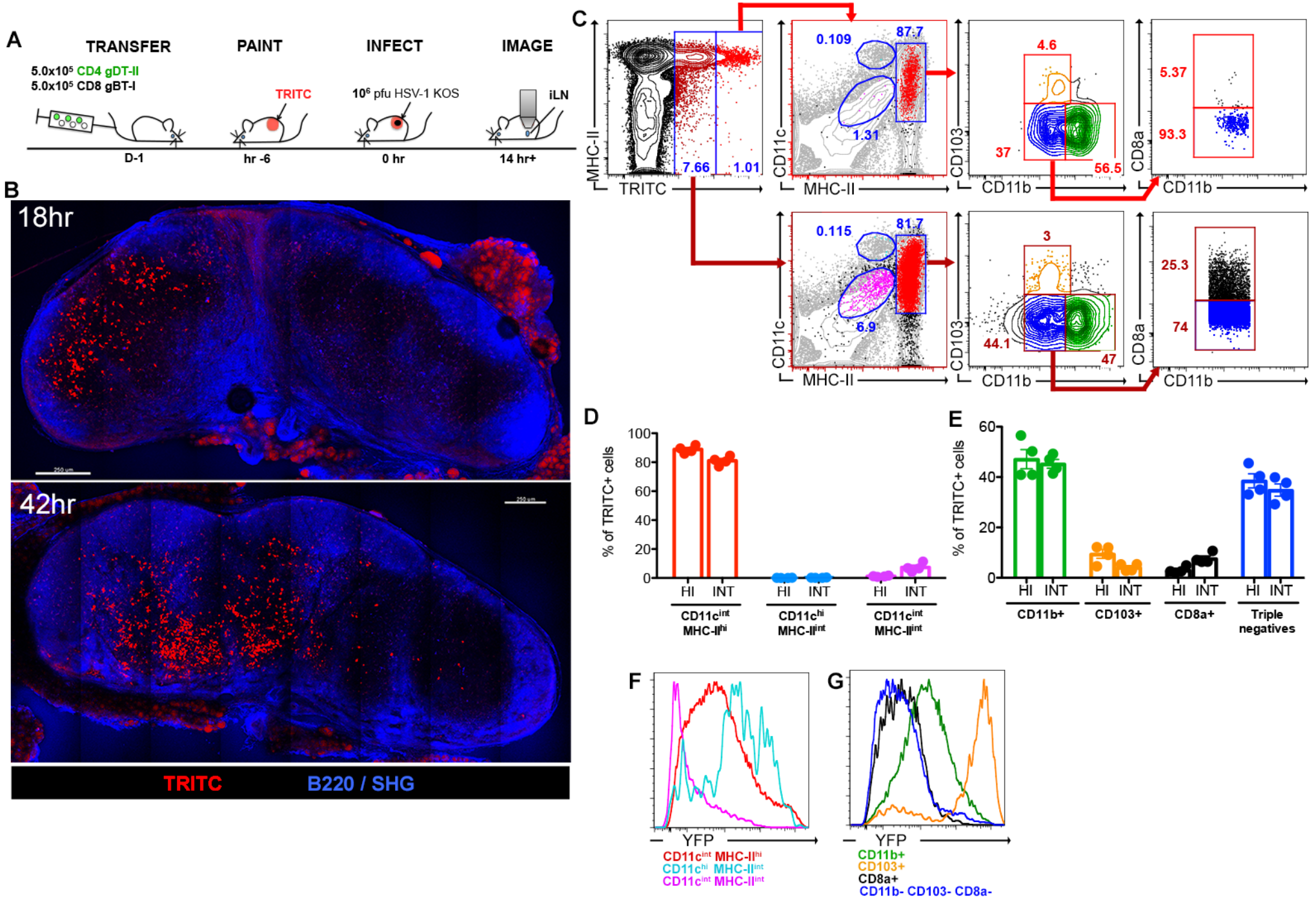
A
TRANSFER
PAINT
INFECT
IMAGE
5.0x10⁵ CD4 gDT-II
5.0x10⁵ CD8 gBT-I
TRITC
10⁶ pfu HSV-1 KOS
iLN
D-1
hr -6
0 hr
14 hr+
B
18hr
42hr
TRITC
B220 / SHG
C
MHC-II
TRITC
7.66
1.01
CD11c
MHC-II
0.109
87.7
1.31
CD103
CD11b
4.6
37
56.5
CD8a
CD11b
5.37
93.3
0.115
81.7
6.9
3
44.1
47
25.3
74
D
% of TRITC+ cells
HI INT
CD11c^int MHC-II^hi
CD11c^hi MHC-II^int
CD11c^int MHC-II^int
E
% of TRITC+ cells
CD11b+
CD103+
CD8a+
Triple negatives
F
YFP
CD11c^int MHC-II^hi
CD11c^hi MHC-II^int
CD11c^int MHC-II^int
G
YFP
CD11b+
CD103+
CD8a+
CD11b- CD103- CD8a-

our results suggested that during infection, migratory DC entered the LN, and in a progressive manner penetrated through the LN parenchyma including the T cell zone, eventually settling in the deep paracortex and medulla.

We also noted some DC migration after skin painting without scarification or infection (data not shown). This indicated a certain degree of DC migration independent of infection, possibly reflecting homeostatic migration, or induced following hair shaving, depilation or the skin painting itself.

To ascertain the identity of the TRITC^{+} migratory cells, we performed flow cytometric analysis on TRITC^{+} cells recovered from the iLNs of CD11c-eYFP mice after skin painting, at 26 hr post-HSV infection. In CD11c-eYFP mice all CD11c-expressing cells express yellow fluorescent protein (YFP). Using flow cytometry, we observed two gradations of TRITC^{+} cells, and divided them into TRITC^{hi} and TRITC^{int} respectively, although both populations appeared to have equivalent proportion of DC subsets (**Fig. 5.7C, D, E**).

In two experiments, we observed ~50-90% of the TRITC^{+} cells to be CD11c^{+} MHC-II^{hi}. Importantly, virtually none of the TRITC^{+} cells were located in the CD11c^{hi} MHC-II^{int} gate, where LN-resident CD8α^{+} DC is typically situated. This ruled out the possibility that dye painted on the skin draining into the LN and are taken up by LN-resident DC. Instead, we found a small proportion (<10%) of TRITC^{int} cells to be CD11c^{int} MHC-II^{int}. This population might represent SCS macrophages that have captured the low level of dye drainage from the skin, and acted as filters to prevent further diffusion of dye molecules to be taken up by LN-resident DC (**Fig. 5.7B**).

As noted above, the majority of TRITC^{+} cells appeared to be CD11c^{+} MHC-II^{hi}, a phenotype consistent with migratory CD11b^{+} dDC . However, further subsetting of these cells showed that only ~45% were CD11b^{+}. Up to 40% of TRITC^{+} CD11c^{+} MHC-II^{hi} cells remained unidentified (CD11b^{-} CD103^{-} CD8α^{-}). Additionally, a small proportion of CD103^{+} (~5%) and CD8α^{+} (~5%) DC were also detected. The latter CD8α+ population might reflect a small number of activated CD8α^{+} DC

after uptake of migratory cells at 26 hr p.i., a time point when ample opportunity exists for antigen handover to occur. Nonetheless, we cannot exclude the possibility of some contaminating CD8α$^+$ cells from our gating strategy. Further experiments examining multiple time points are required to substantiate this hypothesis.

Interestingly, we found that CD103$^+$ DC expressed high levels of YFP in CD11c-eYFP mice (**Fig. 5.7G**, orange). LN-resident CD11c^{hi} MHC-II^{int} CD8α$^+$ DC also expressed relatively bright YFP (**Fig. 5.7F**, cyan), albeit at a slightly lower level than CD103$^+$ DC (**Fig. 5.7G**, orange). In contrast, CD11b$^+$ DC expressed only moderate levels of YFP (**Fig. 5.7G**, green). Combining with TRITC painting, this presented a possibility for distinguishing migratory CD11b$^+$ and CD103$^+$ dDC in the LN during intravital imaging based on their expression of dim and bright YFP respectively.

5.2.9 CD4$^+$ T cells preferentially cluster with migratory dermal DC.

To determine if T cell clusters formed around TRITC$^+$ migratory APC, we transferred 5x10^5 CD4$^+$ gDT-II and CD8$^+$ gBT-I cells each, labelled with fluorescent dyes CellTrace Violet and CellTracker Deep Red respectively and examined thick sections of the draining iLN harvested at early (18 hr) and late (42 hr) time points. We found that while many CD4$^+$ gDT-II cells clustered with TRITC$^+$ DC during the early phase, later in the response many clusters of CD4$^+$ and CD8$^+$ T cell were not directly associated with TRITC$^+$ DC (**Fig. 5.8A**). This suggested that early CD4$^+$ T cell activation involved migratory CD11b$^+$ DC, while LN-resident DC were involved later in the response. To test this hypothesis, we co-stained LN sections with anti-CD69 antibody to examine where T cells were activated. Early CD4$^+$ gDT-II clusters associated with TRITC$^+$ DC stained positive for CD69, while CD8$^+$ gBT-I had yet to upregulate CD69 (**Fig. 5.8B**). During the late phase, however, CD8$^+$ gBT-I clusters were also seen upregulating CD69 but these cells did not cluster around TRITC$^+$ DC (**Fig. 5.8B**). Together, our data indicated that migratory and LN-resident DC might play distinct roles in the activation of CD4$^+$ and CD8$^+$ T cells.

Next, we wanted to examine the *in vivo* dynamics of T cell-DC interactions in the draining LN. To perform *in vivo* imaging of mouse iLN after skin TRITC painting, we transferred $5x10^5$ EGFP-expressing or CellTracker Deep Red-labelled $CD4^+$ gDT-II cells, as well as CellTrace Violet-labelled $CD8^+$ gBT-I cells prior to *in situ* TRITC painting and HSV-1 infection ~6 hr later (**Fig. 5.7A**). At between 14 hr and 24 hr p.i., $TRITC^+$ DC could be readily visualised in the paracortex of iLN and many $CD4^+$ gDT-II cells were seen clustering around these migratory DC, suggesting that migratory $CD11b^+$ dDC presented antigen to $CD4^+$ T cells (**Fig. 5.8C**, **Movie S4A**).

As controls, we also imaged the LN of mice painted with TRITC but mock-infected with saline. As anticipated we observed some $TRITC^+$ cells in the LN paracortex (**Fig. 5.8C**, **Movie S4B**). However, $CD4^+$ T cells did not arrest or form prolonged interactions with these $TRITC^+$ DC, further underscoring that T cell-$TRITC^+$ APC interactions observed after infection constituted antigen presentation and priming of $CD4^+$ T cells by migratory DC.

Calculating the mean velocities of the $CD4^+$ gDT-II cell tracks in both HSV-infected or naïve mice showed the measured values to be highly comparable to our initial characterisation of the cellular migration as described in **Section 5.2.2** (data not shown). This suggested that skin painting with dye and their uptake by migratory DC did not affect cellular behaviour of $CD4^+$ and $CD8^+$ T cells.

To further assess and quantitate T-DC interactions, we developed an automated analysis tool to track contact duration between T cells and $TRITC^+$ DC (**Appendices A.3**, **A.4**). By measuring the distance between T cell centroid and

---

Movie S4. $CD4^+$ T cell clustering with migratory DC during early HSV- 1 infection. (LINK)
Mice were adoptively transferred with $CD4^+$ gDT-II (green) and $CD8^+$ gBT-I (white) T cells prior to skin painting with TRITC (red), epicutaneous HSV-1 infection and intravital imaging of the inguinal LN. **S4A**, three examples of clustering of $CD4^+$ T cells with TRITC+ migratory DC, 14-22 hr after HSV-1 infection. **S4B**, two examples depicting the absence of any T cell clustering behavior after mock infection of mice with PBS.

surface of TRITC$^+$ cells, we defined a 15μm distance as the 'contact distance' between both cells to take into account T cell diameter and also resolution limit during deep intravital LN imaging, where the detector might not sufficiently capture fine dendritic projections. The proportion of time a T cell spent in contact with migratory DC was then calculated by dividing the number of frames the T cell is situated within the defined 'contact distance' (<15μm) by the total number of frames the T cell is present within the movie.

By plotting the frequencies of T cell-DC contact duration from multiple movies, we showed that during early priming after HSV infection (14-24 hr p.i.), there was a preferential skewing of CD4$^+$ gDT-II cells toward forming sustained interactions with migratory DC (**Fig. 5.8D, E**, **Movie S5**). In contrast, for CD8$^+$ T cells as well as for both T cells in mock-infected mice, there was virtually no stable or prolonged interaction with migratory DC observed. Together, our data here demonstrated that early during HSV infection, migratory CD11b$^+$ dDC were the dominant, if not the only, DC subset to prime CD4$^+$ T cells.

5.2.10 CD8$^+$ T cells interact with LN-resident DC during the late priming phase

While we have established that CD4$^+$ T cells interact stably with migratory DC during early priming, the DC subset with which CD8$^+$ T cells interact *in vivo* had yet to be demonstrated. To visualise all DC in the LN, and to separate migratory DC from LN-resident DC, we combined skin TRITC dye painting method with CD11c-eYFP mice to simultaneously visualise both DC subsets.

Movie S5. Quantitating interactions between CD4$^+$ and CD8$^+$ T cells and migratory DC during early HSV-1 infection. (LINK)

Mice were adoptively transferred with CD4$^+$ gDT-II (green) and CD8$^+$ gBT-I (white) T cells prior to skin painting with TRITC (red), epicutaneous HSV-1 infection and intravital imaging of the inguinal LN at 14-22 hr p.i. Cells were tracked for contact with TRITC-painted migratory DC. Cells were marked with color-coded squares and tracks (showing prior 20 frames) to show contact with TRITC$^+$ cells (yellow) or no contact (light blue).

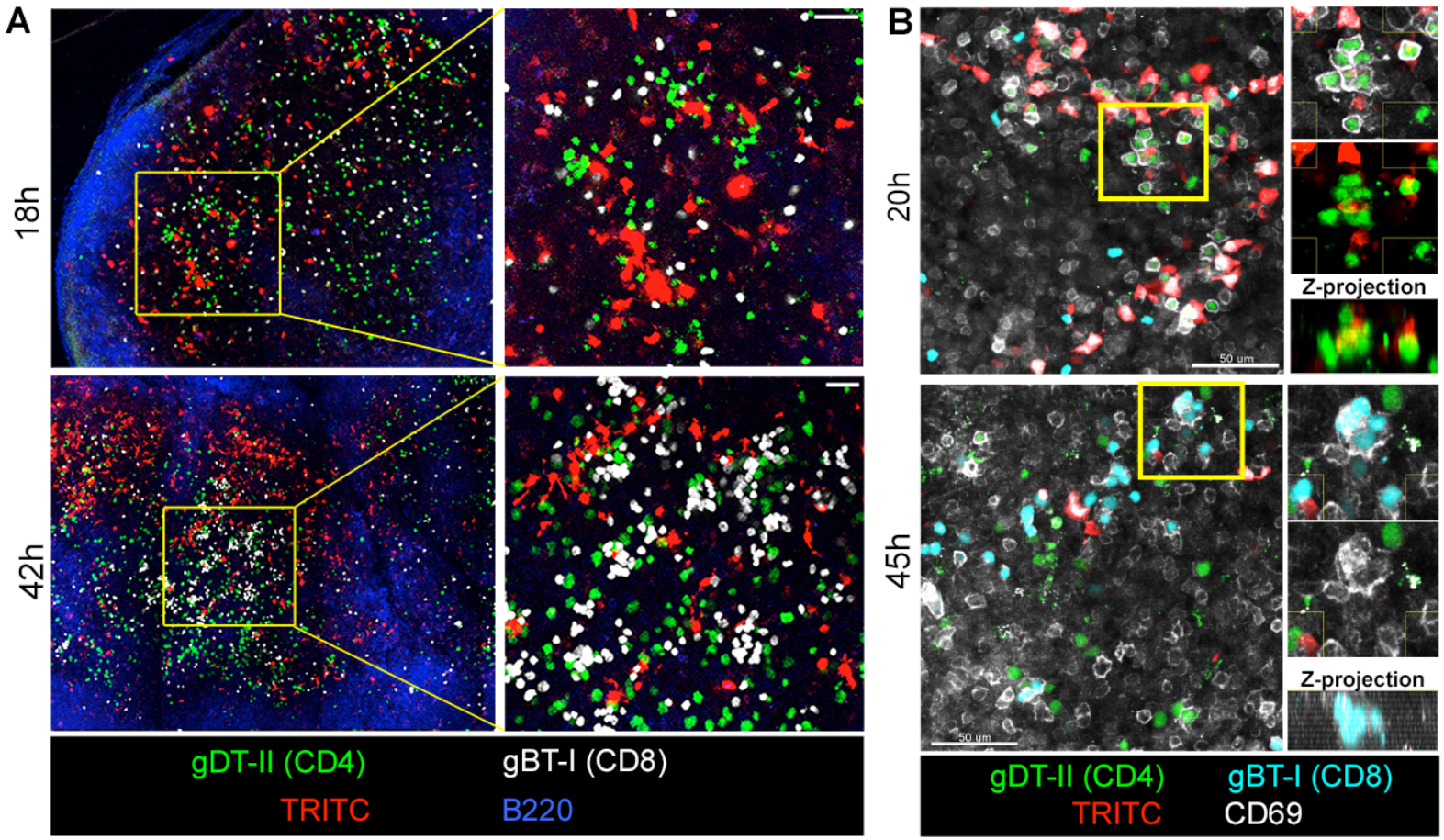

Figure 5.8 Preferential clustering of CD4⁺ T cells with migratory APC during early HSV-1 infection

$5x10^5$ CellTrace Violet-labelled CD4⁺ gDT-II.EGFP and CellTracker Deep Red-labelled CD8⁺ gBT-I were adoptively transferred into recipient C57BL/6 mice prior to skin TRITC painting and epicutaneous HSV-1 infection.

(A) Maximum intensity projection images of thick iLN sections showing localisation of TRITC⁺ cells (red), CD4⁺ gDT-II (green) and CD8⁺ gBT-I (white) T cells at early (top) and late (bottom) phases of infection. Scale bars represent 100µm. Panels to the right show close up of selected regions.

(B) Maximum intensity projection images of thick iLN sections showing anti-CD69 staining (white), gDT-II (green), gBT-I (cyan), and TRITC (red). Scale bars represent 50µm. Panels to the right show close up of selected regions.

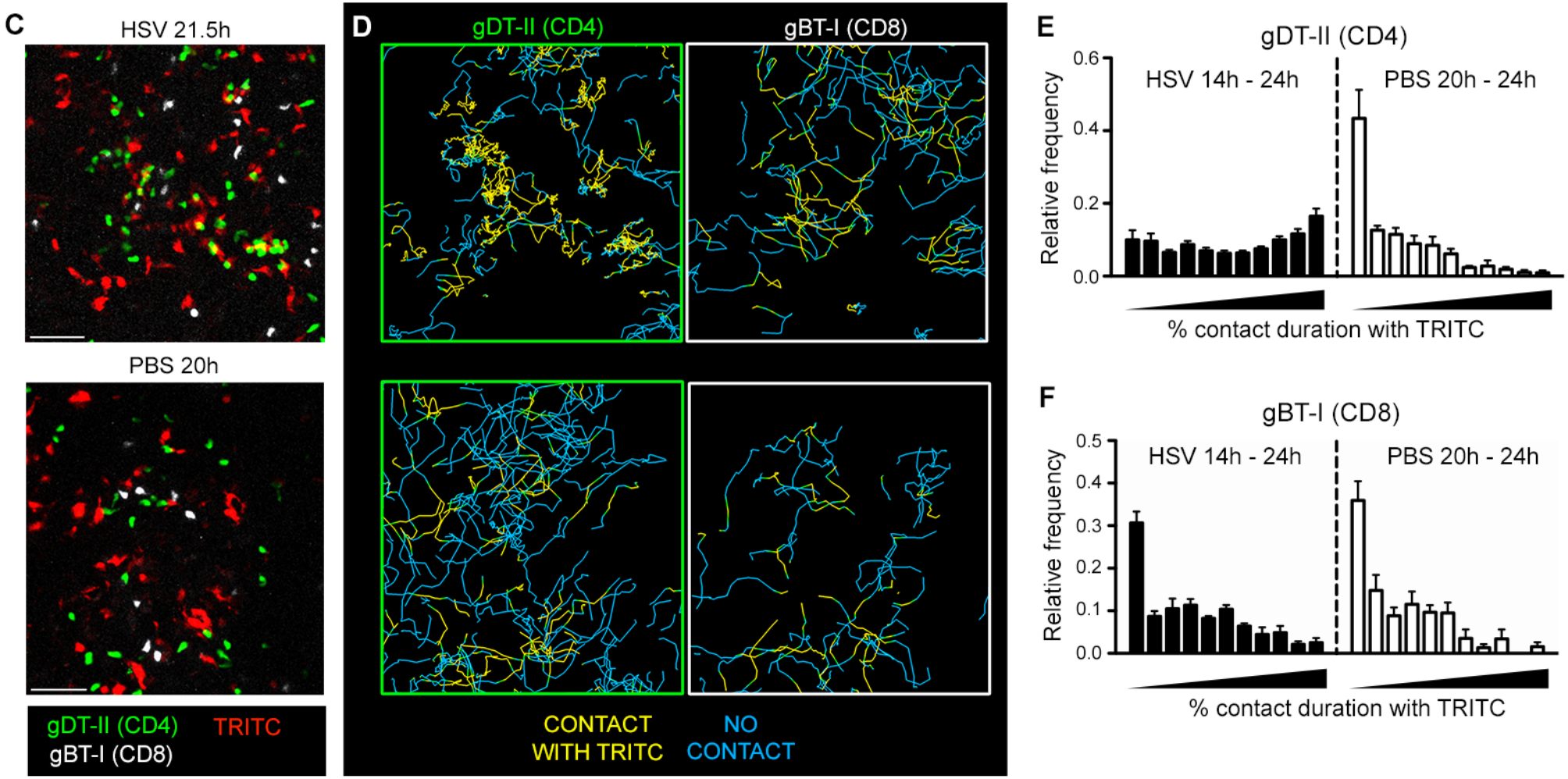

(C) Maximum intensity projection images from time-lapse movies showing interactions between CD4⁺ gDT-II (green) and CD8⁺ gBT-I (white) cells with TRITC-painted cells (red) in early infected (top) and mock infected (bottom) mice. Scale bars represent 50μm. See also **Movie S4**.

(D) Cell tracks colour-coded to show contact (yellow) or no contact (light blue) with TRITC⁺ DCs. CD4⁺ gDT-II (green box) and CD8⁺ gBT-I (white box) tracks correspond to (C) and **Movie S4**. See also **Movie S5**.

(E) Contact duration with TRITC⁺ cells by CD4⁺ gDT-II (left) and CD8⁺ gBT-I (right) cells in early infected (black bars) and mock infected (white bars) mice.

Data pooled from 1-2 independent experiments; n=4-9 mice per time point; Error bars represent mean ± SEM.

Later in the response (40-48 hr p.i.), where $CD8^+$ T cells were previously shown to upregulate CD69, we noted preferential clustering of $CD8^+$ gBT-I cells with non-migratory DC, as indicated by their expression of YFP but not marked with TRITC (**Fig. 5.9A**, **Movie S6**). Nonetheless, we cannot exclude the possibility that these $TRITC^-$ DC represented migratory DC that did not originate from the painted skin. Apart from rare occasions, which may reflect infrequent instances of infected migratory DC, we observed almost no clustering of $CD8^+$ gBT-I cells with $TRITC^+$ migratory DC. We also quantitated $CD8^+$ T cell contact with migratory DC (as described in **Section 5.2.9**) and found an absence of sustained interaction with migratory DC (**Fig. 5.9B, C**). This is consistent with previous findings that LN-resident $CD8\alpha^+$ DC are mainly responsible for antigen presentation to $CD8^+$ T cells during HSV infection (Allan et al., 2006; Bedoui et al., 2009). Interestingly, we also observed some CD4+ T cells clustering with $TRITC^-$ DC (**Movie S6**, example 2).

Taken together, we have established that $CD4^+$ and $CD8^+$ T cell priming was temporally regulated during localised HSV-1 infection, and that the burden of antigen presentation was also segregated between migratory and LN-resident DC subsets, underscoring the complexity and breadth of multiple immune cells involved in the mounting of adaptive immune response against peripheral viral infection.

5.2.11 $CD8^+$ T cells cluster with $XCR1^+$ DC.

As we could not specifically identify the non-migratory DC subset that $CD8^+$ T cells interacted with in CD11c-eYFP mice, we stained tissue sections with antibodies against a chemokine receptor expressed by LN-resident $CD8\alpha^+$ DC, XCR1. It has been demonstrated that XCR1 is only expressed by DC ontogenically

---

Movie S6. Preferential clustering of gBT-I with non-migratory DC. (LINK)
$CD4^+$ gDT-II (purple) and $CD8^+$ gBT-I (white) T cells were adoptively transferred into CD11c-EYFP (green) mice prior to skin painting with TRITC (red), epicutaneous HSV-1 infection and intravital imaging of the inguinal LN at 41.5-45 hr p.i. Three examples of $CD8^+$ T cell clustering close to $CD11c\text{-}EYFP^+$ cells, and one example of $CD4^+$ T cell clustering around $CD11c\text{-}EYFP^+$ cells (Example #2) are shown.

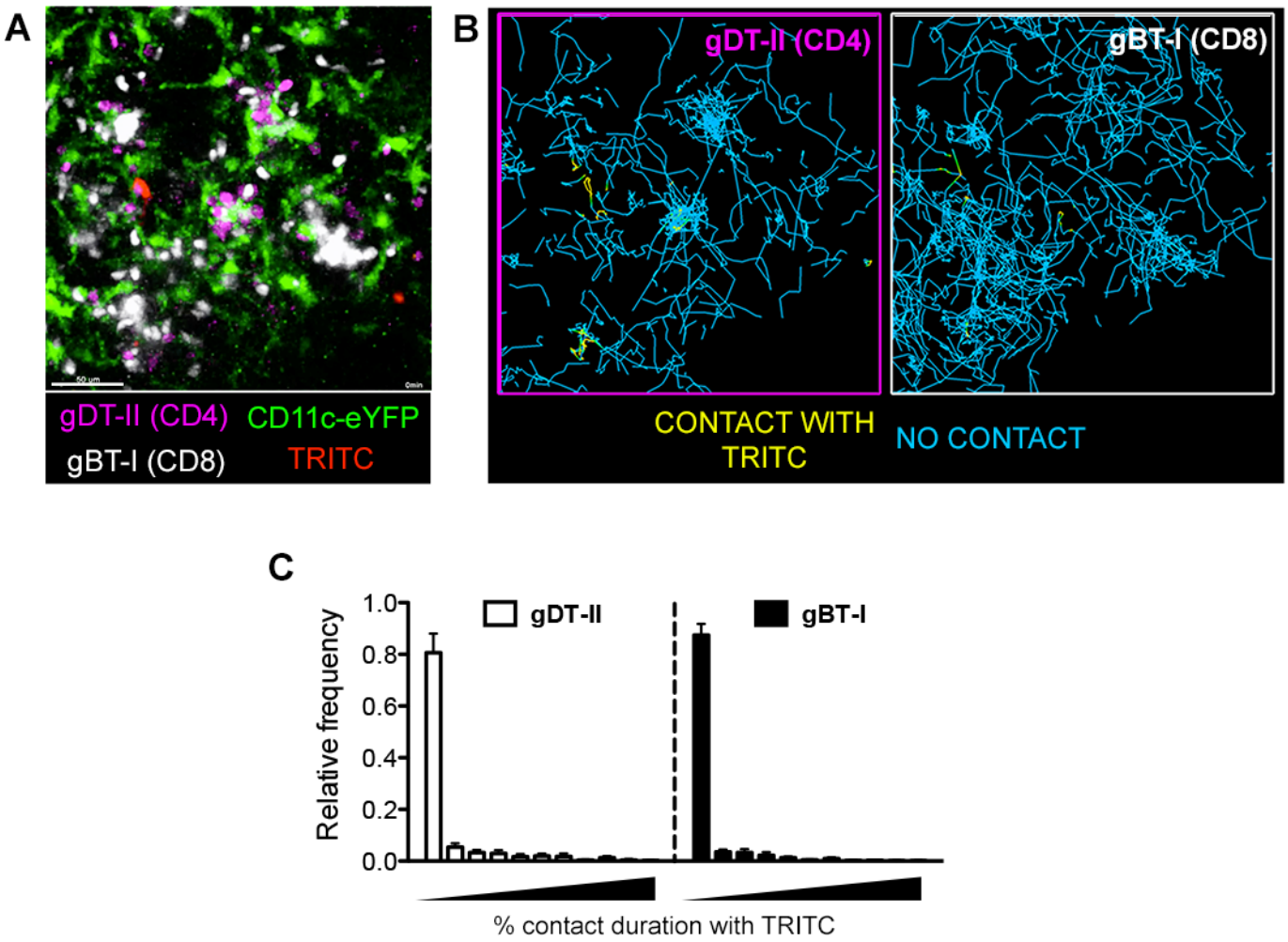

Figure 5.9 CD8⁺ T cells interact with LN-resident DC during late priming phase

5x10⁵ CellTrace Violet-labelled CD4⁺ gDT-II.EGFP and CellTracker Deep Red-labelled CD8⁺ gBT-I were adoptively transferred into recipient CD11c-EYFP mice prior to skin TRITC painting and epicutaneous HSV-1 infection.

(A) Maximum intensity projection images from time-lapse movies of iLN in HSV-infected CD11c-EYFP mice at 40 hr+ p.i. showing TRITC⁺ migratory (red) and TRITC⁻ non-migratory DC (green). CD4⁺ gDT-II and CD8⁺ gBT-I cells were shown in magenta and white respectively. See also **Movie S6**.

(B) Colour-coded cell tracks corresponding to (A) and **Movie S6** showing contact (yellow) or no contact (light blue) paths of CD4⁺ gDT-II (magenta box) and CD8⁺ gBT-I (white box) with TRITC⁺ DC.

(C) Duration of contact between CD4⁺ gDT-II (white bars) and CD8⁺ gBT-I (black bars) with TRITC⁺ cells.

Data pooled from 2 independent experiments; n=5-6 mice per group. Error bars represent mean ± SEM.

derived from a Batf3-IRF8-Id2 transcription factor lineage, which includes LN-resident CD8α$^+$ DC and their migratory counterpart CD103$^+$ DC (Bachem et al., 2012; Kroczek & Henn, 2012).

Co-staining thick LN sections with anti-XCR1 and anti-CD11c allowed us to distinguish between XCR1$^+$ and XCR1$^-$ DC subsets. Importantly, in XCR1$^{-/-}$ mice anti-XCR1 staining was completely absent, confirming the specificity of the antibody marker (data not shown). We found that later in the response CD8$^+$ gBT-I clusters exclusively aggregated around CD11c$^+$ XCR1$^+$ cells (**Fig. 5.10A, B**).

Furthermore, preliminary intravital imaging performed using XCR1-venus mice, where XCR1$^+$ cells are specifically marked with yellow fluorescent protein (Yamazaki et al., 2013), demonstrated CD8$^+$ gBT-I clustering with XCR1$^+$ DC (**Movie S7**, example 1). In at least one instance, we also observed CD4$^+$ T cells clustering and 'swarming' around XCR1$^+$ DC (**Movie S7**, example 2). However, further experiments using these transgenic XCR1-venus mice are required to confirm our observations. In short, our data here suggested that LN-resident XCR1$^+$ DC is the primary antigen-presenting DC subset to CD8$^+$ T cells *in vivo* during HSV-1 infection.

5.2.12 CD4$^+$ T cells transiently interacted with CD8$^+$ T cell clusters.

Provision of CD4$^+$ T cell help is mediated through cognate interaction with DC via CD40-CD40L interaction, resulting in DC 'licensing' (Bennett et al., 1998; Ridge et al., 1998; Schoenberger et al., 1998). The requirement for such molecular interactions predicted close encounters between DC and activated CD4$^+$ T cells.

In **Section 5.2.2** we described T cell clusters during late priming to be largely homogeneous in composition. However, on a number of occasions we also noted

---

Movie S7. CD8$^+$ gBT-I cluster with XCR1$^+$ DC. (LINK)
XCR1-venus (green) mice were adoptively transferred with CD4$^+$ gDT-II (purple) and CD8$^+$ gBT-I (white) T cells prior to receiving skin TRITC painting (red) and epicutaneous HSV-1 infection. Intravital imaging of draining inguinal LN were performed ~42-50 hr p.i. Two examples of CD8$^+$ T cell clustering with XCR1$^+$ DC (green) were shown.

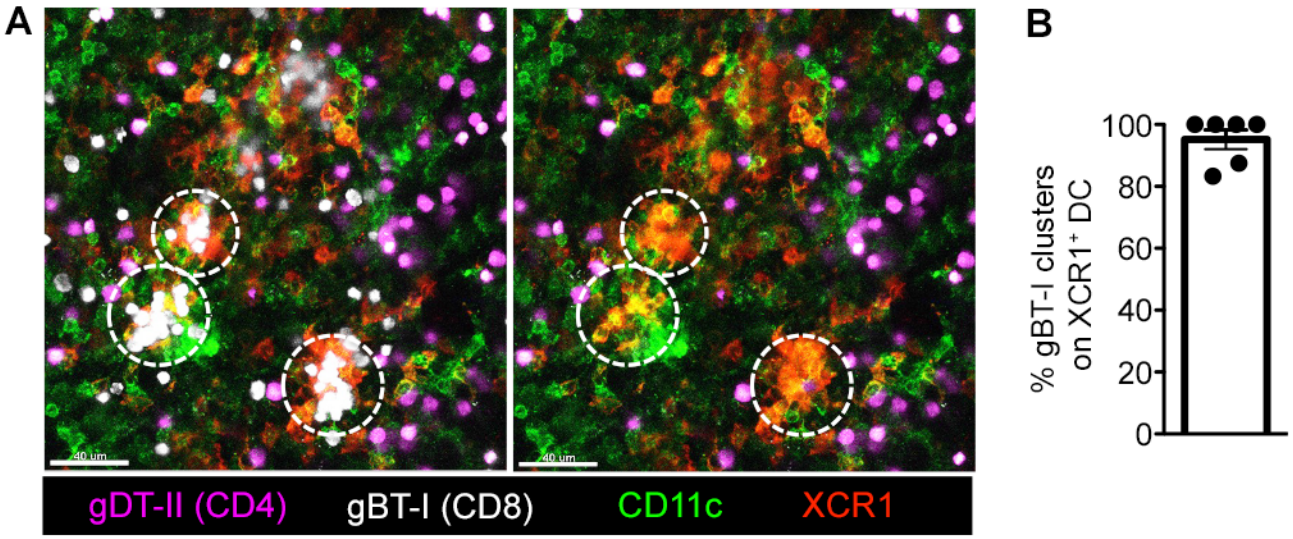

Figure 5.10 CD8⁺ T cells cluster with XCR1⁺ DC

5x10⁵ CellTrace Violet-labelled CD4⁺ gDT-II (purple) and CellTracker Deep Red-labelled CD8⁺ gBT-I (white) cells were adoptively transferred into recipient C57BL/6 mice prior to epicutaneous HSV-1 infection.

(A) Maximum intensity projection images of thick iLN slices at 42 hr p.i. showing localisation of CD8⁺ gBT-I clusters (white) relative to XCR1⁺ (red) CD11c⁺ (green) DC. Dotted circles denote gBT-I clusters. Right panel shows image without CD8⁺ gBT-I cells. Scale bars represent 50μm.

(B) Fraction of CD8⁺ gBT-I clusters closely associated with XCR1⁺ CD11c⁺ DC per mouse.

Data pooled from 2 independent experiments; n=6 mice. Error bars represent mean ± SEM.

intermittent interactions between small numbers of CD4+ T cells with CD8+ T cell clusters. As these swarming interactions might reflect contact between CD4+ T cells and XCR1+ DC that primes CD8+ T cells, which can lead to provision of help, we measured the retention tendency of these CD4+ T cells around CD8+ T cell clusters. By examining 11 occasions of CD4+ T cells swarming around CD8+ T cell clusters (defined as a minimum of 5-minute CD4+ T cell contact with CD8+ T cell clusters in movies of at least 30 minutes duration) over the length of recording period, we found that most of these CD4+ T cells established prolonged contact, averaging ~80% of total movie duration (**Fig. 5.11A, B**, **Movie S8**). These CD4+ T cells interacted with the clusters in a transient and dynamic manner, as opposed to forming stable and sustained interaction as observed in CD8+ T cells. While further experiments are required to confirm our hypothesis, CD4+ T cells likely interacted with XCR1+ DC post-activation, which provides opportunity for the delivery of molecular signals to 'license' XCR1+ DC.

5.2.13 XCR1 is dispensable for CD8+ T cell priming.

DC and lymphocyte chemotaxis are pivotal to facilitating their encounters within the SLO. In the following sections, we explored the functional significance of the chemokine receptor XCR1 and the chemokine CCL19 in CTL priming.

XCR1 is a chemokine receptor uniquely expressed on LN-resident CD8α+ DC and migratory CD103+ DC (collectively XCR1+ DC), known for their exceptional cross presentation ability (Kroczek and Henn, 2012). Its target ligand XCL1 is a chemoattractant secreted by various immune cells including activated CD8+ T cells, and is thought to promote prolonged interaction between CD8+ T cells and

---

Movie S8. CD4+ T cell interactions with gBT-I T cell clusters during late HSV-1 infection. (LINK)

Mice were adoptively transferred with CD4+ gDT-II (purple) and CD8+ gBT-I (white) T cells prior to epicutaneous HSV-1 infection and intravital imaging of the inguinal LN at 39.5-45 hr p.i. Two examples of dynamic interactions between CD4+ gDT-II T cells and CD8+ gBT-I T cell clusters are shown. gDT-II T cells that made contact with gBT-I clusters are marked with color-coded squares and tracks (prior 20 frames) to show contact (yellow) or no contact (light blue) in each frame.

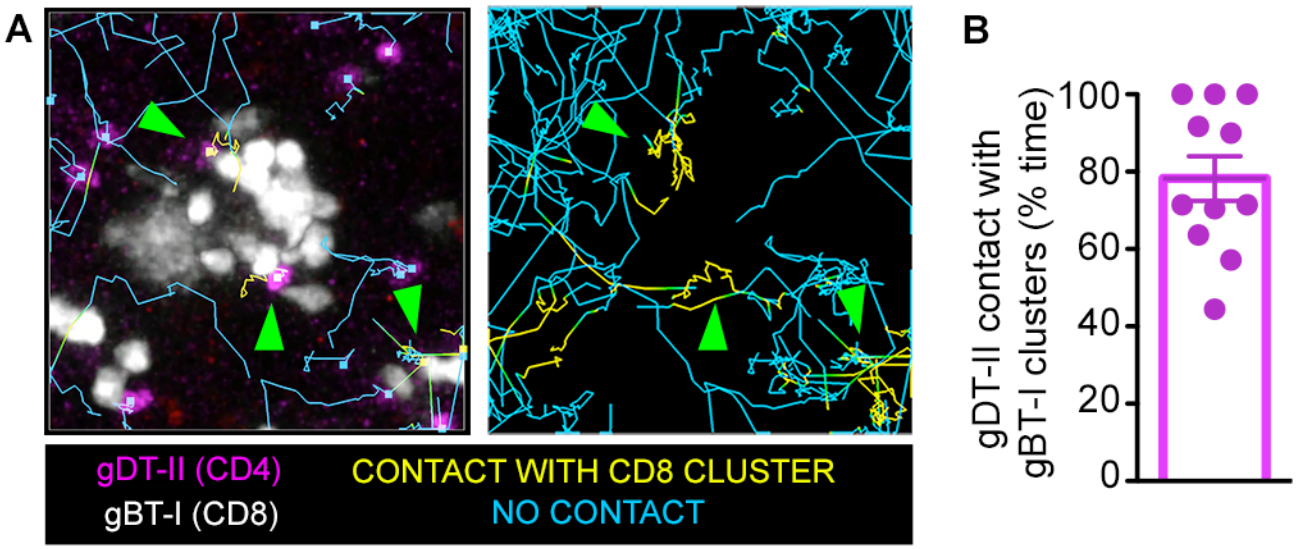

Figure 5.11 Quantitating CD4⁺ T cell interaction with CD8⁺ T cell clusters
(A) 2P image of iLN showing CD4⁺ gDT-II (magenta) interacting with CD8⁺ gBT-I clusters (white). Cell tracks colour-coded to show contact with gBT-I clusters (yellow) or non-contact (blue) are depicted with a history of 20 frames. Full cell tracks are shown on the right panel. Green arrows denote CD4⁺ T cells in contact with gBT-I clusters. See also **Movie S8**.
(B) Proportion of time CD4⁺ gDT-II were in contact with CD8⁺ gBT-I clusters per movie. Only CD4⁺ T cells establishing contact for >5 min with gBT-I clusters were analysed.
Data from one representative experiment of two are shown. Error bars represent mean ± SEM.

XCR1$^+$ DC, in addition to recruiting other XCR1$^+$ cells to the reactive centre of antigen presentation (Dorner et al., 2009).

We hypothesised that the XCR1-XCL1 axis might mediate encounters and interactions between CD8$^+$ T cells and antigen-bearing XCR1$^+$ DC during HSV-1 infection. To determine if XCR1 plays a major role in the priming of CD8$^+$ T cells, we adoptively transferred 5x10^5 CellTrace Violet-labelled CD8$^+$ gBT-I cells into wildtype B6 as well as XCR1$^{-/-}$ mice prior to HSV-1 infection. At D3 p.i., there were no appreciable difference in the expression of activation markers CD69 (**Fig. 5.12A**) and CD25 (not shown) in CD8$^+$ gBT-I cells in draining bLN between wildtype and XCR1$^{-/-}$ mice. Similarly, the proportion as well as total number of divided CD8$^+$ gBT-I cells remained relatively equal between both groups (**Fig. 5.12B**). Our results thus indicated that XCR1 expression on cross-presenting DC did not significantly impact upon the priming and expansion of HSV-specific CD8$^+$ T cells *in vivo*.

To investigate if the role of XCR1 is more prominent under physiological condition, where T cell precursors are naturally low in number, we also examined the expansion of endogenous HSV gB-specific CD8$^+$ T cells using tetramer staining at D7 p.i. In both the spleen and bLN, we noted no significant difference in the numbers of recovered gB-tetramer$^+$ cells between wildtype and XCR1$^{-/-}$ mice (**Fig. 5.12C**). Although we cannot exclude a minor effect of XCR1-XCL1 signalling, together our data suggested that XCR1 chemotactic deficiency did not lead to impaired priming of CD8$^+$ T cells.

5.2.14 CCL19 is dispensable for CD8$^+$ T cell priming.

CCL19 is a major component of chemokines that regulate cellular migration into and within the LN. Although CCL21 alone – which shares the same chemokine receptor CCR7 – has been shown to be adequate for DC migration in the LN (Britschgi et al., 2010), CCL19 may be crucial for migration of these DC from the subcapsular region into the T cell zone (M. Sixt, personal communication).

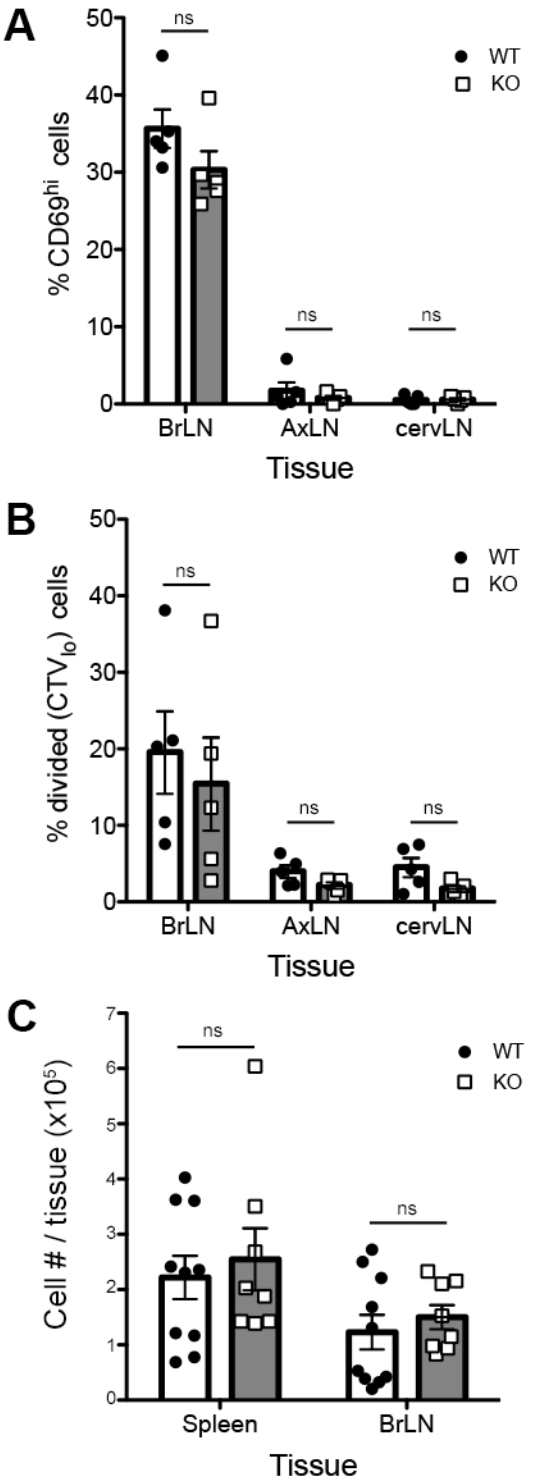

Figure 5.12 XCR1 is dispensable for CD8⁺ T cell priming

(A-B) 5x10⁵ CellTrace Violet-labelled CD8⁺ gBT-I cells were adoptively transferred into C57BL/6 (WT) or XCR1$^{-/-}$ (KO) mice prior to receiving epicutaneous 10⁶ pfu HSV-1 infection. Graphs (A) and (B) showed proportion of CD69^{hi} (A) and divided CD8⁺ gBT-I cells (CellTrace Violet$_{lo}$) (B) at 72 hr p.i. in draining bLN and non-draining aLN, cLN.

Data from one experiment; n=5 mice per group. Error bars represent mean ± SEM.

(C) D7 p.i. spleens and bLN from C57BL/6 (WT) or XCR1$^{-/-}$ (KO) mice infected with 10⁶ pfu HSV-1 were stained with H2-K^{b}-gB tetramer and total number of cells enumerated in each tissue.

Data pooled from two independent experiments; n=7-10 mice per group. Error bars represent mean ± SEM. Mann-Whitney *U* test. ns, not significant.

To examine this hypothesis, we performed experiments similar to **Section 5.2.13** with CCL19$^{-/-}$ mice. At D3 p.i., our data showed no difference in the priming (CD69 upregulation) as well as proliferative kinetics (CellTrace Violet dilution) of CD8^{+} gBT-I in the draining bLN (**Fig. 5.13A, B**). Endogenous CD8^{+} T cell responses measured using gB-specific tetramer were not significantly different between WT and CCL19$^{-/-}$ mice at D7 p.i. (**Fig. 5.13C**) Together these results suggested that CCL19 might be dispensable for the priming and proliferation of CD8^{+} T cells during skin HSV-1 infection.

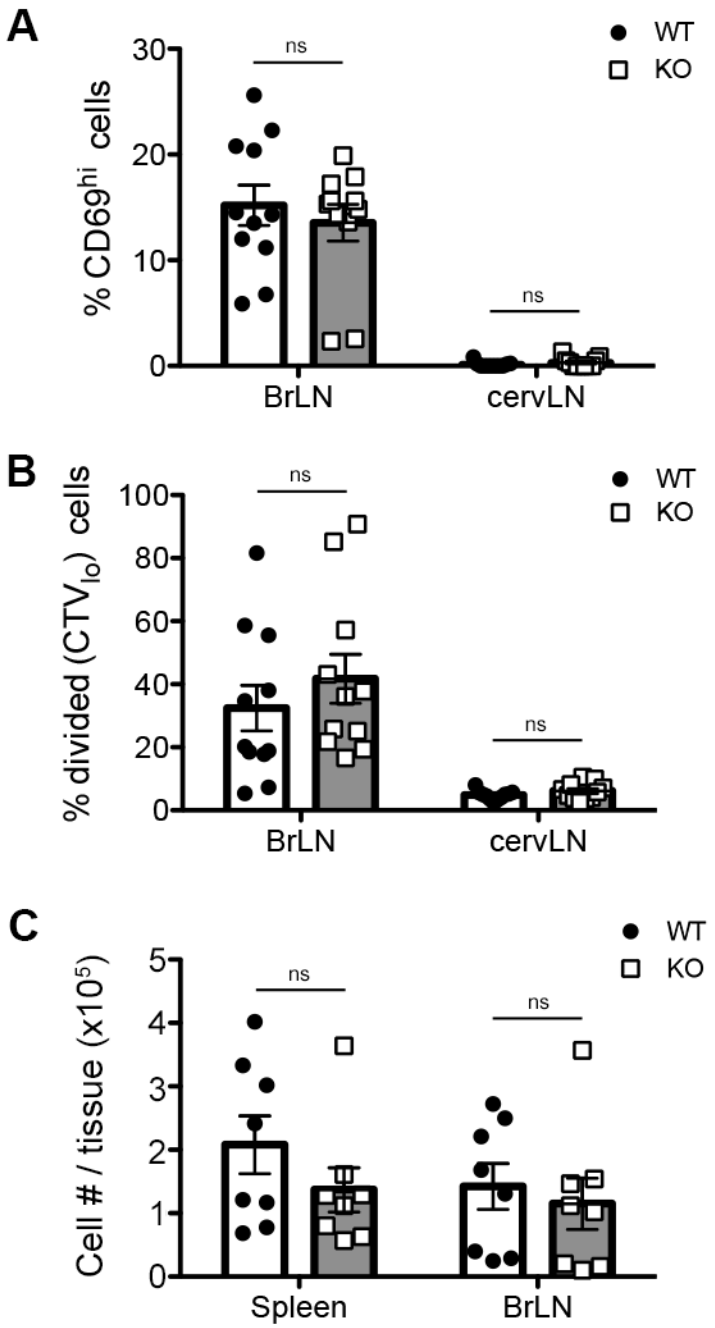

Figure 5.13 CCL19 is dispensable for CD8⁺ T cell priming

(A-B) 5x10^5 CellTrace Violet-labelled CD8$^+$ gBT-I cells were adoptively transferred into C57BL/6 (WT) or CCL19$^{-/-}$ (KO) mice prior to receiving epicutaneous 10^6 pfu HSV-1 infection. Graphs (A) and (B) showed proportion of CD69^{hi} (A) and divided CD8$^+$ gBT-I cells (CellTrace Violet$_{lo}$) (B) at 72 hr p.i. in draining bLN and non-draining cLN.

Data from pooled from two independent experiments; n=11 mice per group. Error bars represent mean ± SEM.

(C) D7 p.i. spleens and bLN from C57BL/6 (WT) or CCL19$^{-/-}$ (KO) mice infected with 10^6 pfu HSV-1 were stained with H2-K^b-gB tetramer and total number of cells enumerated in each tissue.

Data pooled from two independent experiments; n=8 mice per group. Error bars represent mean ± SEM. Mann-Whitney *U* test. ns, not significant.

5.3 DISCUSSION

The magnitude and quality of an immune response is highly regulated to ensure effective immunity while minimising collateral damage to the host tissues. This is often achieved through integrative signalling at molecular, biochemical and cellular levels, the latter of which is comprised of interactions involving an elaborate set of immune cell types. Cooperation between helper and cytotoxic T cells augments CTL capability and primes memory cells capable of responding robustly to subsequent re-challenges (Bevan, 2004). Recent advances in intravital imaging technology have permitted glimpses into such events and contributed to an understanding of the complex and dynamic nature of an immune response.

In this chapter, we established a mouse skin-draining LN imaging model that permitted visualisation of cellular events during T cell priming after cutaneous HSV-1 infection. Combining the use of transgenic mice with fluorescent DC and dye painting of the skin to track migratory cells, our setup enables simultaneous visualisation of the key players during immune priming: both LN-resident and migratory DC, as well as $CD4^+$ and $CD8^+$ T cells. This will be vital for interrogating the dynamics of how different components of the immune system contribute to priming, including how $CD4^+$ T cells deliver help in a timely manner.

Furthermore, we also developed automated analysis tools for rapid quantitation of cellular events on thick LN cross-sections. We have thus far been able to quantitate both $CD4^+$ and $CD8^+$ T cell clustering in draining LN and mapped their spatial distribution and abundance over time. Our quantitation tool can also be applied to whole tissue imaging, owing to the growing prominence of optical clearing techniques, and as such may be useful for quantitation at a global, whole-tissue level.

Using this method, we mapped the localisation of T cell clustering as readout of T cell activation, and showed that most T cell priming during epicutaneous HSV-1 infection occurred in the T cell zone. Our observation is in contrast to previous

studies employing subcutaneous injection of pathogens that demonstrated re-distribution of $CD8^+$ T cells to the LN periphery, near the LN capsule as well as in the interfollicular region (Hickman et al., 2008; Sung et al., 2012). This likely reflected the accessibility of the antigen in which DC situated to the LN periphery could readily sample drained pathogens from the lymphatic sinuses or acquire the antigen from macrophages lining the SCS (Gerner et al., 2015; Hickman et al., 2011). When inoculating mice via the subcutaneous route of infection, we found that only with a high inoculating dose did $CD8^+$ T cells significantly alter their priming location and cluster around virally-infected cells in the interfollicular region. In contrast, few $CD8^+$ T cells were seen interacting with infected cells in the periphery when inoculated with a lower dose. This suggested that substantial infection of the LN might be required to promote $CD8^+$ T cell migration towards the LN periphery where they can be primed by infected cells. This could be influenced by pathogen dose or the tropism of the infecting agent. Interestingly, $CD4^+$ T cells clustered with uninfected DC whereas $CD8^+$ T cells with HSV-infected cells, implicating the contribution of direct priming to $CD8^+$ T cells in the subcutaneous infection model. Our observation is also in agreement with a number of recently published studies using vaccinia virus or model antigen, where distinct clustering of $CD4^+$ and $CD8^+$ T cells was also reported (Gerner et al., 2015; Eickoff et al., 2015; Kitano et al., 2016).

$CD4^+$ and $CD8^+$ T cells also clustered in spatially distinct locations during epicutaneous infection with HSV-1. However, we found no evidence indicating direct priming of $CD8^+$ T cells in this model. We did not detect HSV using plaque assays, and were unable to detect infected cells by immunofluorescence microscopy (data not shown). This supports prior work showing very little HSV DNA (1-4 copies) in LN DC at 24 hr p.i. (Allan et al., 2006). Furthermore, previous studies showed that excision of the infected skin at 2 hr p.i. (when virions accessing the lymphatic sinuses would have sufficient drained, but prior to migratory APC trafficking) abrogated $CD8^+$ T cell priming (Stock et al., 2004).

Instead, $CD4^+$ and $CD8^+$ T cells preferentially clustered with migratory dDC and LN-resident $XCR1^+$ DC respectively at distinct phases of infection. Interestingly,

CD4+ and CD8+ T cell clusters also appeared to populate relatively distinct regions of the LN. We noted that CD4+ T cell clusters are broadly situated across the T cell zone, whereas CD8+ T cell clusters appeared to reside within more specific, regional locales of the LN. We speculate that such occurrence might in part be attributed to the differential distribution of migratory CD11b+ dDC and LN-resident XCR1+ DC in the LN: while migratory DCs traverse and spread through the T cell zone, it is possible that only small clusters of XCR1+ DC receive sufficient antigenic material for subsequent CTL priming.

The functional segregation of DC subsets in their antigen presentation capability has been noted in numerous studies. XCR1+ DC, ontogenically-derived from the Batf3-IRF8-Id2 transcription factor-dependent lineage (Hildner et al., 2008; Hashimoto et al., 2011), which comprises LN-resident CD8α+ DC and its migratory CD103+ counterpart, exhibits superior cross-presentation of cell-associated antigen to CD8+ T cells (Schnorrer et al., 2006; Shortman and Heath, 2010). On the other hand, CD11b+ DC, now characterised as IRF4-dependent lineage (Schlitzer et al., 2013; Persson et al., 2013), are specialised in antigen presentation to CD4+ T cells via MHC-II instead (Mount et al., 2008; Dudziak et al., 2007). Our experimental data thus supports the view that DC subsets have distinct roles in antigen presentation and T cell activation. Although the unique expression of the chemokine receptor XCR1 itself appeared dispensable (**Section 5.2.13**), data presented here also confirmed previous *ex vivo* presentation assays demonstrating that LN-resident CD8α+ DC is uniquely capable of presenting HSV-derived antigen to CD8+ T cells during cutaneous infection (Allan et al., 2006; Bedoui et al., 2009).

Our experimental results thus anticipate a complex and dynamic interplay between a varied set of DC and T cells in mounting an effective cellular-mediated immune response against localised infection. First, upon acquiring viral antigen from the skin, migratory CD11b+ dDC mobilise to the local draining LN. These incoming DC provided early antigen presentation via MHC-II to CD4+ T cells. The delay in CD8+ T cell priming remains elusive; however, a number of prerequisites for robust CD8+ T cell priming are now known: (1) LN-resident XCR1+ DC must

for $CD8^+$ T cell priming (Mueller et al., 2003); and (3) $CD4^+$ T cells must become activated and 'license' $XCR1^+$ DC via CD40-CD40L interactions (Smith et al., 2004). Either or all of these factors could contribute to the temporally lagging activation of $CD8^+$ T cells.

Our results suggest that LN-resident $XCR1^+$ DC occupy a unique role integral for priming T cells. Since $XCR1^+$ DC are ultimately responsible for presenting antigen to $CD8^+$ T cells, it also serves as the only platform for $CD4^+$ T cells to deliver help. Spatially distinct activation of $CD4^+$ and $CD8^+$ T cells by different DC subsets observed in a number of recent studies utilising particulate and soluble antigen immunisation further supports the notion of functional segregation of DC subsets in the priming of different T cell populations (Gerner et al., 2015; Kitano et al., 2016). Indeed, using mixed bone marrow chimeras reconstituted with MHC-$II^{-/-}$ cells and diphtheria toxin receptor expressing $XCR1^+$ cells, Eickoff et al. (2015) recently showed that ablation of MHC-II-expressing $XCR1^+$ cells (thus leaving only $MHC^{-/-}$ $XCR1^+$ DC incapable of receiving help signals) impaired memory programming of $CD8^+$ T cells after vaccinia virus infection. In this study lack of $CD4^+$ T cell help did not diminish the primary $CD8^+$ T cell response, as opposed to reduced responses observed during subcutaneous HSV-1 infection (Smith et al., 2004). This difference may be due to contributions from direct priming during vaccinia infection; whereas cross presentation remains the primary mode of antigen presentation to CTL during low dose of subcutaneous HSV-1 infection (Singh and Cresswell, 2010). Furthermore, the use of a high inoculating dose delivered subcutaneously, which can result in higher antigen levels and greater inflammation, might abrogate the requirement for help during the primary response (Smith et al., 2004). Further experiments are required to ascertain whether ablation of $XCR1^+$ DC affects both the primary response as well as the memory formation of CTL during epicutaneous HSV-1 infection.

Finally, our imaging setup involving simultaneous imaging of both T cell subsets with $XCR1^+$ DC has allowed us to examine the dynamics of CD4 help provision. The mode by which $CD4^+$ T cells deliver help has remained largely elusive. Although CD40 ligation provides a 'help signal' for DC (Bennett et al., 1998; Ridge

et al., 1998; Schoenberger et al., 1998), when and how of these cells interact within the lymphoid tissues have not been thoroughly explored. There are currently two competing models describing the mode of CD4 help provision: 1) 'three-cell cluster' model, which postulates that $CD4^+$ and $CD8^+$ T cells simultaneously engage the APC, forming a ternary cluster and allowing the requisite signals (including CD40, IL-2, and lymphotoxin receptor signalling) to be delivered concurrently; and 2) a 'licensing' model, where $CD4^+$ T cells migrate around and 'license' multiple DC serially through transient interactions.

Our experimental results thus far have provided some mechanistic insight regarding the provision of help by $CD4^+$ T cells. We observed two types of interactions: 1) with $CD4^+$ T cells clustering with LN-resident $XCR1^+$ DC in the absence of CTL during late priming phase, which suggests the possibility of delivering 'help signals' prior to antigen-specific interaction with $CD8^+$ T cells; and also 2) some instances of $CD4^+$ T cells swarming around $CD8^+$ T cell clusters transiently, which may allow $CD4^+$ T cells to provide 'help signals' for DC to fully activate CTL through serial, transient interactions before dissociating and engaging a different DC (further discussed in **Chapter 7**).

In summary, we characterised the cellular dynamics of $CD4^+$ and $CD8^+$ T cell activation during localised HSV-1 infection and provided *in vivo* evidence of the functional segregation of DC subsets, namely migratory $CD11b^+$ DC and LN-resident $XCR1^+$ DC, in the priming of $CD4^+$ and $CD8^+$ T cells respectively. Our work also illustrated the critical role of $XCR1^+$ DC in orchestrating not only the priming of CTL, but also potentially serving as a platform for the delivery of $CD4^+$ T cell help.

CHAPTER SIX:

ROLE OF DOCK8 IN SKIN T_{RM} FORMATION

6.1 INTRODUCTION

Dedicator of cytokinesis 8 (DOCK8) mutations have recently been linked to immunodeficiencies in patients with autosomal recessive hyper-IgE syndrome (Zhang et al., 2009). Clinical presentations are commonly characterised by heightened serum IgE levels, recurrent respiratory infections, asthma, allergies, and skin pathologies including eczema and abscesses. However, different from classical hyper-IgE syndrome, a hallmark feature of DOCK8 deficiency is an increased susceptibility to severe and recurrent cutaneous viral infections, which typically include HSV, human papillomavirus (HPV), molluscum contagiosum virus (MCV), and varicella-zoster virus (VZV) (Su, 2010).

DOCK8 functions as an atypical guanine nucleotide exchange factor (GEF) for the Rho family of GTPases (Cote and Vuori, 2002; Ruusala and Aspenstrom, 2004). Loss of DOCK8 affects lymphocyte activation, proliferation, survival of memory cells (Randall et al., 2011), as well as formation of immunological synapses (Randall et al., 2009). Recently, DOCK8 was demonstrated to be the GEF specific for CDC42 (Harada et al., 2012), a master regulator responsible for cell polarity in eukaryotic organisms (Pruyne and Bretscher, 2000; Etienne-Manneville and Hall, 2002). Importantly, this study showed that DOCK8-deficient DC exhibited impaired interstitial migration in 3D collagen environment simulating dermal interstitium (Harada et al., 2012).

The skin is composed of dense bundles of collagenous fibrils in the dermis, and tightly adhering keratinocytes in the superficial epidermis, also serving as a natural barrier against the external environment. The densely packed connective tissues in the interstitial dermis make DC migration strenuous, and cells are observed to squeeze between the fibrillar collagen bundles (Stoitzner et al., 2002; Ng et al., 2008). In the same vein, after cutaneous HSV-1 infection $CD8^+$ T_{RM} localise between keratinocytes in the epidermis, and their permanent residence requires navigation of this dense environment (Zaid et al., 2014).

In this chapter, we study the formation of $CD8^+$ T_{RM} after skin HSV-1 infection and determine whether this process requires functional DOCK8, which is important for migration within constrained environments. We found that DOCK8-deficient HSV-specific $CD8^+$ T cells were unable to survive and form T_{RM} in the epidermis, leading to loss of protection against secondary HSV-1 challenge.

6.2 RESULTS

6.2.1 DOCK8-deficient CD8$^+$ T cells exhibited reduced memory formation after HSV-1 infection.

To determine if DOCK8-deficient CD8$^+$ T cells showed impaired T_{RM} formation in the skin, we co-transferred naïve WT and DOCK8$^{-/-}$ CD8$^+$ gBT-I T cells into recipient mice at 1:1 ratio prior to infecting the mice with HSV-1 epicutaneously. At D7 p.i., DOCK8$^{-/-}$ CD8$^+$ gBT-I cells exhibited reduced expansion in both the spleen and draining bLN (~3-fold lower than WT), with a similar ratio of WT:DOCK8$^{-/-}$ CD8$^+$ gBT-I cells observed in the skin (**Fig. 6.1A, B**). However, DOCK8$^{-/-}$ CD8$^+$ gBT-I cells consistently showed poorer long-term survival when examined at D14 p.i. (early memory phase) and at D31 p.i. (late memory phase) in the skin (**Fig. 6.1C, D**). While there was a corresponding increase in the WT:DOCK8$^{-/-}$ CD8$^+$ gBT-I cells ratio in the spleen (averaging 15:1) (**Fig. 6.1C, E**), the loss of DOCK8$^{-/-}$ CD8$^+$ gBT-I cells in the skin was more pronounced, with an average of ~180-fold reduction at D31 p.i. (**Fig. 6.1C**) Most importantly, only a minor proportion (less than 20%) of the few remaining DOCK8$^{-/-}$ CD8$^+$ gBT-I cells in the skin at D31 p.i. upregulated CD103, a distinguishing marker expressed by T_{RM} (Mackay et al., 2013), and a phenotype observed in most of the WT CD8$^+$ gBT-I cells (more than 80%) at this stage (**Fig. 6.1F, G**). This pronounced survival defect of DOCK8$^{-/-}$ CD8$^+$ gBT-I was also reflected in intravital imaging of the skin, where at D17 p.i. only very few DOCK8$^{-/-}$ cells could be detected, with an almost total loss by D30 p.i. (data not shown).

6.2.2 DOCK8-deficient CD8$^+$ T cells failed to establish tissue residence in the skin.

As DOCK8 deficiency is known to interfere with T cell priming and their proliferation, which we also observed in the preceding section, we wished to further rule out the possibility that the pronounced loss of DOCK8$^{-/-}$ CD8$^+$ T cells was caused by defective T cell activation, expansion or migration from lymphoid tissue to the skin. CD8$^+$ T_{RM} can be seeded independent of infection by lodging *in vitro*-activated T cells through intradermal injection (Mackay et al., 2013). This

bypasses the typical priming and proliferation phases of T cell, as well as their subsequent migration to the skin during HSV-1 infection, and allows us to control the initial precursor of T cells lodged in the skin.

By injecting equal numbers of WT and DOCK8$^{-/-}$ CD8^{+} gBT-I cells intradermally, we found that DOCK8$^{-/-}$ cells rapidly disappeared from the skin as early as D4 post-injection (**Fig. 6.2A**). This loss was unlikely to be caused by their emigration from the skin as well, since there was also a slight corresponding drop in numbers recovered from the spleen, when compared to their WT counterparts from the same mouse (**Fig. 6.2B**). At D23 post-injection, only very few DOCK8$^{-/-}$ cells remained in the skin, while WT cells remained at relatively high numbers (**Fig. 6.2A**). Importantly, the vast majority of DOCK8$^{-/-}$ cells by D23 p.i. were negative for expression of CD103, resulting in only very low number of enumerated T_{RM} (**Fig. 6.2C**). While up to 60% of WT gBT-I cells expressed CD103 by D23 p.i., only ~20% of their DOCK8$^{-/-}$ counterparts upregulated CD103 (**Fig. 6.2D**), suggesting that even when lodged directly in the skin, DOCK8$^{-/-}$ CD8^{+} T cells survived poorly and failed to form T_{RM}.

6.2.3 DOCK8-deficient CD8^{+} T cells failed to protect against cutaneous HSV-1 challenge.

Finally, we examined if pre-seeding DOCK8-deficient CD8^{+} T_{RM} could provide protective immunity against HSV-1 challenge. CD8^{+} T_{RM} can be seeded in the skin through adoptive transfer of *in vitro*-activated CD8^{+} T cells combined with treating the skin with the chemical sensitiser 2,4-dinitrofluorobenzine (DNFB). This results in immigration of effector T cells into the treated skin and ultimately in their T_{RM} formation (Mackay et al., 2012). 30 days after DNFB treatment, we challenged the treated skin with HSV-1 and measured viral titres in the skin 5 days after infection. While mice receiving WT effector CD8^{+} gBT-I cells showed enhanced protection against HSV-1 challenge, as is evident from the substantially lower viral titres in the skin, mice that received DOCK8$^{-/-}$ effector cells showed similar viral titres compared to control mice that did not receive any activated CD8^{+} T cells (**Fig. 6.3**). Together, our data showed that CD8^{+} T cells

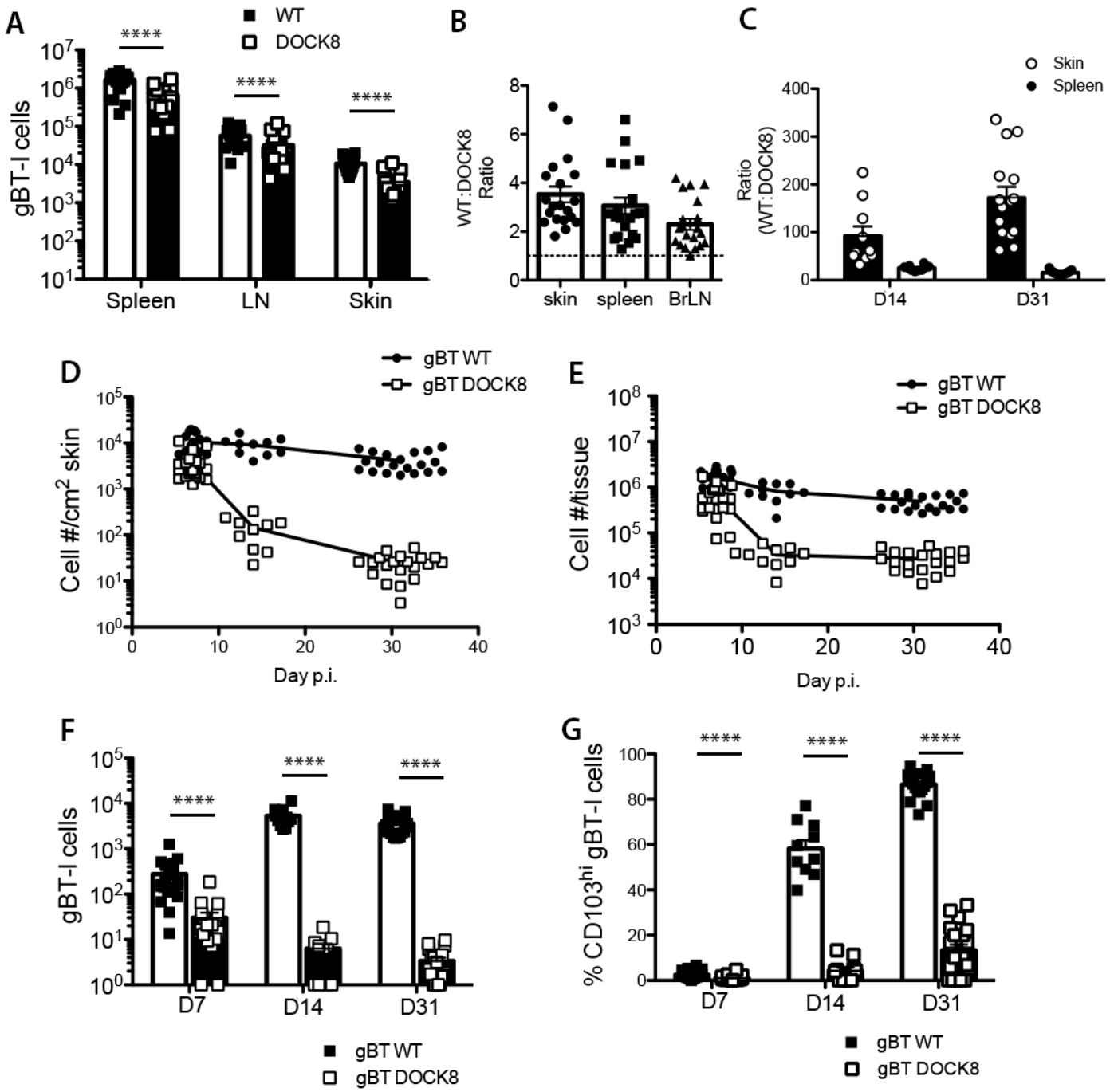

Figure 6.1 Poor survival of DOCK8-deficient memory CD8⁺ T cells after HSV-1 infection

$5x10^4$ WT and DOCK8$^{-/-}$ CD8⁺ gBT-I T cells were adoptively transferred into recipient C57BL/6 mice one day prior to epicutaneous HSV-1 infection. (A) WT (white bars) and DOCK8$^{-/-}$ (black bars) gBT-I T cells in the spleen, bLN and 1cm² skin containing the infected site at D7 p.i.

(B) Ratio of WT:DOCK8$^{-/-}$ gBT-I cells in the skin, spleen and bLN at D7 p.i.

(C) Ratio of WT:DOCK8$^{-/-}$ gBT-I cells in the spleen (white bars) and skin (black bars) at D14 and D31 p.i.

(D-E) Time course showing total WT (black dots) and DOCK8$^{-/-}$ (white dots) gBT-I cells in 1cm² infected skin (D) and the spleen (E) from D7 to D31 p.i.

(F-G) Total (F) and proportion of (G) CD103^{hi} WT (white bars) and DOCK8$^{-/-}$ (black bars) gBT-I T_{RM} in 1cm² infected skin at D7, D14 and D31 p.i.

Data pooled from 2-4 independent experiments; n = 10-20 mice for each time point. Error bars represent mean ± SEM. ****p<0.0001, paired Student t test.

lacking DOCK8 exhibited poor long-term survival and T_{RM} formation in the skin, and resulted in ineffectual protective immunity against skin HSV-1 challenge.

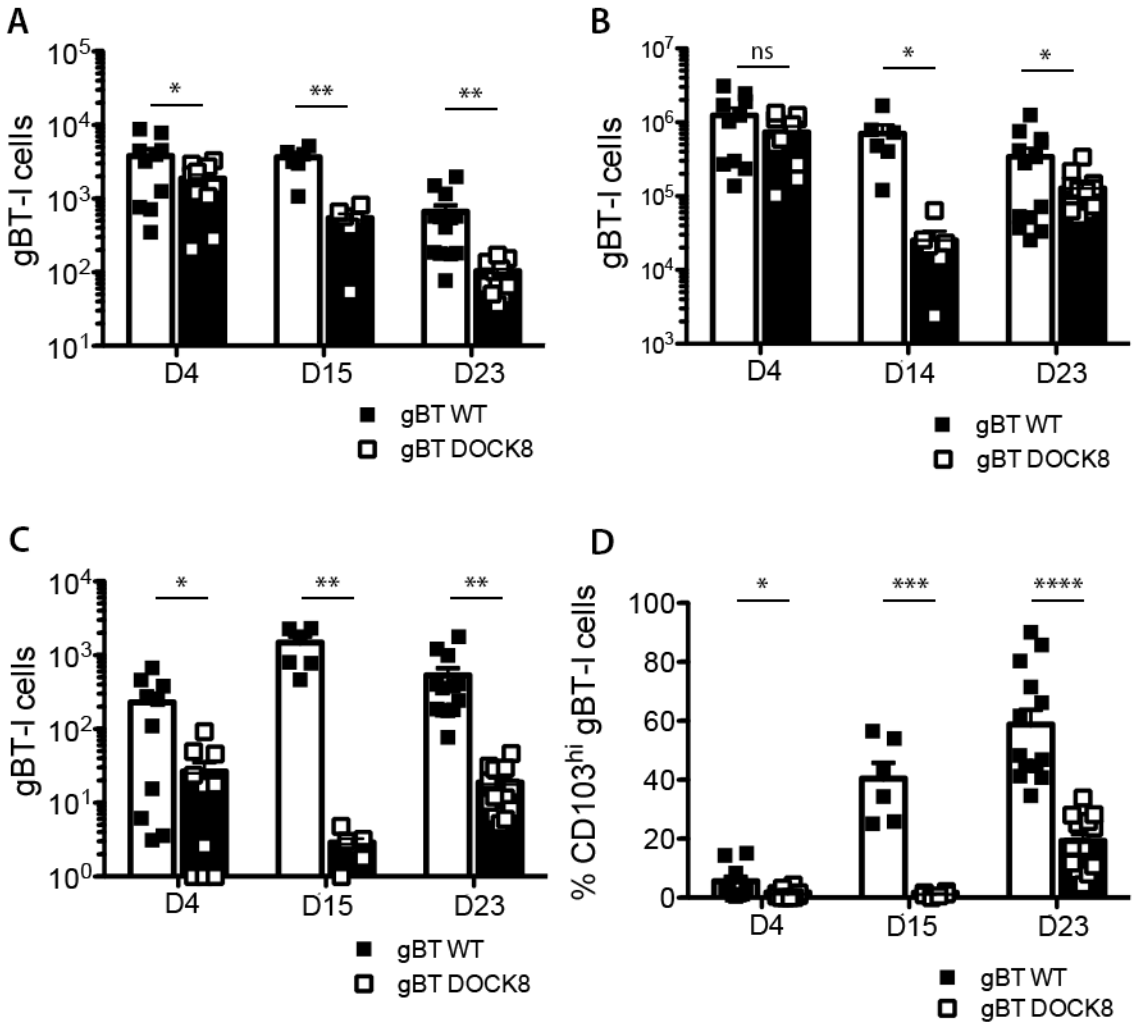

Figure 6.2 DOCK8-deficient CD8⁺ T cells fail to form Trm in the skin

1x10⁶ WT and DOCK8$^{-/-}$ CD8⁺ gBT-I T cells were injected i.d. into flank skin of recipient C57BL/6 mice.

(A-B) WT (white bars) and DOCK8$^{-/-}$ (black bars) gBT-I T cells in 1cm² injected skin (A) and the spleen (B) at D4, D15 and D23 p.i.

(C-D) Total (C) and proportion of (D) CD103^{hi} WT (white bars) and DOCK8$^{-/-}$ (black bars) gBT-I T_{RM} cells in 1cm² injected skin at D4, D15 and D23 p.i.

Data pooled from at least 2 independent experiments; n = 6-13 mice for each time point. Error bars represent mean ± SEM. *p<0.05, **p<0.01, ***p<0.001, ****p<0.0001, paired Student t test. ns, not significant.

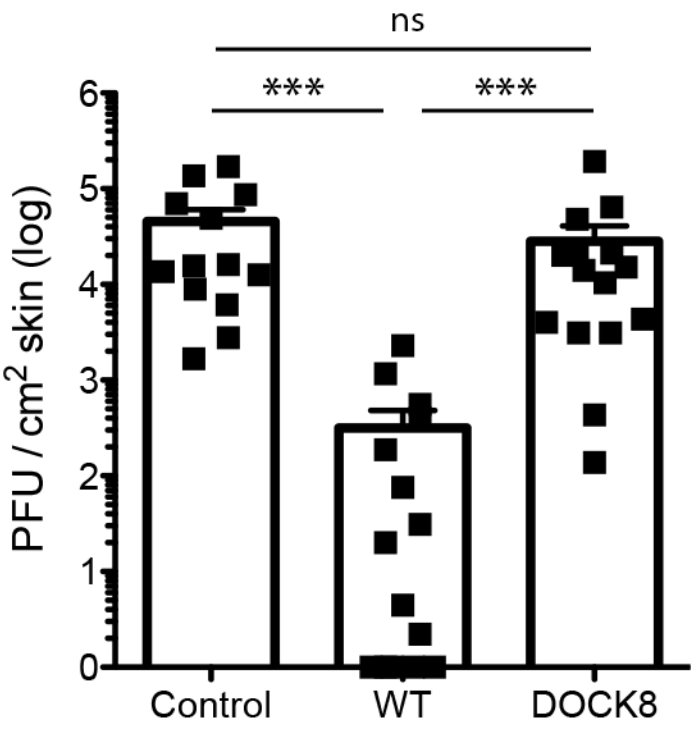

Figure 6.3 DOCK8-deficient CD8⁺ T cells fail to protect against cutaneous HSV-1 challenge

C57BL/6 mice received effector WT or DOCK8$^{-/-}$ CD8^{+} gBT-I T cells and were treated with DNFB on the left flank. At D30 post-treatment, mice were epicutaneously infected with HSV-1 and viral titres of 1cm^2 of infected skin assayed at D5 p.i. in mice without receiving cell transfer (left), transferred with WT (middle) or DOCK8$^{-/-}$ gBT-I cells (right).

Data pooled from 3 independent experiments; n = 13-15 mice for group. Error bars represent mean ± SEM. ***p<0.001, one-way ANOVA, Tukey's multiple comparisons on log transformed values. ns, not significant.

6.3 DISCUSSION

$CD8^+$ T_{RM} cells are critical for providing early immune surveillance against peripheral viral infections, including HSV-1, which is a common skin infection manifested in patients with DOCK8 deficiency. Here, we provide *in vivo* evidence that $CD8^+$ T cells lacking DOCK8 failed to persist and form T_{RM} in skin, which leads to inadequate immune protection against HSV-1 challenge.

DOCK8 deficiency has been shown to disturb various immunological functions including attenuation of T cell activation and proliferation. Defects in DC migration have also been observed, including an inability to exit the skin and impaired crossing of the SCS into the LN (Harada et al., 2012). Our work from the preceding chapters indicated a dominant role for migratory dDC in presenting antigen to $CD4^+$ T cells. Indeed, a recent study investigating DOCK8-deficient mice using a cutaneous HSV-1 infection model showed severely impaired $CD4^+$ T cell expansion and infiltration into the skin (Flesch et al., 2015). However, infiltration of $CD8^+$ T cells appeared unaffected, and this was consistent with our current results showing only a slight reduction of $DOCK8^{-/-}$ $CD8^+$ T cell numbers compared to WT cells in the initial infiltration of the skin.

Our data would argue that the diminished expansion of $CD8^+$ T cells after HSV-1 infection alone could not explain their reduced presence in the skin, since intradermal insertion of equal numbers of WT and DOCK8-deficient T cells also led to a loss of DOCK8-deficient T cell retention in the skin. However, it was possible that disappearance of DOCK8-deficient cells was simply due to them being outcompeted by WT counterparts in the co-transfer experiments (Lambe et al., 2011; Randall et al., 2011). Indeed, CDC42-deficient and memory DOCK8-deficient $CD8^+$ T cells have reduced expression of the survival marker IL-7R (Guo et al., 2010; Randall et al, 2011), which places DOCK8-deficient T cells at a competitive disadvantage to WT cells. Nonetheless, our results showed that when only DOCK8-deficient CD8 T cells were transferred into recipient mice to seed T_{RM} formation, these T cells also failed to confer protective immunity against HSV-1 challenge, thus arguing that despite the absence of WT $CD8^+$ T

cells, there were insufficient DOCK8-deficient $CD8^+$ T_{RM} to protect against the ensuing skin viral infection.

Interstitial migration of lymphocytes in the skin involves navigating through narrow three-dimensional spaces enmeshed by fibrillar collagenous network. Furthermore, entering the epidermis necessitates crossing the dense basement membrane at the dermo-epidermal junction. $CD8^+$ T_{RM} cells provide immunosurveillance of the epidermal skin barrier, which is composed of tightly spaced keratinocytes joined by tight junctions. Intravital microscopy has revealed that T cells manifest squeezing and contorted cellular morphology as they navigate among the epidermis (Gebhardt et al., 2011; Zaid et al., 2014), suggesting a basic requirement for regulating cytoskeletal reorganisation and integrity of cell shape to sustain migration and residence within the strenuous and compact environment. A recent study demonstrated that T cells lacking DOCK8, which results in dysfunction of CDC42 and PAK crucial for cytoskeletal rearrangement, formed abnormally elongated morphologies in three-dimensional collagen matrix, leading to nuclear deformation and cell fragmentation (Zhang et al., 2014). Together, these data provided a possible mechanistic account for the poor immunity against cutaneous viral infections commonly manifested by DOCK8-deficient patients.

CHAPTER SEVEN: GENERAL DISCUSSION

Major findings of this thesis

1. An early, transient wave of neutrophils and inflammatory monocytes infiltrate HSV-infected skin and dLN in a largely viral-independent manner. Few neutrophils migrated from the skin to the dLN and neutrophils were dispensable for the priming of HSV-specific $CD4^+$ and $CD8^+$ T cells and their subsequent migration to the skin (Chapter 3).

2. HSV-specific $CD4^+$ and $CD8^+$ T cells are activated in distinct phases following cutaneous infection (Chapter 4), and antigen presentation to both $CD4^+$ and $CD8^+$ T cell subsets is mediated by migratory $CD11b^+$ and LN-resident $XCR1^+$ DC subsets respectively (Chapter 5). The results revealed highly coordinated cellular interactions, marked by functional segregation and a complex interplay between multiple T cell and DC subsets during the induction of cell-mediated immunity against localised viral infection.

3. $CD4^+$ T helper cells engage dynamically with LN-resident $XCR1^+$ DC that are presenting antigen to $CD8^+$ T cells (Chapter 5). These dynamic interactions shed light on the long-standing question of how $CD4^+$ T cells deliver help signals to antigen-bearing DC, supporting the 'licensing' model where T helper cells move around providing help to multiple DC through transient interactions.

4. DOCK8, critical for the regulation of cytoskeletal rearrangement, in $CD8^+$ T cells is crucial for forming protective memory against secondary cutaneous infection with HSV-1 (Chapter 6). HSV-specific $CD8^+$ T cells require DOCK8 to navigate through the highly constrictive tissue environment in the epidermis and to survive and form T_{RM}.

7.1 Antigen transfer: does it matter who transports the antigen?

The mode of antigen delivery can drastically affect the distribution of antigen, how it is acquired and the type of APC acquiring the antigen. For many studies involving needle injection of antigen or pathogens into animals, the mechanism through which APC acquire antigen is less important since access into lymphatic or circulatory systems allows these injected antigens to promptly enter the immunosurveillance network by being directly captured by APC in the LN or the spleen. For localised infections, however, antigen retention in peripheral tissues requires capture by tissue DC and subsequent transport to local dLN to initiate the immune response (Carbone et al., 2004).

Numerous studies in recent years have also provided evidence of DC subset specialisation, whereby different subsets of migratory and lymphoid tissue-resident DC perform distinct and complementary roles in the events responsible for the induction of T cell responses. In particular, XCR1$^+$ DC specialise in cross-presentation of exogenous antigen on MHC-I, while XCR1$^-$ DC lack such capacity and present antigen on MHC-II.

The notion that antigen transfer takes place during skin HSV-1 infection was first proposed by Belz et al. (2004), in which they found that co-culture of TAP-1-deficient airway-derived CD8α$^-$ DC from influenza infected mice (which prevented viral antigen presentation) with naïve CD8α$^+$ DC led to CTL proliferation. Subsequently, Allan et al. (2006) demonstrated that only LN-resident CD8α$^+$ (also XCR1$^+$) DC were capable of presenting HSV antigen to CD8$^+$ T cells, but required dDC migration from the skin. These results suggested that migratory dDC first acquire antigen in the skin and then handover the antigen to CD8α$^+$ DC after migrating to dLN. The actual mechanism underlying this process remains unknown, and there is currently no direct evidence either *in vivo* or *ex vivo* that demonstrates the exchange of antigenic material between DC subsets. One hypothesis suggests that an intrinsic property of XCR1$^+$ DC: the expression of CLEC9A (DNGR-1), a C-type lectin receptor functioning as dead cell sensor crucial for dead-cell-associated antigen cross-presentation (Sancho et al., 2009), allows them to present HSV antigen acquired from apoptotic infected migratory

dDC. However, HSV-infected DC often showed impaired migration *in vitro* (Salio et al., 1999; Prechtel et al., 2005), and there is currently no evidence unequivocally demonstrating the presence of HSV-infected DC in dLN (Allan et al., 2006; Eidsmo et al., 2009; unpublished data).

A possible scenario involves the phagocytosis of apoptotic infected migratory DC *en route* to the dLN by uninfected migratory dDC (Bosnjak et al., 2005). Whether these secondary, uninfected DC later undergo apoptosis after their arrival at the LN, thus facilitating uptake by XCR1$^+$ DC, is not known. However, induction of apoptosis does not appear to require viral DNA synthesis (Bosnjak et al., 2005), and as such it remains possible that HSV antigen-bearing, uninfected migratory DC undergo apoptosis at later phase of infection. This scenario also coincides with our observation that CD8$^+$ T cell priming by XCR1$^+$ DC occurs at a later stage, suggesting that these DC could potentially die in the LN and be scavenged by LN-resident XCR1$^+$ DC. Alternatively, active processes may be involved in the handover of antigen between DC subsets, through such mechanisms as exosomes (Thery et al., 2009) or gap junctions (Saccheri et al., 2010; Mazzini et al., 2014).

A major finding of this thesis revolves around the functional segregation of DC subsets in regards to antigen presentation during localised HSV-1 infection. We found that CD8$^+$ T cells have delayed priming kinetics and are predominantly activated by LN-resident XCR1$^+$ DC; conversely, CD4$^+$ T cells receive early antigen presentation from migratory CD11b$^+$ dDC. Although the underlying cause of activation timing disparity between T cell subsets has yet to be fully elucidated, this delay might be explained by a temporal requirement for antigen transfer to occur between migratory and LN-resident DC.

Our results suggest that innate immune cells such as neutrophils and monocytes were not required for the delivery of antigen to the LN (see Chapter 3). CD11c$^+$ DC were the predominant migrants and were found to interact with HSV-specific CD4$^+$ T cells, indicating a major role in the capture and processing of HSV antigen. The two major subsets of migratory DC in the skin, CD103$^+$ and CD11b$^+$ DC, are the likely antigen carriers. However, it should be noted that CD103$^+$ DC

were found to be absent during the early wave of antigen presentation after cutaneous HSV-1 infection (Bedoui et al., 2009). This was also reflected in our analysis of *in situ* dye-labelled migratory cells arriving at the LN (**Section 5.2.8**). Thus, migratory CD11b$^+$ dDC appeared to be primarily responsible for antigen transport to the draining LN early during skin HSV infection.

Intrinsic differences between the migratory dDC subsets could be important to explain the delayed CTL priming. A key distinction between CD103$^+$ and CD11b$^+$ dDC pertains to the ability of XCR1$^+$ CD103$^+$ DC to cross-present exogenous cell-associated antigen to CD8$^+$ T cells (del Rio et al., 2007; GeurtsvanKessel et al., 2008). XCR1$^+$ CD8α$^+$ DC are capable of preventing rapid degradation of internalised antigens by maintaining low proteolytic activity and higher pH levels in their endosomes (Savina et al., 2006; Savina et al., 2009). This allows epitopes suitable for cross-presentation to be preserved adequately for cytosolic export. If antigen transport is primarily conducted by CD11b$^+$ dDC, which possess a higher proteolytic activity, given the time required for migration from the skin then the availability of antigen sufficiently preserved for cross-presentation may be greatly reduced upon arrival in the LN. For presentation of HSV antigens, a substantial amount of gB antigen, through sustained synthesis by infected epithelial cells, may be required to facilitate sufficient antigen presentation by LN-resident XCR1$^+$ DC. This hypothesis accounts for the requirement of *de novo* gB antigen synthesis during HSV-1 infection (Mueller et al., 2003). In short, while virion-derived antigen is efficiently processed and loaded on MHC-II for presentation to CD4$^+$ T cells by migratory CD11b$^+$ dDC, the preservation of antigen suitable for cross-presentation on MHC-I in the same DC may be suboptimal. Therefore, the intrinsic properties of the DC subsets, and the requirement for antigen transfer from the skin, might partly explain the delayed priming kinetics of CD8$^+$ T cells.

7.2 Delayed CTL priming: what does it tell us about the specialisation and redundancy in the induction of adaptive immunity?

CTL responses are critical for clearance of intracellular pathogens as well as mitigating disease pathology. At the cellular level, communication between multiple immune cells allows for integration of signals that drive eventual immune decisions. Our experimental results have demonstrated an elaborate process leading to induction of CTL priming against localised viral infection, which encompasses intricate interactions between multiple T cell and DC subsets. However, our results also revealed delayed CTL priming kinetics, suggesting that a rapid induction of cell-mediated immunity was at least partially compromised.

Briefly, in our experimental model with HSV-1, migratory CD11b$^+$ DC present antigen to CD4$^+$ T cells, which then can provide 'help' signals to LN-resident XCR1$^+$ DC. Meanwhile, CD11b$^+$ DC also serve as a source of antigen for transfer to LN-resident XCR1$^+$ DC, conferring the capacity to present antigen to CD8$^+$ T cells.

So how does this elaborate interaction between immune cells fit into our current understanding of T cell activation and the specialisation of DC subsets for peripheral immunity? Here, we argue that functional specialisation of DC is important for anticipating a broad context of host-pathogen interactions. In short, we propose that in the skin (i) migratory CD103$^+$ DC are dispensable for acute CTL priming following peripheral infection, and that (ii) in their absence LN-resident CD8α$^+$ DC take over the role of CTL priming resulting in delayed CTL activation kinetics due to antigen availability; and (iii) CD4 help may be crucial for augmenting CTL priming sensitivity under low antigen density or inflammatory conditions.

The late priming of CD8$^+$ T cells can be attributed to the lack of cross-presentation capacity on the part of migratory CD11b$^+$ DC. While viral infection of DC would allow direct presentation of newly synthesised antigenic peptide on MHC-I to CD8$^+$ T cells (Kim and Braciale, 2009), in cases where pathogens subvert the antigen presentation capability of DC, or inhibit their migrational

capacity, an ability to cross-present exogenously sampled antigen could prove invaluable for a prompt CTL response. XCR1$^+$ DC excel at cross-presentation relative to other DC subsets. We surmise that LN-resident CD8α$^+$ DC are specialised for cross-priming CTL with antigens that enter the LN, either extracellularly or within cells; on the contrary, migratory XCR1$^+$ CD103$^+$ DC specialise in the priming of CTL with antigen sampled from peripheral tissues. Additionally, CD103$^+$ DC have also been shown to resist certain viral infections (Helft et al., 2012). The absence of CD103$^+$ DC participation during the initial phase of antigen presentation during cutaneous HSV-1 infection (Bedoui et al., 2009) likely contributed to the delayed CTL response. It is tempting to speculate that CTL may not have experienced a delayed priming kinetics if CD103$^+$ DC were also initially involved in antigen presentation, in conjunction with CD11b$^+$ dDC.

It remains unclear why CD103$^+$ DC failed to participate in early antigen presentation, but it should also be noted that CD103$^+$ DC comprise <3% of skin DC, and as such the limited size of the HSV-infected site in our model might not induce the migration of large numbers of CD103$^+$ DC to dLN during the early phase. Indeed, migration of CD103$^+$ DC from HSV-infected skin is minimal (see Chapter 5, also Bedoui et al., 2009). In contrast, in a model employing subcutaneous immunisation of ovalbumin antigen, Kitano et al (2016) showed that CD4$^+$ T cells preferentially clustered with CD11b$^+$ DC while CD8$^+$ T cells clustered with migratory XCR1$^+$ CD103$^+$ DC. During respiratory influenza and respiratory syncytial virus (RSV) infections, CD103$^+$ DC are major antigen-presenting cells to CD8$^+$ T cell priming (GeurtsvanKessel et al., 2008; Kim and Braciale, 2009; Desch et al., 2011; Lukens et al., 2009). Thus, the tissue environment, the route of infection or antigen dose could alter T cell priming dynamics in part through the involvement of migratory CD103$^+$ DC. In the absence of this, the rate of CD11b$^+$ DC migration from the skin and the handover of antigen to LN-resident XCR1$^+$ DC may control CTL priming kinetics. This may also explain why adoptive transfer of activated HSV-specific CD4$^+$ T cells failed to accelerate CTL priming, but that in MHC-II knockout mice (where CD4 help is

absent), there was a further delay in the activation of CTL (**Fig. 4.13**), since the rate-limiting step probably occurs in the antigen handover phase.

It is clear that during skin HSV-1 infection LN-resident XCR1$^+$ CD8α$^+$ DC are sufficient to prime CTL responses. Less clear is whether models involving migratory XCR1$^+$ CD103$^+$ DC also require LN-resident XCR1$^+$ DC for efficient or complete T cell priming or the delivery of CD4$^+$ T cell help. To examine this, a model restricting antigen presentation to tissue-derived DC would be required.

In summary, efficient T cell responses during localised infection are orchestrated by the dynamic interactions of multiple specialised immune cells, each of which is critical to rapid induction of immunity but also backed by redundant components to anticipate for a wide range of host-pathogen relationship.

7.3 Provision of CD4 help (1): the dynamics of CD4 help delivery

XCR1$^+$ DCs receive help from activated T helper cells, which in turn allows them to fully activate CTL and provide appropriate signals for memory formation. It has been postulated that the dependency for help is closely associated with the strength of inflammatory signal, namely that antigen with poor inflammatory responses requires CD4 help to induce robust CTL priming (Bevan, 2004). CD4 'licensing' of XCR1$^+$ DC likely lowers the threshold for CTL priming through amplification of innate signals, including cytokine production such as IL-15 in the case of skin HSV-1 infection (Greyer et al., 2016). Tempered type I IFN responses during HSV-1 infection may necessitate CD4 help to enhance XCR1$^+$ DC activation and CTL priming.

However, when and how CD4 T helper cells provide help signals to antigen-bearing DC is unclear. The classical 'three cell cluster' model postulates that both antigen-specific CD4$^+$ and CD8$^+$ T cells simultaneously engage the same APC (Mitchison and O'Malley, 1987; **Fig. 1.3A**). This would permit the contact-dependent CD40-CD40L interaction between CD4$^+$ T helper cell and APC (Bennett et al., 1998; Schoenberger et al., 1998; Feau et al., 2011), though it has

also been proposed that CD40-dependent help mechanism may also be delivered directly to $CD8^+$ T cells (Bourgeois et al., 2002). Nonetheless, considering the low initial precursor frequency for both antigen-specific $CD4^+$ and $CD8^+$ T cells, and assuming random migration, the probability of *two* low frequency antigen-specific lymphocytes engaging the same APC concurrently would be highly inefficient. Alternate models have been proposed, including the 'licensing' model where helper T cells interact only transiently to 'license' DC, which frees them to move along to 'license' other DCs through serial interactions without engaging with the same DC for hours (Ridge et al., 1998; Lanzavecchia, 1998; **Fig. 1.3B**).

Using intravital imaging, data presented here allowed us to begin to dissect the dynamic interplay of help-provision by $CD4^+$ T cells during localised viral infection. We observed at least two types of interactions between $CD4^+$ T cells and LN-resident DCs that might potentially involve DC 'licensing'. First, we found $CD4^+$ T cells forming homogeneous clusters with LN-resident $XCR1^+$ DC during the late priming phase. Whether these were naïve $CD4^+$ T cells being activated or previously activated $CD4^+$ T cells is not known, but such interactions likely involved the delivery of CD40L signals for DC licensing. This type of antigen-specific interaction could amplify secretion of chemokines such as CCL4 and CCL5 for attracting naïve CTL (Castellino et al., 2006; also further discussed in the next section). Our results suggested that provision of help could occur independently of $CD8^+$ T cells, thus absolving the requirement for both $CD4^+$ and $CD8^+$ T cells to encounter the same DC within the same period of time.

Secondly, although most $CD8^+$ T cell clusters were relatively homogeneous, in some instances $CD4^+$ T cells were seen interacting with these clusters in a transient, dynamic manner and 'swarming' around these clusters. Although the nature of such interactions has yet to be determined, these activated $CD4^+$ T cells could potentially engage with $XCR1^+$ DC presenting antigen to $CD8^+$ T cells. This mode of interaction would allow help to be delivered to the antigen-presenting DC *while* CTLs are undergoing activation, and also potentially to DC that have yet to encounter with antigen-specific CTL, in a rapid and efficient manner. As such, the help signal required to fully activate $CD8^+$ T cells may be delivered to

antigen-presenting DC at any stages during or prior to $CD8^+$ T cell priming, thereby substantially broaden the time window for antigen-specific $CD4^+$ and $CD8^+$ T cells to encounter with the same APC. This strategy might be particularly effective given the very low frequency of antigen-specific T cell precursors, and allow help signals to be efficiently distributed to multiple DC through transient, serial interactions (Heath and Carbone, 2001).

Thus, after activation by migratory $CD11b^+$ DC, $CD4^+$ T cells locate $XCR1^+$ DC and deliver help (**Fig. 7.1**). A similar observation has recently been reported by Eickoff et al. (2015) using subcutaneous vaccinia virus infection, in which $CD4^+$ and $CD8^+$ T cells transferred late during infection were observed to co-cluster around $XCR1^+$ DC. The authors proposed that after initial activation of $CD4^+$ and $CD8^+$ T cells by uninfected and infected migratory DCs, respectively, both T cell subsets eventually convene with $XCR1^+$ DC for help signals to be transmitted. However, the mode of CD4 help delivery was not examined in the study and it was not clear if activated $CD4^+$ T cells first encounter $XCR1^+$ DC, and through such interaction promoted the recruitment of $CD8^+$ T cells.

In short, this thesis presented data that could help elucidate the dynamic mechanism of CD4 help provision. We showed at least two types of interactions that permit efficient delivery of helper signals that are compatible with the current models described for provision of CD4 help. It is important to note that these two types of interactions are not mutually exclusive and may both occur. Thus, how help is delivered remains an open question and a subject for future experiments.

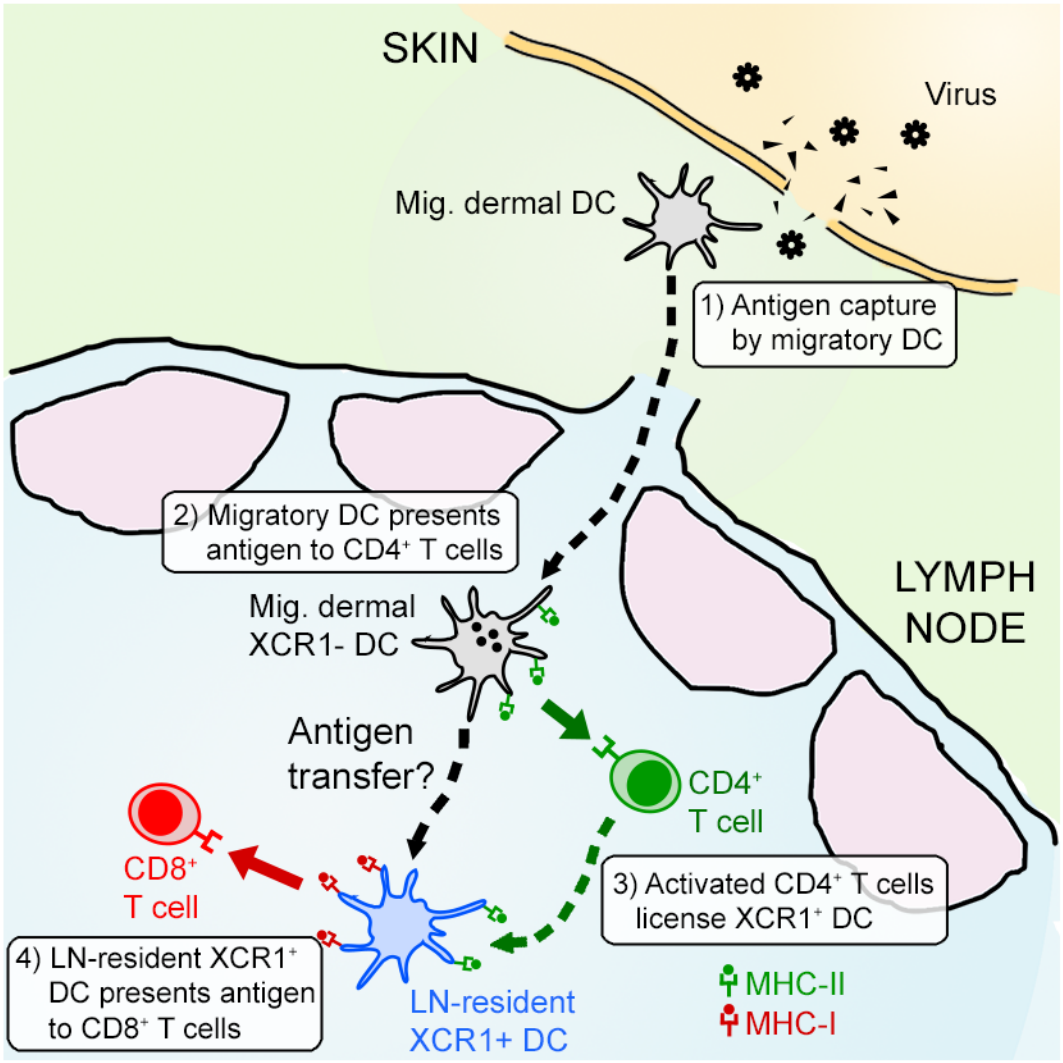

Figure 7.1 Distinct DC populations involved in the priming of CD4⁺ and CD8⁺ T cells during HSV-1 infection

Migratory CD11b⁺ XCR1⁻ dDC acquires viral antigen upon cutaneous HSV-1 infection, and migrates to the draining LN and presents antigen to CD4⁺ T cells via MHC-II. After priming by migratory dDC, activated CD4⁺ T cells locate for LN-resident XCR1⁺ DC to deliver 'help', which in turn presents antigen to CD8⁺ T cells through MHC-I.

7.4 Provision of CD4 help (2): how do CD4$^+$ and CD8$^+$ T cells rendezvous with the same DC?

In its simplest form, the 'three cell cluster' model of CD4 help provision (see previous section) relies on chance encounters of antigen-specific CD4$^+$ and CD8$^+$ T cells with the same APC. The very low number of initial T cell precursors, however, renders the probability of such random encounter highly unlikely. Castellino et al. (2006) demonstrated a CCR5-mediated mechanism whereby antigen-specific CD4$^+$ T cells first encountered DC and delivered help, and in turn the 'helped' DC augment production of chemokines CCL3 and CCL4 that attracted naïve CD8$^+$ T cells that had upregulated CCR5 upon entering the inflamed LN. This mechanism provided an explanation for how lymphocytes encounter antigen-bearing APC efficiently via non-random migration, and the authors proposed that this resolves the mathematical improbability of 'three cell cluster' model in which both helper and CTL are required to engage in sustained interaction with APC.

However, results from this thesis demonstrated that after HSV infection, CD4$^+$ T cells were first activated by CD11b$^+$ dDC, and subsequently located antigen-bearing LN-resident XCR1$^+$ DC to deliver help. This suggested that the first point of contact for CD4$^+$ helper T cells was unlikely to be the same DC that subsequently receive help. Instead, our model requires that CD4$^+$ helper T cells also efficiently find a *second* DC population for help provision after their initial priming. Furthermore, we also noted considerably fewer HSV-specific CD8$^+$ T cell clusters compared to CD4$^+$ T cell clusters, suggesting that antigen-bearing XCR1$^+$ DC capable of priming CD8$^+$ T cells were relatively scarce during the initial phase of the response.

Similarly, as described in previous section, a recent study by Eickoff et al. (2015) also proposed that both CD4$^+$ and CD8$^+$ T cells initially clustered separately, and then later with XCR1$^+$ DC during where help was delivered. The mechanism that attracts both lymphocyte subsets to the XCR1$^+$ DC, however, is not known. In light of these recent observations, and the involvement of multiple DC subsets

during priming, the long-standing question of how rare CD4$^+$ and CD8$^+$ T cells come together with the same APC is worth re-visiting here.

Interestingly, both our observations and those of Eickoff et al. (2015) argue that since XCR1$^+$ DC are ultimately responsible for full CTL activation, they remain the *only* platform on which CD4 help can be delivered. This opens up the possibility that antigen-bearing XCR1$^+$ DC may attract activated CD4$^+$ T cells through guidance from specific chemokines, amidst other DC subsets that are also capable of priming CD4$^+$ T cells.

Here, we speculate that this may involve the chemokine receptor CXCR3, which is characteristically upregulated by Th1-polarised helper cells both *in vitro* (Langenkamp et al., 2003) and *in vivo* (Kim et al., 2001). Groom et al. (2012) showed that antigen-presenting DC production of the CXCR3 ligand CXCL10 was important for attracting CD4$^+$ T cells as well as promoting Th1 differentiation. Although we have observed increased LN mRNA level of CXCL10 at 18 hr and D3.5 p.i. (**Fig. 4.5**), we have not dissected the cellular sources of this chemokine production. Interestingly, a number of studies have reported that XCR1$^+$ DC may be the principal DC subset that expresses CXCL10. In a hepatic model of *Propionibacterium acnes* infection, LN DEC-205$^+$ DC (also a phenotype for XCR1$^+$ DC) produced CXCL10 that was critical for the cluster formation of proliferating Th1 cells (Yoneyama et al., 2002). Similarly, CXCL10 production was highly induced in splenic XCR1$^+$ DC during secondary *Listeria monocytogenes* infection (Alexandre, 2016). In humans, CD141^{hi} DC (also XCR1$^+$ and homologue of mouse XCR1$^+$ CD8α$^+$ DC; Bachem et al., 2010) have been demonstrated to express high levels of CXCL10 upon TLR3 stimulation (Jongbloed et al., 2010; Haniffa et al., 2012; Martinez et al., 2015), where TLR3 is crucial for the host defence against HSV-1 in human patients (Zhang et al., 2007).

Successful encounter between helper T cells and XCR1$^+$ DC, which leads to DC 'licensing', could further amplify the chemokine signals and draw naïve CD8$^+$ T cells to the appropriate DC. In fact, it is possible that differential chemokine receptor-mediated guidance could function to facilitate the encounter of CD4$^+$

and CD8$^+$ T cells separately with the same APC. With XCR1$^+$ DC serving as a platform for the delivery of help, CXCR3 ligands may first help to attract activated CD4$^+$ helper cells, leading to help provision. In turn, the 'helped' XCR1$^+$ DC amplify CCR5 ligands production and recruit naïve CTL to the site of antigen presentation.

Additionally, activated CD8$^+$ T cells secrete XCL1 (Dorner et al., 2009), which could attract XCR1$^+$ DC and potentially concentrate XCR1$^+$ DC to distinct locales of the LN and amplify CCL3/CCL4 chemokine signals for robust attraction of CD8$^+$ T cells. Although our data did not indicate a role for the chemokine receptor XCR1 in CTL priming and expansion during HSV-1 infection (**Fig. 5.12**) minor contributions from this pathway cannot be excluded. It remains to be determined if there are other chemokines at play that participate in the recruitment of T cells to activated DCs.

7.5 Concluding remarks

Overall, this thesis has examined the complex interplay between key immune components throughout the initiation of cell-mediated immunity against localised viral infection, from investigating the bridging roles of innate immune cells in modulating T cell responses, to dissecting the cellular dynamics of antigen presentation. Our work has uncovered a complex orchestration involving multiple DC and T cell subsets, with XCR1$^+$ DC serving as a critical platform for the provision of help as well as CTL activation, highlighting the importance of functional specialisation during induction of immunity *in vivo*. Finally, our work cast new light on the mode by which CD4$^+$ T cells deliver help to 'license' DC for robust CTL priming.

APPENDIX A:
MATLAB Scripts for Imaris XT

A.1 Cluster detection (single time frame only)

```
% Cluster detection for Imaris (single time frame only)
% Updated December 2014, J.L. Hor

function cluster_main()

aImarisApplicationID = 0;

% connect to Imaris interface
if ~isa(aImarisApplicationID, 'Imaris.IApplicationPrxHelper')
    javaaddpath ImarisLib.jar
    vImarisLib = ImarisLib;
    if ischar(aImarisApplicationID)
        aImarisApplicationID = round(str2double(aImarisApplicationID));
    end
    vImarisApplication = vImarisLib.GetApplication(aImarisApplicationID);
else
    vImarisApplication = aImarisApplicationID;
end

% the user has to create a scene with some spots and surface
vSurpassScene = vImarisApplication.GetSurpassScene;
if isequal(vSurpassScene, [])
    msgbox('Please create some Spots in the Surpass scene!')
    return
end

% get the spots and the surface object
vSpots =
vImarisApplication.GetFactory.ToSpots(vImarisApplication.GetSurpassSelection);

vSpotsSelected = ~isequal(vSpots, []);
if vSpotsSelected
    vParent = vSpots.GetParent;
else
    vParent = vSurpassScene;
end

% get the spots and surfaces
vSpotsSelection = 1;
vNumberOfSpots = 0;
vSpotsList = [];
vSpotsName = {};
for vIndex = 1:vParent.GetNumberOfChildren
    vItem = vParent.GetChild(vIndex-1);
    if vImarisApplication.GetFactory.IsSpots(vItem)
        vNumberOfSpots = vNumberOfSpots + 1;
        vSpotsList(vNumberOfSpots) = vIndex;
        vSpotsName{vNumberOfSpots} = char(vItem.GetName);

        if vSpotsSelected && isequal(vItem.GetName, vSpots.GetName)
            vSpotsSelection = vNumberOfSpots;
        end
    end
end

if min(vNumberOfSpots) == 0
    msgbox('Please create minimum one spots object!')
    return
end

if vNumberOfSpots>1
    [vSpotsSelection,vOk] = listdlg('ListString',vSpotsName, ...
```

```
        'InitialValue', vSpotsSelection, 'SelectionMode','multiple', ...
        'ListSize',[300 300], 'Name','Find Spots Close To Surface', ...
        'PromptString',{'Please select the spots:'});
    if vOk<1, return, end
end

vNumberOfSpotsSelected = numel(vSpotsSelection);

for vSpotsIndex = 1:vNumberOfSpotsSelected
        vItem = vParent.GetChild(vSpotsList( ...
            vSpotsSelection(vSpotsIndex)) - 1);
        vSpots = vImarisApplication.GetFactory.ToSpots(vItem);



[mDistThres, mMinClusterSize,mMinContactPoint,mUseRadiusHack,mMinRadius,...
  mMaxRadius] = inputGUI();



 vSpotsValues = struct2cell(struct(vSpots.Get));
 [vSpotsXYZ,vSpotsTime,vSpotsRadius] = vSpotsValues{:};
 vNumberOfSpots = size(vSpotsXYZ, 1);

 [mDistTable] = SpotsDistance(vSpotsXYZ, vSpotsTime);

 [mSpotTable] = ContactPoints(mDistTable, mDistThres);

 [mSpotClusterT, mClusterSize] = ClusterDetection(mSpotTable, mMinClusterSize, ...
     mMinContactPoint);

 SpotsCreation(vImarisApplication, mSpotClusterT, mClusterSize, vSpotsXYZ, ...
     vSpotsTime, vParent, vNumberOfSpots, mUseRadiusHack, mMinRadius, ...
     mMaxRadius, vSpots, vSpotsRadius);

    end

end




% Generate table for distance between spots
function [vDistTable3D] = SpotsDistance(aSpotsXYZ, aSpotsTime)

    for vTimeIndex = 0:max(aSpotsTime)
        vSpotsT = aSpotsTime == vTimeIndex;
        vSpotsIndex = find(vSpotsT');
            for vIndex = vSpotsIndex
                vOthers = vSpotsT;
                vOthers(vIndex) = false;
                vX = aSpotsXYZ(vOthers, 1) - aSpotsXYZ(vIndex, 1);
                vY = aSpotsXYZ(vOthers, 2) - aSpotsXYZ(vIndex, 2);
                vZ = aSpotsXYZ(vOthers, 3) - aSpotsXYZ(vIndex, 3);
                vDist = sqrt(sum( ([vX, vY, vZ]).^2, 2 ));

                vDistTable3D(vIndex, vOthers) = vDist;
            end
     end

    csvwrite('DistTable3D.csv', vDistTable3D);

end




% Determine number of contact points per spot
function [spot_table3D] = ContactPoints(aDistTable, aDistThres)

% Read spots distance matrix, time index, track ID
```

```
if isempty(aDistTable)
magic = [];
magic = dlmread('DistTable.csv');
else
magic = aDistTable;
end

% Get Threshold value from user-input form
vThreshold = aDistThres;

magic_thres = magic;
magic_thres(magic_thres > vThreshold) = 0;
magic_thres(magic_thres > 0 & magic_thres <= vThreshold) = 1;

% assign temp table into Spot Table (whole sheet on cell array)
spot_table3D = magic_thres;

csvwrite('spot_table3D.csv', spot_table3D);

end




% Cluster detection module
function [vSpotClusterT, vSpotClusterSize] = ClusterDetection(spot_table3D, ...
    aMinClusterSize, aMinParallelContact)

% PARALLEL MODE is selected here:
aParallel = true;

if isempty(spot_table3D)
vTable = csvread('spot_table3D.csv');
else
vTable = spot_table3D;
end

vElements = 1:size(vTable,1);
vClusterID = 1;

vSpotClusterT = zeros(size(vElements));
vSpotClusterT = vSpotClusterT.';
vSpotClusterSize = zeros(size(vElements));
vSpotClusterSize = vSpotClusterSize.';
disp(size(vSpotClusterT));



curClusterNeighbours = {};
curClusterNeighbours{vClusterID} = [];

vClusterSize = [];

% ONLY APPLICABLE IF PARALLEL MODE IS ACTIVE
vPointsofContact = zeros(size(vElements'));
vSpotstoIgnore = [];

% Progress Bar
vProgressTotalCount = max(vElements);
vProgressDisplay = waitbar(0, 'Cluster Detection');
vProgressCount = 0;



% FIRST LOOP: vRootTrack
for vRootSpot = 1:max(vElements)

    if vSpotClusterT(vRootSpot)==0 && ~ismember(vRootSpot, vSpotstoIgnore)

        % SECOND LOOP: Individually check every track (vCurTrack) against root track
```

```
        for vCurSpot = 1:max(vElements)

            tempClusterT = vTable(vCurSpot, :);

            % vPointsofContact for the current track is registered before
            % the current track is added to it. Only applicable for
            % PARALLEL mode.
            curCluster = find(tempClusterT > 0);
            vPointsofContact(vCurSpot) = numel(curCluster);
            curCluster = [vCurSpot curCluster];
            curCluster = unique(curCluster);

            if numel(curCluster) > 1

               A = cellfun('isempty', curClusterNeighbours);

               if A(vClusterID) == 1
                    curClusterNeighbours{vClusterID} = vRootSpot;
               end

               if numel(intersect(curCluster, curClusterNeighbours{vClusterID})) > 0

                curClusterNeighbours{vClusterID} = ...
                    [curClusterNeighbours{vClusterID} curCluster];
                curClusterNeighbours{vClusterID} = ...
                    unique(curClusterNeighbours{vClusterID});

                    % If PARALLEL mode is ON, then all tracks within the
                    % cluster will be added to root TrackstoIgnore.
                    % Otherwise non-qualified tracks within a cluster will
                    % not be registered with a clusterID and will be
                    % processed again and overwrite all the old tracks with
                    % a new clusterID.

                    if aParallel == true
                            vSpotstoIgnore = [vSpotstoIgnore curCluster];
                            vSpotstoIgnore = unique(vSpotstoIgnore);
                    end
               end

            end

            if vCurSpot == max(vElements)

                % If PARALLEL mode is ON, find intersection index of
                % curClusterNeighbours and those with less points of
                % contact than defined. They will be removed from the
                % current curClusterNeighbours{vClusterID}.
                % The overall size of the cluster will be determined in the
                % next conditional block and see if all the remaining cells
                % are qualified to be a cluster.

                if aParallel == true

                    P = find(vPointsofContact < aMinParallelContact);
                    [~, iR, ~] = intersect(curClusterNeighbours{vClusterID}, P);
                    curClusterNeighbours{vClusterID}(iR) = [];
                end

                if numel(curClusterNeighbours{vClusterID}) >= aMinClusterSize;
                    vSpotClusterT(curClusterNeighbours{vClusterID}) = vClusterID;
                    vClusterSize(vClusterID) =
numel(curClusterNeighbours{vClusterID});
                    vSpotClusterSize(curClusterNeighbours{vClusterID}) = ...
                        vClusterSize(vClusterID);
                    vClusterID = vClusterID + 1;
                    curClusterNeighbours{vClusterID} = [];
                    disp('new vClusterID:');
                    disp(vClusterID);
                end
```

```
                if numel(curClusterNeighbours{vClusterID}) < aMinClusterSize;
                    curClusterNeighbours{vClusterID} = [];
                end


            end
        end


    end

    vProgressCount = vProgressCount + 1;
    waitbar(vProgressCount/vProgressTotalCount, vProgressDisplay)

end

csvwrite('SpotClusterID.csv',vSpotClusterT);
csvwrite('ClusterSize.csv',vClusterSize.');
csvwrite('SpotClusterSize.csv',vSpotClusterSize);
close(vProgressDisplay);

end




% Spots Creation module and add statistics back to Imaris
function SpotsCreation(vImarisApplication, aSpotClusterT, aClusterSize, ...
    vSpotsXYZ, vSpotsTime, vParent, aNumberofSpots, aUseRadiusHack, ...
    aMinRadius, aMaxRadius, aSpots, aSpotsRadius)

if isempty(aSpotClusterT)
vSpotClusterID = csvread('SpotClusterID.csv');
else
vSpotClusterID = aSpotClusterT;
end

% Use Radius Hack to generate colour-coded spots through a range of radius
% size
vSpotsRadiusHacked = zeros(aNumberofSpots, 1);

vRadiiHack = aUseRadiusHack;
vRadiiMin = aMinRadius;
vRadiiMax = aMaxRadius;
vRadiiStep = 0;



if vRadiiHack == true
    disp('vRadiiHack TRUE');
   vRadiiStep = ((vRadiiMax-vRadiiMin)/max(vSpotClusterID));
end

disp('Generating stats');
       vSpotsStats = aSpots.GetStatistics;
       aFactorNames = cell(vSpotsStats.mFactorNames);

% Spot Cluster ID
sName = cell(aNumberofSpots,1);
sUnits = cell(aNumberofSpots,1);
sFactors = cell(4, aNumberofSpots);
sValues = zeros(aNumberofSpots,1);
sids = zeros(aNumberofSpots,1);

% Spot Cluster Size
sName2 = cell(aNumberofSpots,1);
sValues2 = zeros(aNumberofSpots,1);

    for i = 1:aNumberofSpots
        sName(i) = {'Spot Cluster ID'};
        sValues(i) = vSpotClusterID(i);
```

```
        sUnits(i) = {''};
        sFactors(:,i) = {'Spot';'';'';num2str(1)};
        sids(i) = i-1;

        sName2(i) = {'Spot Cluster Size'};
        sValues2(i) = aClusterSize(i);

        if vRadiiHack == true
            if sValues(i)>0
               vSpotsRadiusHacked(i) = vRadiiMin + (vRadiiStep*sValues(i));
               disp(vSpotsRadiusHacked(i));
            else
               vSpotsRadiusHacked(i) = vRadiiMin;
            end
        end

    end

    csvwrite('sValues.csv',sValues);


        vNewSpots = vImarisApplication.GetFactory.CreateSpots;
        vNewSpots.SetColorRGBA(hex2dec('ff00ff'));
        vNewSpots.SetName(sprintf('New %s', ...
        char(aSpots.GetName)));

          if vRadiiHack == true
              vRadii = vSpotsRadiusHacked;
          else
              vRadii = aSpotsRadius;
          end

         vNewSpots.Set(vSpotsXYZ(:, :), ...
              vSpotsTime(:), vRadii(:));

          vParent.AddChild(vNewSpots, -1);


vNewSpots.AddStatistics(sName,sValues,sUnits,sFactors,aFactorNames,sids);
vNewSpots.AddStatistics(sName2,sValues2,sUnits,sFactors,aFactorNames,sids);

end

% User-input GUI
function [mDistThres, mMinClusterSize,mMinContactPoint,mUseRadiusHack,mMinRadius,...
  mMaxRadius] = inputGUI()

% Create figure
h.f = figure('units','pixels','position',[200,200,400,400],...
             'toolbar','none','menu','none');

% Create text and input
txt1 = sprintf('Distance Threshold [um]');
txt2 = sprintf('Min contact duration\n(frame)');
txt3 = sprintf('Max Gap');
txt4 = sprintf('Min Cluster Size');
txt5 = sprintf('Min Contact Point');

panel1 = uipanel('Title', '1) Distance Measurement', 'Position', [.1, .75, .8, .15]);
h.text1 = uicontrol(panel1, 'style','text','units','normalized',...
          'Position', [.05 .55 .8 .3],'string',txt1,...
          'HorizontalAlignment','left');
h.dist_thres = uicontrol(panel1, 'style','edit','units','normalized',...
          'position', [.5 .525 .15 .325],'string','15',...
         'HorizontalAlignment','left');

panel2 = uipanel('Title', '2) Track-to-track Contact', 'Position', [.1, .525, .8,
.2]);
```

```
panel3 = uipanel('Title', '3)Cluster Detection', 'Position', [.1, .3, .8, .2]);
h.text4 = uicontrol(panel3, 'style','text','units','normalized',...
          'Position', [.05 .45 .8 .5],'string',txt4,...
          'HorizontalAlignment','left');
h.min_cluster_size = uicontrol(panel3, 'style','edit','units','normalized',...
          'position', [.5 .675 .15 .25],'string','3',...
         'HorizontalAlignment','left');
h.text5 = uicontrol(panel3, 'style','text','units','normalized',...
          'Position', [.05 .05 .8 .5],'string',txt5,...
          'HorizontalAlignment','left');
h.min_contact_point = uicontrol(panel3, 'style','edit','units','normalized',...
          'position', [.5 .3 .15 .25],'string','1',...
         'HorizontalAlignment','left');


panel4 = uipanel('Title', '4)Spots Creation', 'Position', [.1, .1, .8, .2]);
h.c1 = uicontrol(panel4, 'style','checkbox','units','normalized',...
    'position',[.05 .6 .8 .5],'string','Use Radius hack?');
h.text6 = uicontrol(panel4, 'style','text','units','normalized',...
          'Position', [.05 .15 .8 .5],'string','Min Radius',...
          'HorizontalAlignment','left');
h.min_radius = uicontrol(panel4, 'style','edit','units','normalized',...
          'position', [.5 .45 .15 .25],'string','8.0',...
         'HorizontalAlignment','left');
h.text7 = uicontrol(panel4, 'style','text','units','normalized',...
          'Position', [.05 .002 .8 .3],'string','Max Radius',...
          'HorizontalAlignment','left');
h.max_radius = uicontrol(panel4, 'style','edit','units','normalized',...
          'position', [.5 .0755 .15 .25],'string','8.1',...
         'HorizontalAlignment','left');
h.p = uicontrol(panel4, 'style','pushbutton','units','normalized',...
                'position',[.7 .1 .25 .25],'string','Execute',...
                'callback',@p_call);

% Pushbutton callback
    function p_call(varargin)



        mDistThres = get(h.dist_thres,'String');
        mDistThres = abs(str2num(mDistThres));



        mMinClusterSize = get(h.min_cluster_size,'String');
        mMinClusterSize = abs(str2num(mMinClusterSize));

        mMinContactPoint = get(h.min_contact_point,'String');
        mMinContactPoint = abs(str2num(mMinContactPoint));

        mUseRadiusHack = get(h.c1,'Value');

        mMinRadius = get(h.min_radius,'String');
        mMinRadius = str2double(mMinRadius);

        mMaxRadius = get(h.max_radius,'String');
        mMaxRadius = str2double(mMaxRadius);




       close(h.f);
    end

uiwait(h.f);
end
```

A.2 Cluster detection/composition (single time frame only)

```
% Cluster detection and composition/heterogeneity check
% for Imaris (single time frame only)
% Updated December 2014, J.L. Hor

function cluster_composition_main()

aImarisApplicationID = 0;

% connect to Imaris interface
if ~isa(aImarisApplicationID, 'Imaris.IApplicationPrxHelper')
    javaaddpath ImarisLib.jar
    vImarisLib = ImarisLib;
    if ischar(aImarisApplicationID)
        aImarisApplicationID = round(str2double(aImarisApplicationID));
    end
    vImarisApplication = vImarisLib.GetApplication(aImarisApplicationID);
else
    vImarisApplication = aImarisApplicationID;
end

% the user has to create a scene with some spots and surface
vSurpassScene = vImarisApplication.GetSurpassScene;
if isequal(vSurpassScene, [])
    msgbox('Please create some Spots in the Surpass scene!')
    return
end

% get the spots and the surface object
vSpots =
vImarisApplication.GetFactory.ToSpots(vImarisApplication.GetSurpassSelection);

vSpotsSelected = ~isequal(vSpots, []);
if vSpotsSelected
    vParent = vSpots.GetParent;
else
    vParent = vSurpassScene;
end

% get the spots and surfaces
vSpotsSelection = 1;
vNumberOfSpots = 0;
vSpotsList = [];
vSpotsName = {};
for vIndex = 1:vParent.GetNumberOfChildren
    vItem = vParent.GetChild(vIndex-1);
    if vImarisApplication.GetFactory.IsSpots(vItem)
        vNumberOfSpots = vNumberOfSpots + 1;
        vSpotsList(vNumberOfSpots) = vIndex;
        vSpotsName{vNumberOfSpots} = char(vItem.GetName);

        if vSpotsSelected && isequal(vItem.GetName, vSpots.GetName)
            vSpotsSelection = vNumberOfSpots;
        end
    end
end

if min(vNumberOfSpots) == 0
    msgbox('Please create minimum one spots object!')
    return
end

if vNumberOfSpots>1
    [vSpotsSelection,vOk] = listdlg('ListString',vSpotsName, ...
        'InitialValue', vSpotsSelection, 'SelectionMode','multiple', ...
        'ListSize',[300 300], 'Name','Find Spots Close To Surface', ...
           'PromptString',{'Please select the spots:'});
    if vOk<1, return, end
end

vNumberOfSpotsSelected = numel(vSpotsSelection);
```

```
vSpotsXYZ = [];
vSpotsTime = [];
vSpotsRadius = [];
vSpotsParentID = [];

for vSpotsIndex = 1:vNumberOfSpotsSelected
        vItem = vParent.GetChild(vSpotsList( ...
            vSpotsSelection(vSpotsIndex)) - 1);
        vSpots = vImarisApplication.GetFactory.ToSpots(vItem);



 fprintf('pass %d', vSpotsIndex);
 vSpotsValues = struct2cell(struct(vSpots.Get));


 disp(vSpotsValues);
[vTempSpotsXYZ,vTempSpotsTime,vTempSpotsRadius] = vSpotsValues{:};


vTempSpotsParentID = [];
vTempSpotsParentID(1:size(vTempSpotsXYZ,1)) = vSpotsIndex;
vTempSpotsParentID = vTempSpotsParentID.';


vSpotsXYZ = [vSpotsXYZ; vTempSpotsXYZ];
vSpotsTime = [vSpotsTime; vTempSpotsTime];
vSpotsRadius = [vTempSpotsRadius; vTempSpotsRadius];
vSpotsParentID = [vSpotsParentID; vTempSpotsParentID];


if vSpotsIndex == vNumberOfSpotsSelected
vNumberOfSpots = size(vSpotsXYZ, 1);
disp(vNumberOfSpots);


 csvwrite('vSpotsParentID.csv', vSpotsParentID);
end


end


[mDistThres, mMinClusterSize,mMinContactPoint,mUseRadiusHack,mMinRadius,...
  mMaxRadius] = inputGUI();


 [mDistTable] = SpotsDistance(vSpotsXYZ, vSpotsTime);


 [mSpotTable] = ContactPoints(mDistTable, mDistThres);


 [mSpotClusterT, mClusterSize, mClusterSpotsParentID, mNewClusterSpots] =...
     ClusterDetection(mSpotTable, mMinClusterSize, mMinContactPoint, vSpotsParentID);



 SpotsCreation(vImarisApplication, mSpotClusterT, mClusterSize, vSpotsXYZ, ...
     vSpotsTime, vParent, vNumberOfSpots, mUseRadiusHack, mMinRadius, ...
     mMaxRadius, vSpots, vSpotsRadius, mClusterSpotsParentID, vSpotsParentID, ...
     mNewClusterSpots);



end


% Generate table for distance between spots
function [vDistTable3D] = SpotsDistance(aSpotsXYZ, aSpotsTime)


    for vTimeIndex = 0:max(aSpotsTime)
        vSpotsT = aSpotsTime == vTimeIndex;
        vSpotsIndex = find(vSpotsT');
            for vIndex = vSpotsIndex
                vOthers = vSpotsT;
                vOthers(vIndex) = false;
                vX = aSpotsXYZ(vOthers, 1) - aSpotsXYZ(vIndex, 1);
                vY = aSpotsXYZ(vOthers, 2) - aSpotsXYZ(vIndex, 2);
                vZ = aSpotsXYZ(vOthers, 3) - aSpotsXYZ(vIndex, 3);
```

```
                vDist = sqrt(sum( ([vX, vY, vZ]).^2, 2 ));

                vDistTable3D(vIndex, vOthers) = vDist;
            end
        end

    csvwrite('DistTable3D.csv', vDistTable3D);

end


% Determine number of contact points per spot
function [spot_table3D] = ContactPoints(aDistTable, aDistThres)

% Read spots distance matrix, time index, track ID
if isempty(aDistTable)
magic = [];
magic = dlmread('DistTable.csv');
else
magic = aDistTable;
end

% Get Threshold value from user-input form
vThreshold = aDistThres;

magic_thres = magic;
magic_thres(magic_thres > vThreshold) = 0;
magic_thres(magic_thres > 0 & magic_thres <= vThreshold) = 1;

% assign temp table into Spot Table (whole sheet on cell array)
spot_table3D = magic_thres;

csvwrite('spot_table3D.csv', spot_table3D);

end

% Cluster detection module
function [vSpotClusterT, vSpotClusterSize, vClusterSpotsParentID, vNewClusterSpots] =
...
    ClusterDetection(spot_table3D, aMinClusterSize, aMinParallelContact,
aSpotsParentID)

% PARALLEL MODE is selected here:
aParallel = true;

aClusterOnlySpots = true;

if isempty(spot_table3D)
vTable = csvread('spot_table3D.csv');
else
vTable = spot_table3D;
end

vElements = 1:size(vTable,1);
vClusterID = 1;

vSpotClusterT = zeros(size(vElements));
vSpotClusterT = vSpotClusterT.';
vSpotClusterSize = zeros(size(vElements));
vSpotClusterSize = vSpotClusterSize.';
disp(size(vSpotClusterT));

vNewClusterSpots = [];

curClusterNeighbours = {};
curClusterNeighbours{vClusterID} = [];

vClusterSize = [];
```

```
vClusterSpotsParentID = [];

% ONLY APPLICABLE IF PARALLEL MODE IS ACTIVE
vPointsofContact = zeros(size(vElements'));
vSpotstoIgnore = [];

% Progress Bar
vProgressTotalCount = max(vElements);
vProgressDisplay = waitbar(0, 'Cluster Detection');
vProgressCount = 0;

% FIRST LOOP: vRootTrack
for vRootSpot = 1:max(vElements)

    if vSpotClusterT(vRootSpot)==0 && ~ismember(vRootSpot, vSpotstoIgnore)

        % SECOND LOOP: Individually check every track (vCurTrack) against root track
        for vCurSpot = 1:max(vElements)

            tempClusterT = vTable(vCurSpot, :);

            % vPointsofContact for the current track is registered before
            % the current track is added to it. Only applicable for
            % PARALLEL mode.
            curCluster = find(tempClusterT > 0);
            vPointsofContact(vCurSpot) = numel(curCluster);
            curCluster = [vCurSpot curCluster];
            curCluster = unique(curCluster);

            if numel(curCluster) > 1

               A = cellfun('isempty', curClusterNeighbours);

               if A(vClusterID) == 1
                    curClusterNeighbours{vClusterID} = vRootSpot;
               end

               if numel(intersect(curCluster, curClusterNeighbours{vClusterID})) > 0

                curClusterNeighbours{vClusterID} = ...
                    [curClusterNeighbours{vClusterID} curCluster];
                curClusterNeighbours{vClusterID} = ...
                    unique(curClusterNeighbours{vClusterID});

                    % If PARALLEL mode is ON, then all tracks within the
                    % cluster will be added to root TrackstoIgnore.
                    % Otherwise non-qualified tracks within a cluster will
                    % not be registered with a clusterID and will be
                    % processed again and overwrite all the old tracks with
                    % a new clusterID.

                    if aParallel == true
                            vSpotstoIgnore = [vSpotstoIgnore curCluster];
                            vSpotstoIgnore = unique(vSpotstoIgnore);
                    end
               end

            end

            % Assign clusterID to all neighbours

            if vCurSpot == max(vElements)

                % If PARALLEL mode is ON, find intersection index of
                % curClusterNeighbours and those with less points of
                % contact than defined. They will be removed from the
                % current curClusterNeighbours{vClusterID}.
                % The overall size of the cluster will be determined in the
```

```
                % next conditional block and see if all the remaining cells
                % are qualified to be a cluster.

                if aParallel == true

                    P = find(vPointsofContact < aMinParallelContact);
                    [~, iR, ~] = intersect(curClusterNeighbours{vClusterID}, P);
                    curClusterNeighbours{vClusterID}(iR) = [];
                end

                if numel(curClusterNeighbours{vClusterID}) >= aMinClusterSize;
                    vSpotClusterT(curClusterNeighbours{vClusterID}) = vClusterID;
                    vClusterSize(vClusterID) = ...
                      numel(curClusterNeighbours{vClusterID});
                    vSpotClusterSize(curClusterNeighbours{vClusterID}) = ...
                        vClusterSize(vClusterID);

                    [count_each_spots] = count_member...
                        (curClusterNeighbours{vClusterID}, aSpotsParentID);

                    for i = 1:max(aSpotsParentID)
                       vClusterSpotsParentID(vClusterID, i) = count_each_spots{i};

                       if i == max(aSpotsParentID)
                           vClusterSpotsParentID(vClusterID, i+1) = ...
                               vClusterSize(vClusterID);
                       end

                    end

                    vClusterID = vClusterID + 1;
                    curClusterNeighbours{vClusterID} = [];

                end

                if numel(curClusterNeighbours{vClusterID}) < aMinClusterSize;
                    curClusterNeighbours{vClusterID} = [];
                end

            end
        end


    end

     if aClusterOnlySpots == true
         vNewClusterSpots = find(vSpotClusterT > 0);
     end


    vProgressCount = vProgressCount + 1;
    waitbar(vProgressCount/vProgressTotalCount, vProgressDisplay)

end


csvwrite('SpotClusterID.csv',vSpotClusterT);
csvwrite('ClusterSize.csv',vClusterSize.');
csvwrite('SpotClusterSize.csv',vSpotClusterSize);
csvwrite('CountSpotMembers.csv', vClusterSpotsParentID);
close(vProgressDisplay);

end

% Spots Creation module and add statistics back to Imaris
function SpotsCreation(vImarisApplication, aSpotClusterT, aClusterSize, ...
    vSpotsXYZ, vSpotsTime, vParent, aNumberofSpots, aUseRadiusHack, ...
    aMinRadius, aMaxRadius, aSpots, aSpotsRadius, aClusterSpotsParentID, ...
```

```
    aSpotsParentID, aNewClusterSpots)

if isempty(aSpotClusterT)
vSpotClusterID = csvread('SpotClusterID.csv');
else
vSpotClusterID = aSpotClusterT;
end

% Use Radius Hack to generate colour-coded spots through a range of radius
% size
vSpotsRadiusHacked = zeros(aNumberofSpots, 1);
aClusterOnlySpots = true;

vRadiiHack = aUseRadiusHack;
vRadiiMin = aMinRadius;
vRadiiMax = aMaxRadius;
vRadiiStep = 0;

% VER1. Radius Hack used to colour-code individual cluster
% if vRadiiHack == true
%     disp('vRadiiHack TRUE');
%    vRadiiStep = ((vRadiiMax-vRadiiMin)/max(vSpotClusterID));
% end

% VER2. Radius Hack used to separate each spot objects
if vRadiiHack == true
    disp('vRadiiHack TRUE');
   vRadiiStep = ((vRadiiMax-vRadiiMin)/(max(aSpotsParentID)));
end



disp('Generating stats');
       vSpotsStats = aSpots.GetStatistics;
       aFactorNames = cell(vSpotsStats.mFactorNames);

% Spot Cluster ID
sName = cell(aNumberofSpots,1);
sUnits = cell(aNumberofSpots,1);
sFactors = cell(4, aNumberofSpots);
sValues = zeros(aNumberofSpots,1);
sids = zeros(aNumberofSpots,1);

% Spot Cluster Size
sName2 = cell(aNumberofSpots,1);
sValues2 = zeros(aNumberofSpots,1);



    for i = 1:aNumberofSpots
        sName(i) = {'Spot Cluster ID'};
        sValues(i) = vSpotClusterID(i);
        sUnits(i) = {''};
        sFactors(:,i) = {'Spot';'';'';num2str(1)};
        sids(i) = i-1;

        sName2(i) = {'Spot Cluster Size'};
        sValues2(i) = aClusterSize(i);

        if vRadiiHack == true
            if aSpotsParentID(i) > 1
               vSpotsRadiusHacked(i) = vRadiiMin + (vRadiiStep*aSpotsParentID(i));
            else
               vSpotsRadiusHacked(i) = vRadiiMin;
            end
        end

    end

     if aClusterOnlySpots == true
        sValues = sValues(aNewClusterSpots);
        sValues2 = sValues2(aNewClusterSpots);
     end
```

```
    csvwrite('sValues.csv',sValues);

    if aClusterOnlySpots == true

        vNewSpots = vImarisApplication.GetFactory.CreateSpots;
        vNewSpots.SetColorRGBA(hex2dec('ff00ff'));
        vNewSpots.SetName(sprintf('Clustered only cells'));

        if vRadiiHack == true
              vRadii = vSpotsRadiusHacked;
          else
              vRadii = aSpotsRadius;
        end

        vNewSpots.Set(vSpotsXYZ(aNewClusterSpots, :), ...
        vSpotsTime(aNewClusterSpots), vRadii(aNewClusterSpots));
        vParent.AddChild(vNewSpots, -1);

   else
        vNewSpots = vImarisApplication.GetFactory.CreateSpots;
        vNewSpots.SetColorRGBA(hex2dec('ff00ff'));
        vNewSpots.SetName(sprintf('New %s', ...
        char(aSpots.GetName())));

          if vRadiiHack == true
              vRadii = vSpotsRadiusHacked;
          else
              vRadii = aSpotsRadius;
          end

         vNewSpots.Set(vSpotsXYZ(:, :), ...
              vSpotsTime(:), vRadii(:));

          vParent.AddChild(vNewSpots, -1);
end

vNewSpots.AddStatistics(sName,sValues,sUnits,sFactors,aFactorNames,sids);
vNewSpots.AddStatistics(sName2,sValues2,sUnits,sFactors,aFactorNames,sids);

end

% User-input GUI
function [mDistThres, mMinClusterSize,mMinContactPoint,mUseRadiusHack,mMinRadius,...
  mMaxRadius] = inputGUI()

% Create figure
h.f = figure('units','pixels','position',[200,200,400,400],...
             'toolbar','none','menu','none');

         % Create text and input
txt1 = sprintf('Distance Threshold [um]');
txt2 = sprintf('Min contact duration\n(frame)');
txt3 = sprintf('Max Gap');
txt4 = sprintf('Min Cluster Size');
txt5 = sprintf('Min Contact Point');

panel1 = uipanel('Title', '1) Distance Measurement', 'Position', [.1, .75, .8, .15]);
h.text1 = uicontrol(panel1, 'style','text','units','normalized',...
          'Position', [.05 .55 .8 .3],'string',txt1,...
          'HorizontalAlignment','left');
h.dist_thres = uicontrol(panel1, 'style','edit','units','normalized',...
          'position', [.5 .525 .15 .325],'string','15',...
         'HorizontalAlignment','left');

panel2 = uipanel('Title', '2) Track-to-track Contact', 'Position', [.1, .525, .8,
.2]);
```

```
panel3 = uipanel('Title', '3)Cluster Detection', 'Position', [.1, .3, .8, .2]);
h.text4 = uicontrol(panel3, 'style','text','units','normalized',...
          'Position', [.05 .45 .8 .5],'string',txt4,...
          'HorizontalAlignment','left');
h.min_cluster_size = uicontrol(panel3, 'style','edit','units','normalized',...
          'position', [.5 .675 .15 .25],'string','3',...
         'HorizontalAlignment','left');
h.text5 = uicontrol(panel3, 'style','text','units','normalized',...
          'Position', [.05 .05 .8 .5],'string',txt5,...
          'HorizontalAlignment','left');
h.min_contact_point = uicontrol(panel3, 'style','edit','units','normalized',...
          'position', [.5 .3 .15 .25],'string','1',...
         'HorizontalAlignment','left');


panel4 = uipanel('Title', '4)Spots Creation', 'Position', [.1, .1, .8, .2]);
h.c1 = uicontrol(panel4, 'style','checkbox','units','normalized',...
    'position',[.05 .6 .8 .5],'string','Use Radius hack?');
h.text6 = uicontrol(panel4, 'style','text','units','normalized',...
          'Position', [.05 .15 .8 .5],'string','Min Radius',...
          'HorizontalAlignment','left');
h.min_radius = uicontrol(panel4, 'style','edit','units','normalized',...
          'position', [.5 .45 .15 .25],'string','8.0',...
         'HorizontalAlignment','left');
h.text7 = uicontrol(panel4, 'style','text','units','normalized',...
          'Position', [.05 .002 .8 .3],'string','Max Radius',...
          'HorizontalAlignment','left');
h.max_radius = uicontrol(panel4, 'style','edit','units','normalized',...
          'position', [.5 .0755 .15 .25],'string','8.1',...
         'HorizontalAlignment','left');
h.p = uicontrol(panel4, 'style','pushbutton','units','normalized',...
                'position',[.7 .1 .25 .25],'string','Execute',...
                'callback',@p_call);

% Pushbutton callback
    function p_call(varargin)



        mDistThres = get(h.dist_thres,'String');
        mDistThres = abs(str2num(mDistThres));



        mMinClusterSize = get(h.min_cluster_size,'String');
        mMinClusterSize = abs(str2num(mMinClusterSize));

        mMinContactPoint = get(h.min_contact_point,'String');
        mMinContactPoint = abs(str2num(mMinContactPoint));

        mUseRadiusHack = get(h.c1,'Value');

        mMinRadius = get(h.min_radius,'String');
        mMinRadius = str2double(mMinRadius);

        mMaxRadius = get(h.max_radius,'String');
        mMaxRadius = str2double(mMaxRadius);




       close(h.f);
    end

uiwait(h.f);
end

% Count number of members per population
function [CountMembers] = count_member(cluster_members, aSpotsParentID)

vTempParentID = aSpotsParentID(cluster_members);
CountMembers = {};
```

```
for i = 1:max(aSpotsParentID)
   CountMembers{i} = sum(vTempParentID == i);
end

end
```

A.3 Spot to Surface Distance

```
%  Detect spots close to surface over 4D dataset
%
%  Modified from "Find Spots Close To Surface for Imaris 7.3.0"
%  to enable four-dimensional tracking
%
%  Updated June 2014, J.L. Hor
%


function SpotsToSurfaceDistance(aImarisApplicationID)

aImarisApplicationID = 0;

% connect to Imaris interface
if ~isa(aImarisApplicationID, 'Imaris.IApplicationPrxHelper')
    javaaddpath ImarisLib.jar
    vImarisLib = ImarisLib;
    if ischar(aImarisApplicationID)
        aImarisApplicationID = round(str2double(aImarisApplicationID));
    end
    vImarisApplication = vImarisLib.GetApplication(aImarisApplicationID);
else
    vImarisApplication = aImarisApplicationID;
end

% the user has to create a scene with some spots and surface
vSurpassScene = vImarisApplication.GetSurpassScene;
if isequal(vSurpassScene, [])
    msgbox('Please create some Spots and Surface in the Surpass scene!')
    return
end

% get the spots and the surface object
vSpots = ...
    vImarisApplication.GetFactory.ToSpots(vImarisApplication.GetSurpassSelection);
vSurfaces = ...
    vImarisApplication.GetFactory.ToSurfaces(vImarisApplication.GetSurpassSelection);

fprintf('Getting surpass selections...\n');

% Get Track edges
vTEdges = vSpots.GetTrackEdges;

vSpotsSelected = ~isequal(vSpots, []);
vSurfaceSelected = ~isequal(vSurfaces, []);
if vSpotsSelected
    vParent = vSpots.GetParent;
elseif vSurfaceSelected
    vParent = vSurfaces.GetParent;
else
    vParent = vSurpassScene;
end

% get the spots and surfaces
vSpotsSelection = 1;
vSurfaceSelection = 1;
vNumberOfSpots = 0;
vNumberOfSurfaces = 0;
vSpotsList = [];
vSurfacesList = [];
vSpotsName = {};
vSurfacesName = {};
for vIndex = 1:vParent.GetNumberOfChildren
    vItem = vParent.GetChild(vIndex-1);
    if vImarisApplication.GetFactory.IsSpots(vItem)
        vNumberOfSpots = vNumberOfSpots + 1;
        vSpotsList(vNumberOfSpots) = vIndex;
        vSpotsName{vNumberOfSpots} = char(vItem.GetName);

        if vSpotsSelected && isequal(vItem.GetName, vSpots.GetName)
            vSpotsSelection = vNumberOfSpots;
```

```
        end
    elseif vImarisApplication.GetFactory.IsSurfaces(vItem)
        vNumberOfSurfaces = vNumberOfSurfaces + 1;
        vSurfacesList(vNumberOfSurfaces) = vIndex;
        vSurfacesName{vNumberOfSurfaces} = char(vItem.GetName);

        if vSurfaceSelected && isequal(vItem.GetName, vSurfaces.GetName)
            vSurfaceSelection = vNumberOfSurfaces;
        end
    end
end

if min(vNumberOfSpots,vNumberOfSurfaces) == 0
    msgbox('Please create some spots AND a surface object!')
    return
end

if vNumberOfSpots>1
    [vSpotsSelection,vOk] = listdlg('ListString',vSpotsName, ...
        'InitialValue', vSpotsSelection, 'SelectionMode','multiple', ...
        'ListSize',[300 300], 'Name','Find Spots Close To Surface', ...
        'PromptString',{'Please select the spots:'});
    if vOk<1, return, end
end
if vNumberOfSurfaces>1
    [vSurfaceSelection,vOk] = listdlg('ListString',vSurfacesName, ...
        'InitialValue', vSurfaceSelection, 'SelectionMode','multiple', ...
        'ListSize',[300 300], 'Name','Find Spots Close To Surface', ...
        'PromptString',{'Please select the surface:'});
    if vOk<1, return, end
end

vAnswer = inputdlg({'Please enter the threshold:'}, ...
    'Find Spots Close To Surface',1,{'5'});
if isempty(vAnswer), return, end
vThreshold = abs(str2double(vAnswer{1}));

vProgressDisplay = waitbar(0,'Finding Spots Close To Surface');

vNumberOfSurfacesSelected = numel(vSurfaceSelection);
vNumberOfSpotsSelected = numel(vSpotsSelection);

for vSurfaceIndex = 1:vNumberOfSurfacesSelected
    vItem = vParent.GetChild(vSurfacesList( ...
        vSurfaceSelection(vSurfaceIndex)) - 1);
    vSurface = vImarisApplication.GetFactory.ToSurfaces(vItem);

    vSurfaceVertices = [];

    vSurfTime = [];



    for vIndex = 0:vSurface.GetNumberOfSurfaces - 1
      vSurfaceVertices = [vSurfaceVertices; vSurface.GetVertices(vIndex)];
      vCurSurfTime = vSurface.GetTimeIndex(vIndex);

      if mod(vIndex, 500) == 0
      fprintf('Getting surface vertices... for object %d\n', vIndex);
      end

      for vTimeIndex = 1:size(vSurface.GetVertices(vIndex),1)
         vSurfTime(end+1) = vCurSurfTime;
      end

    end



    vNumberOfVertices = size(vSurfaceVertices, 1);

vInputStr = sprintf('Surface Vertices Limit: (1 to %d)', vNumberOfVertices);
```

```
vSVAnswer = inputdlg(vInputStr, ...
    'Surface Vertices Limit',1,{'50000'});
if isempty(vAnswer), return, end
vLimit = abs(str2double(vSVAnswer{1}));

    if vNumberOfVertices > vLimit
        vIndices = round(linspace(1, vNumberOfVertices, vLimit));
        vSurfaceVertices = vSurfaceVertices(vIndices, :);
        vSurfTime = vSurfTime(vIndices);
        vNumberOfVertices = vLimit;
    end

    fprintf('Limited to: %d\n', vNumberOfVertices);

    vSparseVertices = 1:vNumberOfVertices;
    vSurfX = cell(size(vSparseVertices, 1),size(vSparseVertices, 1),max(vSurfTime)+1);
    vSurfY = cell(size(vSparseVertices, 1),size(vSparseVertices, 1),max(vSurfTime)+1);
    vSurfZ = cell(size(vSparseVertices, 1),size(vSparseVertices, 1),max(vSurfTime)+1);



for vTimeIndex = 0:max(vSurfTime)



  vTempSurfPreIdx = 1:size(vSurfaceVertices,1);
  vTempSurfIndex = [];
  vTempSurfIndex = vTempSurfPreIdx(vSurfTime==vTimeIndex);

  vTempVertices = zeros(size(vSurfaceVertices));
  vTempVertices(vTempSurfIndex,:) = vSurfaceVertices(vTempSurfIndex,:);

  vSurfX{vTimeIndex+1} = sparse(vSparseVertices, vSparseVertices, ...
                                double(vTempVertices(:,1)));
  vSurfY{vTimeIndex+1} = sparse(vSparseVertices, vSparseVertices, ...
                                double(vTempVertices(:,2)));
  vSurfZ{vTimeIndex+1} = sparse(vSparseVertices, vSparseVertices, ...
                                double(vTempVertices(:,3)));

end

clear vSurfaceVertices;

for vSpotsIndex = 1:vNumberOfSpotsSelected
        vItem = vParent.GetChild(vSpotsList( ...
            vSpotsSelection(vSpotsIndex)) - 1);
        vSpots = vImarisApplication.GetFactory.ToSpots(vItem);

        vSpotsValues = struct2cell(struct(vSpots.Get));
        [vSpotsPosition,vSpotsTime,vSpotsRadius] = vSpotsValues{:};
        vNumberOfSpots = size(vSpotsPosition, 1);



        fprintf('\nTotal number of spots: %d\n', size(vSpotsPosition,1));

        vTempSpotIndex=cell(size(vSpotsPosition,1),1,max(vSpotsTime)+1);

for vTimeIndex = 0:max(vSpotsTime)
    fprintf('Generating spot indices for time point %d...\n', vTimeIndex);

    vTempSpotIndex{vTimeIndex+1} = zeros(size(vSpotsPosition,1));
    vTempSpotIndex{vTimeIndex+1} = vSpotsTime==vTimeIndex;

    vTempIndexPos{vTimeIndex+1} = find(vTempSpotIndex{vTimeIndex+1});

    vTempSpots = vSpotsPosition(vTempIndexPos{vTimeIndex+1},:);
    vTempSpotIndex{vTimeIndex+1} = [];

    vOnes = ones(vNumberOfVertices, size(vTempSpots,1));
    vDistX = vOnes*diag(vTempSpots(:, 1)) - vSurfX{vTimeIndex+1}*vOnes;
```

```
    vDistY = vOnes*diag(vTempSpots(:, 2)) - vSurfY{vTimeIndex+1}*vOnes;
    vDistZ = vOnes*diag(vTempSpots(:, 3)) - vSurfZ{vTimeIndex+1}*vOnes;



    vDistances{vTimeIndex+1} = sqrt( min( vDistX.^2+vDistY.^2+vDistZ.^2, [], 1 ) );
    vSurfX{vTimeIndex+1} = [];
    vSurfY{vTimeIndex+1} = [];
    vSurfZ{vTimeIndex+1} = [];

end

       vNewDistances = zeros(vNumberOfSpots, 1);

       vTempIndexPos = cellfun(@transpose, vTempIndexPos,'UniformOutput', false);



       for i = 1:size(vDistances,2)

            vNewDistances(vTempIndexPos{i}) = vDistances{i};
            vDistances{i} = [];
       end

       clear vDistances;
       clear vSurfX;
       clear vSurfY;
       clear vSurfZ;

        vSpots.SetVisible(false);

        vSpotsClose = vNewDistances <= vThreshold;
        vSpotsFar = vNewDistances > vThreshold;

        if any(vSpotsClose)
        vRadii(vSpotsClose) = 4;
        end

        if any(vSpotsFar)
        vRadii(vSpotsFar) = 3.9;
        end

    vSpotsI=vSpotsClose + vSpotsFar;
    vSpotsI = logical(vSpotsI);

    fprintf('Creating spots...');
    if any(vSpotsI)
    vNewSpotsClose = vImarisApplication.GetFactory.CreateSpots;
    vNewSpotsClose.SetColorRGBA(hex2dec('ff00ff'));
          vNewSpotsClose.SetName(sprintf('New %s (close to %s [%.2f])', ...
              char(vSpots.GetName), char(vSurface.GetName), vThreshold));

         vNewSpotsClose.Set(vSpotsPosition(vSpotsI, :), ...
              vSpotsTime(vSpotsI), vRadii(vSpotsI));

          vParent.AddChild(vNewSpotsClose, -1);

        waitbar((vNumberOfSpotsSelected*(vSurfaceIndex-1)+vSpotsIndex) / ...
            (vNumberOfSpotsSelected*vNumberOfSurfacesSelected));
    end

    vNewSpotsClose.SetTrackEdges(vTEdges);

    end


end

close(vProgressDisplay);
```

A.4 Track contact duration

```
% Track contact duration
%
% Detect track contact duration over 4D dataset based on spots radius
% after spots-surface distance detection module
%
% Updated June 2014, J.L. Hor
%

function TrackContactDuration()

aImarisApplicationID = 0;

% connect to Imaris interface
if ~isa(aImarisApplicationID, 'Imaris.IApplicationPrxHelper')
  javaaddpath ImarisLib.jar
  vImarisLib = ImarisLib;
  if ischar(aImarisApplicationID)
    aImarisApplicationID = round(str2double(aImarisApplicationID));
  end
  vImarisApplication = vImarisLib.GetApplication(aImarisApplicationID);
else
  vImarisApplication = aImarisApplicationID;
end

fprintf('Establishing Imaris connection...\n');

% the user has to create a scene with some tracks
vSurpassScene = vImarisApplication.GetSurpassScene;
if isequal(vSurpassScene, [])
  msgbox('Please create some tracks in the surpass scene!');
  return
end

fprintf('Getting surpass selection...\n');

vSpots =
vImarisApplication.GetFactory.ToSpots(vImarisApplication.GetSurpassSelection);
vParent = vSpots.GetParent;

vTEdges = vSpots.GetTrackEdges;
vTID = vSpots.GetTrackIds;

vSpotsValues = struct2cell(struct(vSpots.Get));
[vSpotsPosition,vSpotsTime,vSpotsRadius] = vSpotsValues{:};

vNumberOfSpots = size(vSpotsPosition, 1);

[vThreshold, vfn, vfnplot, vc1, vc2, vc3] = inputGUI(max(vSpotsTime)+1);

if vc1 + vc2 + vc3 == 0
    return, end

fprintf('Contact duration threshold: %d\n',vThreshold);
fprintf('Generate plot matrix: %s\n',logical(vc1));
if vc2==1
fprintf('Saving plot in: %s\n',vfnplot);
end

fprintf('Generate contact duration table: %s\n', logical(vc2));
if vc2==1
fprintf('Saving data in: %s\n',vfn);
end
fprintf('Generate new tracks based on contact duration threshold:
%s\n\n',logical(vc3));

% Build far/close map
vSpotsClose = vSpotsRadius == 4.0;
```

```
vIndexCount = 0;

fprintf('Retrieving spot indices for all tracks...\n');

for vIndex=min(vTID):max(vTID)

    vCurrent = find(vTID==vIndex);
    vIndexCount = vIndexCount + 1;
    vCurEdge = [];

    for vEdgeIndex = min(vCurrent):max(vCurrent)
       if vEdgeIndex == min(vCurrent)
           vCurEdge = vTEdges(vEdgeIndex, 1);
           vCurEdge(end+1) = vTEdges(vEdgeIndex,2);
       else
          vCurEdge(end+1) = vTEdges(vEdgeIndex,2);
       end

    end

    vTrackCell{vIndexCount} = vCurEdge;

end

vMainTracks = nan(numel(vTrackCell),max(vSpotsTime)+1);

for vIndexCell = 1:numel(vTrackCell)

    vCurSpots = vTrackCell{vIndexCell};

    for vIndexTrack = 1:numel(vCurSpots)

        vProperSpotIndex = vCurSpots(vIndexTrack) + 1;
        vTrackTimeIndex=vSpotsTime(vProperSpotIndex) + 1;
        vMainTracks(vIndexCell,vTrackTimeIndex) = vSpotsClose(vProperSpotIndex);

    end

end

if vc2==1
fprintf('Generating contact duration database in %s\n', vfn);

vMainTracks3 = vMainTracks;
vMainTracks3(vMainTracks3==0)=1;
vMainTracks3(isnan(vMainTracks3))=0;
[~,vFirst] = max(vMainTracks3,[],2);
[~,vLast] = max(cumsum(vMainTracks3'~=0));
vLast = vLast';

vLength = vLast-vFirst+1;



vMainTracks2 = vMainTracks;
vMainTracks2(isnan(vMainTracks2))=0;

vContactDurations(:,1) = 1:numel(vTrackCell);
vContactDurations(:,2) = sum(vMainTracks2, 2);
vContactDurations(:,3) = vLength;

csvwrite(vfn, vContactDurations);

end

% Call generateNewTracks
if vc3==1
```

```
fprintf('Generating new tracks...\n');
generateNewTracks(vImarisApplication, vSpots, vNumberOfSpots, vMainTracks, ...
    vTrackCell, vSpotsPosition, vSpotsTime, vSpotsRadius, vThreshold, vParent);
end

if vc1==1
% Contact duration matrix
[r,c] = size(vMainTracks);
h = imagesc(((1:c)+0.5), ((1:r)+0.5), vMainTracks);
colormap(jet);
caxis([-1 1.2]);
axis equal;
vwidth = 0.65*max(vSpotsTime);
vheight = 0.56*numel(vTrackCell);
set(gca,'XTick',0:(c),'YTick',0:(r),...
        'XLim',[1 c+1],'YLim',[1 r+1],...
        'GridLineStyle','-','XGrid','on','YGrid','on');
set(gcf,'PaperPosition',[0 0 vwidth vheight]);
print('-r300','-dpng',vfnplot);
end

end

% Generate new tracks
function generateNewTracks(aImarisApplication, aSpots, aNumberofSpots, ...
    aMainTracks, aTrackCell, aCoords, aTimes, aRadius, aThreshold, aParent)

vTrackCountPos = 0;
vTrackCountNeg = 0;

vNewTrackEdgesPos = [];
vNewTrackEdgesNeg = [];

vNewSpotsIDPos = [];
vNewSpotsIDNeg = [];

[vTracks, trackidx2] = TrackIndices(aSpots, aNumberofSpots);

for vIndex = 1:size(aMainTracks, 1)

    if numel(find(aMainTracks(vIndex,:)>0)) >= aThreshold

        vSpotsI = aTrackCell{vIndex};
        vSpotsI = vSpotsI + 1;

        if isempty(vNewSpotsIDPos)

           vNewSpotsIDPos = vSpotsI;
        else
            vNewSpotsIDPos = [vNewSpotsIDPos vSpotsI];
        end

        for vIndexTrack = vTrackCountPos:vTrackCountPos+numel(vSpotsI)-2

            if isempty(vNewTrackEdgesPos)
            vNewTrackEdgesPos=[vTrackCountPos vTrackCountPos+1];
            vTrackCountPos = vTrackCountPos + 1;
            else
            vNewTrackEdgesPos=[vNewTrackEdgesPos; [vTrackCountPos vTrackCountPos+1]];
            vTrackCountPos = vTrackCountPos + 1;
            end
       end
      vTrackCountPos = vTrackCountPos + 1;

    else

        vSpotsI = aTrackCell{vIndex};
        vSpotsI = vSpotsI + 1;

        if isempty(vNewSpotsIDNeg)
```

```
            vNewSpotsIDNeg = vSpotsI;
        else
            vNewSpotsIDNeg = [vNewSpotsIDNeg vSpotsI];
        end

        for vIndexTrack = vTrackCountNeg:vTrackCountNeg+numel(vSpotsI)-2

            if isempty(vNewTrackEdgesNeg)
            vNewTrackEdgesNeg=[vTrackCountNeg vTrackCountNeg+1];
            vTrackCountNeg = vTrackCountNeg + 1;
            else
            vNewTrackEdgesNeg=[vNewTrackEdgesNeg; [vTrackCountNeg vTrackCountNeg+1]];
            vTrackCountNeg = vTrackCountNeg + 1;
            end
       end
      vTrackCountNeg = vTrackCountNeg + 1;

    end


end



vNewSpotsPos = aImarisApplication.GetFactory.CreateSpots;
vNewSpotsPos.SetColorRGBA(hex2dec('ff00ff'));
vNewSpotsPos.SetName(sprintf('Contact positive [min %d frames]', aThreshold));
    vNewSpotsPos.Set(aCoords(vNewSpotsIDPos, :), ...
          aTimes(vNewSpotsIDPos), aRadius(vNewSpotsIDPos));
          aParent.AddChild(vNewSpotsPos, -1);

vNewSpotsNeg = aImarisApplication.GetFactory.CreateSpots;
vNewSpotsNeg.SetColorRGBA(hex2dec('ffff00'));
vNewSpotsNeg.SetName(sprintf('Contact negative [< %d frames]', aThreshold));
    vNewSpotsNeg.Set(aCoords(vNewSpotsIDNeg, :), ...
          aTimes(vNewSpotsIDNeg), aRadius(vNewSpotsIDNeg));
          aParent.AddChild(vNewSpotsNeg, -1);


         vNewSpotsPos.SetTrackEdges(vNewTrackEdgesPos);
         vNewSpotsNeg.SetTrackEdges(vNewTrackEdgesNeg);


end

% User-input GUI
function [vThreshold, vfn, vfnplot, vc1, vc2, vc3] = inputGUI(total)

vThreshold = 0;
vfn = '';
vfnplot = '';
vc1 = 0;
vc2 = 0;
vc3 = 0;
% Create figure
h.f = figure('units','pixels','position',[400,400,250,200],...
             'toolbar','none','menu','none');
% Create text and input
txt = sprintf('Contact duration threshold (1 to %d frames):', total);

h.text1 = uicontrol('style','text','units','pixels',...
          'position', [10,170,240,15],'string',txt,...
          'HorizontalAlignment','left');
h.thres = uicontrol('style','edit','units','pixels',...
          'position', [10,150,240,15],'string','10',...
         'HorizontalAlignment','left');
% Create yes/no checkboxes
h.c1 = uicontrol('style','checkbox','units','pixels',...
    'position',[10,125,240,15],'string','Generate plot/contact duration matrix');

h.fnplot = uicontrol('style','edit','units','pixels',...
          'position', [10,105,240,15],'string','map.png',...
         'HorizontalAlignment','left');
```

```
h.c2 = uicontrol('style','checkbox','units','pixels',...
    'position',[10,80,240,15],'string','Generate duration database');

h.fn = uicontrol('style','edit','units','pixels',...
          'position', [10,60,240,15],'string','map.csv',...
         'HorizontalAlignment','left');

h.c3 = uicontrol('style','checkbox','units','pixels',...
    'position',[10,35,240,15],'string','Generate new tracks based on threshold');

% Create OK pushbutton
h.p = uicontrol('style','pushbutton','units','pixels',...
                'position',[40,5,70,20],'string','OK',...
                'callback',@p_call);
    % Pushbutton callback
    function p_call(varargin)



        vThreshold = get(h.thres,'String');
        vThreshold = abs(str2num(vThreshold));


        vfn = get(h.fn,'String');
        vfnplot = get(h.fnplot,'String');


        vc1 = get(h.c1, 'Value');
        vc2 = get(h.c2, 'Value');
        vc3 = get(h.c3, 'Value');
       close(h.f);
    end
uiwait(h.f);
end

% Get Track indices
function [vTracks, trackidx2] = TrackIndices(aSpots, aNumberofSpots)

vIndicesT = aSpots.GetIndicesT;
csvwrite('timeidx.csv', vIndicesT);

vTrackIds = aSpots.GetTrackIds;
vTEdges = aSpots.GetTrackEdges;
vTracks = [vTrackIds vTEdges+1];

vNewTracks = size(aNumberofSpots,1);
dlmwrite('vTracks.csv', vTracks, 'precision', 10);

trackidx = num2str(vTracks(:,1));

trackidx2 = trackidx(:, end-3:end);
trackidx2 = str2num(trackidx2)+1;

end
```

APPENDIX B:
Download links for Movies

Chapter 3:

Movie R1:
https://www.dropbox.com/s/5gxzj7fj79qfa08/Movie R1.mov?dl=0

Chapter 5:

Movie S1:
https://www.dropbox.com/s/1c3bn5o9jl9wabp/Movie S1.mov?dl=0

Movie S2:
https://www.dropbox.com/s/ejir9pczs9jcun8/Movie%20S2.mov?dl=0

Movie S3:
https://www.dropbox.com/s/t6ji0trc80nx1gd/Movie%20S3.mov?dl=0

Movie S4:
https://www.dropbox.com/s/j1u0fk52pq1xh8z/Movie%20S4.mov?dl=0

Movie S5:
https://www.dropbox.com/s/43uh8gpuojrm641/Movie%20S5.mov?dl=0

Movie S6:
https://www.dropbox.com/s/132olgtk7dnrqoi/Movie%20S6.mov?dl=0

Movie S7:
https://www.dropbox.com/s/0whqvdjj0hs05fo/Movie%20S7.mov?dl=0

Movie S8:
https://www.dropbox.com/s/7tr0igmrshpm8kp/Movie%20S8.mov?dl=0

REFERENCES

Abadie, V., Badell, E., Douillard, P., Ensergueix, D., Leenen, P.J.M., Tanguy, M., Fiette, L., Saeland, S., Gicquel, B., and Winter, N. (2005). Neutrophils rapidly migrate via lymphatics after Mycobacterium bovis BCG intradermal vaccination and shuttle live bacilli to the draining lymph nodes. Blood 106, 1843–1850.

Abadie, V., Bonduelle, O., Duffy, D., Parizot, C., Verrier, B., and Combadiere, B. (2009). Original encounter with antigen determines antigen-presenting cell imprinting of the quality of the immune response in mice. PLoS ONE 4, e8159.

Abraham, S.N., and St John, A.L. (2010). Mast cell-orchestrated immunity to pathogens. Nat Rev Immunol 10, 440–452.

Abtin, A., Jain, R., Mitchell, A.J., Roediger, B., Brzoska, A.J., Tikoo, S., Cheng, Q., Ng, L.G., Cavanagh, L.L., von Andrian, U.H., et al. (2014). Perivascular macrophages mediate neutrophil recruitment during bacterial skin infection. Nat. Immunol. 15, 45–53.

Adorini, L., Muller, S., Cardinaux, F., Lehmann, P.V., Falcioni, F., and Nagy, Z.A. (1988). In vivo competition between self peptides and foreign antigens in T-cell activation. Nature 334, 623–625.

Alexandre, Y.O., Ghilas, S., Sanchez, C., Le Bon, A., Crozat, K., and Dalod, M. (2016). XCR1+ dendritic cells promote memory CD8+ T cell recall upon secondary infections with Listeria monocytogenes or certain viruses. Journal of Experimental Medicine 213, 75–92.

Allan, R.S., Smith, C.M., Belz, G.T., van Lint, A.L., Wakim, L.M., Heath, W.R., and Carbone, F.R. (2003). Epidermal viral immunity induced by CD8alpha+ dendritic cells but not by Langerhans cells. Science 301, 1925–1928.

Allan, R.S., Waithman, J., Bedoui, S., Jones, C.M., Villadangos, J.A., Zhan, Y., Lew, A.M., Shortman, K., Heath, W.R., and Carbone, F.R. (2006). Migratory dendritic cells transfer antigen to a lymph node-resident dendritic cell population for efficient CTL priming. Immunity 25, 153–162.

Ansel, K.M., Ngo, V.N., Hyman, P.L., Luther, S.A., Förster, R., Sedgwick, J.D., Browning, J.L., Lipp, M., and Cyster, J.G. (2000). A chemokine-driven positive feedback loop organizes lymphoid follicles. Nature 406, 309–314.

Ariotti, S., Hogenbirk, M.A., Dijkgraaf, F.E., Visser, L.L., Hoekstra, M.E., Song, J.-Y., Jacobs, H., Haanen, J.B., and Schumacher, T.N. (2014). T cell memory. Skin-resident memory $CD8^+$ T cells trigger a state of tissue-wide pathogen alert. Science 346, 101–105.

Austrup, F., Vestweber, D., Borges, E., Löhning, M., Bräuer, R., Herz, U., Renz, H., Hallmann, R., Scheffold, A., Radbruch, A., et al. (1997). P- and E-selectin mediate recruitment of T-helper-1 but not T-helper-2 cells into inflamed tissues. Nature 385, 81–83.

Awasthi, S., and Friedman, H.M. (2014). A paradigm shift: vaccine-induced antibodies as an immune correlate of protection against herpes simplex virus type 1 genital herpes. J. Infect. Dis. 209, 813–815.

Azar, G.A., Lemaître, F., Robey, E.A., and Bousso, P. (2010). Subcellular dynamics of T cell immunological synapses and kinapses in lymph nodes. Proc. Natl. Acad. Sci. U.S.a. 107, 3675–3680.

Babbitt, B.P., Matsueda, G., Haber, E., Unanue, E.R., and Allen, P.M. (1986). Antigenic competition at the level of peptide-Ia binding. Proc. Natl. Acad. Sci. U.S.a. 83, 4509–4513.

Bachem, A., Güttler, S., Hartung, E., Ebstein, F., Schaefer, M., Tannert, A., Salama, A., Movassaghi, K., Opitz, C., Mages, H.W., et al. (2010). Superior antigen cross-presentation and XCR1 expression define human CD11c+CD141+ cells as homologues of mouse CD8+ dendritic cells. Journal of Experimental Medicine 207, 1273–1281.

Bachem, A., Hartung, E., Güttler, S., Mora, A., Zhou, X., Hegemann, A., Plantinga, M., Mazzini, E., Stoitzner, P., Gurka, S., et al. (2012). Expression of XCR1 Characterizes the Batf3-Dependent Lineage of Dendritic Cells Capable of Antigen Cross-Presentation. Front Immunol 3.

Bajénoff, M., Granjeaud, S., and Guerder, S. (2003). The strategy of T cell antigen-presenting cell encounter in antigen-draining lymph nodes revealed by imaging of initial T cell activation. J. Exp. Med. 198, 715–724.

Bajénoff, M., Egen, J.G., Koo, L.Y., Laugier, J.P., Brau, F., Glaichenhaus, N., and Germain, R.N. (2006). Stromal cell networks regulate lymphocyte entry, migration, and territoriality in lymph nodes. Immunity 25, 989–1001.

Bankovich, A.J., Shiow, L.R., and Cyster, J.G. (2010). CD69 suppresses sphingosine 1-phosophate receptor-1 (S1P1) function through interaction with membrane helix 4. J. Biol. Chem. 285, 22328–22337.

Barnden, M.J., Allison, J., Heath, W.R., and Carbone, F.R. (1998). Defective TCR expression in transgenic mice constructed using cDNA-based alpha- and beta-chain genes under the control of heterologous regulatory elements. Immunol. Cell Biol. 76, 34–40.

Beauchamp, N.M., Busick, R.Y., and Alexander-Miller, M.A. (2010). Functional divergence among CD103+ dendritic cell subpopulations following pulmonary poxvirus infection. J. Virol. 84, 10191–10199.

Beauvillain, C., Delneste, Y., Scotet, M., Peres, A., Gascan, H., Guermonprez, P., Barnaba, V., and Jeannin, P. (2007). Neutrophils efficiently cross-prime naive T cells in vivo. Blood 110, 2965–2973.

Bedoui, S., Whitney, P.G., Waithman, J., Eidsmo, L., Wakim, L., Caminschi, I., Allan, R.S., Wojtasiak, M., Shortman, K., Carbone, F.R., et al. (2009). Cross-presentation of viral and self antigens by skin-derived CD103+ dendritic cells. Nat. Immunol. 10, 488–495.

Belshe, R.B., Heineman, T.C., Bernstein, D.I., Bellamy, A.R., Ewell, M., van der Most, R., and Deal, C.D. (2014). Correlate of immune protection against HSV-1 genital disease in vaccinated women. J. Infect. Dis. 209, 828–836.

Beltman, J.B., Marée, A.F.M., Lynch, J.N., Miller, M.J., and de Boer, R.J. (2007). Lymph node topology dictates T cell migration behavior. J. Exp. Med. 204, 771–780.

Belz, G.T., Smith, C.M., Kleinert, L., Reading, P., Brooks, A., Shortman, K., Carbone, F.R., and Heath, W.R. (2004). Distinct migrating and nonmigrating dendritic cell populations are involved in MHC class I-restricted antigen presentation after lung infection with virus. Proc. Natl. Acad. Sci. U.S.a. 101, 8670–8675.

BenMohamed, L., Bertrand, G., McNamara, C.D., Gras-Masse, H., Hammer, J., Wechsler, S.L., and Nesburn, A.B. (2003). Identification of novel immunodominant CD4+ Th1-type T-cell peptide epitopes from herpes simplex virus glycoprotein D that confer protective immunity. J. Virol. 77, 9463–9473.

Bennett, S.R., Carbone, F.R., Karamalis, F., Flavell, R.A., Miller, J.F., and Heath, W.R. (1998). Help for cytotoxic-T-cell responses is mediated by CD40 signalling. Nature 393, 478–480.

Beuneu, H., Lemaître, F., Deguine, J., Moreau, H.D., Bouvier, I., Garcia, Z., Albert, M.L., and Bousso, P. (2010). Visualizing the Functional Diversification of CD8(+) T Cell Responses in Lymph Nodes. Immunity 33, 412–423.

Bevan, M.J. (2004). Helping the CD8(+) T-cell response. Nat Rev Immunol 4, 595–602.

Blomgran, R., and Ernst, J.D. (2011). Lung neutrophils facilitate activation of naive antigen-specific CD4+ T cells during Mycobacterium tuberculosis infection. J. Immunol. 186, 7110–7119.

Blyth, W.A., Harbour, D.A., and Hill, T.J. (1984). Pathogenesis of zosteriform spread of herpes simplex virus in the mouse. J. Gen. Virol. 65 (Pt 9), 1477–1486.

Bollampalli, V.P., Harumi Yamashiro, L., Feng, X., Bierschenk, D., Gao, Y., Blom, H., Henriques-Normark, B., Nylén, S., and Rothfuchs, A.G. (2015). BCG Skin Infection Triggers IL-1R-MyD88-Dependent Migration of EpCAMlow CD11bhigh Skin Dendritic cells to Draining Lymph Node During CD4+ T-Cell Priming. PLoS Pathog. 11, e1005206.

Bonneau, R.H., Salvucci, L.A., Johnson, D.C., and Tevethia, S.S. (1993). Epitope specificity of H-2Kb-restricted, HSV-1-, and HSV-2-cross-reactive cytotoxic T lymphocyte clones. Virology 195, 62–70.

Bosnjak, L., Miranda-saksena, M., Koelle, D.M., Boadle, R.A., Jones, C.A., and Cunningham, A.L. (2005). Herpes simplex virus infection of human dendritic cells induces apoptosis and allows cross-presentation via uninfected dendritic cells. J. Immunol. 174, 2220–2227.

Bourgeois, C., Rocha, B., and Tanchot, C. (2002). A role for CD40 expression on CD8+ T cells in the generation of CD8+ T cell memory. Science 297, 2060–2063.

Bousso, P., and Robey, E. (2003). Dynamics of CD8+ T cell priming by dendritic cells in intact lymph nodes. Nat. Immunol. 4, 579–585.

Bousso, P. (2008). T-cell activation by dendritic cells in the lymph node: lessons from the movies. Nat Rev Immunol 8, 675–684.

Braciale, T.J., and Hahn, Y.S. (2013). Immunity to viruses. Immunol. Rev. 255, 5–12.

Breart, B., Lemaître, F., Celli, S., and Bousso, P. (2008). Two-photon imaging of intratumoral CD8+ T cell cytotoxic activity during adoptive T cell therapy in mice. J. Clin. Invest. 118, 1390–1397.

Britschgi, M.R., Favre, S., and Luther, S.A. (2010). CCL21 is sufficient to mediate DC migration, maturation and function in the absence of CCL19. Eur. J. Immunol. 40, 1266–1271.

Bursch, L.S., Wang, L., Igyarto, B., Kissenpfennig, A., Malissen, B., Kaplan, D.H., and Hogquist, K.A. (2007). Identification of a novel population of Langerin+ dendritic cells. J. Exp. Med. 204, 3147–3156.

Cairns, T.M., Shaner, M.S., Zuo, Y., Ponce-de-Leon, M., Baribaud, I., Eisenberg, R.J., Cohen, G.H., and Whitbeck, J.C. (2006). Epitope mapping of herpes simplex virus type 2 gH/gL defines distinct antigenic sites, including some associated with biological function. J. Virol. 80, 2596–2608.

Cantin, E.M., Hinton, D.R., Chen, J., and Openshaw, H. (1995). Gamma interferon expression during acute and latent nervous system infection by herpes simplex virus type 1. J. Virol. 69, 4898–4905.

Cao, W., Henry, M.D., Borrow, P., Yamada, H., Elder, J.H., Ravkov, E.V., Nichol, S.T., Compans, R.W., Campbell, K.P., and Oldstone, M.B. (1998). Identification of alpha-dystroglycan as a receptor for lymphocytic choriomeningitis virus and Lassa fever virus. Science 282, 2079–2081.

Carbone, F.R., Belz, G.T., and Heath, W.R. (2004). Transfer of antigen between migrating and lymph node-resident DCs in peripheral T-cell tolerance and immunity. Trends Immunol. 25, 655–658.

Castellino, F., Huang, A.Y., Altan-Bonnet, G., Stoll, S., Scheinecker, C., and Germain, R.N. (2006). Chemokines enhance immunity by guiding naive CD8+ T cells to sites of CD4+ T cell-dendritic cell interaction. Nature 440, 890–895.

Castellino, F., and Germain, R.N. (2006). Cooperation between CD4+ and CD8+ T cells: when, where, and how. Annu. Rev. Immunol. 24, 519–540.

Catron, D.M., Rusch, L.K., Hataye, J., Itano, A.A., and Jenkins, M.K. (2006). CD4+ T cells that enter the draining lymph nodes after antigen injection participate in the primary response and become central-memory cells. J. Exp. Med. 203, 1045–1054.

Celli, S., Lemaître, F., and Bousso, P. (2007). Real-time manipulation of T cell-dendritic cell interactions in vivo reveals the importance of prolonged contacts for CD4+ T cell activation. Immunity 27, 625–634.

Chang, J.T., Palanivel, V.R., Kinjyo, I., Schambach, F., Intlekofer, A.M., Banerjee, A., Longworth, S.A., Vinup, K.E., Mrass, P., Oliaro, J., et al. (2007). Asymmetric T lymphocyte division in the initiation of adaptive immune responses. Science 315, 1687–1691.

Chang, J.T., Ciocca, M.L., Kinjyo, I., Palanivel, V.R., McClurkin, C.E., Dejong, C.S., Mooney, E.C., Kim, J.S., Steinel, N.C., Oliaro, J., et al. (2011). Asymmetric proteasome segregation as a mechanism for unequal partitioning of the transcription factor T-bet during T lymphocyte division. Immunity 34, 492–504.

Chew, T., Taylor, K.E., and Mossman, K.L. (2009). Innate and adaptive immune responses to herpes simplex virus. Viruses 1, 979–1002.

Chtanova, T., Han, S.-J., Schaeffer, M., van Dooren, G.G., Herzmark, P., Striepen, B., and Robey, E.A. (2009). Dynamics of T cell, antigen-presenting cell, and pathogen interactions during recall responses in the lymph node. Immunity 31, 342–355.

Cockburn, I.A., Amino, R., Kelemen, R.K., Kuo, S.C., Tse, S.-W., Radtke, A., Mac-Daniel, L., Ganusov, V.V., Zavala, F., and Ménard, R. (2013). In vivo imaging of CD8+ T cell-mediated elimination of malaria liver stages. Proc. Natl. Acad. Sci. U.S.a. 110, 9090–9095.

Corse, E., Gottschalk, R.A., and Allison, J.P. (2011). Strength of TCR-peptide/MHC interactions and in vivo T cell responses. J. Immunol. 186, 5039–5045.

Cosgrove, D., Gray, D., Dierich, A., Kaufman, J., Lemeur, M., Benoist, C., and Mathis, D. (1991). Mice lacking MHC class II molecules. Cell 66, 1051–1066.

Côté, J.-F., and Vuori, K. (2002). Identification of an evolutionarily conserved superfamily of DOCK180-related proteins with guanine nucleotide exchange activity. J. Cell. Sci. 115, 4901–4913.

Croft, N.P., Purcell, A.W., and Tscharke, D.C. (2015). Quantifying epitope presentation using mass spectrometry. Mol. Immunol. 68, 77–80.

Cyster, J.G., and Schwab, S.R. (2012). Sphingosine-1-phosphate and lymphocyte egress from lymphoid organs. Annu. Rev. Immunol. 30, 69–94.

D'Souza, W.N., and Hedrick, S.M. (2006). Cutting edge: latecomer CD8 T cells are imprinted with a unique differentiation program. J. Immunol. 177, 777–781.

del Rio, M.-L., Rodriguez-Barbosa, J.-I., Kremmer, E., and Förster, R. (2007). CD103- and CD103+ bronchial lymph node dendritic cells are specialized in presenting and cross-presenting innocuous antigen to CD4+ and CD8+ T cells. J. Immunol. 178, 6861–6866.

Denk, W., Strickler, J.H., and Webb, W.W. (1990). Two-photon laser scanning fluorescence microscopy. Science 248, 73–76.

Desch, A.N., Randolph, G.J., Murphy, K., Gautier, E.L., Kedl, R.M., Lahoud, M.H., Caminschi, I., Shortman, K., Henson, P.M., and Jakubzick, C.V. (2011). CD103+ pulmonary dendritic cells preferentially acquire and present apoptotic cell-associated antigen. Journal of Experimental Medicine 208, 1789–1797.

Dieu, M.C., Vanbervliet, B., Vicari, A., Bridon, J.M., Oldham, E., Aït-Yahia, S., Brière, F., Zlotnik, A., Lebecque, S., and Caux, C. (1998). Selective recruitment of immature and mature dendritic cells by distinct chemokines expressed in different anatomic sites. J. Exp. Med. 188, 373–386.

Dilulio, N.A., Engeman, T., Armstrong, D., Tannenbaum, C., Hamilton, T.A., and Fairchild, R.L. (1999). Groalpha-mediated recruitment of neutrophils is required for elicitation of contact hypersensitivity. Eur. J. Immunol. 29, 3485–3495.

Dorner, B.G., Dorner, M.B., Zhou, X., Opitz, C., Mora, A., Güttler, S., Hutloff, A., Mages, H.W., Ranke, K., Schaefer, M., et al. (2009). Selective expression of the chemokine receptor XCR1 on cross-presenting dendritic cells determines cooperation with CD8+ T cells. Immunity 31, 823–833.

Dudziak, D., Kamphorst, A.O., Heidkamp, G.F., Buchholz, V.R., Trumpfheller, C., Yamazaki, S., Cheong, C., Liu, K., Lee, H.-W., Park, C.G., et al. (2007). Differential antigen processing by dendritic cell subsets in vivo. Science 315, 107–111.

Duffy, D., Perrin, H., Abadie, V., Benhabiles, N., Boissonnas, A., Liard, C., Descours, B., Reboulleau, D., Bonduelle, O., Verrier, B., et al. (2012). Neutrophils transport antigen from the dermis to the bone marrow, initiating a source of memory CD8+ T cells. Immunity 37, 917–929.

Dustin, M.L., Bromley, S.K., Kan, Z., Peterson, D.A., and Unanue, E.R. (1997). Antigen receptor engagement delivers a stop signal to migrating T lymphocytes. Proc. Natl. Acad. Sci. U.S.a. 94, 3909–3913.

Dustin, M.L. (2008). T-cell activation through immunological synapses and kinapses. Immunol. Rev. 221, 77–89.

Edelson, B.T., Kc, W., Juang, R., Kohyama, M., Benoit, L.A., Klekotka, P.A., Moon, C., Albring, J.C., Ise, W., Michael, D.G., et al. (2010). Peripheral CD103+ dendritic cells form a unified subset developmentally related to CD8alpha+ conventional dendritic cells. Journal of Experimental Medicine 207, 823–836.

Egen, J.G., Rothfuchs, A.G., Feng, C.G., Horwitz, M.A., Sher, A., and Germain, R.N. (2011). Intravital imaging reveals limited antigen presentation and T cell effector function in mycobacterial granulomas. Immunity 34, 807–819.

Eickhoff, S., Brewitz, A., Gerner, M.Y., Klauschen, F., Komander, K., Hemmi, H., Garbi, N., Kaisho, T., Germain, R.N., and Kastenmüller, W. (2015). Robust Anti-viral Immunity Requires Multiple Distinct T Cell-Dendritic Cell Interactions. Cell 162, 1322–1337.

Eidsmo, L., Allan, R., Caminschi, I., van Rooijen, N., Heath, W.R., and Carbone, F.R. (2009). Differential migration of epidermal and dermal dendritic cells during skin infection. J. Immunol. 182, 3165–3172.

Eidsmo, L., Stock, A.T., Heath, W.R., Bedoui, S., and Carbone, F.R. (2012). Reactive murine lymph nodes uniquely permit parenchymal access for T cells that enter via the afferent lymphatics. J. Pathol. 226, 806–813.

Engeman, T., Gorbachev, A.V., Kish, D.D., and Fairchild, R.L. (2004). The intensity of neutrophil infiltration controls the number of antigen-primed CD8 T cells recruited into cutaneous antigen challenge sites. J. Leukoc. Biol. 76, 941–949.

Etienne-Manneville, S., and Hall, A. (2002). Rho GTPases in cell biology. Nature 420, 629–635.

Faroudi, M., Zaru, R., Paulet, P., Müller, S., and Valitutti, S. (2003). Cutting edge: T lymphocyte activation by repeated immunological synapse formation and intermittent signaling. J. Immunol. 171, 1128–1132.

Faust, N., Varas, F., Kelly, L.M., Heck, S., and Graf, T. (2000). Insertion of enhanced green fluorescent protein into the lysozyme gene creates mice with green fluorescent granulocytes and macrophages. Blood 96, 719–726.

Feau, S., Arens, R., Togher, S., and Schoenberger, S.P. (2011). Autocrine IL-2 is required for secondary population expansion of CD8(+) memory T cells. Nat. Immunol. 12, 908–913.

Feau, S., Garcia, Z., Arens, R., Yagita, H., Borst, J., and Schoenberger, S.P. (2012). The $CD4^+$ T-cell help signal is transmitted from APC to $CD8^+$ T-cells via CD27-CD70 interactions. Nat Comms 3, 948.

Flesch, I.E.A., Randall, K.L., Hollett, N.A., Di Law, H., Miosge, L.A., Sontani, Y., Goodnow, C.C., and Tscharke, D.C. (2015). Delayed control of herpes simplex virus infection and impaired CD4(+) T-cell migration to the skin in mouse models of DOCK8 deficiency. Immunol. Cell Biol. 93, 517–521.

Förg, P., von Hoegen, P., Dalemans, W., and Schirrmacher, V. (1998). Superiority of the ear pinna over muscle tissue as site for DNA vaccination. Gene Ther. 5, 789–797.

Förster, R., Schubel, A., Breitfeld, D., Kremmer, E., Renner-Müller, I., Wolf, E., and Lipp, M. (1999). CCR7 coordinates the primary immune response by establishing functional microenvironments in secondary lymphoid organs. Cell 99, 23–33.

Früh, K., Ahn, K., Djaballah, H., Sempé, P., van Endert, P.M., Tampé, R., Peterson, P.A., and Yang, Y. (1995). A viral inhibitor of peptide transporters for antigen presentation. Nature 375, 415–418.

Galli, S.J., Borregaard, N., and Wynn, T.A. (2011). Phenotypic and functional plasticity of cells of innate immunity: macrophages, mast cells and neutrophils. Nat. Immunol. 12, 1035–1044.

Garcia, Z., Pradelli, E., Celli, S., Beuneu, H., Simon, A., and Bousso, P. (2007). Competition for antigen determines the stability of T cell-dendritic cell interactions during clonal expansion. Proc. Natl. Acad. Sci. U.S.a. 104, 4553–4558.

Gebhardt, T., Wakim, L.M., Eidsmo, L., Reading, P.C., Heath, W.R., and Carbone, F.R. (2009). Memory T cells in nonlymphoid tissue that provide enhanced local immunity during infection with herpes simplex virus. Nat. Immunol. 10, 524–530.

Gebhardt, T., Whitney, P.G., Zaid, A., Mackay, L.K., Brooks, A.G., Heath, W.R., Carbone, F.R., and Mueller, S.N. (2011). Different patterns of peripheral migration by memory CD4+ and CD8+ T cells. Nature 477, 216–219.

Gerlach, C., van Heijst, J.W.J., Swart, E., Sie, D., Armstrong, N., Kerkhoven, R.M., Zehn, D., Bevan, M.J., Schepers, K., and Schumacher, T.N.M. (2010). One naive T cell, multiple fates in CD8+ T cell differentiation. Journal of Experimental Medicine 207, 1235–1246.

Germain, R.N., Bajénoff, M., Castellino, F., Chieppa, M., Egen, J.G., Huang, A.Y.C., Ishii, M., Koo, L.Y., and Qi, H. (2008). Making friends in out-of-the-way places: how cells of the immune system get together and how they conduct their business as revealed by intravital imaging. Immunol. Rev. 221, 163–181.

Gerner, M.Y., Kastenmüller, W., Ifrim, I., Kabat, J., and Germain, R.N. (2012). Histo-cytometry: a method for highly multiplex quantitative tissue imaging analysis applied to dendritic cell subset microanatomy in lymph nodes. Immunity 37, 364–376.

Gerner, M.Y., Torabi-Parizi, P., and Germain, R.N. (2015). Strategically localized dendritic cells promote rapid T cell responses to lymph-borne particulate antigens. Immunity 42, 172–185.

GeurtsvanKessel, C.H., Willart, M.A.M., van Rijt, L.S., Muskens, F., Kool, M., Baas, C., Thielemans, K., Bennett, C., Clausen, B.E., Hoogsteden, H.C., et al. (2008). Clearance of influenza virus from the lung depends on migratory langerin+CD11b- but not

plasmacytoid dendritic cells. Journal of Experimental Medicine 205, 1621–1634.

Ghiasi, H., Cai, S., Perng, G., Nesburn, A.B., and Wechsler, S.L. (1999). Perforin pathway is essential for protection of mice against lethal ocular HSV-1 challenge but not corneal scarring. Virus Res. 65, 97–101.

Girard, J.-P., Moussion, C., and Förster, R. (2012). HEVs, lymphatics and homeostatic immune cell trafficking in lymph nodes. Nat Rev Immunol 12, 762–773.

Gonzalez, S.F., Lukacs-Kornek, V., Kuligowski, M.P., Pitcher, L.A., Degn, S.E., Kim, Y.-A., Cloninger, M.J., Martinez-Pomares, L., Gordon, S., Turley, S.J., et al. (2010). Capture of influenza by medullary dendritic cells via SIGN-R1 is essential for humoral immunity in draining lymph nodes. Nat. Immunol. 11, 427–434.

Gorlino, C.V., Ranocchia, R.P., Harman, M.F., García, I.A., Crespo, M.I., Morón, G., Maletto, B.A., and Pistoresi-Palencia, M.C. (2014). Neutrophils exhibit differential requirements for homing molecules in their lymphatic and blood trafficking into draining lymph nodes. J. Immunol. 193, 1966–1974.

Gowans, J.L., and Knight, E.J. (1964). The Route of Re-Circulation of Lymphocytes in the Rat. Proceedings of the Royal Society B: Biological Sciences 159, 257–282.

Gretz, J.E., Anderson, A.O., and Shaw, S. (1997). Cords, channels, corridors and conduits: critical architectural elements facilitating cell interactions in the lymph node cortex. Immunol. Rev. 156, 11–24.

Gretz, J.E., Norbury, C.C., Anderson, A.O., Proudfoot, A.E., and Shaw, S. (2000). Lymph-borne chemokines and other low molecular weight molecules reach high endothelial venules via specialized conduits while a functional barrier limits access to the lymphocyte microenvironments in lymph node cortex. J. Exp. Med. 192, 1425–1440.

Greyer, M., Whitney, P.G., Stock, A.T., Davey, G.M., Tebartz, C., Bachem, A., Mintern, J.D., Strugnell, R.A., Turner, S.J., Gebhardt, T., et al. (2016). T Cell Help Amplifies Innate Signals in CD8(+) DCs for Optimal CD8(+) T Cell Priming. Cell Rep 14, 586–597.

Grigorova, I.L., Schwab, S.R., Phan, T.G., Pham, T.H.M., Okada, T., and Cyster, J.G. (2009). Cortical sinus probing, S1P1-dependent entry and flow-based capture of egressing T cells. Nat. Immunol. 10, 58–65.

Grigorova, I.L., Panteleev, M., and Cyster, J.G. (2010). Lymph node cortical sinus organization and relationship to lymphocyte egress dynamics and antigen exposure. Proc. Natl. Acad. Sci. U.S.a. 107, 20447–20452.

Groom, J.R., Richmond, J., Murooka, T.T., Sorensen, E.W., Sung, J.H., Bankert, K., von Andrian, U.H., Moon, J.J., Mempel, T.R., and Luster, A.D. (2012). CXCR3 Chemokine Receptor-Ligand Interactions in the Lymph Node Optimize CD4+ T Helper 1 Cell Differentiation. Immunity 37, 1091–1103.

Gunzer, M., Schäfer, A., Borgmann, S., Grabbe, S., Zänker, K.S., Bröcker, E.B., Kämpgen, E., and Friedl, P. (2000). Antigen presentation in extracellular matrix: interactions of T cells with dendritic cells are dynamic, short lived, and sequential. Immunity 13, 323–332.

Guo, F., Hildeman, D., Tripathi, P., Velu, C.S., Grimes, H.L., and Zheng, Y. (2010). Coordination of IL-7 receptor and T-cell receptor signaling by cell-division cycle 42 in T-cell homeostasis. Proc. Natl. Acad. Sci. U.S.a. 107, 18505–18510.

Halle, S., Keyser, K.A., Stahl, F.R., Busche, A., Marquardt, A., Zheng, X., Galla, M., Heissmeyer, V., Heller, K., Boelter, J., et al. (2016). In Vivo Killing Capacity of Cytotoxic T Cells Is Limited and Involves Dynamic Interactions and T Cell Cooperativity. Immunity 44, 233–245.

Hampton, H.R., Bailey, J., Tomura, M., Brink, R., and Chtanova, T. (2015). Microbe-dependent lymphatic migration of neutrophils modulates lymphocyte proliferation in lymph nodes. Nat Comms 6, 7139.

Handler, C.G., Eisenberg, R.J., and Cohen, G.H. (1996). Oligomeric structure of glycoproteins in herpes simplex virus type 1. J. Virol. 70, 6067–6070.

Haniffa, M., Shin, A., Bigley, V., McGovern, N., Teo, P., See, P., Wasan, P.S., Wang, X.-N., Malinarich, F., Malleret, B., et al. (2012). Human tissues contain CD141hi cross-presenting dendritic cells with functional homology to mouse CD103+ nonlymphoid dendritic cells. Immunity 37, 60–73.

Hanke, T., Graham, F.L., Rosenthal, K.L., and Johnson, D.C. (1991). Identification of an immunodominant cytotoxic T-lymphocyte recognition site in glycoprotein B of herpes simplex virus by using recombinant adenovirus vectors and synthetic peptides. J. Virol. 65, 1177–1186.

Harada, Y., Tanaka, Y., Terasawa, M., Pieczyk, M., Habiro, K., Katakai, T., Hanawa-Suetsugu, K., Kukimoto-Niino, M., Nishizaki, T., Shirouzu, M., et al. (2012). DOCK8 is a Cdc42 activator critical for interstitial dendritic cell migration during immune responses. Blood 119, 4451–4461.

Hashimoto, D., Miller, J., and Merad, M. (2011). Dendritic cell and macrophage heterogeneity in vivo. Immunity 35, 323–335.

Heath, W.R., and Carbone, F.R. (2001). Cross-presentation in viral immunity and self-tolerance. Nat Rev Immunol 1, 126–134.

Helft, J., Manicassamy, B., Guermonprez, P., Hashimoto, D., Silvin, A., Agudo, J., Brown, B.D., Schmolke, M., Miller, J.C., Leboeuf, M., et al. (2012). Cross-presenting CD103+ dendritic cells are protected from influenza virus infection. J. Clin. Invest. 122, 4037–4047.

Henri, S., Poulin, L.F., Tamoutounour, S., Ardouin, L., Guilliams, M., de Bovis, B., Devilard, E., Viret, C., Azukizawa, H., Kissenpfennig, A., et al. (2010). CD207+ CD103+ dermal dendritic cells cross-present keratinocyte-derived antigens

irrespective of the presence of Langerhans cells. J. Exp. Med. 207, 189–206.

Henrickson, S.E., Mempel, T.R., Mazo, I.B., Liu, B., Artyomov, M.N., Zheng, H., Peixoto, A., Flynn, M.P., Senman, B., Junt, T., et al. (2008). T cell sensing of antigen dose governs interactive behavior with dendritic cells and sets a threshold for T cell activation. Nat. Immunol. 9, 282–291.

Herold, B.C., WuDunn, D., Soltys, N., and Spear, P.G. (1991). Glycoprotein C of herpes simplex virus type 1 plays a principal role in the adsorption of virus to cells and in infectivity. J. Virol. 65, 1090–1098.

Herold, B.C., Visalli, R.J., Susmarski, N., Brandt, C.R., and Spear, P.G. (1994). Glycoprotein C-independent binding of herpes simplex virus to cells requires cell surface heparan sulphate and glycoprotein B. J. Gen. Virol. 75 (Pt 6), 1211–1222.

Hickman, H.D., Takeda, K., Skon, C.N., Murray, F.R., Hensley, S.E., Loomis, J., Barber, G.N., Bennink, J.R., and Yewdell, J.W. (2008). Direct priming of antiviral CD8+ T cells in the peripheral interfollicular region of lymph nodes. Nat. Immunol. 9, 155–165.

Hickman, H.D., Li, L., Reynoso, G.V., Rubin, E.J., Skon, C.N., Mays, J.W., Gibbs, J., Schwartz, O., Bennink, J.R., and Yewdell, J.W. (2011). Chemokines control naive CD8+ T cell selection of optimal lymph node antigen presenting cells. Journal of Experimental Medicine 208, 2511–2524.

Hickman, H.D., Reynoso, G.V., Ngudiankama, B.F., Rubin, E.J., Magadán, J.G., Cush, S.S., Gibbs, J., Molon, B., Bronte, V., Bennink, J.R., et al. (2013). Anatomically Restricted Synergistic Antiviral Activities of Innate and Adaptive Immune Cells in the Skin. Cell Host Microbe 13, 155–168.

Hildner, K., Edelson, B.T., Purtha, W.E., Diamond, M., Matsushita, H., Kohyama, M., Calderon, B., Schraml, B.U., Unanue, E.R., Diamond, M.S., et al. (2008). Batf3 deficiency reveals a critical role for CD8alpha+ dendritic cells in cytotoxic T cell immunity. Science 322, 1097–1100.

Hildner, K., Edelson, B.T., Purtha, W.E., Diamond, M., Matsushita, H., Kohyama, M., Calderon, B., Schraml, B.U., Unanue, E.R., Diamond, M.S., et al. (2008). Batf3 deficiency reveals a critical role for CD8alpha+ dendritic cells in cytotoxic T cell immunity. Science 322, 1097–1100.

Hill, A.B., Barnett, B.C., McMichael, A.J., and McGeoch, D.J. (1994). HLA class I molecules are not transported to the cell surface in cells infected with herpes simplex virus types 1 and 2. J. Immunol. 152, 2736–2741.

Hill, A., Jugovic, P., York, I., Russ, G., Bennink, J., Yewdell, J., Ploegh, H., and Johnson, D. (1995). Herpes simplex virus turns off the TAP to evade host immunity. Nature 375, 411–415.

Hochrein, H., Schlatter, B., O'Keeffe, M., Wagner, C., Schmitz, F., Schiemann, M., Bauer, S., Suter, M., and Wagner, H. (2004). Herpes simplex virus type-1 induces IFN-alpha production via Toll-like receptor 9-dependent and -independent pathways. Proc. Natl. Acad. Sci. U.S.a. 101, 11416–11421.

Hogquist, K.A., Jameson, S.C., Heath, W.R., Howard, J.L., Bevan, M.J., and Carbone, F.R. (1994). T cell receptor antagonist peptides induce positive selection. Cell 76, 17–27.

Howden, B.P., Seemann, T., Harrison, P.F., McEvoy, C.R., Stanton, J.-A.L., Rand, C.J., Mason, C.W., Jensen, S.O., Firth, N., Davies, J.K., et al. (2010). Complete genome sequence of Staphylococcus aureus strain JKD6008, an ST239 clone of methicillin-resistant Staphylococcus aureus with intermediate-level vancomycin resistance. J. Bacteriol. 192, 5848–5849.

Hufford, M.M., Richardson, G., Zhou, H., Manicassamy, B., García-Sastre, A., Enelow, R.I., and Braciale, T.J. (2012). Influenza-infected neutrophils within the infected lungs act as antigen presenting cells for anti-viral CD8(+) T cells. PLoS ONE 7, e46581.

Hugues, S., Scholer, A., Boissonnas, A., Nussbaum, A., Combadière, C., Amigorena, S., and Fetler, L. (2007). Dynamic imaging of chemokine-dependent CD8+ T cell help for CD8+ T cell responses. Nat. Immunol. 8, 921–930.

Huppa, J.B., Gleimer, M., Sumen, C., and Davis, M.M. (2003). Continuous T cell receptor signaling required for synapse maintenance and full effector potential. Nat. Immunol. 4, 749–755.

Iijima, N., and Iwasaki, A. (2014). A local macrophage chemokine network sustains protective tissue-resident memory CD4 T cells. Science 346, 93–98.

Iijima, N., Linehan, M.M., Zamora, M., Butkus, D., Dunn, R., Kehry, M.R., Laufer, T.M., and Iwasaki, A. (2008). Dendritic cells and B cells maximize mucosal Th1 memory response to herpes simplex virus. Journal of Experimental Medicine 205, 3041–3052.

Imperiali, M., Thoma, C., Pavoni, E., Brancaccio, A., Callewaert, N., and Oxenius, A. (2005). O Mannosylation of alpha-dystroglycan is essential for lymphocytic choriomeningitis virus receptor function. J. Virol. 79, 14297–14308.

Iyoda, T., Shimoyama, S., Liu, K., Omatsu, Y., Akiyama, Y., Maeda, Y., Takahara, K., Steinman, R.M., and Inaba, K. (2002). The CD8+ dendritic cell subset selectively endocytoses dying cells in culture and in vivo. J. Exp. Med. 195, 1289–1302.

Jakubzick, C., Gautier, E.L., Gibbings, S.L., Sojka, D.K., Schlitzer, A., Johnson, T.E., Ivanov, S., Duan, Q., Bala, S., Condon, T., et al. (2013). Minimal differentiation of classical monocytes as they survey steady-state tissues and transport antigen to lymph nodes. Immunity 39, 599–610.

Janssen, E.M., Lemmens, E.E., Wolfe, T., Christen, U., von Herrath, M.G., and Schoenberger, S.P. (2003). CD4+ T cells are required for secondary expansion and memory in CD8+ T lymphocytes. Nature 421, 852–856.

Johansson-Lindbom, B., and Agace, W.W. (2007). Generation of gut-homing T cells and their localization to the small intestinal mucosa. Immunol. Rev. 215, 226–242.

John, B., Harris, T.H., Tait, E.D., Wilson, E.H., Gregg, B., Ng, L.G., Mrass, P., Roos, D.S., Dzierszinski, F., Weninger, W., et al. (2009). Dynamic Imaging of CD8(+) T cells and dendritic cells during infection with Toxoplasma gondii. PLoS Pathog. 5, e1000505.

Johnson, A.J., Chu, C.-F., and Milligan, G.N. (2008). Effector CD4+ T-cell involvement in clearance of infectious herpes simplex virus type 1 from sensory ganglia and spinal cords. J. Virol. 82, 9678–9688.

Jones, C.A., Fernandez, M., Herc, K., Bosnjak, L., Miranda-Saksena, M., Boadle, R.A., and Cunningham, A. (2003). Herpes simplex virus type 2 induces rapid cell death and functional impairment of murine dendritic cells in vitro. J. Virol. 77, 11139–11149.

Jongbloed, S.L., Kassianos, A.J., McDonald, K.J., Clark, G.J., Ju, X., Angel, C.E., Chen, C.-J.J., Dunbar, P.R., Wadley, R.B., Jeet, V., et al. (2010). Human CD141+ (BDCA-3)+ dendritic cells (DCs) represent a unique myeloid DC subset that cross-presents necrotic cell antigens. Journal of Experimental Medicine 207, 1247–1260.

Jongerius, I., Köhl, J., Pandey, M.K., Ruyken, M., van Kessel, K.P.M., van Strijp, J.A.G., and Rooijakkers, S.H.M. (2007). Staphylococcal complement evasion by various convertase-blocking molecules. J. Exp. Med. 204, 2461–2471.

Junker, J.P.E., Kamel, R.A., Caterson, E.J., and Eriksson, E. (2013). Clinical Impact Upon Wound Healing and Inflammation in Moist, Wet, and Dry Environments. Adv Wound Care (New Rochelle) 2, 348–356.

Junt, T., Moseman, E.A., Iannacone, M., Massberg, S., Lang, P.A., Boes, M., Fink, K., Henrickson, S.E., Shayakhmetov, D.M., Di Paolo, N.C., et al. (2007). Subcapsular sinus macrophages in lymph nodes clear lymph-borne viruses and present them to antiviral B cells. Nature 450, 110–114.

Kaech, S.M., and Ahmed, R. (2001). Memory CD8+ T cell differentiation: initial antigen encounter triggers a developmental program in naïve cells. Nat. Immunol. 2, 415–422.

Kamenyeva, O., Boularan, C., Kabat, J., Cheung, G.Y.C., Cicala, C., Yeh, A.J., Chan, J.L., Periasamy, S., Otto, M., and Kehrl, J.H. (2015). Neutrophil recruitment to lymph nodes limits local humoral response to Staphylococcus aureus. PLoS Pathog. 11, e1004827.

Kastenmüller, W., Brandes, M., Wang, Z., Herz, J., Egen, J.G., and Germain, R.N. (2013). Peripheral prepositioning and local CXCL9 chemokine-mediated guidance orchestrate rapid memory CD8+ T cell responses in the lymph node. Immunity 38, 502–513.

Katakai, T., Hara, T., Lee, J.-H., Gonda, H., Sugai, M., and Shimizu, A. (2004). A novel reticular stromal structure in lymph node cortex: an immuno-platform for interactions among dendritic cells, T cells and B cells. International Immunology 16, 1133–1142.

Kawashima, Y., Sugimura, M., Hwang, Y.C., and Kudo, N. (1964). The Lymph System in Mice. Japanese Journal of Veterinary Research 12, 69–77.

Khanna, K.M., Bonneau, R.H., Kinchington, P.R., and Hendricks, R.L. (2003). Herpes simplex virus-specific memory CD8+ T cells are selectively activated and retained in latently infected sensory ganglia. Immunity 18, 593–603.

Kim, T.S., and Braciale, T.J. (2009). Respiratory dendritic cell subsets differ in their capacity to support the induction of virus-specific cytotoxic CD8+ T cell responses. PLoS ONE 4, e4204.

Kim, C.H., Rott, L., Kunkel, E.J., Genovese, M.C., Andrew, D.P., Wu, L., and Butcher, E.C. (2001). Rules of chemokine receptor association with T cell polarization in vivo. J. Clin. Invest. 108, 1331–1339.

Kim, M.-H., Liu, W., Borjesson, D.L., Curry, F.-R.E., Miller, L.S., Cheung, A.L., Liu, F.-T., Isseroff, R.R., and Simon, S.I. (2008). Dynamics of neutrophil infiltration during cutaneous wound healing and infection using fluorescence imaging. J. Invest. Dermatol. 128, 1812–1820.

Kissenpfennig, A., Henri, S., Dubois, B., Laplace-Builhé, C., Perrin, P., Romani, N., Tripp, C.H., Douillard, P., Leserman, L., Kaiserlian, D., et al. (2005). Dynamics and function of Langerhans cells in vivo: dermal dendritic cells colonize lymph node areas distinct from slower migrating Langerhans cells. Immunity 22, 643–654.

Kitano, M., Yamazaki, C., Takumi, A., Ikeno, T., Hemmi, H., Takahashi, N., Shimizu, K., Fraser, S.E., Hoshino, K., Kaisho, T., et al. (2016). Imaging of the cross-presenting dendritic cell subsets in the skin-draining lymph node. Proc. Natl. Acad. Sci. U.S.a. 113, 1044–1049.

Kroczek, R.A., and Henn, V. (2012). The Role of XCR1 and its Ligand XCL1 in Antigen Cross-Presentation by Murine and Human Dendritic Cells. Front Immunol 3, 14.

Kumamoto, Y., Mattei, L.M., Sellers, S., Payne, G.W., and Iwasaki, A. (2011). CD4+ T cells support cytotoxic T lymphocyte priming by controlling lymph node input. Proc. Natl. Acad. Sci. U.S.a. 108, 8749–8754.

Lambe, T., Crawford, G., Johnson, A.L., Crockford, T.L., Bouriez-Jones, T., Smyth, A.M., Pham, T.H.M., Zhang, Q., Freeman, A.F., Cyster, J.G., et al. (2011). DOCK8 is essential for T-cell survival and the maintenance of CD8+ T-cell memory. Eur. J. Immunol. 41, 3423–3435.

Langenkamp, A., Nagata, K., Murphy, K., Wu, L., Lanzavecchia, A., and Sallusto, F. (2003). Kinetics and expression patterns of chemokine receptors in human CD4+ T lymphocytes primed by myeloid or plasmacytoid dendritic cells. Eur. J. Immunol. 33, 474–482.

Lanzavecchia, A. (1998). Immunology. Licence to kill. Nature 393, 413–414.

Lauber, K., Bohn, E., Kröber, S.M., Xiao, Y.-J., Blumenthal, S.G., Lindemann, R.K., Marini, P., Wiedig, C., Zobywalski, A., Baksh, S., et al. (2003). Apoptotic cells induce migration of phagocytes via caspase-3-mediated release of a lipid attraction signal. Cell 113, 717–730.

Lee, K.-H., Holdorf, A.D., Dustin, M.L., Chan, A.C., Allen, P.M., and Shaw, A.S. (2002). T cell receptor signaling precedes immunological synapse formation. Science 295, 1539–1542.

Lee, B.O., Hartson, L., and Randall, T.D. (2003). CD40-deficient, influenza-specific CD8 memory T cells develop and function normally in a CD40-sufficient environment. J. Exp. Med. 198, 1759–1764.

Lee, H.K., Zamora, M., Linehan, M.M., Iijima, N., Gonzalez, D., Haberman, A., and Iwasaki, A. (2009). Differential roles of migratory and resident DCs in T cell priming after mucosal or skin HSV-1 infection. J. Exp. Med. 206, 359–370.

Lee, H.K., Zamora, M., Linehan, M.M., Iijima, N., Gonzalez, D., Haberman, A., and Iwasaki, A. (2009). Differential roles of migratory and resident DCs in T cell priming after mucosal or skin HSV-1 infection. J. Exp. Med. 206, 359–370.

Leib, D.A., Harrison, T.E., Laslo, K.M., Machalek, M.A., Moorman, N.J., and Virgin, H.W. (1999). Interferons regulate the phenotype of wild-type and mutant herpes simplex viruses in vivo. J. Exp. Med. 189, 663–672.

Leoni, V., Gianni, T., Salvioli, S., and Campadelli-Fiume, G. (2012). Herpes simplex virus glycoproteins gH/gL and gB bind Toll-like receptor 2, and soluble gH/gL is sufficient to activate NF-κB. J. Virol. 86, 6555–6562.

Lim, K., Hyun, Y.-M., Lambert-Emo, K., Capece, T., Bae, S., Miller, R., Topham, D.J., and Kim, M. (2015). Neutrophil trails guide influenza-specific $CD8^+$ T cells in the airways. Science 349, aaa4352.

Lindquist, R.L., Shakhar, G., Dudziak, D., Wardemann, H., Eisenreich, T., Dustin, M.L., and Nussenzweig, M.C. (2004). Visualizing dendritic cell networks in vivo. Nat. Immunol. 5, 1243–1250.

Liu, T., Tang, Q., and Hendricks, R.L. (1996). Inflammatory infiltration of the trigeminal ganglion after herpes simplex virus type 1 corneal infection. J. Virol. 70, 264–271.

Liu, L., Fuhlbrigge, R.C., Karibian, K., Tian, T., and Kupper, T.S. (2006). Dynamic programming of CD8+ T cell trafficking after live viral immunization. Immunity 25, 511–520.

Livak, K.J., and Schmittgen, T.D. (2001). Analysis of relative gene expression data using real-time quantitative PCR and the 2(-Delta Delta C(T)) Method. Methods 25, 402–408.

Loret, S., Guay, G., and Lippé, R. (2008). Comprehensive characterization of extracellular herpes simplex virus type 1 virions. J. Virol. 82, 8605–8618.

Lubinski, J.M., Jiang, M., Hook, L., Chang, Y., Sarver, C., Mastellos, D., Lambris, J.D., Cohen, G.H., Eisenberg, R.J., and Friedman, H.M. (2002). Herpes simplex virus type 1 evades the effects of antibody and complement in vivo. J. Virol. 76, 9232–9241.

Lubinski, J.M., Lazear, H.M., Awasthi, S., Wang, F., and Friedman, H.M. (2011). The herpes simplex virus 1 IgG fc receptor blocks antibody-mediated complement activation and antibody-dependent cellular cytotoxicity in vivo. J. Virol. 85, 3239–3249.

Lukens, M.V., Kruijsen, D., Coenjaerts, F.E.J., Kimpen, J.L.L., and van Bleek, G.M. (2009). Respiratory syncytial virus-induced activation and migration of respiratory dendritic cells and subsequent antigen presentation in the lung-draining lymph node. J. Virol. 83, 7235–7243.

Luker, G.D., Prior, J.L., Song, J., Pica, C.M., and Leib, D.A. (2003). Bioluminescence imaging reveals systemic dissemination of herpes simplex virus type 1 in the absence of interferon receptors. J. Virol. 77, 11082–11093.

Lund, J., Sato, A., Akira, S., Medzhitov, R., and Iwasaki, A. (2003). Toll-like receptor 9-mediated recognition of Herpes simplex virus-2 by plasmacytoid dendritic cells. J. Exp. Med. 198, 513–520.

Lund, J.M., Linehan, M.M., Iijima, N., and Iwasaki, A. (2006). Cutting Edge: Plasmacytoid dendritic cells provide innate immune protection against mucosal viral infection in situ. J. Immunol. 177, 7510–7514.

Luther, S.A., Tang, H.L., Hyman, P.L., Farr, A.G., and Cyster, J.G. (2000). Coexpression of the chemokines ELC and SLC by T zone stromal cells and deletion of the ELC gene in the plt/plt mouse. Proc. Natl. Acad. Sci. U.S.a. 97, 12694–12699.

Ma, C.S., Deenick, E.K., Batten, M., and Tangye, S.G. (2012). The origins, function, and regulation of T follicular helper cells. Journal of Experimental Medicine 209, 1241–1253.

Mackay, L.K., Stock, A.T., Ma, J.Z., Jones, C.M., Kent, S.J., Mueller, S.N., Heath, W.R., Carbone, F.R., and Gebhardt, T. (2012). Long-lived epithelial immunity by tissue-resident memory T (TRM) cells in the absence of persisting local antigen presentation. Proc. Natl. Acad. Sci. U.S.a. 109, 7037–7042.

Mackay, L.K., Rahimpour, A., Ma, J.Z., Collins, N., Stock, A.T., Hafon, M.-L., Vega-Ramos, J., Lauzurica, P., Mueller, S.N., Stefanovic, T., et al. (2013). The developmental pathway for CD103(+)CD8+ tissue-resident memory T cells of skin. Nat. Immunol. 14, 1294–1301.

Macleod, B.L., Bedoui, S., Hor, J.L., Mueller, S.N., Russell, T.A., Hollett, N.A., Heath, W.R., Tscharke, D.C., Brooks, A.G., and Gebhardt, T. (2014). Distinct APC subtypes drive spatially segregated CD4+ and CD8+ T-cell effector activity during skin infection with HSV-1. PLoS Pathog. 10, e1004303.

Mandl, J.N., Liou, R., Klauschen, F., Vrisekoop, N., Monteiro, J.P., Yates, A.J., Huang, A.Y., and Germain, R.N. (2012). Quantification of lymph node transit times reveals differences in antigen surveillance strategies of naive CD4+ and CD8+ T cells. Proc. Natl. Acad. Sci. U.S.a.

Mantovani, A., Cassatella, M.A., Costantini, C., and Jaillon, S. (2011). Neutrophils in the activation and regulation of innate and adaptive immunity. Nat Rev Immunol 11, 519–531.

Martín-Fontecha, A., Sebastiani, S., Höpken, U.E., Uguccioni, M., Lipp, M., Lanzavecchia, A., and Sallusto, F. (2003). Regulation of dendritic cell migration to the draining lymph node: impact on T lymphocyte traffic and priming. J. Exp. Med. 198, 615–621.

Martínez, V.G., Canseco, N.M., Hidalgo, L., Valencia, J., Entrena, A., Fernández-Sevilla, L.M., Hernández-López, C., Sacedón, R., Vicente, A., and Varas, A. (2015). A discrete population of IFN λ-expressing BDCA3hi dendritic cells is present in human thymus. Immunol. Cell Biol. 93, 673–678.

Masopust, D., and Schenkel, J.M. (2013). The integration of T cell migration, differentiation and function. Nat Rev Immunol 13, 309–320.

Mazzini, E., Massimiliano, L., Penna, G., and Rescigno, M. (2014). Oral tolerance can be established via gap junction transfer of fed antigens from $CX3CR1^+$ macrophages to $CD103^+$ dendritic cells. Immunity 40, 248–261.

McFadden, G. (2005). Poxvirus tropism. Nat Rev Micro 3, 201–213.

Melchjorsen, J., Matikainen, S., and Paludan, S.R. (2009). Activation and evasion of innate antiviral immunity by herpes simplex virus. Viruses 1, 737–759.

Mempel, T.R., Henrickson, S.E., and von Andrian, U.H. (2004). T-cell priming by dendritic cells in lymph nodes occurs in three distinct phases. Nature 427, 154–159.

Meszaros, A.J., Reichner, J.S., and Albina, J.E. (2000). Macrophage-induced neutrophil apoptosis. J. Immunol. 165, 435–441.

Mikloska, Z., Sanna, P.P., and Cunningham, A.L. (1999). Neutralizing antibodies inhibit axonal spread of herpes simplex virus type 1 to epidermal cells in vitro. J. Virol. 73, 5934–5944.

Miller, M.J., Wei, S.H., Cahalan, M.D., and Parker, I. (2003). Autonomous T cell trafficking examined in vivo with intravital two-photon microscopy. Proc. Natl. Acad. Sci. U.S.a. 100, 2604–2609.

Miller, M.J., Safrina, O., Parker, I., and Cahalan, M.D. (2004a). Imaging the single cell dynamics of CD4+ T cell activation by dendritic cells in lymph nodes. J. Exp. Med. 200, 847–856.

Miller, M.J., Hejazi, A.S., Wei, S.H., Cahalan, M.D., and Parker, I. (2004b). T cell repertoire scanning is promoted by dynamic dendritic cell behavior and random T cell motility in the lymph node. Proc. Natl. Acad. Sci. U.S.a. 101, 998–1003.

Milligan, G.N., and Bernstein, D.I. (1997). Interferon-gamma enhances resolution of herpes simplex virus type 2 infection of the murine genital tract. Virology 229, 259–268.

Milligan, G.N., Bernstein, D.I., and Bourne, N. (1998). T lymphocytes are required for protection of the vaginal mucosae and sensory ganglia of immune mice against reinfection with herpes simplex virus type 2. J. Immunol. 160, 6093–6100.

Mitchison, N.A., and O'Malley, C. (1987). Three-cell-type clusters of T cells with antigen-presenting cells best explain the epitope linkage and noncognate requirements of the in vivo cytolytic response. Eur. J. Immunol. 17, 1579–1583.

Moon, J.J., Chu, H.H., Pepper, M., McSorley, S.J., Jameson, S.C., Kedl, R.M., and Jenkins, M.K. (2007). Naive CD4(+) T cell frequency varies for different epitopes and predicts repertoire diversity and response magnitude. Immunity 27, 203–213.

Moreau, H.D., Lemaître, F., Terriac, E., Azar, G., Piel, M., Lennon-Dumenil, A.-M., and Bousso, P. (2012). Dynamic in situ cytometry uncovers T cell receptor signaling during immunological synapses and kinapses in vivo. Immunity 37, 351–363.

Morrison, L.A., Zhu, L., and Thebeau, L.G. (2001). Vaccine-induced serum immunoglobin contributes to protection from herpes simplex virus type 2 genital infection in the presence of immune T cells. J. Virol. 75, 1195–1204.

Mount, A.M., Smith, C.M., Kupresanin, F., Stoermer, K., Heath, W.R., and Belz, G.T. (2008). Multiple dendritic cell populations activate CD4+ T cells after viral stimulation. PLoS ONE 3, e1691.

Mueller, S.N., Heath, W., McLain, J.D., Carbone, F.R., and Jones, C.M. (2002a). Characterization of two TCR transgenic mouse lines specific for herpes simplex virus. Immunol. Cell Biol. 80, 156–163.

Mueller, S.N., Jones, C.M., Smith, C.M., Heath, W.R., and Carbone, F.R. (2002b). Rapid cytotoxic T lymphocyte activation occurs in the draining lymph nodes after cutaneous herpes simplex virus infection as a result of early antigen presentation and not the presence of virus. J. Exp. Med. 195, 651–656.

Mueller, S.N., Jones, C.M., Chen, W., Kawaoka, Y., Castrucci, M.R., Heath, W.R., and Carbone, F.R. (2003). The early expression of glycoprotein B from herpes simplex virus can be detected by antigen-specific CD8+ T cells. J. Virol. 77, 2445–2451.

Mueller, S.N., Hosiawa-Meagher, K.A., Konieczny, B.T., Sullivan, B.M., Bachmann, M.F., Locksley, R.M., Ahmed, R., and Matloubian, M. (2007). Regulation of homeostatic chemokine expression and cell trafficking during immune responses. Science 317, 670–674.

Mueller, S.N., and Germain, R.N. (2009). Stromal cell contributions to the homeostasis and functionality of the immune system. Nat Rev Immunol 9, 618–629.

Müller, A.J., Filipe-Santos, O., Eberl, G., Aebischer, T., Späth, G.F., and Bousso, P. (2012). CD4(+) T Cells Rely on a Cytokine Gradient to Control Intracellular Pathogens beyond Sites of Antigen Presentation. Immunity.

Nakanishi, Y., Lu, B., Gerard, C., and Iwasaki, A. (2009). CD8(+) T lymphocyte mobilization to virus-infected tissue requires CD4(+) T-cell help. Nature 462, 510–513.

Nathan, C. (2006). Neutrophils and immunity: challenges and opportunities. Nat Rev Immunol 6, 173–182.

Neefjes, J., Jongsma, M.L.M., Paul, P., and Bakke, O. (2011). Towards a systems understanding of MHC class I and MHC class II antigen presentation. Nat Rev Immunol 11, 823–836.

Negulescu, P.A., Krasieva, T.B., Khan, A., Kerschbaum, H.H., and Cahalan, M.D. (1996). Polarity of T cell shape, motility, and sensitivity to antigen. Immunity 4, 421–430.

Nestle, F.O., Di Meglio, P., Qin, J.-Z., and Nickoloff, B.J. (2009). Skin immune sentinels in health and disease. Nat Rev Immunol 9, 679–691.

Ng, L.G., Hsu, A., Mandell, M.A., Roediger, B., Hoeller, C., Mrass, P., Iparraguirre, A., Cavanagh, L.L., Triccas, J.A., Beverley, S.M., et al. (2008). Migratory dermal dendritic cells act as rapid sensors of protozoan parasites. PLoS Pathog. *4*, e1000222.

Norbury, C.C., Malide, D., Gibbs, J.S., Bennink, J.R., and Yewdell, J.W. (2002). Visualizing priming of virus-specific CD8+ T cells by infected dendritic cells in vivo. Nat. Immunol. 3, 265–271.

Obar, J.J., Khanna, K.M., and Lefrançois, L. (2008). Endogenous naive CD8+ T cell precursor frequency regulates primary and memory responses to infection. Immunity 28, 859–869.

Obst, R., van Santen, H.-M., Mathis, D., and Benoist, C. (2005). Antigen persistence is required throughout the expansion phase of a CD4(+) T cell response. J. Exp. Med. 201, 1555–1565.

Obst, R. (2015). The Timing of T Cell Priming and Cycling. Front Immunol 6, 563.

Oxenius, A., Bachmann, M.F., Zinkernagel, R.M., and Hengartner, H. (1998). Virus-specific MHC-class II-restricted TCR-transgenic mice: effects on humoral and cellular immune responses after viral infection. Eur. J. Immunol. 28, 390–400.

Oyoshi, M.K., He, R., Li, Y., Mondal, S., Yoon, J., Afshar, R., Chen, M., Lee, D.M., Luo, H.R., Luster, A.D., et al. (2012). Leukotriene B4-driven neutrophil recruitment to the skin is essential for allergic skin inflammation. Immunity 37, 747–758.

Pape, K.A., Catron, D.M., Itano, A.A., and Jenkins, M.K. (2007). The humoral immune response is initiated in lymph nodes by B cells that acquire soluble antigen directly in the follicles. Immunity 26, 491–502.

Persson, E.K., Uronen-Hansson, H., Semmrich, M., Rivollier, A., Hägerbrand, K., Marsal, J., Gudjonsson, S., Håkansson, U., Reizis, B., Kotarsky, K., et al. (2013). IRF4 transcription-factor-dependent CD103(+)CD11b(+) dendritic cells drive mucosal T helper 17 cell differentiation. Immunity 38, 958–969.

Pflicke, H., and Sixt, M. (2009). Preformed portals facilitate dendritic cell entry into afferent lymphatic vessels. J. Exp. Med. 206, 2925–2935.

Pham, T.H.M., Okada, T., Matloubian, M., Lo, C.G., and Cyster, J.G. (2008). S1P1 receptor signaling overrides retention mediated by G alpha i-coupled receptors to promote T cell egress. Immunity 28, 122–133.

Phan, T.G., Green, J.A., Gray, E.E., Xu, Y., and Cyster, J.G. (2009). Immune complex relay by subcapsular sinus macrophages and noncognate B cells drives antibody affinity maturation. Nat. Immunol. 10, 786–793.

Pircher, H., Baenziger, J., Schilham, M., Sado, T., Kamisaku, H., Hengartner, H., and Zinkernagel, R.M. (1987). Characterization of virus-specific cytotoxic T cell clones from allogeneic bone marrow chimeras. Eur. J. Immunol. 17, 159–166.

Pircher, H., Bürki, K., Lang, R., Hengartner, H., and Zinkernagel, R.M. (1989). Tolerance induction in double specific T-cell receptor transgenic mice varies with antigen. Nature 342, 559–561.

Piston, D.W. (1999). Imaging living cells and tissues by two-photon excitation microscopy. Trends Cell Biol. 9, 66–69.

Prechtel, A.T., Turza, N.M., Kobelt, D.J., Eisemann, J.I., Coffin, R.S., McGrath, Y., Hacker, C., Ju, X., Zenke, M., and Steinkasserer, A. (2005). Infection of mature dendritic cells with herpes simplex virus type 1 dramatically reduces lymphoid chemokine-mediated migration. J. Gen. Virol. 86, 1645–1657.

Progatzky, F., Dallman, M.J., and Celso, Lo, C. (2013). From seeing to believing: labelling strategies for in vivo cell-tracking experiments. Interface Focus 3, 20130001.

Pruyne, D., and Bretscher, A. (2000). Polarization of cell growth in yeast. J. Cell. Sci. 113 (Pt 4), 571–585.

Puttur, F.K., Fernandez, M.A., White, R., Roediger, B., Cunningham, A.L., Weninger, W., and Jones, C.A. (2010). Herpes simplex virus infects skin gamma delta T cells before Langerhans cells and impedes migration of infected Langerhans cells by inducing apoptosis and blocking E-cadherin downregulation. J. Immunol. 185, 477–487.

Qi, H., Egen, J.G., Huang, A.Y.C., and Germain, R.N. (2006). Extrafollicular activation of lymph node B cells by antigen-bearing dendritic cells. Science 312, 1672–1676.

Rahemtulla, A., Fung-Leung, W.P., Schilham, M.W., Kündig, T.M., Sambhara, S.R., Narendran, A., Arabian, A., Wakeham, A., Paige, C.J., and Zinkernagel, R.M. (1991). Normal development and function of CD8+ cells but markedly decreased helper cell activity in mice lacking CD4. Nature 353, 180–184.

Ramundo, J. (2012). Wound debridement. In Acute and Chronic Wounds: Current Management Concepts (4th ed.) ,R. Bryant, and D. Nix, eds. (St. Louis, MO: Elsevier Mosby), pp. 279-299.

Randall, K.L., Lambe, T., Johnson, A.L., Johnson, A., Treanor, B., Kucharska, E., Domaschenz, H., Whittle, B., Tze, L.E., Enders, A., et al. (2009). Dock8 mutations cripple B cell immunological synapses, germinal centers and long-lived antibody production. Nat. Immunol. 10, 1283–1291.

Randall, K.L., Chan, S.S.Y., Ma, C.S., Fung, I., Mei, Y., Yabas, M., Tan, A., Arkwright, P.D., Suwairi, Al, W., Lugo Reyes, S.O., et al. (2011). DOCK8 deficiency impairs CD8 T cell survival and function in humans and mice. Journal of Experimental Medicine 208, 2305–2320.

Randolph, G.J., Ochando, J., and Partida-Sánchez, S. (2008). Migration of dendritic cell subsets and their precursors. Annu. Rev. Immunol. 26, 293–316.

Rawls, W.E., Laurel, D., Melnick, J.L., Glicksman, J.M., and Kaufman, R.H. (1968). A search for viruses in smegma, premalignant and early malignant cervical tissues. The isolation of Herpesviruses with distinct antigenic properties. Am. J. Epidemiol. 87, 647–655.

Reiss, Y., Proudfoot, A.E., Power, C.A., Campbell, J.J., and Butcher, E.C. (2001). CC chemokine receptor (CCR)4 and the CCR10 ligand cutaneous T cell-attracting chemokine (CTACK) in lymphocyte trafficking to inflamed skin. J. Exp. Med. 194, 1541–1547.

Ridge, J.P., Di Rosa, F., and Matzinger, P. (1998). A conditioned dendritic cell can be a temporal bridge between a CD4+ T-helper and a T-killer cell. Nature 393, 474–478.

Rodero, M.P., Licata, F., Poupel, L., Hamon, P., Khosrotehrani, K., Combadière, C., and Boissonnas, A. (2014). In vivo imaging reveals a pioneer wave of monocyte recruitment into mouse skin wounds. PLoS ONE 9, e108212.

Rodgers, B., and Mims, C.A. (1981). Interaction of influenza virus with mouse macrophages. Infect. Immun. 31, 751–757.

Romani, N., Clausen, B.E., and Stoitzner, P. (2010). Langerhans cells and more: langerin-expressing dendritic cell subsets in the skin. Immunol. Rev. 234, 120–141.

Ruusala, A., and Aspenström, P. (2004). Isolation and characterisation of DOCK8, a member of the DOCK180-related regulators of cell morphology. FEBS Lett. 572, 159–166.

Saccheri, F., Pozzi, C., Avogadri, F., Barozzi, S., Faretta, M., Fusi, P., and Rescigno, M. (2010). Bacteria-induced gap junctions in tumors favor antigen cross-presentation and antitumor immunity. Sci Transl Med 2, 44ra57.

Sadik, C.D., Kim, N.D., and Luster, A.D. (2011). Trends in Immunology - Neutrophils cascading their way to inflammation. Trends Immunol. 32, 452–460.

Salio, M., Cella, M., Suter, M., and Lanzavecchia, A. (1999). Inhibition of dendritic cell maturation by herpes simplex virus. Eur. J. Immunol. 29, 3245–3253.

Sallusto, F., Schaerli, P., Loetscher, P., Schaniel, C., Lenig, D., Mackay, C.R., Qin, S., and Lanzavecchia, A. (1998). Rapid and coordinated switch in chemokine receptor expression during dendritic cell maturation. Eur. J. Immunol. 28, 2760–2769.

Sallusto, F., Geginat, J., and Lanzavecchia, A. (2004). Central memory and effector memory T cell subsets: function, generation, and maintenance. Annu. Rev. Immunol. 22, 745–763.

Sancho, D., Joffre, O.P., Keller, A.M., Rogers, N.C., Martínez, D., Hernanz-Falcón, P., Rosewell, I., and Reis e Sousa, C. (2009). Identification of a dendritic cell receptor that couples sensing of necrosis to immunity. Nature 458, 899–903.

Sato, A., Linehan, M.M., and Iwasaki, A. (2006). Dual recognition of herpes simplex viruses by TLR2 and TLR9 in dendritic cells. Proc. Natl. Acad. Sci. U.S.a. 103, 17343–17348.

Savina, A., Jancic, C., Hugues, S., Guermonprez, P., Vargas, P., Moura, I.C., Lennon-Dumenil, A.-M., Seabra, M.C., Raposo, G., and Amigorena, S. (2006). NOX2 controls phagosomal pH to regulate antigen processing during crosspresentation by dendritic cells. Cell 126, 205–218.

Savina, A., Peres, A., Cebrian, I., Carmo, N., Moita, C., Hacohen, N., Moita, L.F., and Amigorena, S. (2009). The small GTPase Rac2 controls phagosomal alkalinization and antigen crosspresentation selectively in CD8(+) dendritic cells. Immunity 30, 544–555.

Schelhaas, M., Jansen, M., Haase, I., and Knebel-Mörsdorf, D. (2003). Herpes simplex virus type 1 exhibits a tropism for basal entry in polarized epithelial cells. J. Gen. Virol. 84, 2473–2484.

Schenkel, J.M., Fraser, K.A., Beura, L.K., Pauken, K.E., Vezys, V., and Masopust, D. (2014). Resident memory CD8 T cells trigger protective innate and adaptive immune responses. Science 346, 98–101.

Schillinger, J.A., Xu, F., Sternberg, M.R., Armstrong, G.L., Lee, F.K., Nahmias, A.J., McQuillan, G.M., Louis, M.E., and Markowitz, L.E. (2004). National seroprevalence and trends in herpes simplex virus type 1 in the United States, 1976-1994. Sex Transm Dis 31, 753–760.

Schlitzer, A., McGovern, N., Teo, P., Zelante, T., Atarashi, K., Low, D., Ho, A.W.S., See, P., Shin, A., Wasan, P.S., et al. (2013). IRF4 transcription factor-dependent CD11b+ dendritic cells in human and mouse control mucosal IL-17 cytokine responses. Immunity 38, 970–983.

Schneider, W.M., Chevillotte, M.D., and Rice, C.M. (2014). Interferon-stimulated genes: a complex web of host defenses. Annu. Rev. Immunol. 32, 513–545.

Schnorrer, P., Behrens, G.M.N., Wilson, N.S., Pooley, J.L., Smith, C.M., El-Sukkari, D., Davey, G., Kupresanin, F., Li, M., Maraskovsky, E., et al. (2006). The dominant role of CD8+ dendritic cells in cross-presentation is not dictated by antigen capture. Proc. Natl. Acad. Sci. U.S.a. 103, 10729–10734.

Schoenberger, S.P., Toes, R.E., van der Voort, E.I., Offringa, R., and Melief, C.J. (1998). T-cell help for cytotoxic T lymphocytes is mediated by CD40-CD40L interactions. Nature 393, 480–483.

Schulz, O., and Reis e Sousa, C. (2002). Cross-presentation of cell-associated antigens by CD8alpha+ dendritic cells is attributable to their ability to internalize dead cells. Immunology 107, 183–189.

Serre, K., Giraudo, L., Siret, C., Leserman, L., and Machy, P. (2006). CD4 T cell help is required for primary CD8 T cell responses to vesicular antigen delivered to dendritic cells in vivo. Eur. J. Immunol. 36, 1386–1397.

Sevilla, N., McGavern, D.B., Teng, C., Kunz, S., and Oldstone, M.B.A. (2004). Viral targeting of hematopoietic progenitors and inhibition of DC maturation as a dual strategy for immune subversion. J. Clin. Invest. 113, 737–745.

Shakhar, G., Lindquist, R.L., Skokos, D., Dudziak, D., Huang, J.H., Nussenzweig, M.C., and Dustin, M.L. (2005). Stable T cell-dendritic cell interactions precede the development of both tolerance and immunity in vivo. Nat. Immunol. 6, 707–714.

Shedlock, D.J., and Shen, H. (2003). Requirement for CD4 T cell help in generating functional CD8 T cell memory. Science 300, 337–339.

Shieh, M.T., WuDunn, D., Montgomery, R.I., Esko, J.D., and Spear, P.G. (1992). Cell surface receptors for herpes simplex virus are heparan sulfate proteoglycans. J. Cell Biol. 116, 1273–1281.

Shiow, L.R., Rosen, D.B., Brdickova, N., Xu, Y., An, J., Lanier, L.L., Cyster, J.G., and Matloubian, M. (2006). CD69 acts downstream of interferon- a / b to inhibit S1P 1 and lymphocyte egress from lymphoid organs. Nature 440, 4–8.

Shortman, K., and Heath, W.R. (2010). The CD8+ dendritic cell subset - Shortman - 2010 - Immunological Reviews - Wiley Online Library. Immunol. Rev. 234, 18–31.

Shukla, D., and Spear, P.G. (2001). Herpesviruses and heparan sulfate: an intimate relationship in aid of viral entry. J. Clin. Invest. 108, 503–510.

Siegal, F.P., Kadowaki, N., Shodell, M., Fitzgerald-Bocarsly, P.A., Shah, K., Ho, S., Antonenko, S., and Liu, Y.J. (1999). The nature of the principal type 1 interferon-producing cells in human blood. Science 284, 1835–1837.

Simmons, A., and Tscharke, D.C. (1992). Anti-CD8 impairs clearance of herpes simplex virus from the nervous system: implications for the fate of virally infected neurons. J. Exp. Med. 175, 1337–1344.

Singh, R., and Cresswell, P. (2010). Defective cross-presentation of viral antigens in GILT-free mice. Science 328, 1394–1398.

Sixt, M., Kanazawa, N., Selg, M., Samson, T., Roos, G., Reinhardt, D.P., Pabst, R., Lutz, M.B., and Sorokin, L. (2005). The conduit system transports soluble antigens from the afferent lymph to resident dendritic cells in the T cell area of the lymph node. Immunity 22, 19–29.

Skokos, D., Shakhar, G., Varma, R., Waite, J.C., Cameron, T.O., Lindquist, R.L., Schwickert, T., Nussenzweig, M.C., and Dustin, M.L. (2007). Peptide-MHC potency governs dynamic interactions between T cells and dendritic cells in lymph nodes. Nat. Immunol. 8, 835–844.

Smith, P.M., Wolcott, R.M., Chervenak, R., and Jennings, S.R. (1994). Control of acute cutaneous herpes simplex virus infection: T cell-mediated viral clearance is dependent upon interferon-gamma (IFN-gamma). Virology 202, 76–88.

Smith, C.M., Wilson, N.S., Waithman, J., Villadangos, J.A., Carbone, F.R., Heath, W.R., and Belz, G.T. (2004). Cognate CD4(+) T cell licensing of dendritic cells in CD8(+) T cell immunity. Nat. Immunol. 5, 1143–1148.

Soderberg, K.A., Payne, G.W., Sato, A., Medzhitov, R., Segal, S.S., and Iwasaki, A. (2005). Innate control of adaptive immunity via remodeling of lymph node feed arteriole. Proc. Natl. Acad. Sci. U.S.a. 102, 16315–16320.

Soehnlein, O., and Lindbom, L. (2010). Phagocyte partnership during the onset and resolution of inflammation. Nat Rev Immunol 10, 427–439.

Sørensen, L.N., Reinert, L.S., Malmgaard, L., Bartholdy, C., Thomsen, A.R., and Paludan, S.R. (2008). TLR2 and TLR9 synergistically control herpes simplex virus infection in the brain. J. Immunol. 181, 8604–8612.

Sozzani, S., Luini, W., Borsatti, A., Polentarutti, N., Zhou, D., Piemonti, L., D'Amico, G., Power, C.A., Wells, T.N., Gobbi, M., et al. (1997). Receptor expression and responsiveness of human dendritic cells to a defined set of CC and CXC chemokines. J. Immunol. 159, 1993–2000.

Spaan, A.N., Surewaard, B.G.J., Nijland, R., and van Strijp, J.A.G. (2013). Neutrophils versus Staphylococcus aureus: a biological tug of war. Annu. Rev. Microbiol. 67, 629–650.

Spear, P.G., and Longnecker, R. (2003). Herpesvirus entry: an update. J. Virol. 77, 10179–10185.

Springer, T.A. (1994). Traffic signals for lymphocyte recirculation and leukocyte emigration: the multistep paradigm. Cell.

Stemberger, C., Huster, K.M., Koffler, M., Anderl, F., Schiemann, M., Wagner, H., and Busch, D.H. (2007). A single naive CD8+ T cell precursor can develop into diverse effector and memory subsets. Immunity 27, 985–997.

Stock, A.T., Mueller, S.N., van Lint, A.L., Heath, W.R., and Carbone, F.R. (2004). Cutting edge: prolonged antigen presentation after herpes simplex virus-1 skin infection. J. Immunol. 173, 2241–2244.

Stock, A.T., Mueller, S.N., Kleinert, L.M., Heath, W.R., Carbone, F.R., and Jones, C.M. (2007). Optimization of TCR transgenic T cells for in vivo tracking of immune responses. Immunol. Cell Biol. 85, 394–396.

Stoitzner, P., Pfaller, K., Stössel, H., and Romani, N. (2002). A close-up view of migrating Langerhans cells in the skin. J. Invest. Dermatol. 118, 117–125.

Su, H.C. (2010). Dedicator of cytokinesis 8 (DOCK8) deficiency. Curr Opin Allergy Clin Immunol 10, 515–520.

Summers deLuca, L., Ng, D., Gao, Y., Wortzman, M.E., Watts, T.H., and Gommerman, J.L. (2011). LTβR signaling in dendritic cells induces a type I IFN response that is required for optimal clonal expansion of CD8+ T cells. Proc. Natl. Acad. Sci. U.S.a. 108, 2046–2051.

Sun, J.C., and Bevan, M.J. (2004). Cutting edge: long-lived CD8 memory and protective immunity in the absence of CD40 expression on CD8 T cells. J. Immunol. 172, 3385–3389.

Sung, J.H., Zhang, H., Moseman, E.A., Alvarez, D., Iannacone, M., Henrickson, S.E., la Torre, de, J.C., Groom, J.R., Luster, A.D., and von Andrian, U.H. (2012). Chemokine Guidance of Central Memory T Cells Is Critical for Antiviral Recall Responses in Lymph Nodes. Cell 150, 1249–1263.

Supajatura, V., Ushio, H., Nakao, A., Akira, S., Okumura, K., Ra, C., and Ogawa, H. (2002). Differential responses of mast cell Toll-like receptors 2 and 4 in allergy and innate immunity. J. Clin. Invest. 109, 1351–1359.

Swiecki, M., and Colonna, M. (2015). The multifaceted biology of plasmacytoid dendritic cells. Nat Rev Immunol 15, 471–485.

Tal, O., Lim, H.Y., Gurevich, I., Milo, I., Shipony, Z., Ng, L.G., Angeli, V., and Shakhar, G. (2011). DC mobilization from the skin requires docking to immobilized CCL21 on lymphatic endothelium and intralymphatic crawling. J. Exp. Med. 208, 2141–2153.

Tate, M.D., Brooks, A.G., Reading, P.C., and Mintern, J.D. (2012). Neutrophils sustain effective CD8(+) T-cell responses in the respiratory tract following influenza infection. Immunol. Cell Biol. 90, 197–205.

Thammavongsa, V., Kim, H.K., Missiakas, D., and Schneewind, O. (2015). Staphylococcal manipulation of host immune responses. Nat Rev Micro 13, 529–543.

Theil, D., Derfuss, T., Paripovic, I., Herberger, S., Meinl, E., Schueler, O., Strupp, M., Arbusow, V., and Brandt, T. (2003). Latent herpesvirus infection in human trigeminal ganglia causes chronic immune response. Am. J. Pathol. 163, 2179–2184.

Theodoridis, A.A., Eich, C., Figdor, C.G., and Steinkasserer, A. (2011). Infection of dendritic cells with herpes simplex virus type 1 induces rapid degradation of CYTIP, thereby modulating adhesion and migration. Blood 118, 107–115.

Théry, C., Ostrowski, M., and Segura, E. (2009). Membrane vesicles as conveyors of immune responses. Nat Rev Immunol 9, 581–593.

Tigges, M.A., Leng, S., Johnson, D.C., and Burke, R.L. (1996). Human herpes simplex virus (HSV)-specific CD8+ CTL clones recognize HSV-2-infected fibroblasts after treatment with IFN-gamma or when virion host shutoff functions are disabled. J. Immunol. 156, 3901–3910.

Tomazin, R., van Schoot, N.E., Goldsmith, K., Jugovic, P., Sempé, P., Früh, K., and Johnson, D.C. (1998). Herpes simplex virus type 2 ICP47 inhibits human TAP but not mouse TAP. J. Virol. 72, 2560–2563.

Tomura, M., Yoshida, N., Tanaka, J., Karasawa, S., Miwa, Y., Miyawaki, A., and Kanagawa, O. (2008). Monitoring cellular movement in vivo with photoconvertible fluorescence protein "Kaede" transgenic mice. Proc. Natl. Acad. Sci. U.S.a. 105, 10871–10876.

Tong, P.L., Roediger, B., Kolesnikoff, N., Biro, M., Tay, S.S., Jain, R., Shaw, L.E., Grimbaldeston, M.A., and Weninger, W. (2015). The skin immune atlas: three-dimensional analysis of cutaneous leukocyte subsets by multiphoton microscopy. J. Invest. Dermatol. 135, 84–93.

Tough, D.F., Borrow, P., and Sprent, J. (1996). Induction of bystander T cell proliferation by viruses and type I interferon in vivo. Science 272, 1947–1950.

Tscharke, D.C., Croft, N.P., Doherty, P.C., and La Gruta, N.L. (2015). Sizing up the key determinants of the CD8(+) T cell response. Nat Rev Immunol 15, 705–716.

Upham, J.P., Pickett, D., Irimura, T., Anders, E.M., and Reading, P.C. (2010). Macrophage receptors for influenza A virus: role of the macrophage galactose-type lectin and mannose receptor in viral entry. J. Virol. 84, 3730–3737.

van den Berg, J.M., Weyer, S., Weening, J.J., Roos, D., and Kuijpers, T.W. (2001). Divergent effects of tumor necrosis factor alpha on apoptosis of human neutrophils. J. Leukoc. Biol. 69, 467–473.

van Faassen, H., Saldanha, M., Gilbertson, D., Dudani, R., Krishnan, L., and Sad, S. (2005). Reducing the stimulation of CD8+ T cells during infection with intracellular bacteria promotes differentiation primarily into a central (CD62LhighCD44high) subset. J. Immunol. 174, 5341–5350.

van Lint, A., Ayers, M., Brooks, A.G., Coles, R.M., Heath, W.R., and Carbone, F.R. (2004). Herpes simplex virus-specific CD8+ T cells can clear established lytic infections from skin and nerves and can partially limit the early spread of virus after cutaneous inoculation. J. Immunol. 172, 392–397.

van Lint, A.L., Kleinert, L., Clarke, S.R.M., Stock, A., Heath, W.R., and Carbone, F.R. (2005). Latent infection with herpes simplex virus is associated with ongoing CD8+ T-cell stimulation by parenchymal cells within sensory ganglia. J. Virol. 79, 14843–14851.

van Stipdonk, M.J.B., Hardenberg, G., Bijker, M.S., Lemmens, E.E., Droin, N.M., Green, D.R., and Schoenberger, S.P. (2003). Dynamic programming of CD8+ T lymphocyte responses. Nat. Immunol. 4, 361–365.

Vandermeulen, G., Vanvarenberg, K., De Beuckelaer, A., De Koker, S., Lambricht, L., Uyttenhove, C., Reschner, A., Vanderplasschen, A., Grooten, J., and Préat, V. (2015). The site of administration influences both the type and the magnitude of the immune response induced by DNA vaccine electroporation. Vaccine 33, 3179–3185.

Vollstedt, S., Arnold, S., Schwerdel, C., Franchini, M., Alber, G., Di Santo, J.P., Ackermann, M., and Suter, M. (2004). Interplay between alpha/beta and gamma interferons with B, T, and natural killer cells in the defense against herpes simplex virus type 1. J. Virol. 78, 3846–3850.

von Andrian, U.H., and Mempel, T.R. (2003). Homing and cellular traffic in lymph nodes. Nat Rev Immunol 3, 867–878.

Wakim, L.M., and Bevan, M.J. (2011). Cross-dressed dendritic cells drive memory CD8+ T-cell activation after viral infection. Nature 471, 629–632.

Wallace, M.E., Keating, R., Heath, W.R., and Carbone, F.R. (1999). The cytotoxic T-cell response to herpes simplex virus type 1 infection of C57BL/6 mice is almost entirely directed against a single immunodominant determinant. J. Virol. 73, 7619–7626.

Wang, L., Bursch, L.S., Kissenpfennig, A., Malissen, B., Jameson, S.C., and Hogquist, K.A. (2008). Langerin expressing cells promote skin immune responses under defined conditions. J. Immunol. 180, 4722–4727.

Weir, J.P. (2001). Regulation of herpes simplex virus gene expression. Gene 271, 117–130.

Whitbeck, J.C., Muggeridge, M.I., Rux, A.H., Hou, W., Krummenacher, C., Lou, H., van Geelen, A., Eisenberg, R.J., and Cohen, G.H. (1999). The major neutralizing antigenic site on herpes simplex virus glycoprotein D overlaps a receptor-binding domain. J. Virol. 73, 9879–9890.

Williams, M.A., and Bevan, M.J. (2007). Effector and memory CTL differentiation. Annu. Rev. Immunol. 25, 171–192.

Williams, M.R., Azcutia, V., Newton, G., Alcaide, P., and Luscinskas, F.W. (2011). Emerging mechanisms of neutrophil recruitment across endothelium. Trends Immunol. 32, 461–469.

Wojtasiak, M., Pickett, D.L., Tate, M.D., Londrigan, S.L., Bedoui, S., Brooks, A.G., and Reading, P.C. (2010a). Depletion of Gr-1+, but not Ly6G+, immune cells exacerbates virus replication and disease in an intranasal model of herpes simplex virus type 1 infection. J. Gen. Virol. 91, 2158–2166.

Wojtasiak, M., Pickett, D.L., Tate, M.D., Bedoui, S., Job, E.R., Whitney, P.G., Brooks, A.G., and Reading, P.C. (2010b). Gr-1+ cells, but not neutrophils, limit virus replication and lesion development following flank infection of mice with herpes simplex virus type-1. Virology 407, 143–151.

Worbs, T., Mempel, T.R., Bölter, J., von Andrian, U.H., and Förster, R. (2007). CCR7 ligands stimulate the intranodal motility of T lymphocytes in vivo. J. Exp. Med. 204, 489–495.

WuDunn, D., and Spear, P.G. (1989). Initial interaction of herpes simplex virus with cells is binding to heparan sulfate. J. Virol. 63, 52–58.

Wülfing, C., Rabinowitz, J.D., Beeson, C., Sjaastad, M.D., McConnell, H.M., and Davis, M.M. (1997). Kinetics and extent of T cell activation as measured with the calcium signal. J. Exp. Med. 185, 1815–1825.

Xu, R.-H., Remakus, S., Ma, X., Roscoe, F., and Sigal, L.J. (2010). Direct presentation is sufficient for an efficient anti-viral CD8+ T cell response. PLoS Pathog. 6, e1000768.

Xu, H., Li, X., Liu, D., Li, J., Zhang, X., Chen, X., Hou, S., Peng, L., Xu, C., Liu, W., et al. (2013). Follicular T-helper cell recruitment governed by bystander B cells and ICOS-driven motility. Nature 496, 523–527.

Yamanaka, Y.J., Gierahn, T.M., and Love, J.C. (2012). The dynamic lives of T cells: new approaches and themes. Trends Immunol.

Yamazaki, C., Sugiyama, M., Ohta, T., Hemmi, H., Hamada, E., Sasaki, I., Fukuda, Y., Yano, T., Nobuoka, M., Hirashima, T., et al. (2013). Critical roles of a dendritic cell subset expressing a chemokine receptor, XCR1. J. Immunol. 190, 6071–6082.

Yang, C.-W., and Unanue, E.R. (2013). Neutrophils control the magnitude and spread of the immune response in a thromboxane A2-mediated process. Journal of Experimental Medicine.

Yoneyama, H., Narumi, S., Zhang, Y., Murai, M., Baggiolini, M., Lanzavecchia, A., Ichida, T., Asakura, H., and Matsushima, K. (2002). Pivotal role of dendritic cell-derived CXCL10 in the retention of T helper cell 1 lymphocytes in secondary lymph nodes. J. Exp. Med. 195, 1257–1266.

Yoon, M., and Spear, P.G. (2002). Disruption of adherens junctions liberates nectin-1 to serve as receptor for herpes simplex virus and pseudorabies virus entry. J. Virol. 76, 7203–7208.

Zaid, A., Mackay, L.K., Rahimpour, A., Braun, A., Veldhoen, M., Carbone, F.R., Manton, J.H., Heath, W.R., and Mueller, S.N. (2014). Persistence of skin-resident memory T cells within an epidermal niche. Proc. Natl. Acad. Sci. U.S.a. 111, 5307–5312.

Zehn, D., Lee, S.Y., and Bevan, M.J. (2009). Complete but curtailed T-cell response to very low-affinity antigen. Nature 458, 211–214.

Zhang, S.-Y., Jouanguy, E., Ugolini, S., Smahi, A., Elain, G., Romero, P., Segal, D., Sancho-Shimizu, V., Lorenzo, L., Puel, A., et al. (2007). TLR3 deficiency in patients with herpes simplex encephalitis. Science 317, 1522–1527.

Zhang, Q., Davis, J.C., Lamborn, I.T., Freeman, A.F., Jing, H., Favreau, A.J., Matthews, H.F., Davis, J., Turner, M.L., Uzel, G., et al. (2009). Combined immunodeficiency associated with DOCK8 mutations. N Engl J Med 361, 2046–2055.

Zhang, Q., Raoof, M., Chen, Y., Sumi, Y., Sursal, T., Junger, W., Brohi, K., Itagaki, K., and Hauser, C.J. (2010). Circulating mitochondrial DAMPs cause inflammatory responses to injury. Nature 464, 104–107.

Zhang, J.-G., Czabotar, P.E., Policheni, A.N., Caminschi, I., Wan, S.S., Kitsoulis, S., Tullett, K.M., Robin, A.Y., Brammananth, R., van Delft, M.F., et al. (2012). The dendritic cell receptor Clec9A binds damaged cells via exposed actin filaments. Immunity 36, 646–657.

Zhang, Q., Dove, C.G., Hor, J.L., Murdock, H.M., Strauss-Albee, D.M., Garcia, J.A., Mandl, J.N., Grodick, R.A., Jing, H., Chandler-Brown, D.B., et al. (2014). DOCK8 regulates lymphocyte shape integrity for skin antiviral immunity. J. Exp. Med. 211, 2549–2566.